29

Polynuclear Iron and Manganese Complexes As Models for Biological Systems

by

David P. Goldberg

B.A., Williams College (1989)

Submitted to the Department of Chemistry
in Partial Fulfillment of the Requirements for the
degree of

Doctor of Philosophy

at the

Massachusetts Institute of Technology

February, 1995

Signature of Author____
Department of Chemistry
October 31, 1994

Certified by____
Professor Stephen J. Lippard
Thesis Supervisor

Accepted by____
Professor Dietmar Seyferth
Chairman, Departmental Committee on Graduate Students

This doctoral thesis has been examined by a Committee of the Department of Chemistry as follows:

Professor Alan Davison, Committee Chairman

Professor Stephen J. Lippard

Arthur Amos Noyes Professor of Chemistry

Professor Moungi Bawendi

Polynuclear Iron and Manganese Complexes As Models for Biological Systems

by

David P. Goldberg

Submitted to the Department of Chemistry on October 31, 1994 in partial fulfillment of the requirements for the degree of Doctor of Philosophy.

Abstract

Chapter 1. Modeling Phenoxyl Radical Metalloenzyme Active Sites.

A phenoxyl radical has been implicated in the functioning of three metalloenzymes, ribonucleotide reductase, galactose oxidase, and prostaglandin H synthase. A brief summary of these three systems is presented, focusing on the role of the metal/phenoxyl radical active site. Several ligand systems designed to provide a phenoxyl radical coordinated to a metal center are described. The synthesis and characterization of the phenol/phenoxyl radical metal complexes from these ligands are presented, and the potential of these compounds to provide small-molecule mimics for the biological systems is discussed. Finally, progress toward modeling the phenoxyl radical diiron center in ribonucleotide reductase is described.

Chapter 2. A Phenoxyl Radical (μ-Oxo)bis(μ-Carboxylato)Diiron(III) Complex as a Model for the Active Site of the R2 Protein of Ribonucleotide Reductase.

The design and synthesis of a new bidentate imidazole donor ligand with a pendant phenoxyl radical arm are described. This ligand, BIDPhE, allowed for the preparation and isolation of the stable phenoxyl radical diiron(III) complex $[Fe_2O(XDK)(BIDPhE)_2(NO_3)_2]$, a model for the active site of the R2 protein in ribonucleotide reductase. Magnetic susceptibility, X-band cw-EPR, and pulsed saturation-recovery cw-EPR investigations of this model complex and revealed behavior strikingly similar to that found for the redox active center in the R2 protein. The mononuclear iron complex $[Fe(BIDPhEH)Cl_2]^+$ has been prepared and crystallographically characterized, providing valuable structural information of relevance to the dinuclear iron system. The mononuclear zinc complex $[Zn(BIDPhE)Cl_2]$, proved to be an important control compound for interpreting the saturation-recovery EPR measurements. A theoretical fit of both the magnetic susceptibility and saturation-recovery data gave results which were fully consistent with one another.

Chapter 3. Ferromagnetic versus Antiferromagnetic Exchange in Five Structurally Analogous Carboxylate-Bridged Trinuclear Ferrous Complexes.

The synthesis, structural characterization and magnetic properties of five linear, trinuclear complexes of general formula $[Fe_3(O_2CR)_6L_2]$ are reported. Addition of $Fe(OAc)_2$ to the bidentate nitrogen donor ligands BIPhOH and

BIDPhEH afforded $[Fe_3(OAc)_6(BIPhOH)_2]\cdot 2MeOH$ (**3**) and $[Fe_3(OAc)_6(BIDPhEH)_2]$ (**4**), respectively. Addition of $Fe(BF_4)_2\cdot 6H_2O$ and sodium benzoate to the ligands ^{i}PrOx and PheMe$_3$Eda yielded compounds $[Fe_3(O_2CPh)_6(^{i}PrOx)_2]$ (**5**) and $[Fe_3(OBz)_6(PheMe_3Eda)_2]$ (**6**), respectively. In all of these complexes, the iron atoms are linked by two bidentate and one unidentate bridging carboxylate ligands. The coordination spheres of the terminal iron atoms are completed by the bidentate nitrogen ligands and, in the case of **5** and **6**, by the second "dangling" oxygen atom of the unidentate bridging carboxylate. We investigated the magnetic properties of these four compounds, as well as that of $[Fe_3(OAc)_6(BIPhMe)_2]$ (**1**). Three of the complexes (**1**, **3** and **4**) exhibit ferromagnetic coupling, resulting in high spin ground states, and the remaining two complexes are antiferromagnetically coupled. The magnetic data were fit to a theoretical model incorporating exchange coupling, single-ion zero-field splitting, and **g**-tensor anisotropy. The X-band EPR spectra of **1**, **3**, and **4** at 4 K displayed broad, low-field signals which are quite similar to those of the reduced, diiron(II) centers found in the non-heme iron proteins methane monooxygenase (MMOH), hemerythrin (Hr), and the R2 protein of ribonucleotide reductase.

Chapter 4. A Decanuclear Manganese Cluster with Oxo and Halide Bridging Ligands : Magnetic Behavior of an S ≥ 12 System.

The bis(phenoxo) donor ligand, deprotonated 2,2'-biphenol, and simple manganese halide salts combine to form a novel mixed-valent decanuclear complex of formula $[Mn_{10}O_4(biphen)_4X_{12}]^{4-}$ (X = Cl^-, Br^-). The syntheses of three related decanuclear manganese complexes, $[Me_4N]_4[Mn_{10}O_4(biphen)_4Cl_{12}]$ (**1**), $[Me_4N]_4[Mn_{10}O_4(biphen)_4Br_{12}]$ (**2**), and $[Mn(CH_3CN)_4(H_2O)_2][Et_3NH]_2[Mn_{10}O_4(biphen)_4Br_{12}]$ (**3**) are described. These complexes have been structurally characterized by X-ray diffraction. They belong to a very small class of high-nuclearity manganese clusters held together by bridging ligands other than the carboxylate moiety. Compound **2** also provides a rare example of bromide ligands bridging between Mn(III) atoms. Compounds **1** - **3** are mixed-valent, with four Mn(III) atoms and six Mn(II) atoms comprising the cluster. All of the manganese centers are valence-localized, and the octahedral Mn(III) sites exhibit marked Jahn-Teller axial elongations. The bridging ligands bind in a variety of modes, with four μ_4-oxo ligands at the core of the cluster. The magnetic properties of compounds **1** - **3** have been studied, revealing remarkably high spin ground states. Magnetic susceptibility, high-field magnetization and X-band cw-EPR measurements have been used to probe the general magnetic behavior and spin ground states of compounds **1** - **3**. Theoretical calculations provide a framework in which to understand the origin of the high spin ground states for these complexes.

Thesis Supervisor: Professor Stephen J. Lippard
Title: Arthur Amos Noyes Professor of Chemistry

Acknowledgements

The most important part of my experience at M.I.T. has been the people I have met in the laboratory. The Lippard lab is extremely fortunate to have a constant flux of a wide variety of people and personalities, providing a truly stimulating scientific environment and fascinating personal landscape. Perhaps the most valuable lesson I have learned here is to try and put the people around you as the top priority, and avoid the selfishness and ill-temper that personal pressures and stress can so easily create. Only through many examples of people helping and working with me have I come to appreciate this concept.

This thesis would not have been possible without the superb research atmosphere that Steve Lippard creates and maintains. Steve's deep well of energy and enthusiasm for science, as well as his knowledge of structural inorganic chemistry are to be commended, along with the freedom and support he gave me down the many paths this thesis has taken. Several people must be thanked for making life in and outside the lab as enjoyable as it was. I was lucky enough to be assigned the new post-doc from Belgium, Axel Masschelein, as a baymate, who must be thanked for his enduring friendship and exemplary personal style. The European tradition continued with the arrival of Andrea Caneschi from Italy. Andrea opened my eyes to the field of magnetism in chemistry and had a profound influence, together with Roberta Sessoli back at the home base in Firenze, on my current scientific direction. Sofi Elmroth, all the way from snowy Lundt, Sweden, was another welcome European import to M.I.T. The most recent arrival from across the Atlantic is Susanna Herold, who has been an excellent addition to my final ten months.

Ken Comess and Amy Rosenzweig gave me many hours of sheer fun in the early years, and continue to do so. Other people with whom I have overlapped for a significant amount of time and should be recognized for their personal and professional contributions are Christy Chow, Steve Brown, Pieter Pil, John Protasiewicz, JoAnne Yun, Steve Dunham, Jonathan Wilker, Sonja Komar-Panicucci, Ann Valentine and Rajesh Manchandra. I was very fortunate that Maria Bautista arrived in time to lend me her computer for finishing this thesis! I am indebted to Kathy Liu for being there for five years.

All the people who made the inorganic synthetic subgroup the one of choice need to be thanked, especially Cecilia Bastos, Steve Watton, King Taft, Laura Pence and Shibao Yu, who gave me a significant amount of help on many levels. Thanks goes to LeAnne Wimmer, a UROP student who worked on part of

the project described in the second chapter. I must also thank Tong Ren for his inspirational command of the literature and superb crystallographic knowledge.

I must thank my housemates for four excellent years at 893 Broadway. I am grateful to Mom, Dad and my sister Sara for much love and support during my graduate school training.

Contents

List of Tables

Chapter 2.

Chapter 3.

Chapter 4.

List of Schemes

Chapter 2.

List of Figures

Chapter 1.

Chapter 2.

Chapter 3.

Chapter 4.

Chapter 1

Modeling Phenoxyl Radical Metalloenzyme Active Sites

INTRODUCTION

Radical cofactors in biological systems have become a subject of increasing interest in recent years (1-3). Tyrosine-based radicals, in particular, have now been identified in several enzymes (4). The tyrosine residue functions as a redox-active cofactor by interconverting between the oxidized phenoxyl radical and the normal phenol or phenolate states. More commonly known redox-active cofactors include transition metal ions, and a few enzymes employ both tyrosine residues and metals as partners in effecting redox chemistry.

Mechanistic pathways that explore this theme have been proposed for three metalloenzymes, ribonucleotide reductase, galactose oxidase and prostaglandin H synthase. In each of these cases mechanisms have been proposed which include one or two transition metals working in concert with a redox-active tyrosine group. Dioxygen and hydrogen peroxide have been implicated as agents responsible for generating these stable tyrosyl radicals, with a concomitant redox change at the metal site. In the present article, we discuss these three systems, concentrating on the properties of the metal active site and the characterization of the tyrosyl radicals. Current mechanistic hypotheses about the generation and function of the tyrosyl radical/metal active sites found in these enzymes are presented. We focus on the metal-radical partnership as well as the roles of dioxygen and hydrogen peroxide in generating and maintaining the tyrosyl radical.

In order to model the oxo-bridged diiron(III) phenoxyl radical active site found in the R2 protein of *Escherichia coli* ribonucleotide reductase (RR), we recently designed and synthesized a new bidentate nitrogen donor ligand which harbors a pendant phenol moiety. Complexes of both the non-radical phenol and phenoxyl radical forms of this ligand are described, including a dinuclear iron compound that reproduces some of the key physical properties of the R2 protein

active site. This work was carried out as part of a broader program in which first row transition metal complexes are synthesized as models for the active sites of a variety of metalloenzymes (5). These activities were recently expanded to include models for the active sites of enzymes containing both first row transition metal ions and phenoxyl radicals. Our ultimate goal is to prepare compounds that can serve as functional mimics for these sites. In particular, we wish to understand better the mechanism of radical generation and the synergistic relationship between the metal ion and phenoxyl radical in the functioning biological systems.

Previous work by other groups has led to the synthesis of various ligands incorporating sterically hindered phenol substituents for the generation of phenoxyl radical metal complexes (*vide infra*). These systems were designed to allow for delocalization of the phenoxyl radical spin from phenyl ring out onto the metal center. Usually, the putative phenoxyl radical complexes were generated in situ from the analogous phenolate complexes by addition of an appropriate oxidizing agent and were characterized mainly by electron paramagnetic resonance spectroscopy. We describe several exemplary ligands employed in this earlier work and summarize the synthesis and characterization of the phenol and phenoxyl radical complexes reported for these systems.

PHENOXYL RADICAL METALLOENZYMES

Ribonucleotide Reductase.

All living organisms depend upon one of three classes of ribonucleotide reductases in the biosynthesis of deoxyribonucleotides from ribonucleotides (6). One class contains a dinuclear iron center and stable tyrosyl radical essential for catalytic activity. The best studied ribonucleotide reductase in this class comes from *E. coli*, and is composed of two homodimeric subunits R1 and R2. Substrate and allosteric effector molecules bind to the R1 subunit, which is believed to be

the site of substrate reduction. The smaller R2 protein contains the diiron core and a proximal tyrosyl radical. This subunit can exist in four states, active R2, met R2, red R2, and apo R2. The active form contains an oxo-bridged diiron(III) core and a tyrosyl radical that is stable for several days at room temperature. The Fe(III)-O-Fe(III) center is maintained in the met R2 form, but the radical has been reduced to a normal tyrosine residue. This form of the enzyme has been characterized by X-ray crystallography at 2.2 Å resolution, and the structure of its diiron(III) site is shown in Figure 1 (7,8).

In the met form, the two ferric ions are bridged by an oxo ligand and the carboxylate side chain of a glutamate residue. The Fe1 atom has a distorted square pyramidal geometry, alternately characterized as pseudo-octahedral if the aspartate residue is assigned as chelating bidentate, whereas Fe2 has nearly perfect octahedral symmetry. In the active form of the enzyme, Tyr 122 has been oxidized to a tyrosyl radical (9) which, as revealed by the X-ray structure of met R2, is located in a hydrophobic pocket with its hydroxyl group 5.3 Å away from Fe1. The pocket does not contain any oxidizable side chains near the radical site, and protects Tyr 122 from solvent or other possible reductants. These features may account for the remarkable stability of the phenoxyl radical generated at Tyr 122.

Formation of the ribonucleotide reductase tyrosyl radical in vivo is believed to occur during the reaction of dioxygen with the reduced, diferrous form of R2. Experiments in vitro confirm that addition of O_2 to red R2 does lead to the immediate generation of the tyrosyl radical, together with the (μ-oxo)-diiron(III) center. Recent studies using stopped-flow absorption, rapid freeze-quench EPR (10) and rapid freeze-quench Mössbauer spectroscopy (11) have detected the presence of two intermediates in the radical-generating reaction, either one of which could be responsible for producing the radical from Tyr 122.

One intermediate may be a dioxygen- or amino acid-derived radical bound to one or both ferric ions, while the other has been tentatively assigned as containing a tryptophan radical(12-14).

Recently, a mutant form of the reduced R2 protein, red R2 S211A, has been crystallographically characterized to 2.2 Å resolution(15), and structural features of its diiron(II) site are shown schematically in Figure 2. Currently there are no X-ray data on wild type (wt) red R2. The structures of wt met R2 and met R2 S211A are nearly identical, including details of the metal coordination sphere, suggesting that the metal sites in wt red R2 and red R2 S211A are probably also the same. In the reduced protein, the bridging oxo group present in the met R2 structure is gone, and Glu 238 has changed from a terminal to a bridging ligand. This movement of Glu 238 is a good example of the ability of carboxylate residues to vary their binding modes in dinuclear iron cores, a property referred to as the carboxylate shift (16). No water ligands were located near the iron atoms in the red R2 S211A structure, and both Fe(II) ions display tetrahedral geometry.

The structural analysis of the red R2 protein revealed two features important to the proposed mechanisms for tyrosyl radical generation (15). The 4-coordinate ferrous ions have available sites for binding dioxygen as either a terminal ligand to one of the iron atoms or as a bridging ligand. The latter binding mode permits a variety of possible structures. The largest change in the structure of red R2 S211A compared to the met form is a 2 Å movement in the position of the hydroxyl group of Tyr 209, a residue not shown in Figs. 1 and 2. This motion opens a channel from the surface of the protein down to the diiron center, creating a possible pathway for O_2 to reach the iron site and nearby hydrophobic patch.

Reactions of the met R2 protein with H_2O_2 (17,18), as well as O-atom donors such as peroxyacids and monoperoxophthalate(18), afford the tyrosyl radical in 25 to 35% yield. The reaction of H_2O_2 and met R2 supports a mechanism in which a diiron(III) peroxide intermediate is involved in the dioxygen-dependent tyrosyl radical generation from the reduced form of the protein. The single oxygen atom donor experiments suggest that a high-valent iron-oxo intermediate, such as an $\{Fe^{IV}O\}$ or $\{Fe^{V}O\}$ species, may also be competent to generate the tyrosyl radical in the R2 protein, possibly being formed in a subsequent step from the peroxide intermediate. Work by Stubbe and coworkers revealing spectroscopic intermediates in the reaction of red R2 with dioxygen shows no evidence for the formation of such a high-valent iron-oxo species, however, leaving the role of a ferryl or perferryl species unlikely(11-14).

Galactose Oxidase.

The enzyme galactose oxidase (19-21), secreted from the fungus *Dactylium dendroides,* is a 68 kDa monomeric polypeptide that effects the transformation of a wide variety of primary alcohols to aldehydes according to the generalized reaction given in eq. 1. Dioxygen is the electron acceptor in this two-electron oxidation of alcoholic substrates. The catalytic reaction is believed to take place

$$RCH_2OH + O_2 \longrightarrow RCHO + H_2O_2 \qquad (1)$$

at or near a mononuclear copper active site. No other metal cofactors have been identified. The source of the second oxidizing equivalent necessary for converting alcohols to aldehydes remains undetermined, but a mounting body of evidence points to the presence of an organic radical cofactor working in

conjunction with the active site Cu(II)/Cu(I) redox couple. Such a radical cofactor has been positively identified as originating from a tyrosine residue (22), which is modified by an unusual thioether linkage involving a nearby cysteine, as discussed below.

Recently, the crystal structure of galactose oxidase from *D. dendroides* was determined to 1.7 Å resolution (23,24). The copper site is located near the solvent-accessible surface. An almost perfect square is formed by four ligands in the equatorial plane of the copper, two nitrogen donors from histidines and two oxygen donors from a monodentate acetate and a tyrosine residue. The acetate ligand comes from the buffer (pH = 4.5) in which the native crystals were grown. Another data set (1.9 Å resolution) collected on native crystals grown in PIPES (1,4-piperazinediethanesulfonic acid) buffer (pH = 7.0) revealed a water molecule, rather than acetate, at a distance of 2.8 Å from the cupric ion. This long Cu···OH_2 distance suggests that the geometry is more tetrahedrally distorted at pH = 7.0, the pH at which the enzyme is active. Such a distortion may lower the redox potential for the Cu(II)/Cu(I) couple proposed to participate in catalytic turnover. A fifth ligand, an oxygen from Tyr 495, occupies the axial position of the square-pyramidal Cu(II) atom, as shown schematically in Figure 3.

The X-ray structure also revealed that the tyrosine bonded in the equatorial plane, Tyr 272, has undergone a remarkable modification. A covalent bond has formed between a carbon atom ortho to the hydroxyl group and a cysteinyl sulfur atom from Cys 228. The cysteinyl carbon atom bonded to the sulfur atom lies in the plane of the tyrosine phenyl ring, suggesting partial double-bond character in the C-S linkage. A further intriguing structural feature is the close contact made by this sulfur atom with a π-stacked tryptophan residue, the distance of S to all carbons in the six-membered ring being 3.84 Å. This stacking interaction is shown schematically in Figure 4. These geometric

features suggest that the tyrosyl radical forms at Tyr 272 and is stabilized by distribution of spin density onto the cysteinyl sulfur atom and possibly over the entire π system of the proximal tryptophan group.

Galactose oxidase is EPR silent, which suggests an antiferromagnetically coupled S = 0 ground state, consistent with the S = 1/2 tyrosyl radical being directly coordinated to the S = 1/2 Cu(II) in the active site. Such direct coupling is in accord with the assignment of Tyr 272 as the tyrosyl radical, since this residue is bonded to the Cu(II) ion. More detailed EPR and ENDOR studies of the apoenzyme and thioether-substituted model compounds provide additional support for Tyr 272 being the radical (25).

Further characterization of galactose oxidase by X-ray absorption spectroscopy has provided strong evidence for the assignment of a +2 oxidation state for the copper ion in both the reduced and oxidized forms (26). Such an assignment is consistent with a possible mechanism for alcohol oxidation by galactose oxidase (27). In this mechanism, shown in Figure 5, the alcohol first binds close to the Cu(II) ion and coordinated tyrosyl radical, then donates two electrons to give aldehyde and a Cu(I)/tyrosine species. The cuprous site is then reoxidized to a Cu(II)/tyrosyl radical species by dioxygen. As in ribonucleotide reductase, the active form of galactose oxidase, which contains the metal in the oxidized state and tyrosyl radical, is thought to be generated by dioxygen.

Prostaglandin H Synthase.

The enzyme PGH synthase is a homodimeric protein consisting of subunits with an approximate molecular weight of 72 kDa and one Fe(III)-protoporphyrin IX prosthetic group per subunit. This protein is responsible for the central reaction in the biosynthesis of prostaglandins and is selectively inhibited by antiinflammatory drugs such as aspirin and indomethacin. Two

independent reactions are effected by the synthase, a cyclooxygenase reaction in which arachidonic acid (AA) is converted into prostaglandin G_2 (PGG_2), and a peroxidase reaction in which PGG_2 is converted to prostaglandin H_2 (PGH_2) (28). A tyrosyl radical (29) has been implicated as the species responsible for the initial step in the cyclooxygenase activity, and a plausible mechanism involving its generation and role in the cyclooxygenase reaction is discussed below. In contrast to this mechanism, some evidence has been reported(30) suggesting that tyrosyl radicals observed spectroscopically during the action of PGH synthase are not catalytically competent intermediates for the cyclooxygenase reaction.

Figure 6 presents a postulated mechanism for these two reactions. In the peroxidase reaction, a hydroperoxide substrate such as PGG_2 converts $\{PPIXFe(III)\}^+$ to $\{PPIXFe(V)O\}^+$ (intermediate I) in a 2-electron redox step to give PGH_2. Intermediate I then removes a hydrogen atom from a nearby tyrosine residue to give $\{PPIXFe(IV)O\}(Tyr\cdot)$ (intermediate II). The tyrosyl radical of intermediate II links the peroxidase and cyclooxygenase reactions. In the first step of the cyclooxygenase mechanism, the tyrosyl radical removes the 13-pro-S hydrogen atom from arachidonic acid, which then goes on to react with molecular oxygen to form PGG_2 (31).

Evidence from EPR spectroscopy supports the presence of a tyrosyl radical in the mechanism described above. A doublet signal appears in the EPR spectrum corresponding to the formation of a tyrosyl radical immediately following addition of arachidonic acid or PGG_2 to resting enzyme. This doublet signal decays within one minute at -12 °C, with concomitant formation of a singlet which may originate from either the same or another tyrosyl radical having a different dihedral angle between the phenyl ring and the benzylic carbon CH_2 group (32) .

In another study, native PGH synthase was treated with tetranitromethane, leading to modification of three tyrosine residues, Tyr 355, Tyr 385, and Tyr 417 (33). These three tyrosines are possibly important to cyclooxygenase activity. When the native enzyme was first incubated with indomethacin, a known cyclooxygenase inhibitor, none of these tyrosine residues was nitrated. In the same work, site-directed mutagenesis was used to replace each of these tyrosines with phenylalanine, and only the mutant Y385F lacked cyclooxygenase activity. This result suggests that Tyr 385 is located near the site of cyclooxygenase activity and is the source of the tyrosyl radical responsible for H atom abstraction from arachidonic acid.

Evidence suggests that the tyrosyl radicals giving rise to either the doublet or singlet signal are not kinetically competent intermediates in the cyclooxygenase pathway (30). In this study, addition of arachidonic acid to Fe-PGH synthase led to the formation of AA metabolic products prior to the detection of either the doublet or singlet EPR signals assigned as tyrosyl radicals. When the Fe-PGH synthase was incubated with the peroxidase-reducing substrate phenol, formation of the tyrosyl radical signals was inhibited, but AA metabolites were still produced. No EPR signals corresponding to tyrosyl radicals were detected for Mn-PGH synthase, but cyclooxygenase activity was still observed for the Mn-reconstituted enzyme. These data led the authors to conclude that the tyrosyl radicals detected by EPR spectroscopy were not catalytically competent intermediates for the cyclooxygenase reaction, but that tyrosyl radicals too short-lived to be observed on the EPR time-scale may still be important in the cyclooxygenase mechanism.

PHENOXYL RADICAL METAL COMPLEXES

A variety of phenoxyl radical metal complexes have been generated in situ by oxidation of the precursor phenol metal complex. Characterization of the resulting radical metal complexes has been mainly by EPR spectroscopy. The phenoxyl radical ligands were used in part as spin probes to interrogate the structures of the metal complexes. In all cases the ligands were designed to provide a pathway for delocalization of phenoxyl radical spin out of the phenyl ring. In several cases delocalization directly onto the metal center was reported to stabilize the phenoxyl radical compared to the corresponding uncomplexed radical ligand. Very few of these radical-metal complexes were isolated as solids, and little crystallographic data were reported for even the stable, non-radical phenol precursor complexes. Representative examples of these systems are discussed below.

Several sterically-hindered phenol ligands were prepared by using Schiff base systems. Condensation of 2-amino-4,6-di-*tert*-butylphenol with the appropriate *ortho*-hydroxy aromatic aldehyde or ketone afforded Schiff base ligands of the kind shown in Figure 7A. The addition of Pd(II), Co(II) and VO^{2+} to these ligands formed 2:1 Schiff base : M(II) complexes which could be isolated as solids. These compounds were treated with lead dioxide to generate phenoxyl radical complexes in situ, which were characterized by EPR spectroscopy. For example, in the case of [((N-3,5-di-*tert*-butyl-2-hydroxyphenyl)salicylaldiminato)$_2$Co(II)], an eight line EPR signal was observed and interpreted as arising from hyperfine splitting of phenoxyl radical electron density delocalized onto the Co(II) (I = 7/2) nucleus. The authors reported that the free ligands, treated in the same manner with lead dioxide, gave only unstable species for which it was difficult to resolve an EPR signal and concluded that chelation to the metal stabilized the phenoxyl radical (34,35).

A similar Schiff base ligand, shown in Figure 7B, was allowed to react with Co(II) and Zn(II) salts to give phenolate complexes characterized by UV-Vis and IR spectroscopy. Treatment of these products with lead dioxide gave EPR signals suggesting Co(III) and Zn(II) phenoxyl radical complexes. The authors, relying on IR data, concluded that they were unable to synthesize the analogous Cu(II) Schiff base complexes, and claimed to have obtained products in which the ligand had rearranged to a quinolide state (36). A later report described the crystallographic characterization of mononuclear and dinuclear copper complexes in which the same Schiff base ligand had been oxidized to give coupled quinone fragments. The authors suggested that dioxygen may have oxidized the coordinated Schiff base ligand to form the coupled products (37).

Another interesting ligand containing a sterically hindered phenol group was designed as an analogue of N-phenylbenzohydroxamic acid, as shown in Figure 7C. This ligand provides two chemically distinct sites for potential radical formation upon oxidation, the phenol fragment for generation of a phenoxyl radical, and the hydroxyamino group to afford a nitroxyl radical. A palladium compound was prepared and characterized by elemental analysis. Its formula was consistent with two ligands bound to one metal, and IR data supported coordination by the carbonyl oxygen atom, most likely accompanied by chelation to the hydroxyamino oxygen atom. Oxidation of this complex with $K_3[Fe(CN)_6]$ gave rise to EPR spectra interpreted as both monoradical and diradical complexes, corresponding to one or both ligands being oxidized to phenoxyl radicals. A "dark-colored" crystalline material was isolated after oxidation and assigned as the diradical complex based on IR and EPR evidence. This diradical complex was reduced with dithionite to give the monoradical and diamagnetic starting material. Attempts were made to generate phenoxyl radical complexes

by using this hydroxamic acid ligand and Zn(II), Co(II), Ni(II), Fe(II), and Fe(III), but in all these trials only nitroxide radical EPR signals were detected (38).

In order to study isomerization and tautomerism in a series of amidine-based ligands, a pendant, di-*tert*-butyl phenol group was attached to the central carbon atom of an amidine framework, as shown in Figure 7D. The phenoxyl radical, generated by oxidation with PbO_2, allowed for the study of processes, such as the 1,3-migration of the amidine H atom and other isomeric equilibria, by EPR spectroscopy. The Hg complex was formed by coordination of the di-*p*-tolyl amidine derivative to a phenylmercury group, and EPR measurements of the corresponding phenoxyl radical Hg complex suggested that 1,3-migration of the phenylmercury group is faster than the EPR time scale (39,40). These amidine ligands provide a good example of the use of phenoxyl radicals as spin probes for intramolecular rearrangements.

The ligand 3-(3,5-di-*tert*-butyl-4-hydroxyanilino)-1-phenyl-2-propen-1-one, shown in Figure 7E, which has a N,O donor set similar to that of Schiff base systems, also displayed prototropic tautomerism as seen in the amidine systems. The phenol prefers the keto-enamine form, but the imino-enol tautomer is favored for the phenoxyl radical. In this case, the phenylmercury derivative was synthesized by addition of PhHgOH to the phenoxyl radical generated in a previous oxidation step. Hyperfine splitting from ^{119}Hg (16.84% natural abundance) was observed in the EPR spectrum of the phenylmercury complex. Complexes of Cu(II), Pd(II), and Ni(II) were formed by addition of $Cu(OAc)_2$, $PdCl_2$, and $Ni(OAc)_2$, respectively, to the phenol form of the ligand. Data from IR spectroscopy and elemental analysis were consistent with formation of 2:1 complexes for these three metals. Oxidation of the Cu and Pd complexes by PbO_2 in THF solutions gave rise to EPR signals suggesting that spin density for

the phenoxyl radical was located in part on the metal center. In the case of Ni(II), oxidation by PbO_2 did not give any stable EPR signals (41).

An early report of an attempt to develop a biomimetic ligand with a stable pendant phenoxyl radical involved the synthesis of a diphenylformazan molecule shown in Figure 7F (42). The authors stated, "square planar coordination of a metal ion with four nitrogen atoms is characteristic of many enzyme systems," as their rationale for the design of this formazan-based ligand system. The complexes $[Ni(L\text{-}OH)_2]$ and $[Pd(L\text{-}OH)_2]$ were prepared and characterized by elemental analysis, electronic spectroscopy and mass spectrometry. Oxidation of benzene solutions of these complexes by aqueous $K_3Fe(CN)_6$ (pH=10) for 5 - 10 minutes led to the appearance of an EPR signal assigned to the monoradical $[M(L\text{-}OH)(L\text{-}O\cdot)]$ complexes. Longer periods of oxidation (30 - 40 minutes) gave rise to a broad singlet in the EPR spectrum attributed to the biradical complexes. Reduction of the complexes in discrete steps from the biradical to monoradical to bis(phenol) complexes was accomplished with sodium dithionite.

The isolation of $[M(L\text{-}O\cdot)_2]$ and $[M(L\text{-}OH)(L\text{-}O\cdot)]$ as dark green crystalline complexes was reported, although data to characterize these complexes were scanty. The compounds were found to be air-stable both in the solid state and in solution. The source of the high stability for these complexes was attributed to delocalization of the unpaired electron over the phenoxyl ring and chelate ring. The syntheses of the Co(II) and Cu(II) complexes of the formazan ligand were reported, although no preparative details or characterization data were given. The corresponding phenoxyl radical complexes of Co(II) or Cu(II) could neither be generated in situ nor isolated (42).

Another attempt at modelling metalloenzyme active sites involved the study of a tetra(4-hydroxy-3,4-di-*tert*-butylphenyl)porphyrin system, shown in

Figure 7G. Once again $K_3Fe(CN)_6$ was employed as the agent of oxidation, and the formation of radicals was monitored by UV-visible and EPR spectroscopy. Initially, oxidation afforded spectra consistent with a bisquinone structure, and further oxidation afforded mono and biradical products according to the EPR data. The Zn(II) porphyrin complex was synthesized and subjected to the same oxidation procedure, which generated the biradical Zn(II) complex, isolated as dark green crystals (43).

In a later paper, complexes of Ni(II), Cu(II), Pd(II), and VO^{2+} ions with the same tetra-substituted porphyrin were reported. Stepwise oxidation of these complexes gave products for which the authors proposed quinonoid, monoradical and diradical structures. The most prolonged oxidations yielded the diradical products, which were isolated as dark purple crystals, relatively stable in air (44). The monoradical vanadyl complex was diamagnetic, suggesting antiferromagnetic coupling between the phenoxyl radical and unpaired electron on vanadium, whereas in the copper complex no such coupling was observed. More detailed studies of these systems seem warranted.

MODEL FOR THE RIBONUCLEOTIDE REDUCTASE R2 PROTEIN

To construct an oxo-, carboxylato-bridged diiron(III) model for the R2 active site, we designed a ligand that could coordinate to Fe(III) and provide a stable phenoxyl radical moiety at a distance from the metal as close as possible to the 5.3 Å distance observed in the crystal structure of the R2 protein. We wanted a ligand that provided a pendant phenoxyl radical in close proximity to the metal, but not directly coordinated to it through the phenolic oxygen atom. For an accurate R2 model, the ligand should not have a delocalization pathway of the radical spin directly onto the metal center, as do all of the ligands discussed above.

The ligand that we designed and synthesized, 1,1-bis[2-(1-methyl-imidazolyl)]-1-(3,5-di-*tert*-butyl-4-oxylphenyl)ethane (BIDPhE), is shown in Figure 8 (45). It contains biomimetic imidazole donors with a pendant, sterically-hindered phenoxyl radical arm. The quaternary carbon atoms in the ortho and para positions of the phenyl ring prevent coupling reactions that occur for unsubstituted phenoxyl radicals (46). The para quaternary center prevents delocalization of the radical spin onto the imidazoles or metal center. A related bidentate nitrogen donor, BIPhMe, had previously been shown to form (μ-oxo)bis(μ-carboxylato)diiron(III) complexes (47,48), and thus inspired our design of BIDPhE.

The phenoxyl radical ligand BIDPhE was generated by oxidation of the precursor phenol, BIDPhE-H, with $K_3Fe(CN)_6$. The radical proved to be quite stable, and was isolated as a pure green solid. This material was used as the ligand to prepare the phenoxyl radical complex $[Zn(BIDPhE)Cl_2]\cdot MeOH$ from $ZnCl_2$. Binding of BIDPhE to Zn(II), allowed us to determine whether any changes in the physical properties of BIDPhE might arise from coordination of the imidazole donors. The use of Zn(II), a spectroscopically silent metal ion incapable of undergoing redox state changes under normal reaction conditions, also minimized the possibility that the metal center might reduce the BIDPhE.

The UV-visible and resonance Raman spectra of BIDPhE and $[Zn(BIDPhE)Cl_2]$ were nearly identical, suggesting that the pendant radical in the Zn(II) complex was largely unaffected by coordination through the imidazole rings. A crystallographic determination of the analogous phenol complex, $[Zn(BIDPhE\text{-}H)Cl_2]$, revealed BIDPhE-H bound to the tetrahedral Zn(II) ion through its imidazole nitrogen atoms, as expected. Comparison of the powder diffraction spectra of the BIDPhE and BIDPhE-H complexes showed them to be

essentially identical, confirming that the radical ligand also coordinates through its imidazole donors, and not through the phenoxyl oxygen atom.

Having established the stability and preferred binding mode of BIDPhE, efforts were next made to prepare a complex of dinuclear iron(III) with oxo and carboxylato-bridges. Attempts to synthesize such a complex by using well-established methods (5,48) employing simple iron salts or basic iron carboxylates as starting materials proved unsuccessful. The remarkably stable solvento complex $[Fe_2O(XDK)(MeOH)_5(H_2O)](NO_3)_2$ (49) (XDK = xylenediamine bis(Kemp's triacid imide, shown in Figure 9) (16,50), however, could be used as starting material to prepare $[Fe_2O(XDK)(BIDPhE)_2(NO_3)_2]$, the first (μ-oxo) bis(μ-carboxylato diiron(III)) phenoxyl radical complex. The solvento starting material allows facile substitution of bidentate nitrogen donors like BIDPhE for the terminal solvent molecules, without rearrangement or other reactions of its $\{Fe_2O(XDK)\}^{2+}$ core .

Addition of the solvento complex to two equivalents of BIDPhE in methylene chloride led to the isolation of $[Fe_2O(XDK)(BIDPhE)_2(NO_3)_2]$ as a dark brown crystalline solid, the proposed structure for which is shown schematically in Figure 10. Although yet to be confirmed by X-ray crystallography, convincing evidence for this structure comes from elemental analysis, UV-vis, and resonance Raman spectroscopy. A characteristic band for the bent μ-oxo bridge appears at 524 cm^{-1} in the resonance Raman spectrum, as shown in Figure 11. A review of dinuclear ferric complexes with bent oxo bridges, including an analysis of their resonance Raman spectra, is available (51). This spectrum also shows a peak at 1504 cm^{-1} arising from the C-O stretch for BIDPhE (52). Included in Figure 11 is the resonance Raman spectrum of the native ribonucleotide reductase R2 protein, illustrating the similarity between the BIDPhE model complex and the active site of the R2 protein.

The magnetic interaction between the tyrosyl radical and the diiron(III) center in R2 has been probed by spin saturation-recovery pulsed EPR experiments (53,54). A J value of -94 cm^{-1} ($H = -2JS_1 \cdot S_2$) for the Fe_2(III) exchange coupling in R2 has been extracted by using these techniques. One value of the BIDPhE model complex is its ability to serve as a small-molecule calibrant for such spin saturation-recovery measurements. The J value obtained from solid state magnetic susceptibility measurements on the BIDPhE model compound can be compared to a J value determined from spin saturation-recovery experiments. Magnetic susceptibility data revealed the iron atoms of the BIDPhE model compound to be antiferromagnetically coupled, with a J value near -120 cm^{-1}, typical for a (μ-oxo)(μ-carboxylato) $Fe(III)_2$ complex (55). From saturation-recovery EPR experiments, a J value of -118 cm^{-1} was obtained for the BIDPhE complex, in excellent agreement with the magnetic susceptibility measurements.

The BIDPhE model complex provides us with a unique opportunity to explore the reactivity of a phenoxyl radical/diiron(III) moiety with a variety of inhibitors of the R2 active site. Several studies have been carried out in which the R2 protein was treated with different radical inhibitors (56-58). The mechanism of inhibition, the oxidation products formed from the inhibitors, and the possible concomitant reactivity of the diiron(III) center with these agents are all subjects of current investigation. The reactivity of the BIDPhE model complex may be more easily studied than that of R2, given the relative ease of handling a small molecule compared to a protein.

CONCLUSIONS

The generation, stability, and function of tyrosyl radicals in ribonucleotide reductase, prostaglandin H synthase and galactose oxidase continue to be active areas of research. The difficulties encountered in preparing and handling these proteins, as well as in probing the physical properties and reactivity of their metal/phenoxyl radical active sites, make the preparation and investigation of stable phenoxyl radical metal model complexes an attractive goal.

The potential of the ligand systems shown in Figure 7 as physical and functional enzyme mimics has not been fully exploited. The porphyrin system described deserves further attention as a model for prostaglandin H synthase. Both the physical properties and possible reactivity of these porphyrin complexes with peroxide and arachidonic acid-related substrates warrant investigation. The copper chemistry reported for the Schiff base system shown in Fig. 7B is intriguing with respect to the galactose oxidase system, especially the reactivity toward dioxygen proposed for the Schiff base Cu(II) complex. Isolation of a Cu(II) phenoxyl radical complex would allow one to test the hypothesis that such a system is capable of effecting the two-electron oxidation of alcohols to aldehydes. The Cu complex reported for the imino-enol ligand in Fig. 7E could be a good candidate for study as such a galactose oxidase model, if it could be isolated in pure form.

Much work remains to be done in developing functional mimics of the diiron center in ribonucleotide reductase, but the BIDPhE system affords some progress toward this goal by showing that it is at least possible to synthesize a diiron(III) phenoxyl radical complex. In a functional model of the R2 protein, one would like to be able to mimic the ability of the enzyme to generate the radical by addition of dioxygen to the reduced diferrous form. Work is under way to obtain the necessary Fe(II)/phenol starting materials with BIDPhE and

related pendant phenol ligand systems. The generation of a diiron(III) phenoxyl radical complex by addition of dioxygen to a diferrous phenol precursor molecule would provide a system for a detailed study of the mechanism by which the iron atoms and dioxygen interact to generate a proximate phenoxyl radical. On the other hand, the failure of such diferrous complexes to generate phenoxyl radicals in the presence of O_2 could lead to a better understanding of the features used by the protein system to make such radical generation reactions possible.

Literature Cited

(1) Stubbe, J. *Annu. Rev. Biochem.* **1989**, *58*, 257-285.

(2) Ochiai, E.-I. *J. Chem Ed.* **1993**, *70*, 128-133.

(3) Pedersen, J. Z.; Finazzi-Agro, A. *FEBS Lett.* **1993**, *325*, 53-58.

(4) Prince, R. C. *TIBS* **1988**, *13*, 152-154.

(5) Lippard, S. J. *Angew. Chem. IEE* **1988**, *27*, 344-361.

(6) Reichard, P. *Science* **1993**, *260*, 1773-1777.

(7) Nordlund, P.; Eklund, H. *J. Mol. Biol.* **1993**, *232*, 123-164.

(8) Nordlund, P.; Sjöberg, B.-M.; Eklund, H. *Nature* **1990**, *345*, 593-598.

(9) Larsson, A.; Sjöberg, B.-M. *EMBO J.* **1986**, *5*, 2037-2040.

(10) Bollinger, J. M., Jr.; Edmondson, D. E.; Huynh, B. H.; Filley, J.; Norton, J. R.; Stubbe, J. *Science* **1991**, *253*, 292-298.

(11) Bollinger, J. M., Jr.; Stubbe, J.; Huynh, B. H.; Edmondson, D. E. *J. Am. Chem. Soc.* **1991**, *113*, 6289-6291.

(12) Ravi, N. J.; Bollinger, M., Jr.; Huynh, B. H.; Edmondson, D. E.; Stubbe, J. *J. Am. Chem. Soc.* **1994**, *116*, 8007-8023.

(13) Bollinger, J. M., Jr.; Tong, W. H.; Ravi, N.; Huynh, B. H.; Edmondson, D. E.; Stubbe, J. *J. Am. Chem. Soc.* **1994**, *116*, 8015-8023.

(14) Bollinger, J. M., Jr.; Tong, W. H.; Ravi, N.; Huynh, B. H.; Edmondson, D. E.; Stubbe, J. *J. Am. Chem. Soc.* **1994**, *116*, 8024-8032.

(15) Åberg, A. **1993**, Doctoral Dissertation, Stockholm University.

(16) Rardin, R. L.; Tolman, W. B.; Lippard, S. J. *New J. Chem.* **1991**, *15*, 417-430.

(17) Sahlin, M.; Sjöberg, B.-M.; Backes, G.; Loehr, T.; Sanders-Loehr, J. *Biochem. Biophys. Res. Commun.* **1990**, *167*, 813-818.

(18) Fontecave, M.; Gerez, C.; Mohammed, A.; Jeunet, A. *Biochem. Biophys. Res. Commun.* **1990**, *168*, 659-664.

(19) Hamilton, G. A. In *Copper Proteins*; T. G. Spiro, Ed.; John Wiley & Sons, Inc.: New York, 1981; Vol. 3; pp 193-218.

(20) Ettinger, M. J.; Kosman, D. J. In *Copper Proteins*; T. G. Spiro, Ed.; John Wiley & Sons, Inc.: New York, 1981; Vol. 3; pp 219-261.

(21) Avigad, G.; Amaral, D.; Asensio, C.; Horecker, B. L. *J. Biol. Chem.* **1962**, *237*, 2736-2743.

(22) Whittaker, M. M.; Whittaker, J. W. *J. Biol. Chem.* **1990**, *265*, 9610-9613.

(23) Ito, N.; Phillips, S. E. V.; Stevens, C.; Ogel, Z. B.; McPherson, M. J.; Keen, J. N.; Yadav, K. D. S.; Knowles, P. F. *Nature* **1991**, *350*, 87-90.

(24) Ito, N.; Phillips, S. E. V.; Yadav, K. D. S. *J. Mol. Biol.* **1994**, *238*, 794-814.

(25) Babcock, G. T.; El-Deeb, M. K.; Sandusky, P. O.; Whittaker, M. M.; Whittaker, J. W. *J. Am. Chem. Soc.* **1992**, *114*, 3727-3734.

(26) Clark, K.; Penner-Hahn, J. E.; Whittaker, M. M.; Whittaker, J. W. *J. Am. Chem. Soc.* **1990**, *112*, 6433-6434.

(27) Whittaker, M. M.; Whittaker, J. W. *J. Biol. Chem.* **1988**, *263*, 6074-6080.

(28) Smith, W. L.; Marnett, L. J. *Biochim. Biophys. Acta* **1991**, *1083*, 1-17.

(29) Smith, W. L.; Eling, T. E.; Kulmacz, R. J.; Marnett, L. J.; Tsai, A.-l. *Biochem.* **1992**, *31*, 3-7.

(30) Lassmann, G.; Odenwaller, R.; Curtis, J. F.; DeGray, J. A.; Mason, R. P.; Marnett, L. J.; Eling, T. E. *J. Biol. Chem.* **1991**, *266*, 20045-20055.

(31) Dietz, R.; Nastainczyk, W.; Ruf, H. H. *Eur. J. Biochem.* **1988**, *171*, 321-328.

(32) Karthein, R.; Dietz, R.; Nastainczyk, W.; Ruf, H. H. *Eur. J. Biochem.* **1988**, *171*, 313-320.

(33) Shimokawa, T.; Kulmacz, R. J.; DeWitt, D. L.; Smith, W. L. *J. Biol. Chem.* **1990**, *265*, 20073-20076.

(34) Kompan, O. E.; Ivakhnenko, E. P.; Lyubchenko, S. N.; Olekhnovich, L. P.; Yanovskii, A. I.; Struchkov, Y. T. *J. Gen. Chem. USSR (Engl. Trans.)* **1990**, 1682-1690.

(35) Ivakhnenko, E. P.; Lyubchenko, S. N.; Kogan, V. A.; Olekhnovich, L. P.; Prokof'ev, A. I. *J. Gen. Chem. USSR (Engl. Trans.)* **1986**, *56*, 765-768.

(36) Medzhidov, A. A.; Kasumov, V. T.; Mamedov, K. S. *Sov. J. Coord. Chem. (Engl. Trans.)* **1981**, *7*, 28-32.

(37) Medzhidov, A. A.; Kasumov, V. T.; Guseinova, M. K.; Mamedov, K. S.; Aliev, V. S. *Dokl. Akad. Nauk. SSSR* **1982**, *259*, 363-365.

(38) Vovk, D. N.; Melezhik, A. V.; Pokhodenko, V. D. *J. Gen. Chem. USSR (Engl. Trans.)* **1982**, *52*, 1201-1206.

(39) Ivakhnenko, E. P.; Shif, A. I.; Prokof'ev, A. I.; Olekhnovich, L. P.; Minkin, V. I. *J. Org. Chem. USSR (Engl. Trans.)* **1989**, *25*, 319-328.

(40) Ivakhnenko, E. P.; Shif, A. I.; Olekhnovich, L. P.; Prokof'ev, A. I.; Minkin, V. I.; Kabachnik, M. I. *Dokl. Akad. Nauk SSSR* **1988**, *299*, 79-82.

(41) Ivakhnenko, E. P.; Lyubchenko, S. N.; Kogan, V. A.; Olekhnovich, L. P.; Prokof'ev, A. I. *J. Gen. Chem. USSR (Engl. Trans.)* **1986**, *56*, 349-352.

(42) Pokhodenko, V. D.; Melezhik, A. V.; Vovk, D. N. *Sov. J. Coord. Chem. (Engl. Trans.)* **1982**, *8*, 667-671.

(43) Melezhik, A. V.; Pokhodenko, V. D. *J. Org. Chem. USSR (Engl. Trans.)* **1982**, *18*, 912-917.

(44) Melezhik, A. V.; Vovk, D. N.; Pokhodenko, V. D. *J. Gen. Chem. USSR (Engl. Trans.)* **1983**, *53*, 1442-1447.

(45) Goldberg, D. P.; Watton, S. P.; Masschelein, A.; Wimmer, L.; Lippard, S. J. *J. Am. Chem. Soc.* **1993**, *115*, 5346-5347.

(46) Altwicker, E. R. *Chem. Rev.* **1967**, *67*, 475-531.

(47) Tolman, W. B.; Liu, S.; Bentsen, J. G.; Lippard, S. J. *J. Am. Chem. Soc.* **1991**, *113*, 152-164.

(48) Taft, K. L.; Masschelein, A.; Liu, S.; Lippard, S. J.; Garfinkel-Shweky, D.; Bino, A. *Inorg. Chim. Acta* **1992**, *198-200*, 627-631.

(49) Watton, S. P.; Masschelein, A.; Rebek, J., Jr.; Lippard, S. J. Submitted for publication.

(50) Rebek, J., Jr.; Marshall, L.; Wolak, R.; Parris, K.; Killoran, M.; Askew, B.; Nemeth, D.; Islam, N. *J. Am. Chem. Soc.* **1985**, *107*, 7476-7481.

(51) Sanders-Loehr, J.; Wheeler, W. D.; Shiemke, A. K.; Averill, B. A.; Loehr, T. M. *J. Am. Chem. Soc.* **1989**, *111*, 8084-8093.

(52) Tripathi, G. N. R.; Schuler, R. H. *J. Chem. Phys.* **1984**, *81*, 113-121.

(53) Sahlin, M.; Petersson, L.; Gräslund, A.; Ehrenberg, A.; Sjöberg, B.-M.; Thelander, L. *Biochem.* **1987**, *26*, 5541-5548.

(54) Hirsh, D. J.; Beck, W. F.; Lynch, J. B.; Que, L., Jr.; Brudvig, G. W. *J. Am. Chem. Soc.* **1992**, *114*, 7475-7481.

(55) Que, L., Jr.; True, A. E. In *Prog. in Inorg. Chem.*; S. J. Lippard, Ed.; John Wiley and Sons: New York, 1990; Vol. 38; pp 97-200.

(56) Atta, M.; Lamarche, N.; Battioni, J.-P.; Massie, B.; Langelier, Y.; Mansuy, D.; Fontecave, M. *Biochem. J.* **1993**, *290*, 807-810.

(57) Lassmann, G.; Thelander, L.; Gräslund, A. *Biochem. Biophys. Res. Commun.* **1992**, *188*, 879-887.

(58) Lam, K.; Fortier, D. G.; Thomson, J. B.; Sykes, A. G. *J. Chem. Soc., Chem. Comm.* **1990**, 658-660.

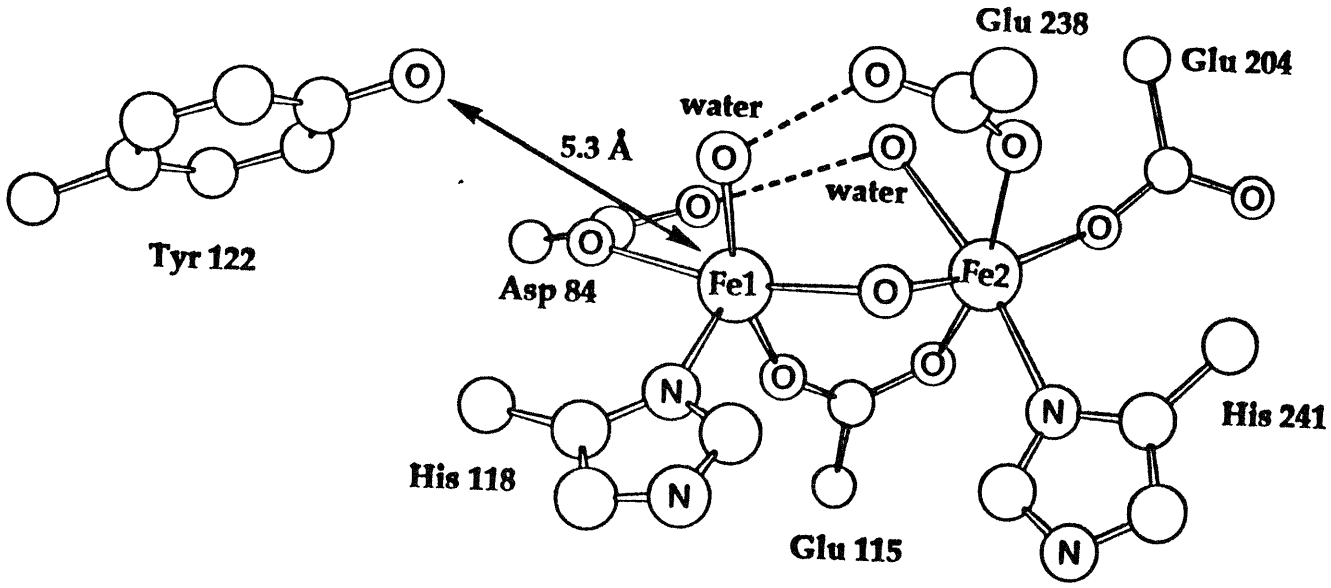

MET R2

Figure 1. Structure of the R2 protein of E. coli ribonucleotide reductase in the met form. Adapted from reference 7, which reports the 2.2 Å crystal structure of the protein. Note that, in ref. 7, Asp 84 is considered to be bidentate and chelating, but we prefer the monodentate, hydrogen-bonded representation depicted above based on an analysis of the Fe-O distances.

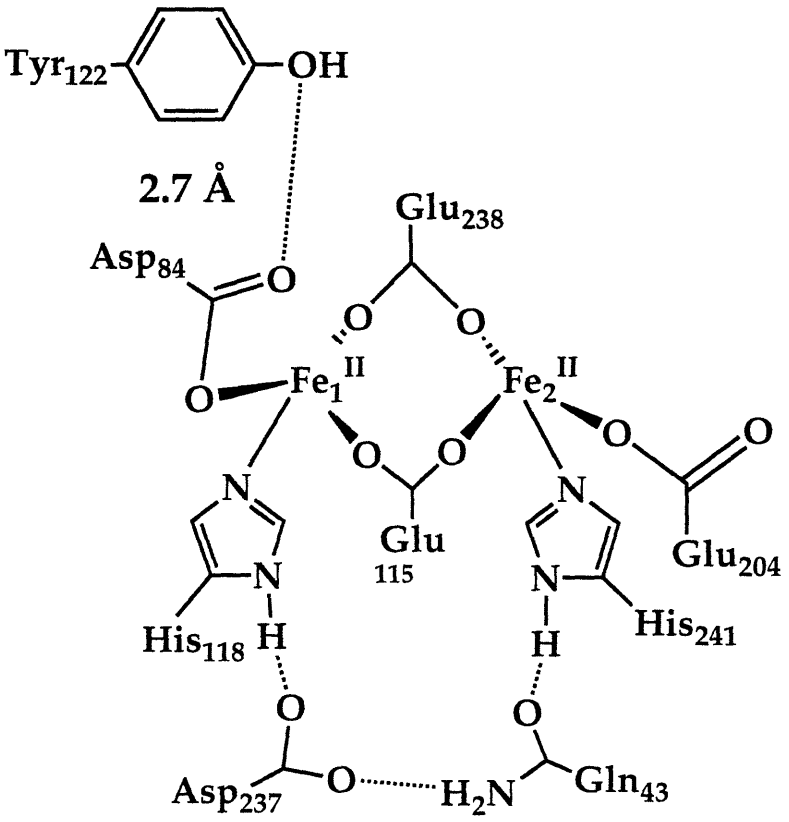

Figure 2. Structure of a S211A mutant of the R2 protein of E. coli ribonucleotide reductase in the reduced form. Adapted from reference 15 reporting the 2.2 Å crystal structure.

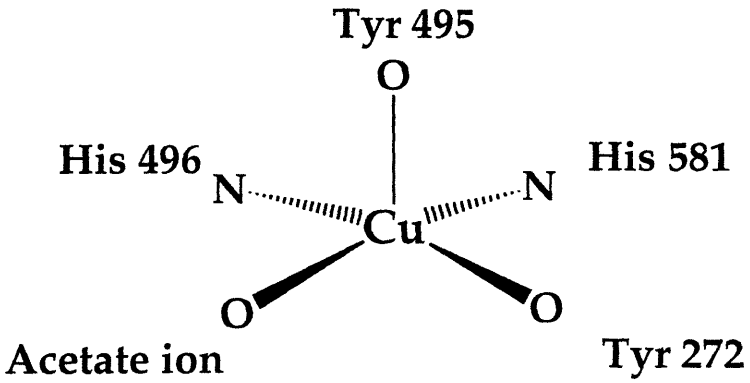

Figure 3. Sketch of the copper coordination in galactose oxidase, as determined by the 1.7 Å resolution crystal structure Adapted from ref. 23.

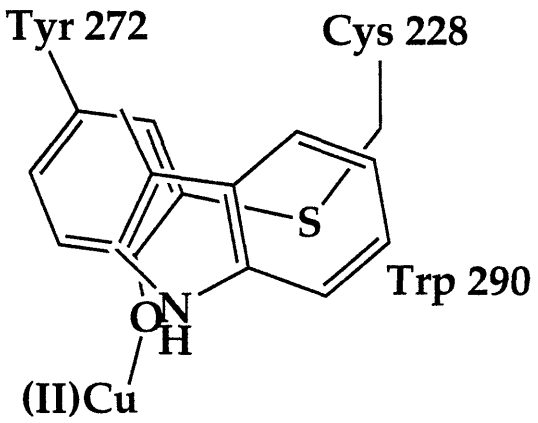

Figure 4. Drawing of the stacking interaction between Trp 290 and the thioether bond formed by Cys 228 with Tyr 272 in galactose oxidase as determined from the crystal structure. Adapted from ref. 23.

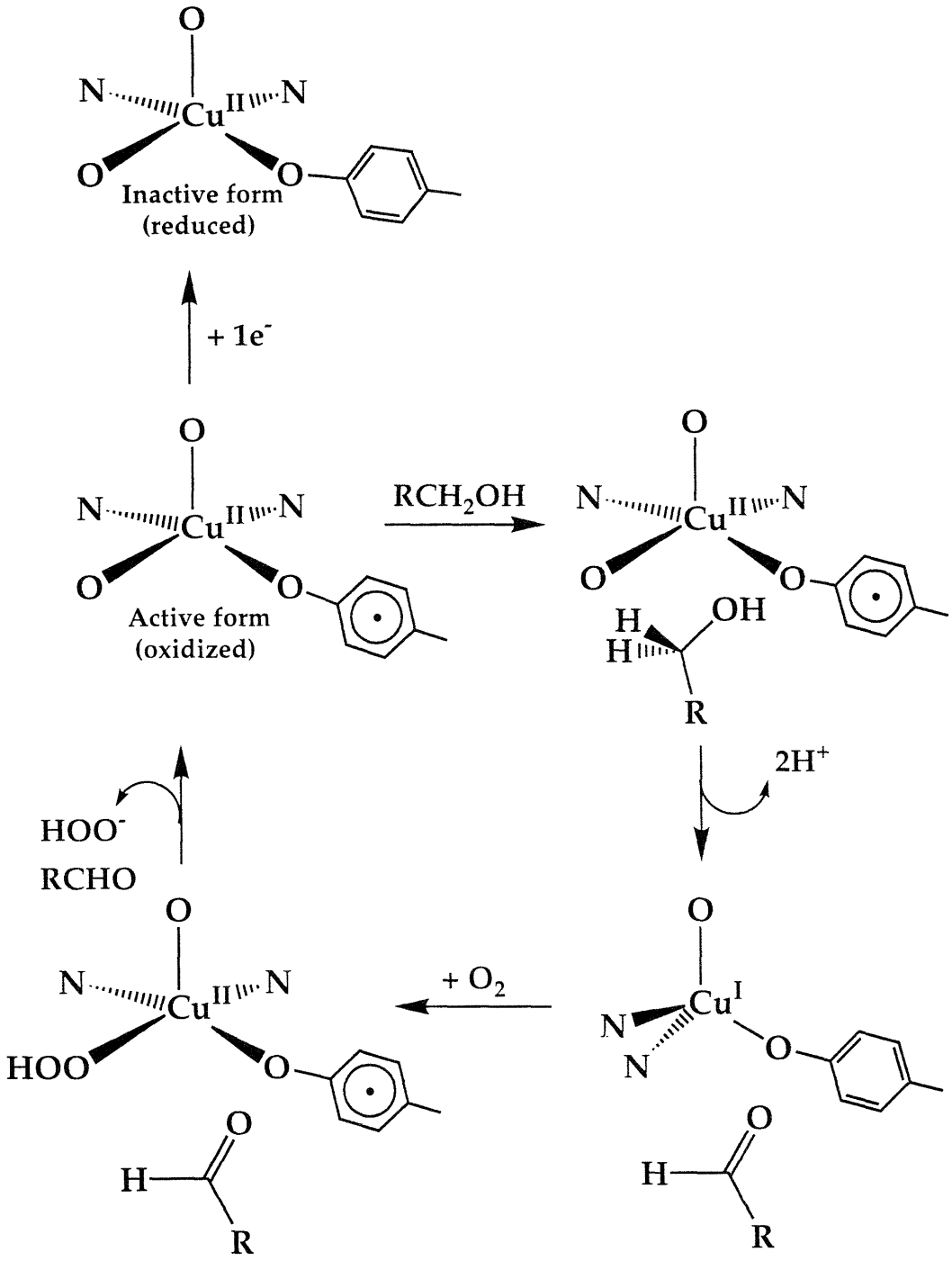

Figure 5. Proposed mechanism of alcohol oxidation for galactose oxidase. Adapted from ref. 27.

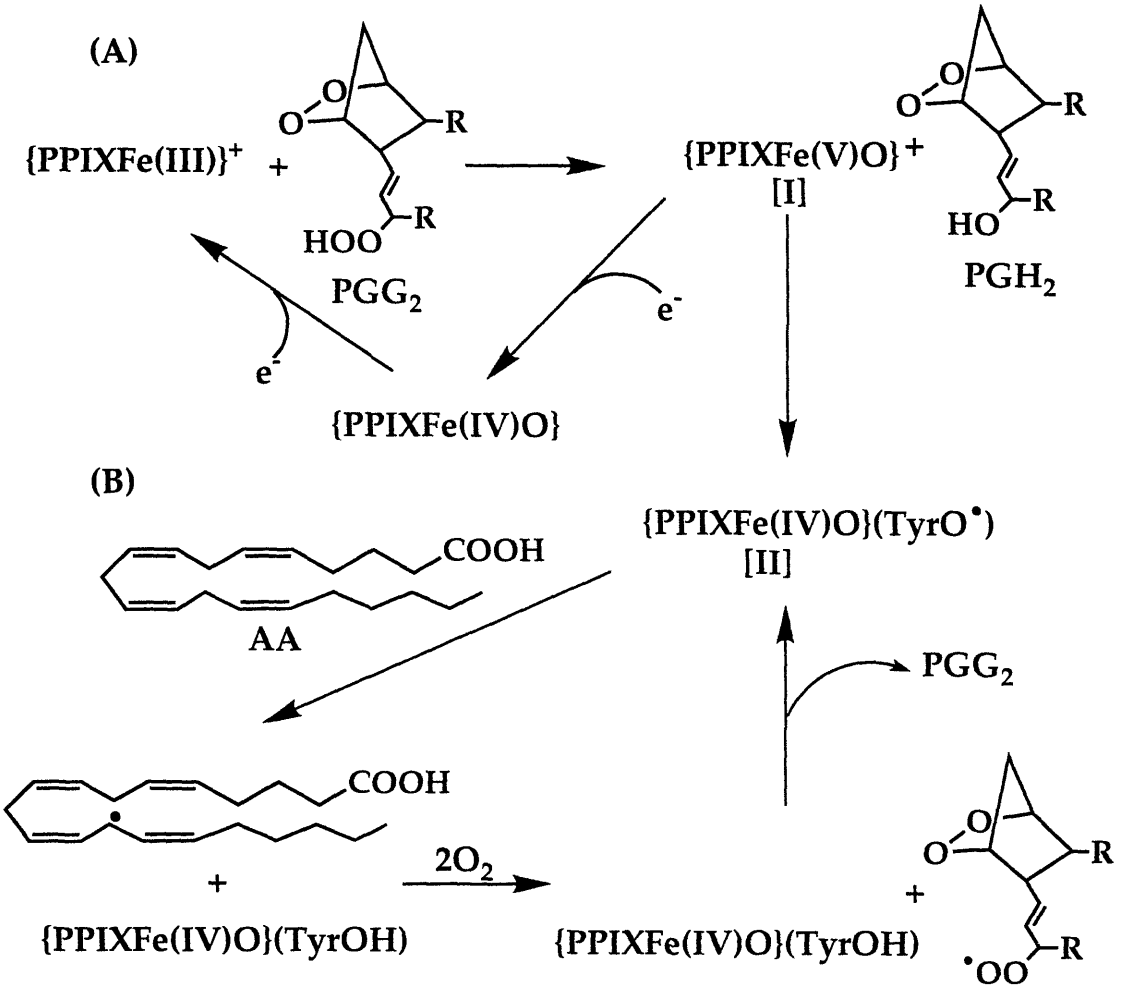

Figure 6. Proposed mechanism for (A) the peroxidase and (B) the cyclooxygenase reactions of prostaglandin H synthase. Adapted from ref. 31.

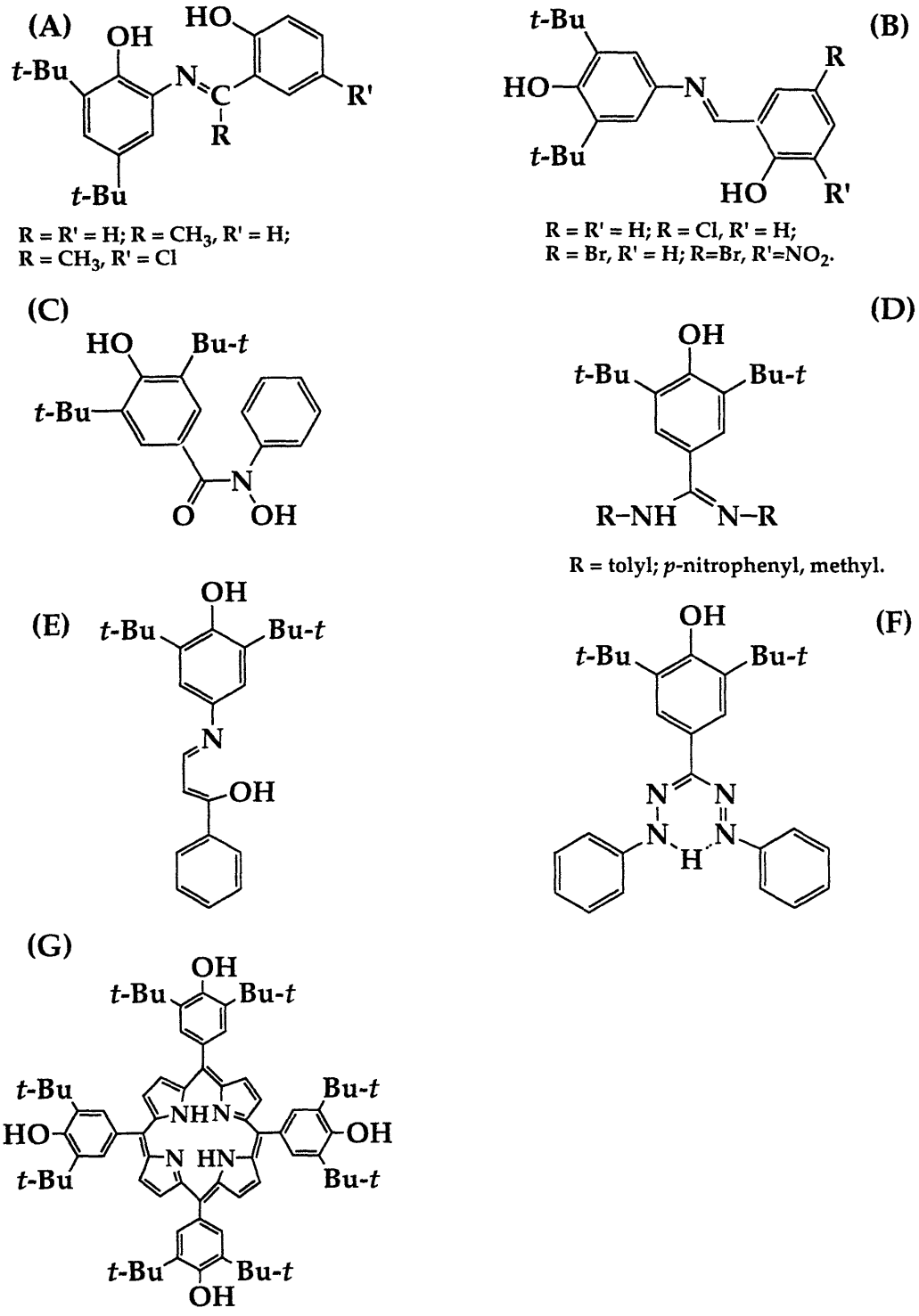

Figure 7. Ligand systems containing sterically-hindered phenol groups. (A) adapted from ref. 34, (B) adapted from ref. 36, (C) adapted from ref. 38, (D) adapted from ref. 39, (E) adapted from Ref. 41, (F) adapted from ref. 42, and (G) adapted from ref. 43.

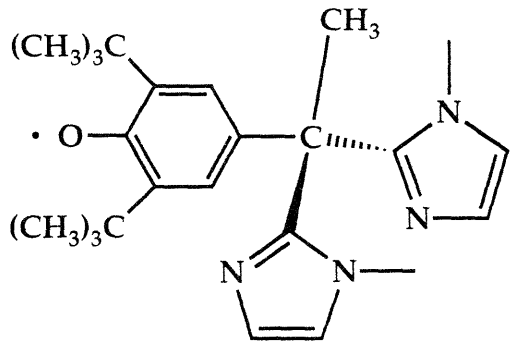

Figure 8. Drawing of BIDPhE.

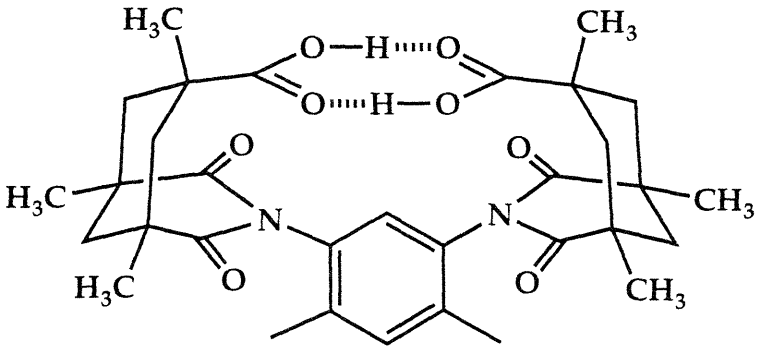

Figure 9. Drawing of $XDKH_2$.

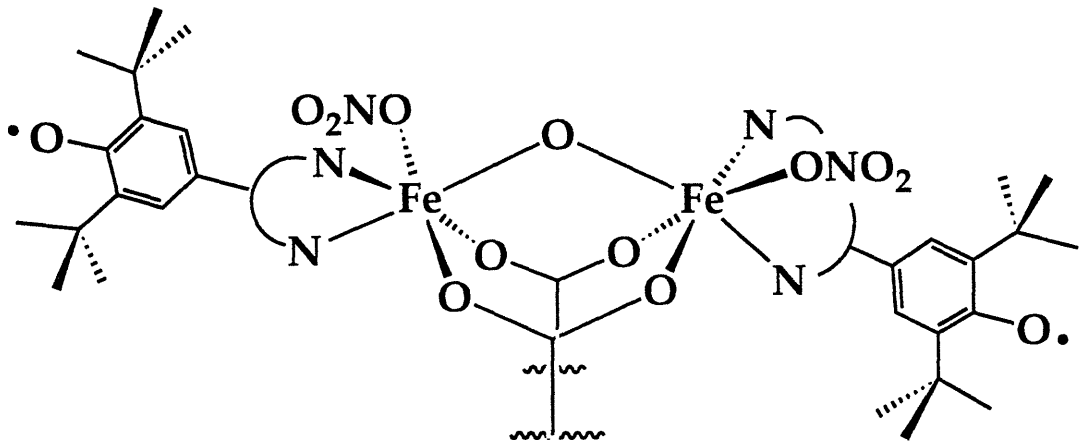

Figure 10. Schematic diagram of the proposed structure for $[Fe_2O(XDK)(BIDPhE)_2(NO_3)_2]$.

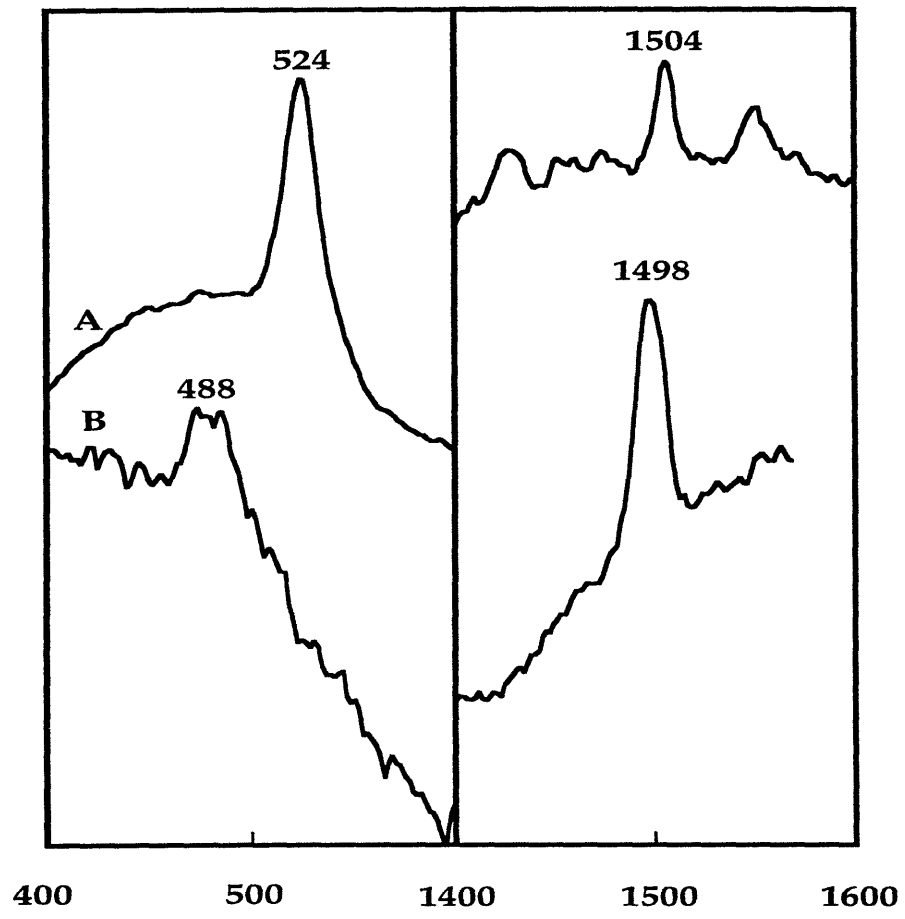

Figure 11. Resonance Raman spectrum of (A) $[Fe_2O(XDK)(BIDPhE)_2(NO_3)_2]\cdot CH_2Cl_2$ dissolved in CH_2Cl_2 and (B) wt ribonucleotide reductase R2 protein from E. coli, strain N6405/PSPS2, dissolved in Tris buffer, pH 7.6, 5% glycerol. All spectra were recorded at room temperature with Kr ion laser excitation at 406.7 nm.

Chapter 2

A Phenoxyl Radical (μ-Oxo)bis(μ-Carboxylato)Diiron(III) Complex as a Model for the Active Site of the R2 Protein of Ribonucleotide Reductase

Introduction

Tyrosyl radicals have been implicated in the functioning of several biological systems,[1-5] including metalloproteins such as photosystem II (PSII),[6] galactose oxidase,[7-9] prostaglandin H synthase (PGH synthase),[10] and the R2 protein of ribonucleotide reductase (RR).[11,12] The manganese-containing protein complex of PSII has two tyrosyl radicals (designated Y_Z and Y_D), one of which (Y_Z) transfers the oxidizing equivalents, necessary for the oxidative coupling of H_2O to dioxygen, to a tetranuclear manganese cluster.[6] Galactose oxidase has been proposed to utilize a Cu(II) center in conjunction with a tyrosyl radical to effect the oxidation of a broad range of alcohols to aldehydes. Recent characterization by X-ray crystallogaphy revealed a mononuclear cupric active site with a novel cysteinyl-modified tyrosine residue bound directly to the copper atom.[13,14] This residue is almost certainly the source of a tyrosyl radical.[15] In PGH synthase, an iron porphyrin-based active site is responsible for transforming arachidonic acid to prostaglandin H_2, the first committed step in the biosynthesis of prostaglandins.[10] Spectroscopic evidence supports the involvement of a tyrosyl radical working together with the heme iron prosthetic group.[16-18] A recent 3.5 Å resolution crystallographic determination of the structure of PGH synthase reveals a tyrosine residue oriented in the active site in a manner fully consistent with a mechanism involving its conversion to the tyrosyl radical form.[19] All of these systems have in common the feature of metal-based active sites with nearby, redox-active tyrosyl residues.

Ribonucleotide reductase enzymes, of which there are three classes,[20] are essential to all living organisms, being required for the conversion of ribonucleotides to deoxyribonucleotides. The RR enzyme from *E. coli* is the best-studied, and belongs to the class which contains a dinuclear iron center and stable tyrosyl radical. Although reduction of the ribose ring occurs within the R1

subunit of RR from *E. coli*, the R2 subunit is responsible for generating and maintaining a stable tyrosyl radical essential to enzyme functioning. An oxo, carboxylato-bridged diiron(III) site has been structurally characterized in a crystallographic study of the R2 protein. The tyrosyl radical, Tyr122, is located in close proximity to the iron atoms, the distance from its phenolic oxygen atom to the nearest iron atom being 5.3 Å.[21,22] A diagram of the active site of the R2 subunit is given in Figure 1.

A molecular mimic of the R2 active site must incorporate at least two important features, a (μ-oxo)(μ-carboxylato)diiron(III) core and a stable phenoxyl radical held close, but not coordinated, to the diferric center. Previous work in our laboratory has afforded synthetic methodology for accessing $[Fe_2X(O_2CR)_2L_2]^{2+}$ complexes, X = H or OH, which have accurately modeled the structural and spectroscopic porperties of the non-heme iron centers in metalloproteins such as ribonucleotide reductase, hemerythyrin, methane monooxygenase, and purple acid phosphatase.[23-30] In these complexes, L can be one of various bidentate or tridentate nitrogen donor ligands. This experience suggested that it should be possible to design a nitrogen donor ligand L containing a stable phenoxyl radical in close proximity, but not coordinated, to the $[Fe_2O(O_2CR)_2]^{2+}$ core.

Although other phenoxyl radical metal complexes have been reported,[31-36] they were not designed to prevent delocalization of the radical spin to the metal center. Moreover, most were only generated in situ and characterized by EPR spectroscopy, and very few were isolated as solids. A recent specific attempt to model metalloenzymes containing tyrosyl radicals afforded two related tris(phenolato)iron(III) complexes which could be oxidized to the $[Fe(L)]^{\cdot+}$ radical cations, one of which was isolated as a stable powder.[37] In these species the oxidizing equivalent is localized on one of the phenolate donors

to give a phenoxyl radical which is coordinated directly to the Fe(III) atom through its oxygen atom.[37] A related report describes the synthesis of a series of sulfur-substituted phenols and their corresponding phenoxyl radicals as models for galactose oxidase.[38]

In the present chapter we describe the synthesis of the novel bidentate nitrogen donor ligand 1,1-bis-2-(1-methylimidazolyl)-1-(3,5-di-*tert*-butyl-4-hydroxyphenyl)ethane (BIDPhEH), which contains biomimetic imidazole donors and a redox-active pendant phenol group. This ligand is closely related to BIPhMe, which was successfully employed in the synthesis of (μ-oxo)bis(μ-carboxylato)diiron(III) complexes.[28,29] A method has been developed for

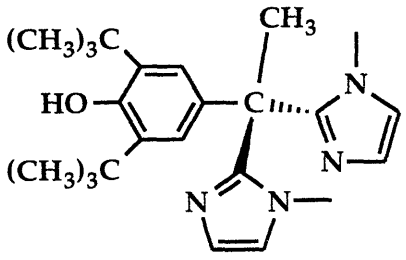

BIDPhEH

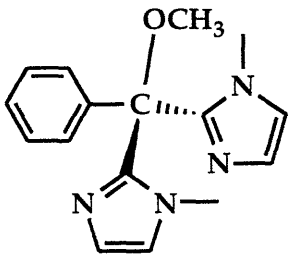

BIPhMe

oxidizing BIDPhEH to the phenoxyl radical form BIDPhE, which was employed as a ligand in the synthesis of a (μ-oxo)bis(μ-carboxylato)diiron(III) complex with two pendant phenoxyl radical capping ligands. This model of the R2 active site was isolated and characterized as a stable crystalline solid. The synthesis and structure of a monuclear BIDPhEH complex of iron(III) are also reported, providing structural information about the coordination of BIDPhE(H) to ferric ion. The phenoxyl radical diiron(III) model complex was probed by magnetic susceptibility and X-band EPR spin saturation-recovery experiments. These methods provide two independent measures of the magnetic exchange coupling constant, J, for the diiron center, in remarkably good agreement with one another. The distance, r, between the phenoxyl radical ligand and the dinuclear

center extracted from the saturation-recovery data was in excellent agreement with the value expected from crystallographic information on $[Fe(BIDPhEH)Cl_2]^+$ and relevant dinuclear iron systems. Aspects of this work have appeared in preliminary form.[39]

Experimental Section

Materials and General Methods. Unless otherwise noted, materials were obtained from commercial sources and used as received. Where appropriate, manipulations and reactions were carried out under an inert atmosphere in a Vacuum Atmospheres drybox or by using standard Schlenk techniques. Solvents THF, C_6H_6 and pentane were distilled from Na/benzophenone ketyl under nitrogen; CH_2Cl_2 was distilled from CaH_2 under nitrogen. All other solvents were purchased as reagent grade and used as received. 1-Methylimidazole, *n*-butyllithium, and methyllithium were purchased and used as received. Methyl 3,5-di-*tert*-butyl4-hydroxybenzoate was prepared in 96% yield by esterification from the corresponding benzoic acid, which was purchased from Aldrich and used as received. $[Fe_2O(XDK)(MeOH)_5(H_2O)](NO_3)_2{\cdot}4H_2O$ and the ligand H_2XDK (XDK = xylenediamine bis(Kemp's triacid imide) were prepared according to literature procedures.[30] $[Zn(BIDPhE)Cl_2]$ was prepared as described elsewhere.[39] A standard solution of $Na_2S_2O_3$ was purchased from J. T. Baker Co. ^1H and ^{13}C NMR spectra were recorded on a Bruker AC250 a Varian XL300 spectrometer. Proton resonances reported in units of ppm downfield from tetramethylsilane (TMS) were referenced to residual solvent protons. Mass spectra were obtained on a Finnigan MAT 8200 mass spectrometer. Melting points are uncorrected.

Bis(1-methylimidazolyl)-3,5-di-*tert*-butyl-4-hydroxyphenylhydroxy-methane (1). A solution containing 39.8 mL (0.499 mol) of 1-methylimidazole

dissolved in 400 mL of freshly distilled THF was cooled to -78 °C under argon, and a 2.5 M solution of *n*-butyllithium in hexanes (200 mL, 0.500 mol) was added dropwise. A solution of methyl 3,5-di-*tert*-butyl-4-hydroxybenzoate (44.0 g, 0.170 mmol) in THF was added to the reaction mixture. The solution was stirred for 1 h at -78 °C and allowed to warm to room temperature, during which time a large amount of white solid precipitated. The heterogeneous mixture was stirred for an additional 12 h, at which point H_2O was added to quench any excess base remaining and dissolve the white precipitate. The pH was brought close to 7 with aq. HCl, and the THF and aqueous phases were separated. In some preparations the product crystallized directly from the THF layer upon standing, in which case the crystals were isolated, washed with ice-cold diethyl ether, and used directly in the next step. The aqueous phase was extracted with CH_2Cl_2, and the extracts were washed with brine. All organic layers were combined and dried over $MgSO_4$. The organic phase was filtered and the solvents were removed under vacuum to give an orange solid. The product was purified by recrystallization from C_6H_6, followed by washing with ice-cold diethyl ether, to give 39.5 g (59%) of a white powder. Mp 166-167.5 °C; ^{1}H NMR ($CDCl_3$, 250 MHz) δ 6.93 (d, J = 1 Hz, Im, 2H); 6.86 (d, J = 1 Hz, Im, 2H), 6.82 (s, phenyl, 2H); 6.43 (s, OH, 1H); 5.26 (s, PhOH, 1H); 3.38 (s, MeIm, 6H); 1.34 (s, *t*-butyl, 18H). ^{13}C {^{1}H} NMR (acetone-d_6, 250 MHz) δ 154.5, 150.0, 137.8, 134.2, 126.0, 124.9, 124.2, 75.9, 35.1, 34.8, 30.6; FAB-MS *m/e* (relative intensity): Calculated *m/e* for $(M+H)^+$ = 397.3; found 397.4 ($(M+H)^+$, 28), 380.4 (-OH, 8), 315.3 (-MeIm, 10).

1,1-Bis-2-(1-methylimidazolyl)-1-(3,5-di-*tert*-butyl-4-hydroxyphenyl)-ethane (BIDPhEH) (2). A solution of **1** (11.98 g, 30.2 mmol) in THF was cooled to -78°C under argon, and a 1.6 M solution of CH_3Li in Et_2O (18.9 mL, 30.2 mmol) was added dropwise. The reaction mixture was stirred for 2 h at -78°C and warmed to room temperature to give a slurry, which was refluxed for 48 h to

afford a bright orange reaction mixture containing the quinone methide intermediate. This species was identified by comparison of its ^1H NMR spectrum with that of an authentic sample (vide infra). This solution was cooled to -78°C, and a 1.6 M solution of CH_3Li in Et_2O (37.8 mL, 48.0 mmol) was added by syringe, causing a color change from orange to red-brown. After 1 h, the reaction mixture was allowed to warm to room temperature and stirred for an additional 12 h.

The reaction mixture was quenched with H_2O, and the pH was adjusted to 7 with the addition of aq. HCl. The THF/H_2O mixture was extracted with CH_2Cl_2 and the combined organic layers were washed with a saturated $NaHCO_3$ solution, then brine, and dried over $MgSO_4$. The organic layer was filtered and evaporated to give 9.50 g of crude product. The product was purified by recrystallization from acetone followed by careful washing with ice-cold acetone and Et_2O, affording 4.39 g (37%) of a white powder. Mp 184.5-185.0 °C; ^1H NMR ($CDCl_3$, 250 MHz) δ 6.98 (d, J = 1 Hz, Im, 2H), 6.85 (s, phenyl, 2H), 6.82 (d, J = 1 Hz, Im, 2H), 5.11 (s, OH, 1H), 3.10 (s, MeIm, 6H), 2.19 (s, CH_3, 3H), 1.34 (s, *t*-Bu, 18H); ^{13}C {^1H} NMR ($CDCl_3$, 300 MHz) δ 152.3, 149.8, 134.8, 133.9, 126.4, 124.6, 122.6, 47.0, 34.2, 33.8, 30.3, 29.1. EI-MS *m/e* (relative intensity) 394 (M^+, 100), 379 (42), 352 (21), 310 (28), 189 (19), 176 (22), 175 (30), 83 (19), 57 (18). Anal. Calcd. for $C_{24}H_{34}N_4O$: C, 73.06, H, 8.69; N, 14.20. Found: C, 73.58; H, 8.80; N, 14.53.

1,1-Bis-2-(1-methylimidazolyl)-1-(3,5-di-*tert*-butyl-4-oxylphenyl)ethane (BIDPhE) (3). The phenol **2** (0.500 g, 1.27 mmol) was dissolved in 20.0 mL of distilled, degassed C_6H_6 in a 100 mL Schlenk flask under argon. A solution of $K_3Fe(CN)_6$ (2.0 g, 6.07 mmol) and NaOH (1.2 g, 30.0 mmol) was prepared by dissolving the solids in 20.0 mL of H_2O and purging with argon for 15-30 min. This solution was transferred to the solution of **2**, and an immediate deep blue color was formed in the organic layer. The two-phase reaction mixture was

stirred for 1.0 h, at which point the aqueous phase was removed. The C_6H_6 layer was washed with 2 x 10 mL portions of degassed H_2O, and then transferred to a 50 mL Schlenk flask containing $MgSO_4$. After 0.5 h, the C_6H_6 layer was filtered and the solvent removed by vacuum over a 2 to 3 h period at ambient temperature to yield 0.440 g (88%) of **2** as a dark green solid. Electronic spectral data in CH_3CN solution (λ_{max}, nm (ε, M^{-1} cm^{-1})): 638 (430), 394 (1700), 378 (1500). The purity of the radical **2** was qualitatively established by TLC (silica gel, CH_3CN/Et_2O 80/20, r_f = 0.3) and quantitated (94%) by iodometric titration.[40]

2,6-di-*tert*-butyl-4-bis[2-(1-methylimidazolyl)]methyl-2,5-cyclohexadienone (4). To a solution of **1** (1.02 g, 2.57 mmol) in THF (50 mL), cooled to -78 °C, was added a 1.6 M solution of *n*-BuLi in hexanes (1 mL, 2.5 mmol), dropwise by syringe, giving a green precipitate. The mixture was warmed to room temperature and stirred for 12 h. A yellow precipitate was observed and the mixture was refluxed for one day to give a red-orange solution. The THF was evaporated and the resulting orange solid was dissolved in CH_2Cl_2 and filtered through a Celite® plug. Removal of the CH_2Cl_2 under vacuum afforded 0.874 g (87%) of an orange powder. Mp 201.5 - 204.5 °C; ^1H NMR (acetone-d_6, 250 MHz) δ 7.65 (s, phenyl, 2H), 7.33 (d, J = 1 Hz, Im, 2H), 7.22 (d, J = 1 Hz, Im, 2H), 3.14 (s, MeIm, 6H), 1.24 (s, *t*-Bu, 18H); ^{13}C {^1H} NMR ($CDCl_3$, 300 MHz) δ 186.5, 149.1, 144.5, 136.1, 130.6, 130.2, 126.0, 123.8, 35.3, 33.1, 29.4. Anal. Calcd. for $C_{23}H_{30}N_4O$: C, 72.98; H, 7.99; N, 14.80. Found: C, 72.86; H, 8.00; N, 14.84.

[Fe(BIDPhEH)$_2$Cl$_2$]Cl·H$_2$O (5a·H$_2$O). An amount of $FeCl_3$ (0.083 g, 0.512 mmol) was combined with BIDPhEH (0.405 g, 1.05 mmol) in CH_3CN (10 mL) to give a red-orange solution. After 1 h, the reaction mixture was filtered, and subsequent vapor diffusion of Et_2O afforded **5a** as red crystals. The supernatant was decanted, and the crystals were washed with Et_2O, crushed, and dried under vacuum at 111 °C for 12 h, affording 0.487 g (52%) of an orange powder.

FTIR (KBr pellet): 3131, 2958, 1556, 1482, 1436, 1395, 1366, 1335, 1280, 1230, 1204, 1157, 1136, 1097, 1076, 953, 890, 813, 775, 732, 709, 666, 549, 538, 482 cm^{-1}. Anal. Calcd for $FeC_{48}H_{70}Cl_3N_8O_3$ (**5a**·H_2O): C, 59.48; H, 7.28; N, 11.56. Found: C, 59.48; H, 7.13; N, 11.51. Three analyses of independent samples of **5a** gave results satisfactory for **5a**·H_2O, with or without heating under vacuum.

[FeL_2Cl_2][$FeCl_4$]·CH_3CN (5b·CH_3CN). An amount of $FeCl_3$ (0.045 g, 0.277) was combined with BIDPhEH (0.110 g, 0.279 mmol) in CH_3CN (5 mL) to give an orange-brown solution. After 24 h, the reaction mixture was filtered, and subsequent vapor diffusion of Et_2O afforded **5b** as orange crystals. FTIR (KBr pellet) 3615, 3566, 3142, 2961, 2873, 1553, 1483, 1434, 1366, 1335, 1281, 1239, 1208, 1135, 953, 892, 811, 758, 731, 705, 536, 481 cm^{-1}. Anal. Calcd for $Fe_2C_{50}H_{71}Cl_6N_9O_2$ (**5b**·CH_3CN): C, 52.01; H, 6.20; N, 10.92. Found: C, 51.74; H, 6.23; N, 10.71.

[Fe_2O(XDK)(BIDPhE)$_2$(NO_3)$_2$]·CH_2Cl_2 (6·CH_2Cl_2). All manipulations were carried out in a drybox. A portion of [Fe_2O(XDK)(MeOH)$_5$(H_2O)](NO_3)$_2$·$4H_2O$ (0.075 g, 0.069 mmol) was added to a deep green solution of BIDPhE (**3**) (0.057 g, 0.145 mmol) in CH_2Cl_2 (3 mL) to give a dark brown-green reaction mixture. This mixture was stirred for 10 min and filtered to remove a small amount of a brown precipitate. Pentane was added dropwise to the filtrate until a small amount of brown powder was formed, and subsequent vapor diffusion of pentane into the solution at -30 to -40 °C afforded a dark brown-green crystalline material. The crystals were isolated by decanting the mother liquor and washed with pentane. The pentane washings showed no blue-green color, indicating that any noncoordinated **3** was removed with the mother liquor; **3** is readily soluble in pentane. Drying the product under vacuum for 15 min gave 0.110 g (72 %) of a dark brown-green crystalline solid. FTIR (KBr pellet): 2972, 2929, 2871, 2367, 2329, 1737, 1695, 1542, 1492, 1461, 1387, 1363, 1334, 1285,

1192, 1146, 1091, 958, 887, 812, 760, 712, 640 cm^{-1}. Anal. Calcd. for $Fe_2C_{81}H_{106}N_{12}Cl_2O_{17}$ (**6**·CH_2Cl_2): C, 57.15; H, 6.28; N, 9.87. Found: C, 57.52; H, 6.20; N, 9.83. The occurrence of CH_2Cl_2 in the lattice was confirmed by the ^1H NMR spectrum of **6**·CH_2Cl_2 in $CDCl_3$. The radical content of **6** was determined by measuring the absorbance of the band found at 644 nm for solutions of **6** in CH_2Cl_2, and taking the extinction coefficient for this band to be $\varepsilon = 430$ M^{-1} cm^{-1}, the value of the 638 nm band in compound **3**. The radical content was typically between 85 - 95% for a given batch of **6** as measured by this assay.

Iodometric Titration of Radical Content. Chemical titration was chosen as the most accurate method for determining the radical content in **3**, and a procedure was developed based on the oxidation of I^- to I_2/I_3^-. The amount of iodine generated in situ was quantitated with a standard aqueous solution of $Na_2S_2O_3$. This assay follows a method used for the phenoxyl radical galvinoxyl.

An amount of NaI (1 g) was dissolved in a previously degassed CH_3CO_2H/C_6H_6 (5/4 v/v, 45 mL) mixture. The appearance of any trace yellow color was an indication of the presence of I_2/I_3^- and taken as evidence that there was O_2 contamination in the system, in which case a fresh NaI solution was prepared. A known amount of **3** (typically ≈50 mg) was added as a solid directly to the NaI solution, and formation of the yellow-brown color of I_2/I_3^- was observed. An amount of H_2O (degassed, 20 mL per 45 mL CH_3CO_2H/C_6H_6 solution) was added to give a 2-phase mixture. The iodine formed in situ was then titrated with a standard solution of $Na_2S_2O_3$ (0.01 M). Titrations were conducted until at least three consecutive values agreed to within 5% of each other.

The reliability and accuracy of the titration procedure were tested by using galvinoxyl as a standard. The value of radical content obtained by the above titration method for galvinoxyl was compared to that calculated from UV-

visible spectra by using the known extinction coefficient, $\varepsilon = 607\ M^{-1}\ cm^{-1}$ (λ_{max} = 767 nm), for galvinoxyl.[40] The chemical titrations and UV-visible assays of the radical content in galvinoxyl agreed to within 2%.

Crystallography. An x-ray diffraction study of $[Fe(BIDPhEH)_2Cl_2][FeCl_4] \cdot CH_3CN$ (**5b** · CH_3CN) was performed with an Enraf-Nonius CAD-4F kappa geometry diffractometer and graphite monochromatized Mo K$\bar{\alpha}$ radiation λ = 0.71069 Å). The crystal temperature (see Table 1) was maintained by the use of an Enraf-Nonius FR558-S liquid nitrogen cryostat. All calculations were performed with a VAXstation 4000-90 computer and the teXsan software package.[41] A diamond-shaped orange crystal (0.20 x 0.10 x 0.25 mm) grown from CH_3CN/Et_2O was mounted on the end of a quartz fiber with silicone grease. The unit cell dimensions were obtained from a least-squares fit of 25 reflections in the range $8° < \theta < 15°$ and revealed the Laue symmetry to be $2/m$., which was confirmed by the examination of axial photographs. The computer program TRACER[42] was employed to provide additional confirmation of the choice of crystal system. The crystal was determined to be of sufficient quality for data collection as judged by the examination of rotational and axial photographs, the unit cell parameter errors, and the measurement of selected low angle peak widths at half-height ($\Delta\bar{\omega}_{1/2}$) by open-counter ω scans.

Intensity data were collected with the ω scan technique. The intensities of three standard reflections were measured every 3600 seconds of exposure time. The data were corrected for Lorentz and polarization effects. No decay correction was necessary during data collection since there was no significant fluctuation in the intensities of the three standard reflections. An absorption correction was applied following the measurement of Ψ scans.[43] The direct methods program SHELXS-86[44] was used for the initial structure solution, and final models were obtained by least-squares refinement in combination with

difference Fourier syntheses. All nonhydrogen atoms were refined by using anisotropic thermal parameters, except for the lattice solvent composed of N(9), C(71), and C(72). Hydrogen atoms were placed at calculated positions (C-H = 0.95 Å), and their B values were fixed at 1.2 times the B_{eq} of the atom to which they were bound. They were included, but not refined, in the final least-squares cycles. Scattering factors for the nonhydrogen[45] and hydrogen atoms[46] and anomalous dispersion terms[41,47] were taken from the usual sources. The largest positive peak in the final difference Fourier map had an electron density of 0.47 $e^-/Å^3$ and was located in the region near C(50).

A summary of crystallographic data for **5b** can be found in Table 1. Selected bond distances and angles are given in Table 2. Atomic coordinates and B_{eq} are given in Table 3. A complete listing of intramolecular bond distances and angles are given in Tables 4 and 5 respectively. Anisotropic thermal parameters are given in Table 6. An ORTEP diagram of the cation of **5b** is shown in Figure 3.

Physical Measurements. Magnetic Susceptibility Studies. Solid state magnetic susceptibility measurements on ≈ 50 mg of **6** · CH_2Cl_2 were made by using a Quantum Design MPMS SQUID susceptometer equipped with a 5.5 T magnet. Samples were loaded in a drybox and sealed in nitrogen-filled vials for transport to the susceptometer. The susceptibilities of the sample holder were measured at the same fields and temperatures for accurate corrections of its contribution to the total measured susceptibility. A diamagnetic correction of -664×10^{-6} was estimated from Pascal's constants[48,49] and subtracted from the experimental susceptibilities.

EPR Studies. Saturation-recovery and continuous wave EPR experiments were performed on a home-built X-band pulsed EPR spectrometer.[50] The magnetic field was set at the zero-crossing point of the first derivative spectrum of the phenoxyl radical (see Figure 5), that is, at the maximum of the

corresponding absorption signal. Temperature control was achieved with an Oxford ESR 900 liquid helium cryostat and calibrated by using a Si-diode sensor at the sample position. At any given temperature, three to four saturation-recovery EPR transients were recorded at different levels of observing microwave power in order to determine T_1^{-1} or $k_{1scalar}$ by linear extrapolation to zero power.[50] A nonlinear regression program written by Dr. D. Hirsh, employing the Marquardt algorithm,[51] was used to obtain fits to the saturation-recovery EPR traces. The radical concentration was ≈ 0.1 mM in the [Zn(BIDPhE)Cl_2] compound and either ≈ 0.2 mM or ≈ 2.0 mM in compound **6**. All samples were prepared in anaerobic CH_2Cl_2/THF (3/1 v/v) solution so as to assure the formation of a good glass upon freezing.

Results and Discussion

Syntheses. The preparation of the BIDPhEH ligand was accomplished in three steps from methyl 3,5-di-*tert*-butyl 4-hydroxy benzoate, as shown in Scheme 1. Addition of the ester to a solution of three equivalents of the 1-methylimidazolate anion in THF afforded alcohol **1** in good yield. The target phenol BIDPhEH (**2**) was synthesized in two steps via the formation of the quinone methide intermediate **4**. Addition of one equivalent of CH_3Li to a solution of **1** in THF, followed by refluxing, led to the formal dehydration of **1**, generating **4** in situ. Although **4** can be prepared independently from **1** by the addition of *n*-butyllithium, we found it unnecessary to isolate **4** in the synthesis of **2** since the conversion of **1** to **4** in situ is nearly quantitative. The addition of nucleophiles to quinone methides is well-known, including the use of carbanions to give the 1,6-addition product.[52,53] Addition of two more equivalents of CH_3Li to the reaction mixture, one of which served as a sacrificial equivalent of base, afforded **2** in typical yields of 40 % after purification by crystallization.

The BIDPhEH ligand was designed to have quarternary carbon atoms at both ortho and para phenol ring positions. Such substituents are necessary to stabilize the phenoxyl radical against electron delocalization and ring coupling reactions.[54] Oxidation of phenols to the corresponding phenoxyl radicals can be accomplished by various methods and oxidizing agents, including the use of PbO_2 and $[Fe(CN)_6]^{3-}$.[55] The former reagent could oxidize **2** to the corresponding radical BIDPhE (**3**), but the conversion was never quantitative. Radical **3** proved to be stable to chromatography on silica gel plates, which always exhibited two major spots corresponding to the phenol starting material and radical product when PbO_2 was used as the oxidizing agent. The radical **3** is not stable to air over long periods (> 1 h) in solution, and the chromatographic separation of **2** and **3** had to be carried out under strict anaerobic conditions.

Use of potassium ferricyanide under basic conditions, as shown in Scheme 1, led to quantitative conversion of **2** to **3**. This procedure is more efficient than the PbO_2 method probably because the oxidizing agent is dissolved, rather than being suspended in the reaction mixture and, more importantly, there is an excess of base present for removal of the phenolic proton. The radical **3** was isolated as a green solid simply by removing solvent from the organic layer. Although recrystallization of **3** can be accomplished from CH_2Cl_2 at -20 °C, this step causes a significant reduction in yield. Quantitation by chemical titration (see Experimental Section) revealed the radical content in **3** to be consistently >90%, making further purification steps unnecessary.

The UV-visible spectrum of a deep green solution of **3** in CH_3CN, shown in Figure 2, exhibits three distinct bands characteristic of substituted phenoxyl radicals.[54] The visible band at 638 nm proved useful in the characterization of the zinc complex $[Zn(BIDPhE)Cl_2]$, as well as for the diferric complex **6**.[39]

Radical **3** is stable in the solid state for ≥ 1 year if stored at -20 °C under anaerobic conditions, as monitored by the intensity of 638 nm band.

The mononuclear complex $[Fe(BIDPhEH)_2Cl_2]^+$ was obtained by reaction of $FeCl_3$ with BIDPhEH. This complex was isolated with Cl^- as counterion (**5a**) when the ratio of BIDPhEH to iron employed was 2 : 1, and with $[FeCl_4]^-$ as counterion (**5b**) when a 1 : 1 ratio was used. An X-ray structure of **5a** revealed the nature of the mononuclear complex, but was complicated by disorder problems. A structure of better quality was obtained with crystals of the $FeCl_4^-$ analogue **5b**, and is discussed below. Crystallization of **5b** typically occured over a period of several weeks, making **5a** the more desirable compound for routine synthesis.

Attempts to prepare oxo, carboxylato-bridged diferric complexes with **2** or **3** as capping ligand from ferric salts and simple carboxylates as starting materials were unsuccessful.[29] We therefore turned to the dinucleating ligand XDK (see Scheme 2). This pre-organized, cleft-shaped bis(carboxylato) ligand has been developed in our laboratory as a general dinucleating ligand for use in the synthesis of a number of carboxylate-bridged diferric and heterodimetallic complexes.[30,56,57] The remarkably stable solvento complex $[Fe_2O(XDK)(MeOH)_5(H_2O)](NO_3)_2$, which is readily prepared in multigram quantities from $Fe(NO_3)_3$ and $XDKH_2$, has been used as a starting material for the preparation of several (μ-oxo)bis(μ-carboxylato)diiron(III) complexes with the bidentate nitrogen donor ligand 2,2'-dipyridyl (bpy), such as $[Fe_2O(XDK)(bpy)_2(NO_3)_2]$, as well as the simple monodentate ligand 1-methylimidazole (1-MeIm).[30] These complexes are formed by substitution of the nitrogen donor ligands for the coordinated solvent molecules. This experience suggested that the solvento complex would be an excellent starting material for preparing the desired (μ-oxo)bis(μ-carboxylato)diiron(III) complex with **3** as

capping ligand, provided that the radical could withstand the synthetic procedures.

Initial attempts to prepare **6** by combining **3** and the solvento complex in a variety of solvents, such as CH_3CN, THF or MeOH, led to significant loss of radical content as judged by monitoring the 640 nm band in the UV-visible spectrum of the reaction mixture. Depending on the solvent employed, as much as 60% radical decay was noted 0.5 to 2.0 h after combination of the starting materials. When MeOH was employed, complete bleaching of the 640 nm band occurred immediately after addition of the solvento complex to a solution of **3**. Although the mechanism of this radical decomposition is presently unknown, a possible cause is reduction by the solvent, which in the case of MeOH would be accompanied by oxidation to form the aldehyde. Interestingly, the BIDPhE ligand alone shows little sign of decay after standing for several hours in MeOH. Oxidation of MeOH to formaldehyde has been implicated in the mechanism of the tyrosyl radical, cupric-containing enzyme galactose oxidase, as discussed elsewhere.[1]

Reaction of **3** with the solvento complex in CH_2Cl_2 gave reaction mixtures in which the radical band at 640 nm showed no decay for several hours at room temperature, making this solvent the best candidate for crystallization of the desired product. The synthesis of $[Fe_2O(XDK)(BIDPhE)_2(NO_3)_2]$ (**6**) is summarized in Scheme 2. Compound **6** was isolated as a crystalline solid from CH_2Cl_2/pentane mixtures at -30 to -40 °C. Spectroscopic characterization of **6**, including resonance Raman data reported elsewhere,[39] confirmed the presence of the noncoordinated phenoxyl radical of ligand **3** as well as the bent oxo-bridged diferric core. All of the data, including magnetic susceptibility and EPR measurements (vide infra), are consistent with the structure of **6** depicted in Scheme 2. This structure is analogous to that of crystallographically

characterized compounds having bpy or 1-MeIm in place of BIDPhE in the external coordination sites.[30]

Molecular Structure of 5. As shown in Figure 3, compound **5** is a mononuclear ferric complex with two cis BIDPhEH ligands coordinated through the imidazole nitrogen atoms, and two chloride ligands completing the coordination sphere. The overall geometry is approximately octahedral, indicated by the angles reported in Table 2. Despite the preference of Fe(III) for oxygen-donor ligands, the bulky *tert*-butyl groups prevent coordination of BIDPhEH through its phenolic oxygen atom, as anticipated in the design of this ligand. The phenolic group is held pendant to the metal center, with an average Fe···O distance of 8.80(9) Å. This value of interest to compare with that extracted from the saturation-recovery EPR experiments on compound **6** (vide infra).

The phenoxyl radical form of the ligand, BIDPhE, is expected to bind in the same manner. Conversion of the pendant phenol to a phenoxyl radical should not affect the chelating properties of the imidazole donor groups, since there is no pathway for delocalization of radical spin density onto the imidazole rings. Comparison of the properties of the radical and nonradical analogues of the mononuclear zinc complexes [Zn(BIDPhEH)Cl_2] and [Zn(BIDPhE)Cl_2] confirmed that BIDPhE and BIDPhEH coordinate in a similar fashion to Zn(II),[39] lending support to the conclusion that BIDPhE and BIDPhEH bind iron in the same fashion.

Magnetic Susceptibility Study of 6. A plot of the temperature dependence of χT for **6** is shown in Figure 4. The decrease in χT with decreasing temperature is characteristic of antiferromagnetic exchange coupling. Such behavior is expected for a (μ-oxo)bis(μ-carboxylato)diiron(III) compound, in which the coupling between two d^5 ($S = 5/2$) iron atoms gives rise to an $S = 0$ ground state.[23] As the temperature is lowered, χT decreases until 40 K, at which

temperature a plateau is observed. This plateau corresponds to the residual paramagnetism arising from the two $S = 1/2$ radical ligands, which are uncoupled and exhibit Curie behavior. The theoretical value expected for the χT product of two such uncoupled spins is 0.75 $cm^3\ mol^{-1}\ K$, assuming $g = 2.00$. The plateau in the χT curve for **6** occurs near 0.74 $cm^3\ mol^{-1}\ K$, very close to the expected theoretical value. The downturn in χT at very low temperatures may be due to a small amount of radical-radical antiferromagnetic exchange, either between neighboring molecules or within the same diiron complex.

The susceptibility data were fit by least-squares[58] to the theoretical model shown in eq. 1, where $P = 2\exp(2J/kT) + 10\exp(6J/kT) + 28\exp(12J/kT) + 60\exp(20J/kT) + 110\exp(30J/kT)$; $Q = 1 + 3\exp(2J/kT) + 5\exp(6J/kT) + 7\exp(12J/kT) + 9\exp(20J/kT) + 11\exp(30J/kT)$; $\chi_{imp} = (Ng^2\mu_B^2/3kT)(S(S+1))$ with $g = 2.00$ and $S = 5/2$, and IMP is a mole percentage of an $S = 5/2$ impurity; TIP = temperature independent paramagnetism; $C_{rad} = (Ng_{rad}^2\mu_B^2/3k)(S(S+1))$; θ_{rad} = Weiss constant; g_{Fe} is the overall isotropic g value for the diiron center; g_{rad} is the overall isotropic g value for the radicals, and the other symbols have their usual meanings. This model includes the familiar expression derived from the Heisenberg isotropic spin exchange Hamiltonian for a dinuclear system, $\mathcal{H} = -2J\cdot S_1\cdot S_2$, as well as a term that takes into account the uncoupled, Curie-Weiss behavior of the two $S = 1/2$ radical sites.

$$\chi_M = \chi_{imp}(IMP) + (1\text{-}IMP)((2Ng_{Fe}^2\mu_B^2/kT)(P/Q)) + TIP + 2(C_{rad}/(T - \theta_{rad})) \qquad (1)$$

The best fit to the data at all temperatures, shown in Figure 4, had only two parameters refined, the J value and the Weiss constant θ_{rad}. Both g values were fixed at 2.00, and IMP and TIP terms were fixed at zero. The refined values were $J = -117.5(4)\ cm^{-1}$ and $\theta = -0.47(2)$ K. A good fit was also obtained by

refining g_{Fe} and g_{rad} along with J and θ, resulting in J = -124(2) cm^{-1}, θ = -0.46(3) K, g_{rad} = 2.00 and g_{Fe} = 2.11. The overall g value for the diferric center in this latter fit is somewhat high compared to the expected value of g = 2.00 for a high-spin d^5 ion, and the fit was only marginally improved. If θ_{rad} was fixed at zero, the data above 25 K were fit well with J values near -120 cm^{-1}, but the theoretical χT product exhibited a plateau close to 0.75 cm^3 mol^{-1} K between 5 and 25 K, and gave a poor fit to the downturn in the experimental curve at low temperatures. The only way in which the downturn in the experimental χT product could be fit successfully was by the inclusion of a small negative θ_{rad} term, suggesting a small amount of interradical antiferromagnetic coupling, either intra- or intermolecular, in the low temperature regime. An excellent fit was also obtained if the data below 35 K were excluded and only the J value was refined, resulting in J = -118.2(6) cm^{-1}, with both g values fixed at 2.00 and all other parameters set to zero. These results clearly indicate a J value of $\approx$ -118 cm^{-1} for the antiferromagnetic exchange coupling constant, a value consistent with those determined for a variety of other (μ-oxo)bis(μ-carboxylato)diiron(III) complexes.[59,60]

The temperature-dependent magnetic behavior of the model complex **6** is strikingly similar to that exhibited by the tyrosyl radical/diferric form of the R2 protein of ribonucleotide reductase, for which a recent magnetic susceptibility study has been conducted.[61] The χT product for the protein also shows the characteristic decrease with decreasing temperature in the range 200 - 50 K for an antiferromagnetically coupled diferric core, followed by a plateau region at T < 50 K. In this case the plateau occurs at $\approx$ 0.45 cm^3 mol^{-1} K, close to half the plateau value for compound **6**, because there is only one radical per diiron unit in the protein active site. A least-squares fit of the data resulted in J = -84 (5) cm^{-1}

for the (μ-oxo)(μ-carboxylato)diferric site in the protein.[61] This value may indicate hydrogen bonding to the oxo bridge.

EPR studies. Saturation-recovery EPR spectrosocopy has recently been used[62,63] to probe the spin-lattice relaxation behavior of the tyrosyl radical (Tyr 122) in ribonucleotide reductase isolated from different sources. The rapid increase in the spin-lattice relaxation rate above ~20 K and the non-single exponential behavior of the saturation-recovery transients obtained at the higher temperature regime were attributed to the onset of a spin-lattice relaxation enhancement mechanism through the pairwise interaction of the tyrosyl radical, a slow-relaxing spin, with the neighboring differic center, a fast relaxing spin. The latter is rendered paramagnetic by population of its first excited spin state (S=1) as the temperature is raised to 20 K. Two major contributions to the spin-lattice relaxation rate of the observed slowly relaxing spin can be discerned: (i) an isotropic term, denoted as $k_{1scalar}$, incorporating the intrinsic relaxation rate of the species (k_{1i}) and the relaxation arising from its exchange coupling (k_{1ex}) through spatial orbital overlap with a neigboring paramagnet, and (ii) an orientation-dependent term, $k_{1\theta}$, arising from the dipole-dipole interaction between the two paramagnets. The random orientation of the interspin vector relative to the applied magnetic field, applicable in the case of a non-oriented protein or an inorganic complex in a frozen glass, results in an angular distribution of the spin-lattice relaxation rates and gives rise to non-single exponential relaxation kinetics. Taking this fact into account, the saturation-recovery EPR transients can be fit by using eq. 2, where I(t) is the intensity of the

$$I(t) = 1 - N \int_0^{\pi} \sin\theta \cdot (\exp\{k_{1scalar} + k_{1\theta}\}t) d\theta) \qquad (2)$$

saturation-recovery EPR transient at time t, N is an adjustable scaling factor, $k_{1scalar} = k_{1i} + k_{1ex}$, and $k_{1\theta}$ is expressed by eqs 3 and 4 below.

As shown in Hirsh et al.,[62] for the case of a dipolar interaction between the tyrosyl radical in RR and the neighboring dinuclear ferric center, the "B" term of the dipolar alphabet is the dominant term in the theoretical expression for $k_{1\theta}$, which is then simplified as indicated by eq. 3:

$$k_{1\theta} = k_{1d}^{B}\cdot(1\text{-}3\cos^2\theta)^2 \tag{3}$$

where

$$k_{1d}^{B} = \frac{\gamma_s^2\mu_f^2}{6r^6}\,\frac{1}{\omega_s^2(1\text{-}g_f/g_s)^2T_{2f}} \tag{4}$$

In eq 4, r is the interspin distance, γ_s, ω_s and g_s are the magnetogyric ratio, the Larmor frequency and the g value of the slow relaxer, respectively, and μ_f, T_{2f} and g_f are the effective magnetic moment, the transverse (spin-spin) relaxation time and the g value of the fast relaxer, respectively. The "dipolar"-model fit to the saturation-recovery EPR transients with the use of eq. 2, affords two rate constants, $k_{1scalar}$ and k_{1d}^{B}. The expression for μ_f for an antiferromagnetically coupled dinuclear ferric center is given by eq. 5, if we assume that only the

$$\mu_f^2 = g_f^2(6\exp(2J_{ex}/kT)) \tag{5}$$

S=0 and S=1 spin states are significantly populated and by using $\mathcal{H} = -2J_{ex}.\mathbf{S}_1\cdot\mathbf{S}_2$ as the Heisenberg exchange Hamiltonian, where J_{ex} is the exchange coupling constant of the dinuclear center and k is the Boltzmann constant. In the case where only μ_f is temperature dependent, equations 4 and 5 predict that a plot of $\ln(k_{1d}^{B})$ vs 1/T will be linear and have a slope of $2J_{ex}/k$.

The insets in figures 5 and 6 show the first-derivative cw-EPR spectra of the phenoxyl radical (**3**) as observed in the mononuclear compound [Zn(BIDPhE)Cl_2] and in the diferric model compound (**6**), respectively. The arrows point to the zero-crossing point (g = 2.00) of the first-derivative spectra, which is the field setting used in the saturation-recovery experiment. The

structureless nature of both cw-EPR signals denotes a lack of proton nuclear hyperfine interaction, which is expected given the presence of the quarternary carbon atoms in the ortho and para phenyl ring positions. The radicals also have the same peak-to-peak widths ($\Delta H_{pp} \approx 9$ Gauss), and these data are fully consistent with the fact that the cw signals arise from identical radical sources.

The intrinsic spin-lattice relaxation rate ($k_{1i} = 1/T_1$) of the phenoxyl radical BIDPhE (**3**) was measured by saturation-recovery EPR experiments on [Zn(BIDPhE)Cl_2]. Since Zn(II) is diamagnetic, the phenoxyl radical is expected to exhibit only its intrinsic relaxation, and consequently the saturation-recovery transients should show single-exponential behavior. A typical transient of the phenoxyl radical, obtained at 9.0 K, is shown in Figure 5a. It is single exponential in nature as clearly shown from the superimposed single-exponential fit and the quality of the residual. The residual obtained by using the dipolar model fit (Figure 5c) is identical with the one of the single exponential fit (Figure 5b), providing additional evidence that one adjustable parameter, $1/T_1$, is sufficient to fit the experimental data satisfactorily. The temperature dependence of the intrinsic relaxation rate of the phenoxyl radical is shown in Figure 7 (cross symbols) and it follows an $\approx T^{2.5}$ temperature dependence. This dependence is very similar to that observed recently for other organic radicals.[64]

The spin-lattice relaxation behavior of the BIDPhE radical in the dinuclear Fe(III) compound (**6**) was examined in the temperature range 6.7 K - 115 K. The saturation-recovery transients showed single exponential kinetics for the range $6.7 \text{ K} < T < 70$ K, which we denote as the "low" temperature regime. A typical experimental transient obtained at T = 6.7 K is shown in Figure 6a, with a single exponential fit superimposed. The temperature dependence ($k_{1i} = 1/T_1 \propto T^{2.5}$) and magnitude of the relaxation rate constants extracted from the single exponential fits are identical, within experimental error, with the ones of the

radical in the [Zn(BIDPhE)Cl_2] compound, as clearly indicated in Figure 7 (open square and cross symbols). Thus, we conclude that any intraradical spin-spin exchange for **6**, either inter- or intramolecular in nature, is too small to enhance the intrinsic spin-lattice relaxation rate.

At temperatures above 70 K, the "high" temperature regime, the experimentally observed saturation-recovery traces of the phenoxyl radical in **6** exhibit non-single exponential kinetic behavior. A typical saturation-recovery curve obtained at 87 K is shown in Figure 8a, with a "dipolar" model fit superimposed. The fit provided by a single exponential is poor as judged from the residual shown in Figure 8b. This situation is reminiscent of the spin-lattice relaxation behavior of the Tyr122 radical in ribonucleotide reductase in its "high" temperature regime. In the present case, the population of the first excited spin-state (S = 1) of the diferric center becomes significant above 70 K, making it a potent relaxation enhancer of the tethered phenoxyl radicals.

The scalar rate constants, $k_{1scalar}$, extracted from the B-term "dipolar" model fit (Figure 7, open circles, 72 K < T < 115 K) closely follow the magnitude and temperature dependence of the intrinsic relaxation rate of the phenoxyl radical as measured independently (Figure 7, open square and cross symbols). This behavior indicates that, in contrast to the case of ribonucleotide reductase, there is no significant exchange interaction due to spatial orbital overlap between the phenoxyl radical and the diferric center of **6**. One reason for this lack of overlap could be that a larger distance (≥ 10 Å) separates the two spin centers in **6** relative to the separation in ribonucleotide reductase, in which the distance between the tyrosyl (Tyr122) radical and the center of the diferric cluster, weighted for the spin density distribution on the phenyl ring, is ~7.7 Å.[63,65]

The dipolar rate constants k_{1d}^{B}, extracted by using the B-term of the dipolar alphabet (Figure 7, full circles, 72 K < T < 115 K), exhibit an $\approx T^{4.0}$

temperature dependence, which is much steeper than the $\approx T^{2.5}$ dependence observed for the intrinsic relaxation rate of the radical at the "low" temperature regime (6.7 K < T < 70 K). It is important to note that the dipolar rate constants obtained are of identical magnitude, within experimental error, for radical concentrations between 0.2 and 2.0 mM, eliminating the possibility of intermolecular interactions playing any significant role in the observed relaxation enhancement effect.

Figure 9 shows a plot of $\ln(k_{1d}^{B})$ vs 1/T for the data in the "high" temperature regime. As predicted from eq. 5, the plot is linear and its slope gives $J_{ex} = (-115 \pm 7)$ cm^{-1} for the antiferromagnetic exchange coupling constant of the diferric center in **6**. This calculation is valid only if the transverse relaxation time, T_{2f}, of the diferric center is not temperature-dependent. A series of arguments against a significant temperature dependence for T_{2f} have already been presented.[62] They also hold in the present case since we are studying a homologous pairwise dipolar interaction between phenoxyl radicals and a diferric center. In addition, the value for J_{ex} determined with the saturation-recovery EPR studies is in excellent agreement with the one determined independently through the magnetic susceptibility measurements. This result provides strong support for the use of the dipolar model to analyze the non-single exponential spin-lattice relaxation kinetics observed at T > 70 K for the phenoxyl radical in **6**. The ≈ 30 cm^{-1} larger value for the exchange coupling constant in **6** relative to *E. coli* ribonucleotide reductase R2 explains the higher temperature required to observe the onset of the dipolar relaxation enhancement of the radical in **6** relative to the protein (87 K vs 34 K).

Finally, it is possible to do a rough calculation of the average distance between the two paramagnets in **6**, the phenoxyl radical and the diferric center. The y-intercept of the expression for $\ln(k_{1d}^{B})$ vs 1/T is given by

$\ln(\gamma_s^2 \cdot g_f^2 / \omega_s^2(1-g_f^2/g_s^2) \cdot T_{2f} \cdot r^6)$, which can be rewritten as $\ln(A/r^6)$ where the constant A incorporates all the terms dependent on γ_s, g_s, g_f, ω_s and T_{2f}. The values of the y-intercept are 15.2 ± 0.2 and 11.8 ± 0.3 for *E. coli* R2 and **6**, respectively. Since in *E. coli* R2, we know that r = 7.7 Å, we can calculate the value of the constant A. By making the assumption that g_f, g_s and T_{2f} are the same in both the protein and the model compound under study, we can make a rough estimate of 13.5 ± 1.2 Å for the average distance r between the phenoxyl radical and the diferric center in **6**.

This value has to be taken with caution since the assumption of identical g_f, g_s and T_{2f} values for **6** and RR may not be valid. On the other hand, the fact that we do not observe any contribution to the spin-lattice relaxation from exchange between the radical and the diferric center indicates that they are located at least 10 Å apart,[66] a value which is in very good agreement with our rough estimate. In addition, we know that the phenolic oxygen atom to iron atom distance in **5b**, as well as the equivalent distance in the [Zn(BIDPhE)Cl_2] compound, is ≈ 9 Å. We can then estimate that the distance from the phenolic oxygen atom to the center of the diferric cluster in **6** must be between 9 and 12.3 Å, given a typical Fe-Fe separation of 3.1 - 3.2 Å for (μ-oxo)bis(μ-carboxylato) complexes of this type.[30,59] The rough value of 13.5 ± 1. Å obtained for the interspin distance in **6** is in satisfactory agreement with all the experimental evidence.

Conclusions

The synthesis of a phenoxyl radical diiron complex (**6**) as a model for the active site in the R2 protein of ribonucleotide reductase has been accomplished by utilizing the dinucleating bis(carboxylato) ligand XDK, as well as the new stable phenoxyl radical ligand BIDPhE. Study of this compound by solid state

magnetic susceptibility measurements and saturation-recovery EPR spectroscopy was facilitated by the fact that **6** could be obtained as a stable solid. Magnetic susceptibility measurements revealed temperature-dependent behavior that mimicked the protein data quite well, and could be fit by a simple spin exchange model that accounted for the presence of two $S = 1/2$ radicals per diiron center and yielded a direct measure of the J value for the antiferromagnetic exchange in the $[Fe_2O(O_2CR)_2]^{2+}$ core.

The diiron model complex **6** and the mononuclear zinc complex $[Zn(BIDPhE)Cl_2]$ both give rise to identical singlets in the X-band cw-EPR spectra, and these signals proved amenable to spin saturation-recovery experiments. From fitting the saturation recovery transients obtained over a range of temperatures to either a single-exponential model, as in the case of $[Zn(BIDPhE)Cl_2]$, or the dipolar model as for **6**, both scalar and dipolar rate constants could be extracted. The zinc complex proved to be an excellent control compound for obtaining the intrinsic relaxation rate constant of the BIDPhE radical when coordinated to a diamagnetic metal, and exhibited the temperature-dependent behavior expected for a simple organic radical. By comparison with the zinc complex, a clear rate enhancement for the BIDPhE radical in the diiron complex is shown in the high temperature range, fully consistent with the population of the first paramagnetic excited state of the nearby antiferromagnetically-coupled diiron center.

From a theoretical model of this behavior, the J value for the antiferromagnetic exchange coupling between the iron atoms in **6** was calculated to be -115 cm^{-1}, in remarkably good agreement with that obtained from the SQUID measurement, $J = -118$ cm^{-1}. The distance from the phenoxyl radical to the center of the diiron core was estimated to be 13.5 Å, also in good agreement with the value expected from an analysis of other structurally-characterized

diiron(XDK) complexes of this type and information obtained from the crystal structure of **5b**. Thus, all of the magnetic data on **6** are fully consistent with the proposed structure in Scheme 2. Both the magnetic susceptibility and spin saturation-recovery EPR techniques revealed overall behavior for the diiron model complex that was quite similar to the R2 active site and could distinguish important differences in parameters that were consistent with the structural differences between the model and the protein.

Acknowledgements. We are grateful to D. Koulougliotis and Professor G. W. Brudvig for obtaining and analyzing the EPR data. We thank K. Ward for help in preparing EPR samples of compound **6**, and Dr. S. Watton and Dr. C. Bastos for useful discussions.

References

(1) Goldberg, D. P.; Lippard, S. J. In *Mechanistic Bioinorganic Chemistry*; H. H. Thorp and V. Pecoraro, Ed.; ACS Books: 1994; in press.

(2) Pedersen, J. Z.; Finazzi-Agro, A. *FEBS Lett.* **1993**, *325*, 53-58.

(3) Ochiai, E.-I. *J. Chem Ed.* **1993**, *70*, 128-133.

(4) Stubbe, J. *Annu. Rev. Biochem.* **1989**, *58*, 257-285.

(5) Prince, R. C. *TIBS* **1988**, *13*, 152-154.

(6) Debus, R. J. *Biochim. Biophys. Acta* **1992**, *1102*, 269-352.

(7) Hamilton, G. A. In *Copper Proteins*; T. G. Spiro, Ed.; John Wiley & Sons, Inc.: New York, 1981; Vol. 3; pp 193-218.

(8) Ettinger, M. J.; Kosman, D. J. In *Copper Proteins*; T. G. Spiro, Ed.; John Wiley & Sons, Inc.: New York, 1981; Vol. 3; pp 219-261.

(9) Avigad, G.; Amaral, D.; Asensio, C.; Horecker, B. L. *J. Biol. Chem.* **1962**, *237*, 2736-2743.

(10) Smith, W. L.; Marnett, L. J. *Biochim. Biophys. Acta* **1991**, *1083*, 1-17.

(11) Fontecave, M.; Nordlund, P.; Eklund, H.; Reichard, P. In *Advances in Enzymology and Related Areas of Molecular Biology*; A. Meister, Ed.; John Wiley and Sons: New York, 1992; Vol. 65; pp 147-183.

(12) Stubbe, J. In *Advances in Enzymology and Related Areas of Molecular Biology*; A. Meister, Ed.; John Wiley and Sons: New York, 1990; Vol. 63; pp 349-420.

(13) Ito, N.; Phillips, S. E. V.; Yadav, K. D. S.; Knowles, P. F. *J. Mol. Biol.* **1994**, *238*, 794-814.

(14) Ito, N.; Phillips, S. E. V.; Stevens, C.; Ogel, Z. B.; McPherson, M. J.; Keen, J. N.; Yadav, K. D. S.; Knowles, P. F. *Nature* **1991**, *350*, 87-90.

(15) Babcock, G. T.; El-Deeb, M. K.; Sandusky, P. O.; Whittaker, M. M.; Whittaker, J. W. *J. Am. Chem. Soc.* **1992**, *114*, 3727-3734.

(16) Kulmacz, R. J.; Palmer, G.; Wei, C.; Tsai, A.-l. *Biochem.* **1994**, *33*, 5428-5439.

(17) Tsai, A.-l.; Hsi, L. C.; Kulmacz, R. J.; Palmer, G.; Smith, W. L. *J. Biol. Chem.* **1994**, *269*, 5085-5091.

(18) Smith, W. L.; Eling, T. E.; Kulmacz, R. J.; Marnett, L. J.; Tsai, A.-l. *Biochem.* **1992**, *31*, 3-7.

(19) Picot, D.; Loll, P. J.; Garavito, R. M. *Nature* **1994**, *367*, 243-249.

(20) Reichard, P. *Science* **1993**, *260*, 1773-1777.

(21) Nordlund, P.; Eklund, H. *J. Mol. Biol.* **1993**, *232*, 123-164.

(22) Nordlund, P.; Sjöberg, B.-M.; Eklund, H. *Nature* **1990**, *345*, 593-598.

(23) Armstrong, W. H.; Spool, A.; Papaefthymiou, G. C.; Frankel, R. B.; Lippard, S. J. *J. Am. Chem. Soc.* **1984**, *106*, 3653.

(24) Lippard, S. J. *Angew. Chem. Int. Ed. Engl.* **1988**, *27*, 344-361.

(25) Beer, R. H.; Tolman, W. B.; Bott, S. G.; Lippard, S. J. *Inorg. Chem.* **1989**, *28*, 4557-4559.

(26) Turowski, P. N.; Armstrong, W. H.; Roth, M. E.; Lippard, S. J. *J. Am. Chem. Soc.* **1990**, *112*, 681-690.

(27) Beer, R. H.; Tolman, W. B.; Bott, S. G.; Lippard, S. J. *Inorg. Chem.* **1991**, *30*, 2082-2092.

(28) Tolman, W. B.; Liu, S.; Bentsen, J. G.; Lippard, S. J. *J. Am. Chem. Soc.* **1991**, *113*, 152-164.

(29) Taft, K. L.; Masschelein, A.; Liu, S.; Lippard, S. J.; Garfinkel-Shweky, D.; Bino, A. *Inorg. Chim. Acta* **1992**, *198-200*, 627-631.

(30) Watton, S. P.; Masschelein, A.; Rebek, J., Jr.; Lippard, S. J. *J. Am. Chem. Soc.* **1994**, *116*, 5196-5205.

(31) Kompan, O. E.; Ivakhnenko, E. P.; Lyubchenko, S. N.; Olekhnovich, L. P.; Yanovskii, A. I.; Struchkov, Y. T. *J. Gen. Chem. USSR (Engl. Trans.)* **1990**, 1682-1690.

(32) Ivakhnenko, E. P.; Lyubchenko, S. N.; Kogan, V. A.; Olekhnovich, L. P.; Prokof'ev, A. I. *J. Gen. Chem. USSR (Engl. Trans.)* **1986**, *56*, 765-768.

(33) Melezhik, A. V.; Vovk, D. N.; Pokhodenko, V. D. *J. Gen. Chem. USSR (Engl. Trans.)* **1983**, *53*, 1442-1447.

(34) Melezhik, A. V.; Pokhodenko, V. D. *J. Org. Chem. USSR (Engl. Trans.)* **1982**, *18*, 912-917.

(35) Pokhodenko, V. D.; Melezhik, A. V.; Vovk, D. N. *Sov. J. Coord. Chem. (Engl. Trans.)* **1982**, *8*, 667-671.

(36) Shultz, D. A.; Knox, D. A.; Morgan, L. W.; Sandberg, K.; Tew, G. N. *Tetrahedron Lett.* **1993**, *34*, 3975-3978.

(37) Hockertz, J.; Steenken, S.; Wieghardt, K.; Hildebrandt, P. *J. Am. Chem. Soc.* **1993**, *115*, 11222-11230.

(38) Whittaker, M. M.; Chuang, Y.-Y.; Whittaker, J. W. *J. Am. Chem. Soc.* **1993**, *115*, 10029-10035.

(39) Goldberg, D. P.; Watton, S. P.; Masschelein, A.; Wimmer, L.; Lippard, S. J. *J. Am. Chem. Soc.* **1993**, *115*, 5346-5347.

(40) Bartlett, P. D.; Funahashi, T. *J. Am. Chem. Soc.* **1962**, *84*, 2596-2601.

(41) Creagh, D. C.; McAuley, W. J. In *International Tables for X-ray Crystallography* Kluwer Academic Publishers: Dordrecht, 1992; Vol. C.; pp 219-222.

(42) Lawton, S. L. TRACER II, *A Fortran Transformation-Cell Reduction Program;* Mobil Oil Corporation: Paulsboro, NJ, 1967.

(43) North, A. C. T.; Phillips, D. C.; Mathews, F. S. *Acta Crystallogr.* **1968**, *A24*, 351-359.

(44) Sheldrick, G. M. *SHELXS86. Program for crystal structure determination;* University of Göttingen: Göttingen, 1986.

(45) Cromer, D. T.; Waber, J. T. In *International Tables for X-ray Crystallography* Kynoch Press: Birmingham, 1974; Vol. 4; pp 71-98.

(46) Stewart, R. F.; Davidson, E. R.; Simpson, W. T. *J. Chem. Phys.* **1965**, *42*, 3175-3187.

(47) Ibers, J. A.; Hamilton, W. C. *Acta Cryst.* **1964**, *17*, 781.

(48) Carlin, R. L. *Magnetochemistry*; Springer-Verlag: New York, 1986.

(49) O'Connor, C. J. *Prog. Inorg. Chem.* **1982**, *29*, 203-283.

(50) Beck, W. F.; Innes, J. B.; Lynch, J. B.; Brudvig, G. W. *J. Magn. Reson.* **1991**, *91*, 12-29.

(51) Press, W. H.; Flannery, B. P.; Teukolsky, S. A.; Vetterling, W. T. *Numerical Recipes in Pascal*; Cambridge University Press: Cambridge, 1989.

(52) Becker, H.-D. *J. Org. Chem.* **1967**, *32*, 4093-4095.

(53) Turner, A. B. *Quart. Rev.* **1964**, *18*, 347-360.

(54) Altwicker, E. A. *Chem. Rev.* **1967**, *67*, 475-531.

(55) Thyagarajan, B. S. *Chem. Rev.* **1958**, *58*, 439-460.

(56) Tanase, T.; Watton, S. P.; Lippard, S. J. *J. Am. Chem. Soc.* **1994**, *116*, 9401-9402.

(57) Watton, S.; Davis, M. I.; Pence, L. E.; Rebek, J., Jr.; Lippard, S. J. *Inorg. Chim. Acta* **1994**, submitted for publication.

(58) Vef, A. *Model2- Fit and Evaluation Program*; Institut für Anorganische Chemie und Analytische Chemie, Johannes-Gutenberg-Universität Mainz, 1989.

(59) Que, L., Jr.; True, A. E. In *Prog. in Inorg. Chem.*; S. J. Lippard, Ed.; John Wiley and Sons: New York, 1990; Vol. 38; pp 97-200.

(60) Kurtz, D. M., Jr. *Chem. Rev.* **1990**, *90*, 585-606.

(61) Atta, M.; Scheer, C.; Fries, P. H.; Fontecave, M.; Latour, J.-M. *Angew. Chem. Int. Ed. Engl.* **1992**, *31*, 1513-1515.

(62) Hirsh, D. J.; Beck, W. F.; Lynch, J. B.; Que L., J.; Brudvig, G. W. *J. Am. Chem. Soc.* **1992**, *114*, 7475-7481.

(63) Galli, C.; Atta, M.; Andersson, K. K.; Gräslund, A.; Brudvig, G. W. *J. Am. Chem. Soc.* **1994**, submitted for publication.

(64) Hirsh, D. J.; Brudvig, G. W. *J. Phys. Chem.* **1993**, *97*, 13216-13222.

(65) Hirsh, J. D., Ph. D. Thesis, Yale University, 1993.

(66) Coffman, R. E.; Buettner, G. R. *J. Phys. Chem.* **1979**, *83*, 2387-2392.

Table 1. Crystallographic Data for $[Fe(BIDPhEH)_2Cl_2][FeCl_4] \cdot CH_3CN$ (**5b** · CH_3CN).

chemical formula	$Fe_2C_{50}H_{71}N_9Cl_6O_4$	octant collected	$+h\ +k\ +l$
formula weight	1154.58	Trans. coeff.	0.905 - 1.000
space group	Pbca	no. of unique data	10940
a (Å)	19.984(8)	Data with $F_o^2 > 3\sigma(F_o^2)$	4742
b (Å)	19.275(6)	R_{merge} (%)	2.2
c (Å)	29.779(14)	no. of variables	607
V (Å^3)	11471(8)	R $(F_o)^a$	0.048
Z	8	R_w $(F_o)^b$	0.057
d calcd, g cm^{-3}	1.34	goodness of fit	1.52
μ, cm^{-1}	8.30	λ (Å)	0.71069
range of 2θ (deg)	3 - 50	Temp (°C)	-72

$^aR = \Sigma| |F_o| - |F_c| |/\Sigma|F_o|$; $^bR_w = [(\Sigma w(|F_o| - |F_c|/\Sigma w|F_o|^2]^{1/2}$; $w = 1/\sigma^2(F_o)$

Table 2. Selected Interatomic Distances (Å) and Angles (deg) for $[Fe(BIDPhEH)_2Cl_2][FeCl_4] \cdot CH_3CN$ (**5b**).[a]

(a) Distances

Fe(1)-Cl(1)	2.317(2)	Fe(2)-Cl(3)	2.190(2)
Fe(1)-Cl(2)	2.325(2)	Fe(2)-Cl(4)	2.195(3)
Fe(1)-N(1)	2.103(5)	Fe(2)-Cl(5)	2.200(2)
Fe(1)-N(3)	2.143(5)	Fe(2)-Cl(6)	2.174(3)
Fe(1)-N(5)	2.109(5)	Fe(1)···O(1)	8.863(5)
Fe(1)-N(7)	2.142(5)	Fe(2)···O(2)	8.725(5)

(b) Angles

Cl(1)-Fe(1)-Cl(2)	93.76(7)	Cl(2)-Fe(1)-N(7)	175.1(1)
Cl(1)-Fe(1)-N(1)	94.7(1)	N(1)-Fe(1)-N(3)	81.9(2)
Cl(1)-Fe(1)-N(3)	174.6(1)	N(1)-Fe(1)-N(5)	169.5(2)
Cl(1)-Fe(1)-N(5)	91.9(1)	N(1)-Fe(1)-N(7)	89.3(2)
Cl(1)-Fe(1)-N(7)	90.3(1)	N(3)-Fe(1)-N(5)	90.9(2)
Cl(2)-Fe(1)-N(1)	93.1(1)	N(3)-Fe(1)-N(7)	85.5(2)
Cl(2)-Fe(1)-N(3)	90.6(1)	N(5)-Fe(1)-N(7)	82.5(2)
Cl(2)-Fe(1)-N(5)	94.6(1)		

[a]For atom-labelling scheme, see Figure 3. Estimated standard deviations in the least significant figure are given in parentheses.

Table 3. Positional Parameters and B(eq) for $[Fe(BIDPhEH)_2Cl_2][FeCl_4] \cdot CH_3CN$ (**5b** · CH_3CN).[a]

atom	x	y	z	B(eq)[b]
Fe(1)	0.80378(4)	0.13753(4)	0.62565(3)	1.53(4)
Fe(2)	0.13681(5)	-0.00449(6)	0.09780(4)	3.72(5)
Cl(1)	0.88250(8)	0.22515(8)	0.63265(5)	2.30(7)
Cl(2)	0.88363(8)	0.04980(8)	0.62436(5)	2.22(7)
Cl(3)	0.0324(1)	0.0211(1)	0.11274(7)	4.1(1)
Cl(4)	0.1573(1)	-0.1132(1)	0.11500(7)	4.4(1)
Cl(5)	0.2016(1)	0.0659(1)	0.13649(9)	5.7(1)
Cl(6)	0.1569(1)	0.0098(2)	0.02664(8)	8.8(2)
O(1)	0.4888(2)	-0.0261(2)	0.8064(1)	2.9(2)
O(2)	0.4904(2)	0.3067(3)	0.4535(2)	4.2(3)
N(1)	0.7878(2)	0.1276(2)	0.6951(1)	1.5(2)
N(2)	0.7481(3)	0.1045(3)	0.7622(2)	1.9(2)
N(3)	0.7250(2)	0.0622(2)	0.6233(2)	1.6(2)
N(4)	0.6644(2)	-0.0317(3)	0.6334(2)	2.0(2)
N(5)	0.8005(2)	0.1490(2)	0.5552(2)	1.6(2)
N(6)	0.7809(3)	0.1791(3)	0.4856(2)	2.1(2)
N(7)	0.7253(2)	0.2131(2)	0.6230(2)	1.7(2)
N(8)	0.6733(3)	0.3115(3)	0.6103(2)	2.4(3)
N(9)	0.1362(8)	0.2357(8)	0.2268(5)	16.6(6)
C(1)	0.7521(3)	0.0825(3)	0.7192(2)	1.6(3)
C(2)	0.7806(3)	0.1666(3)	0.7650(2)	2.0(3)
C(3)	0.8057(3)	0.1800(3)	0.7242(2)	1.8(3)
C(4)	0.7163(4)	0.0743(4)	0.8023(2)	3.3(4)
C(5)	0.7248(3)	0.0122(3)	0.7026(2)	1.5(3)

Table 3 contd. Positional Parameters and B(eq) for [Fe(BIDPhEH)$_2$Cl$_2$]-[FeCl$_4$] · CH$_3$CN (**5b** · CH$_3$CN).[a]

atom	x	y	z	B(eq)[b]
C(6)	0.7800(3)	-0.0431(3)	0.7098(2)	2.2(3)
C(7)	0.7061(3)	0.0145(3)	0.6528(2)	1.5(3)
C(8)	0.6562(3)	-0.0122(3)	0.5893(2)	2.4(3)
C(9)	0.6932(3)	0.0451(3)	0.5835(2)	2.1(3)
C(10)	0.6314(4)	-0.0939(4)	0.6511(2)	3.5(4)
C(11)	0.6594(3)	-0.0039(3)	0.7289(2)	1.6(3)
C(12)	0.6065(3)	0.0419(3)	0.7230(2)	1.6(3)
C(13)	0.5466(3)	0.0354(3)	0.7467(2)	1.8(3)
C(14)	0.5433(3)	-0.0183(3)	0.7782(2)	1.9(3)
C(15)	0.5942(3)	-0.0687(3)	0.7832(2)	1.8(3)
C(16)	0.6518(3)	-0.0587(3)	0.7576(2)	1.7(3)
C(17)	0.4892(3)	0.0861(3)	0.7382(2)	2.0(3)
C(18)	0.5015(3)	0.1307(3)	0.6959(2)	2.9(3)
C(19)	0.4820(3)	0.1363(4)	0.7780(2)	3.1(3)
C(20)	0.4224(3)	0.0469(4)	0.7298(2)	3.1(3)
C(21)	0.5856(3)	-0.1320(3)	0.8140(2)	2.4(3)
C(22)	0.6458(4)	-0.1802(3)	0.8112(2)	3.2(4)
C(23)	0.5810(4)	-0.1089(4)	0.8634(2)	4.1(4)
C(24)	0.5240(4)	-0.1735(4)	0.8007(3)	4.3(4)
C(25)	0.7713(3)	0.1962(3)	0.5294(2)	1.6(3)
C(26)	0.8170(3)	0.1185(3)	0.4841(2)	2.6(3)
C(27)	0.8293(3)	0.1006(3)	0.5268(2)	2.3(3)
C(28)	0.7594(4)	0.2138(4)	0.4437(2)	3.5(4)
C(29)	0.7375(3)	0.2641(3)	0.5435(2)	1.5(3)

Table 3 contd. Positional Parameters and B(eq) for $[Fe(BIDPhEH)_2Cl_2]$-$[FeCl_4] \cdot CH_3CN$ (**5b** $\cdot CH_3CN$).[a]

atom	x	y	z	B(eq)[b]
C(30)	0.7909(3)	0.3212(3)	0.5388(2)	2.5(3)
C(31)	0.7143(3)	0.2622(3)	0.5929(2)	1.9(3)
C(32)	0.6570(3)	0.2909(4)	0.6526(2)	2.8(3)
C(33)	0.6887(3)	0.2317(3)	0.6609(2)	2.4(3)
C(34)	0.6462(4)	0.3758(4)	0.5904(3)	4.7(4)
C(35)	0.6739(3)	0.2753(3)	0.5153(2)	1.7(3)
C(36)	0.6650(3)	0.3300(3)	0.4865(2)	2.0(3)
C(37)	0.6045(3)	0.3421(3)	0.4641(2)	2.1(3)
C(38)	0.5520(3)	0.2958(4)	0.4728(2)	2.4(3)
C(39)	0.5592(3)	0.2393(3)	0.5023(2)	2.1(3)
C(40)	0.6211(3)	0.2305(3)	0.5227(2)	1.9(3)
C(41)	0.5967(3)	0.4059(4)	0.4332(2)	2.6(3)
C(42)	0.5750(4)	0.3855(4)	0.3860(2)	4.0(4)
C(43)	0.6626(4)	0.4442(4)	0.4278(2)	3.4(4)
C(44)	0.5464(4)	0.4568(4)	0.4544(3)	3.9(4)
C(45)	0.5001(3)	0.1906(4)	0.5134(2)	3.0(3)
C(46)	0.5209(4)	0.1337(4)	0.5468(3)	5.1(5)
C(47)	0.4437(4)	0.2318(4)	0.5353(3)	4.2(4)
C(48)	0.4753(4)	0.1535(4)	0.4708(3)	4.6(4)
C(49)	0.107(1)	0.215(1)	0.1997(6)	13.6(6)
C(50)	0.0575(7)	0.1887(7)	0.1669(5)	11.4(4)
H(1)	0.785	0.195	0.791	2.4
H(2)	0.832	0.219	0.716	2.2
H(3)	0.683	0.105	0.813	3.9

Table 3 contd. Positional Parameters and B(eq) for $[Fe(BIDPhEH)_2Cl_2][FeCl_4] \cdot CH_3CN$ (**5b** $\cdot CH_3CN$).[a]

atom	x	y	z	B(eq)[b]
H(4)	0.696	0.031	0.795	3.9
H(5)	0.749	0.067	0.825	3.9
H(6)	0.630	-0.035	0.567	2.8
H(7)	0.697	0.070	0.556	2.6
H(8)	0.584	-0.089	0.648	4.2
H(9)	0.646	-0.133	0.635	4.2
H(10)	0.643	-0.099	0.682	4.2
H(11)	0.764	-0.087	0.700	2.6
H(12)	0.819	-0.031	0.693	2.6
H(13)	0.791	-0.045	0.741	2.6
H(14)	0.611	0.079	0.702	2.0
H(15)	0.687	-0.091	0.760	2.1
H(16)	0.542	0.157	0.700	3.5
H(17)	0.505	0.101	0.670	3.5
H(18)	0.465	0.162	0.692	3.5
H(19)	0.522	0.163	0.781	3.7
H(20)	0.445	0.166	0.773	3.7
H(21)	0.475	0.111	0.805	3.7
H(22)	0.387	0.080	0.725	3.7
H(23)	0.427	0.018	0.704	3.7
H(24)	0.412	0.019	0.755	3.7
H(25)	0.639	-0.219	0.831	3.8
H(26)	0.651	-0.196	0.781	3.8
H(27)	0.685	-0.156	0.820	3.8

Table 3 contd. Positional Parameters and B(eq) for [Fe(BIDPhEH)$_2$Cl$_2$]-[FeCl$_4$] · CH$_3$CN (**5b** · CH$_3$CN).[a]

atom	x	y	z	B(eq)[b]
H(28)	0.621	-0.086	0.872	4.9
H(29)	0.544	-0.078	0.867	4.9
H(30)	0.575	-0.148	0.882	4.9
H(31)	0.486	-0.145	0.803	5.2
H(32)	0.529	-0.190	0.771	5.2
H(33)	0.519	-0.212	0.821	5.2
H(34)	0.854	0.061	0.536	2.7
H(35)	0.830	0.094	0.458	3.1
H(36)	0.736	0.255	0.451	4.2
H(37)	0.798	0.225	0.426	4.2
H(38)	0.731	0.184	0.427	4.2
H(39)	0.687	0.206	0.688	2.8
H(40)	0.628	0.315	0.673	3.4
H(41)	0.659	0.414	0.608	5.7
H(42)	0.663	0.381	0.561	5.7
H(43)	0.599	0.373	0.589	5.7
H(44)	0.828	0.311	0.558	3.0
H(45)	0.805	0.324	0.508	3.0
H(46)	0.772	0.365	0.548	3.0
H(47)	0.701	0.361	0.482	2.5
H(48)	0.627	0.192	0.542	2.3
H(49)	0.533	0.362	0.387	4.8
H(50)	0.570	0.426	0.368	4.8
H(51)	0.608	0.356	0.373	4.8
H(52)	0.695	0.414	0.415	4.1

Table 3 contd. Positional Parameters and B(eq) for $[Fe(BIDPhEH)_2Cl_2][FeCl_4] \cdot CH_3CN$ (**5b** $\cdot$ CH_3CN).[a]

atom	x	y	z	B(eq)[b]
H(53)	0.656	0.484	0.409	4.1
H(54)	0.678	0.459	0.456	4.1
H(55)	0.563	0.472	0.483	4.7
H(56)	0.541	0.496	0.435	4.7
H(57)	0.504	0.434	0.458	4.7
H(58)	0.483	0.105	0.554	6.1
H(59)	0.555	0.106	0.534	6.1
H(60)	0.537	0.155	0.574	6.1
H(61)	0.459	0.252	0.562	5.0
H(62)	0.429	0.267	0.515	5.0
H(63)	0.407	0.202	0.542	5.0
H(64)	0.438	0.125	0.478	5.5
H(65)	0.462	0.187	0.449	5.5
H(66)	0.510	0.126	0.459	5.5
H(67)	0.017	0.177	0.182	13.6
H(68)	0.048	0.224	0.145	13.6
H(69)	0.075	0.149	0.152	13.6

[a]Estimated standard deviations in the least significant figures are given in parentheses. For atom-labelling scheme, see Figure 3. [b]$B(\text{eq}) = 8/3\pi^2 (U_{11}(aa^*)^2 + U_{22}(bb^*)^2 + U_{33}(cc^*)^2 + 2U_{12}aa^*bb^*\cos\gamma + 2U_{13}aa^*cc^*\cos\beta + 2U_{23}bb^*cc^*\cos\alpha)$

Table 4. Intramolecular Bond Distances for $[Fe(BIDPhEH)_2Cl_2][FeCl_4] \cdot CH_3CN$ (**5b** · CH_3CN).[a]

atom	atom	distance	atom	atom	distance
Fe(1)	Cl(1)	2.317(2)	N(6)	C(28)	1.482(8)
Fe(1)	Cl(2)	2.325(2)	N(7)	C(31)	1.321(7)
Fe(1)	N(1)	2.103(5)	N(7)	C(33)	1.392(7)
Fe(1)	N(3)	2.143(5)	N(8)	C(31)	1.356(7)
Fe(1)	N(5)	2.109(5)	N(8)	C(32)	1.359(8)
Fe(1)	N(7)	2.142(5)	N(8)	C(34)	1.478(8)
Fe(2)	Cl(3)	2.190(2)	N(9)	C(49)	1.08(2)
Fe(2)	Cl(4)	2.195(3)	C(1)	C(5)	1.542(8)
Fe(2)	Cl(5)	2.200(2)	C(2)	C(3)	1.340(8)
Fe(2)	Cl(6)	2.174(3)	C(5)	C(6)	1.549(8)
O(1)	C(14)	1.384(7)	C(5)	C(7)	1.530(8)
O(2)	C(38)	1.374(7)	C(5)	C(11)	1.556(7)
N(1)	C(1)	1.333(7)	C(8)	C(9)	1.340(8)
N(1)	C(3)	1.377(7)	C(11)	C(12)	1.388(8)
N(2)	C(1)	1.350(7)	C(11)	C(16)	1.369(8)
N(2)	C(2)	1.364(7)	C(12)	C(13)	1.396(8)
N(2)	C(4)	1.473(8)	C(13)	C(14)	1.396(8)
N(3)	C(7)	1.326(7)	C(13)	C(17)	1.529(8)
N(3)	C(9)	1.384(7)	C(14)	C(15)	1.416(8)
N(4)	C(7)	1.350(7)	C(15)	C(16)	1.393(8)
N(4)	C(8)	1.377(7)	C(15)	C(21)	1.535(8)
N(4)	C(10)	1.467(8)	C(17)	C(18)	1.545(9)
N(5)	C(25)	1.328(7)	C(17)	C(19)	1.537(8)
N(5)	C(27)	1.384(7)	C(17)	C(20)	1.553(9)

Table 4 contd. Intramolecular Bond Distances for $[Fe(BIDPhEH)_2Cl_2]$-$[FeCl_4] \cdot CH_3CN$ (**5b** $\cdot CH_3CN$).[a]

atom	atom	distance	atom	atom	distance
N(6)	C(25)	1.357(7)	C(21)	C(22)	1.524(9)
N(6)	C(26)	1.373(8)	C(21)	C(23)	1.540(9)
C(21)	C(24)	1.520(9)	C(37)	C(41)	1.544(8)
C(25)	C(29)	1.531(8)	C(38)	C(39)	1.405(9)
C(26)	C(27)	1.341(8)	C(39)	C(40)	1.388(8)
C(29)	C(30)	1.540(8)	C(39)	C(45)	1.545(9)
C(29)	C(31)	1.544(8)	C(41)	C(42)	1.522(9)
C(29)	C(35)	1.539(8)	C(41)	C(43)	1.519(9)
C(32)	C(33)	1.329(9)	C(41)	C(44)	1.540(9)
C(35)	C(36)	1.371(8)	C(45)	C(46)	1.54(1)
C(35)	C(40)	1.382(8)	C(45)	C(47)	1.53(1)
C(36)	C(37)	1.401(8)	C(45)	C(48)	1.54(1)
C(37)	C(38)	1.402(9)	C(49)	C(50)	1.47(2)

[a]Distances are in angstroms. For atom-labelling scheme see Figure 3. Estimated standard deviations in the least significant figure are given in parentheses.

Table 5. Intramolecular Bond Angles for $[Fe(BIDPhEH)_2Cl_2][FeCl_4] \cdot CH_3CN$ (**5b** · CH_3CN).[a]

atom	atom	atom	angle	atom	atom	atom	angle
Cl(1)	Fe(1)	Cl(2)	93.76(7)	C(2)	N(2)	C(4)	120.2(5)
Cl(1)	Fe(1)	N(1)	94.7(1)	Fe(1)	N(3)	C(7)	131.0(4)
Cl(1)	Fe(1)	N(3)	174.6(1)	Fe(1)	N(3)	C(9)	121.8(4)
Cl(1)	Fe(1)	N(5)	91.9(1)	C(7)	N(3)	C(9)	105.8(5)
Cl(1)	Fe(1)	N(7)	90.3(1)	C(7)	N(4)	C(8)	107.5(5)
Cl(2)	Fe(1)	N(1)	93.1(1)	C(7)	N(4)	C(10)	131.6(5)
Cl(2)	Fe(1)	N(3)	90.6(1)	C(8)	N(4)	C(10)	121.0(5)
Cl(2)	Fe(1)	N(5)	94.6(1)	Fe(1)	N(5)	C(25)	131.4(4)
Cl(2)	Fe(1)	N(7)	175.1(1)	Fe(1)	N(5)	C(27)	121.6(4)
N(1)	Fe(1)	N(3)	81.9(2)	C(25)	N(5)	C(27)	106.8(5)
N(1)	Fe(1)	N(5)	169.5(2)	C(25)	N(6)	C(26)	108.3(5)
N(1)	Fe(1)	N(7)	89.3(2)	C(25)	N(6)	C(28)	131.1(5)
N(3)	Fe(1)	N(5)	90.9(2)	C(26)	N(6)	C(28)	120.5(5)
N(3)	Fe(1)	N(7)	85.5(2)	Fe(1)	N(7)	C(31)	129.4(4)
N(5)	Fe(1)	N(7)	82.5(2)	Fe(1)	N(7)	C(33)	122.0(4)
Cl(3)	Fe(2)	Cl(4)	110.16(9)	C(31)	N(7)	C(33)	106.1(5)
Cl(3)	Fe(2)	Cl(5)	108.4(1)	C(31)	N(8)	C(32)	107.1(5)
Cl(3)	Fe(2)	Cl(6)	110.2(1)	C(31)	N(8)	C(34)	131.0(6)
Cl(4)	Fe(2)	Cl(5)	110.89(9)	C(32)	N(8)	C(34)	121.9(6)
Cl(4)	Fe(2)	Cl(6)	108.3(1)	N(1)	C(1)	N(2)	109.7(5)
Cl(5)	Fe(2)	Cl(6)	108.9(1)	N(1)	C(1)	C(5)	126.1(5)
Fe(1)	N(1)	C(1)	132.1(4)	N(2)	C(1)	C(5)	124.0(5)
Fe(1)	N(1)	C(3)	120.7(4)	N(2)	C(2)	C(3)	106.9(5)
C(1)	N(1)	C(3)	106.2(5)	N(1)	C(3)	C(2)	109.3(5)

Table 5 contd. Intramolecular Bond Angles for $[Fe(BIDPhEH)_2Cl_2][FeCl_4] \cdot CH_3CN$ (**5b** $\cdot CH_3CN$).[a]

atom	atom	atom	angle	atom	atom	atom	angle
C(1)	N(2)	C(2)	107.8(5)	C(1)	C(5)	C(6)	107.9(5)
C(1)	N(2)	C(4)	132.0(5)	C(1)	C(5)	C(7)	111.9(5)
C(1)	C(5)	C(11)	108.1(5)	C(18)	C(17)	C(19)	107.1(5)
C(6)	C(5)	C(7)	109.2(5)	C(18)	C(17)	C(20)	106.1(5)
C(6)	C(5)	C(11)	113.0(5)	C(19)	C(17)	C(20)	110.5(5)
C(7)	C(5)	C(11)	106.9(5)	C(15)	C(21)	C(22)	111.4(5)
N(3)	C(7)	N(4)	110.5(5)	C(15)	C(21)	C(23)	110.3(5)
N(3)	C(7)	C(5)	126.4(5)	C(15)	C(21)	C(24)	110.7(6)
N(4)	C(7)	C(5)	123.1(5)	C(22)	C(21)	C(23)	106.0(6)
N(4)	C(8)	C(9)	106.4(5)	C(22)	C(21)	C(24)	107.7(5)
N(3)	C(9)	C(8)	109.8(5)	C(23)	C(21)	C(24)	110.6(6)
C(5)	C(11)	C(12)	116.7(5)	N(5)	C(25)	N(6)	109.1(5)
C(5)	C(11)	C(16)	124.2(5)	N(5)	C(25)	C(29)	128.3(5)
C(12)	C(11)	C(16)	119.1(5)	N(6)	C(25)	C(29)	122.3(5)
C(11)	C(12)	C(13)	122.1(5)	N(6)	C(26)	C(27)	106.4(5)
C(12)	C(13)	C(14)	116.5(6)	N(5)	C(27)	C(26)	109.4(6)
C(12)	C(13)	C(17)	120.1(6)	C(25)	C(29)	C(30)	106.3(5)
C(14)	C(13)	C(17)	123.4(5)	C(25)	C(29)	C(31)	112.0(5)
O(1)	C(14)	C(13)	121.7(6)	C(25)	C(29)	C(35)	109.5(5)
O(1)	C(14)	C(15)	115.2(5)	C(30)	C(29)	C(31)	108.1(5)
C(13)	C(14)	C(15)	123.1(5)	C(30)	C(29)	C(35)	115.0(5)
C(14)	C(15)	C(16)	116.2(5)	C(31)	C(29)	C(35)	106.0(5)
C(14)	C(15)	C(21)	121.9(5)	N(7)	C(31)	N(8)	110.1(5)
C(16)	C(15)	C(21)	121.9(5)	N(7)	C(31)	C(29)	127.8(5)
C(11)	C(16)	C(15)	122.7(6)	N(8)	C(31)	C(29)	121.9(5)

Table 5 contd. Intramolecular Bond Angles for $[Fe(BIDPhEH)_2Cl_2][FeCl_4] \cdot CH_3CN$ (**5b** $\cdot CH_3CN$).[a]

atom	atom	atom	angle	atom	atom	atom	angle
C(13)	C(17)	C(18)	111.9(5)	N(7)	C(33)	C(32)	108.7(6)
C(13)	C(17)	C(19)	110.1(5)	C(29)	C(35)	C(36)	123.9(5)
C(13)	C(17)	C(20)	111.1(5)	C(35)	C(40)	C(39)	122.3(6)
C(29)	C(35)	C(40)	117.1(5)	C(37)	C(41)	C(42)	112.0(6)
C(36)	C(35)	C(40)	118.8(6)	C(37)	C(41)	C(43)	111.3(5)
C(35)	C(36)	C(37)	122.5(6)	C(37)	C(41)	C(44)	109.2(5)
C(36)	C(37)	C(38)	116.9(6)	C(42)	C(41)	C(43)	105.9(6)
C(36)	C(37)	C(41)	120.2(6)	C(42)	C(41)	C(44)	110.9(6)
C(38)	C(37)	C(41)	122.8(6)	C(43)	C(41)	C(44)	107.4(6)
O(2)	C(38)	C(37)	119.6(6)	C(39)	C(45)	C(46)	111.4(6)
O(2)	C(38)	C(39)	118.2(6)	C(39)	C(45)	C(47)	110.0(6)
C(37)	C(38)	C(39)	122.1(6)	C(39)	C(45)	C(48)	110.6(6)
C(38)	C(39)	C(40)	117.3(6)	C(46)	C(45)	C(47)	107.2(7)
C(38)	C(39)	C(45)	121.7(6)	C(46)	C(45)	C(48)	106.8(6)
C(40)	C(39)	C(45)	120.9(6)	C(47)	C(45)	C(48)	110.8(6)
N(8)	C(32)	C(33)	108.0(6)	N(9)	C(49)	C(50)	171(2)

[a]Angles are in degrees. For atom-labelling scheme see Figure 3. Estimated standard deviations in the least significant figure are given in parentheses.

Table 6. U values for $[Fe(BIDPhEH)_2Cl_2][FeCl_4] \cdot CH_3CN$ (**5b** · CH_3CN).[a]

atom	U11	U22	U33	U12	U13	U23
Fe(1)	0.0165(5)	0.0206(4)	0.0211(4)	0.0011(4)	0.0003(4)	0.0010(4)
Fe(2)	0.0379(6)	0.0689(8)	0.0348(6)	-0.0091(6)	-0.0025(5)	0.0074(6)
Cl(1)	0.0245(9)	0.0285(9)	0.035(1)	-0.0068(7)	-0.0006(7)	0.0024(7)
Cl(2)	0.0247(9)	0.0281(8)	0.0316(9)	0.0070(7)	0.0014(7)	-0.0001(7)
Cl(3)	0.042(1)	0.060(1)	0.055(1)	0.001(1)	-0.000(1)	0.006(1)
Cl(4)	0.044(1)	0.058(1)	0.065(1)	-0.001(1)	-0.010(1)	-0.013(1)
Cl(5)	0.062(2)	0.056(1)	0.098(2)	-0.016(1)	-0.030(1)	0.008(1)
Cl(6)	0.080(2)	0.212(4)	0.042(1)	-0.014(2)	0.009(1)	0.037(2)
O(1)	0.033(3)	0.040(3)	0.039(3)	-0.003(2)	0.021(2)	0.007(2)
O(2)	0.023(3)	0.086(4)	0.051(4)	0.010(3)	-0.014(2)	0.002(3)
N(1)	0.019(3)	0.022(3)	0.018(3)	-0.005(2)	-0.003(2)	-0.003(2)
N(2)	0.019(3)	0.036(3)	0.018(3)	-0.002(3)	0.004(2)	0.001(2)
N(3)	0.019(3)	0.019(3)	0.021(3)	-0.003(2)	-0.001(2)	0.001(2)
N(4)	0.028(3)	0.024(3)	0.024(3)	-0.011(3)	0.004(2)	-0.003(2)
N(5)	0.016(3)	0.021(3)	0.022(3)	0.001(2)	-0.000(2)	0.001(2)
N(6)	0.031(3)	0.030(3)	0.021(3)	0.000(3)	0.002(2)	0.004(2)
N(7)	0.019(3)	0.025(3)	0.019(3)	0.003(2)	0.004(2)	0.001(2)
N(8)	0.034(3)	0.028(3)	0.028(3)	0.011(3)	-0.005(3)	-0.001(3)
C(1)	0.013(3)	0.026(3)	0.021(3)	-0.001(3)	-0.002(3)	0.003(3)
C(2)	0.021(3)	0.032(4)	0.023(4)	-0.003(3)	-0.002(3)	-0.012(3)
C(3)	0.027(4)	0.016(3)	0.026(4)	-0.004(3)	-0.002(3)	0.004(3)
C(4)	0.051(5)	0.054(5)	0.020(4)	-0.020(4)	-0.000(3)	-0.006(3)
C(5)	0.020(3)	0.016(3)	0.019(3)	-0.003(3)	0.005(3)	0.002(3)
C(6)	0.020(3)	0.031(4)	0.033(4)	0.003(3)	0.003(3)	0.002(3)
C(7)	0.018(3)	0.020(3)	0.021(3)	0.004(3)	-0.001(3)	-0.004(3)

Table 6 contd. U values for $[Fe(BIDPhEH)_2Cl_2][FeCl_4] \cdot CH_3CN$ (**5b** · CH_3CN).[a]

atom	U11	U22	U33	U12	U13	U23
C(8)	0.027(4)	0.038(4)	0.026(4)	-0.008(3)	-0.006(3)	-0.003(3)
C(9)	0.023(3)	0.036(4)	0.022(3)	-0.008(3)	-0.004(3)	-0.000(3)
C(10)	0.056(5)	0.041(4)	0.036(4)	-0.028(4)	0.007(4)	-0.002(3)
C(11)	0.019(3)	0.024(3)	0.017(3)	-0.005(3)	0.004(3)	-0.005(3)
C(12)	0.023(3)	0.019(3)	0.022(3)	-0.005(3)	0.003(3)	-0.002(3)
C(13)	0.018(3)	0.027(3)	0.025(3)	0.000(3)	0.000(3)	-0.004(3)
C(14)	0.024(4)	0.028(4)	0.022(3)	-0.007(3)	0.006(3)	-0.005(3)
C(15)	0.025(4)	0.019(3)	0.024(3)	-0.003(3)	0.001(3)	-0.003(3)
C(16)	0.026(4)	0.015(3)	0.024(4)	-0.000(3)	-0.005(3)	-0.001(3)
C(17)	0.017(3)	0.034(4)	0.025(4)	0.003(3)	0.001(3)	-0.002(3)
C(18)	0.026(4)	0.032(4)	0.052(5)	0.010(3)	-0.004(3)	0.011(4)
C(19)	0.034(4)	0.039(4)	0.045(4)	0.009(4)	0.002(3)	-0.010(4)
C(20)	0.028(4)	0.047(5)	0.041(4)	0.005(4)	0.004(3)	-0.002(4)
C(21)	0.047(4)	0.017(3)	0.027(4)	-0.002(3)	0.010(3)	-0.001(3)
C(22)	0.049(5)	0.029(4)	0.043(5)	0.005(4)	0.012(4)	0.013(3)
C(23)	0.076(6)	0.037(4)	0.041(5)	0.003(4)	0.014(4)	0.008(4)
C(24)	0.048(5)	0.034(4)	0.083(7)	-0.011(4)	0.006(5)	0.005(4)
C(25)	0.012(3)	0.028(4)	0.020(3)	-0.005(3)	0.003(3)	0.000(3)
C(26)	0.039(4)	0.037(4)	0.022(4)	0.003(3)	0.010(3)	-0.004(3)
C(27)	0.031(4)	0.026(4)	0.028(4)	0.009(3)	0.007(3)	-0.001(3)
C(28)	0.064(5)	0.052(5)	0.016(4)	0.015(4)	0.002(4)	-0.000(3)
C(29)	0.013(3)	0.020(3)	0.022(3)	0.001(3)	-0.000(2)	0.003(3)
C(30)	0.029(4)	0.028(4)	0.038(4)	-0.005(3)	-0.004(3)	0.012(3)
C(31)	0.017(3)	0.028(3)	0.029(4)	-0.002(3)	0.000(3)	-0.006(3)
C(32)	0.030(4)	0.052(5)	0.024(4)	0.014(4)	0.003(3)	-0.007(3)

Table 6 contd. U values for $[Fe(BIDPhEH)_2Cl_2][FeCl_4] \cdot CH_3CN$ (**5b** · CH_3CN).[a]

atom	U11	U22	U33	U12	U13	U23
C(33)	0.021(4)	0.035(4)	0.035(4)	0.005(3)	0.009(3)	0.004(3)
C(34)	0.089(7)	0.049(5)	0.041(5)	0.041(5)	0.002(5)	0.001(4)
C(35)	0.017(3)	0.025(4)	0.022(3)	0.001(3)	-0.003(3)	-0.003(3)
C(36)	0.024(4)	0.030(4)	0.024(4)	0.003(3)	-0.001(3)	0.005(3)
C(37)	0.021(4)	0.038(4)	0.019(3)	0.003(3)	-0.001(3)	0.002(3)
C(38)	0.028(4)	0.040(4)	0.024(4)	0.002(3)	-0.005(3)	-0.003(3)
C(39)	0.018(3)	0.033(4)	0.031(4)	-0.005(3)	-0.001(3)	-0.006(3)
C(40)	0.023(4)	0.022(3)	0.028(4)	0.008(3)	0.005(3)	-0.002(3)
C(41)	0.028(4)	0.043(4)	0.027(4)	0.004(3)	-0.001(3)	0.006(3)
C(42)	0.047(5)	0.069(6)	0.037(5)	0.000(4)	-0.006(4)	0.008(4)
C(43)	0.052(5)	0.038(4)	0.041(5)	0.007(4)	-0.004(4)	0.019(4)
C(44)	0.050(5)	0.049(5)	0.050(5)	0.018(4)	0.009(4)	0.009(4)
C(45)	0.023(4)	0.040(4)	0.050(5)	-0.007(4)	-0.001(4)	-0.008(4)
C(46)	0.034(5)	0.055(6)	0.104(8)	-0.017(4)	-0.005(5)	0.033(5)
C(47)	0.031(4)	0.065(6)	0.064(6)	-0.006(4)	0.008(4)	-0.003(5)
C(48)	0.034(5)	0.054(5)	0.086(7)	-0.005(4)	-0.004(5)	-0.025(5)

[a]Estimated standard deviations in the least significant figure are given in parentheses. The anisotropic temperature factors are of the form $\exp[-2\pi^2 (U_{11}h^2a^{*2}... + 2U_{12}hka^*b^* + ...)]$.

Scheme 1

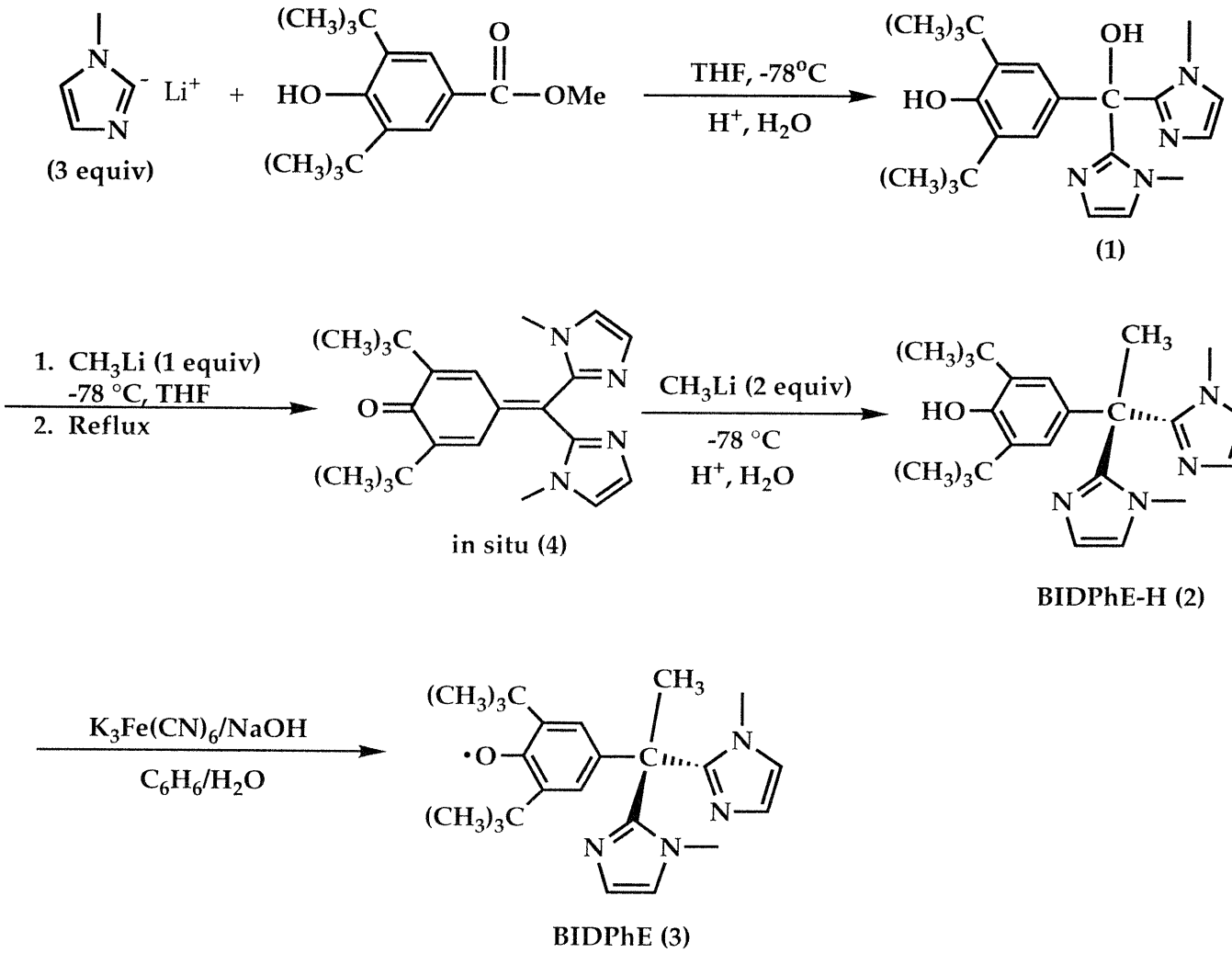
(3 equiv)
THF, -78°C
H+, H2O
(1)
1. CH3Li (1 equiv)
-78 °C, THF
2. Reflux
in situ (4)
CH3Li (2 equiv)
-78 °C
H+, H2O
BIDPhE-H (2)
K3Fe(CN)6/NaOH
C6H6/H2O
BIDPhE (3)

Scheme 2

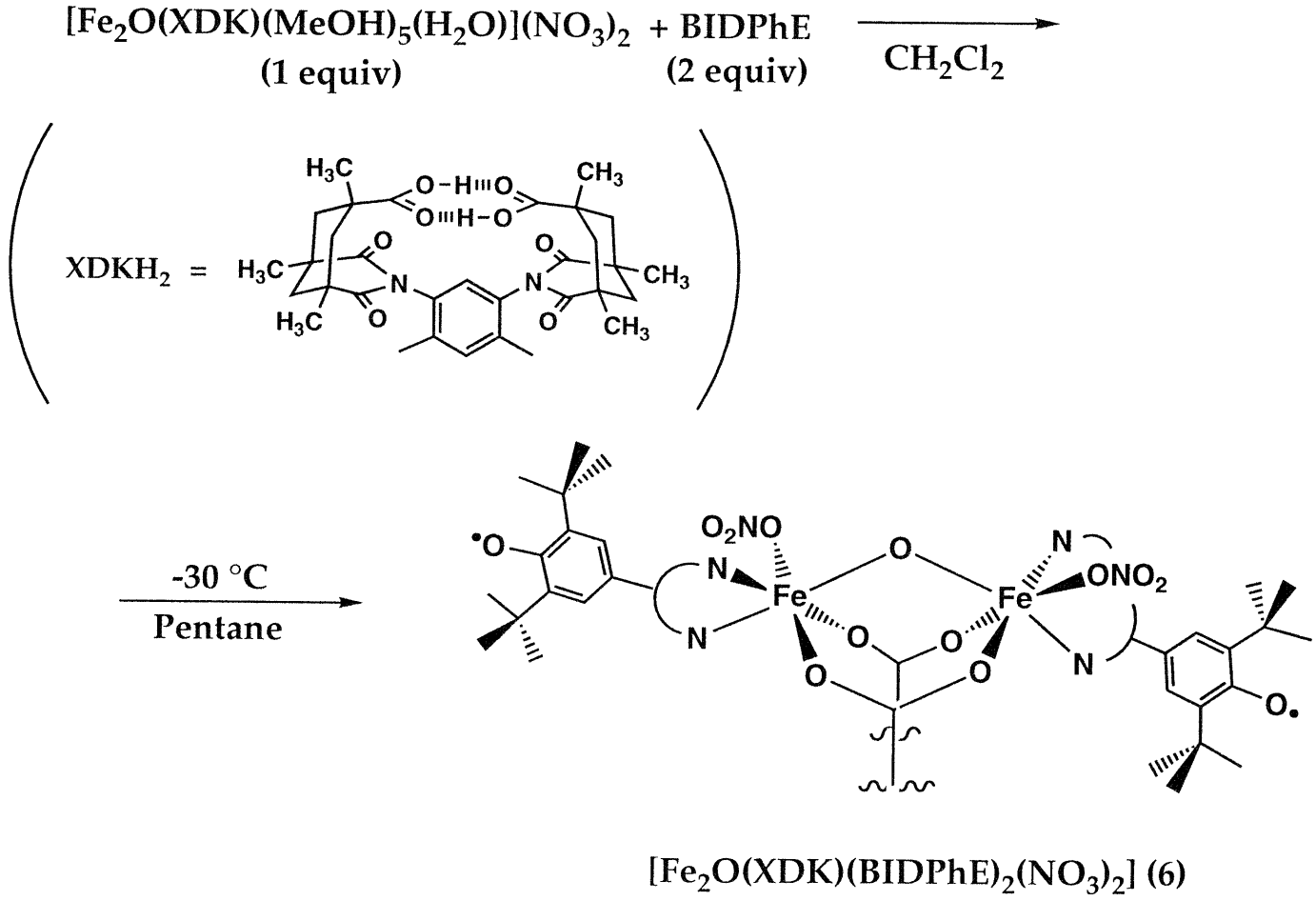
[Fe2O(XDK)(MeOH)5(H2O)](NO3)2
(1 equiv)
+ BIDPhE
(2 equiv)
CH2Cl2
XDKH2 =
-30 °C
Pentane
[Fe2O(XDK)(BIDPhE)2(NO3)2] (6)

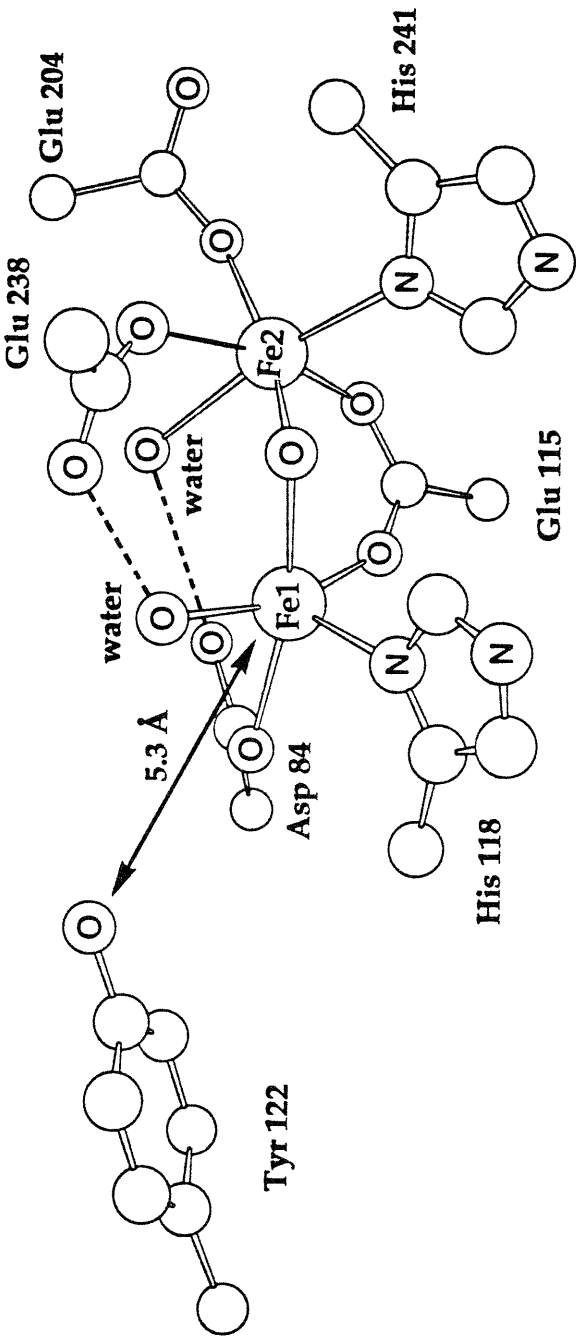

Figure 1. Active site structure of the met form of the R2 protein of ribonucleotide reductase.

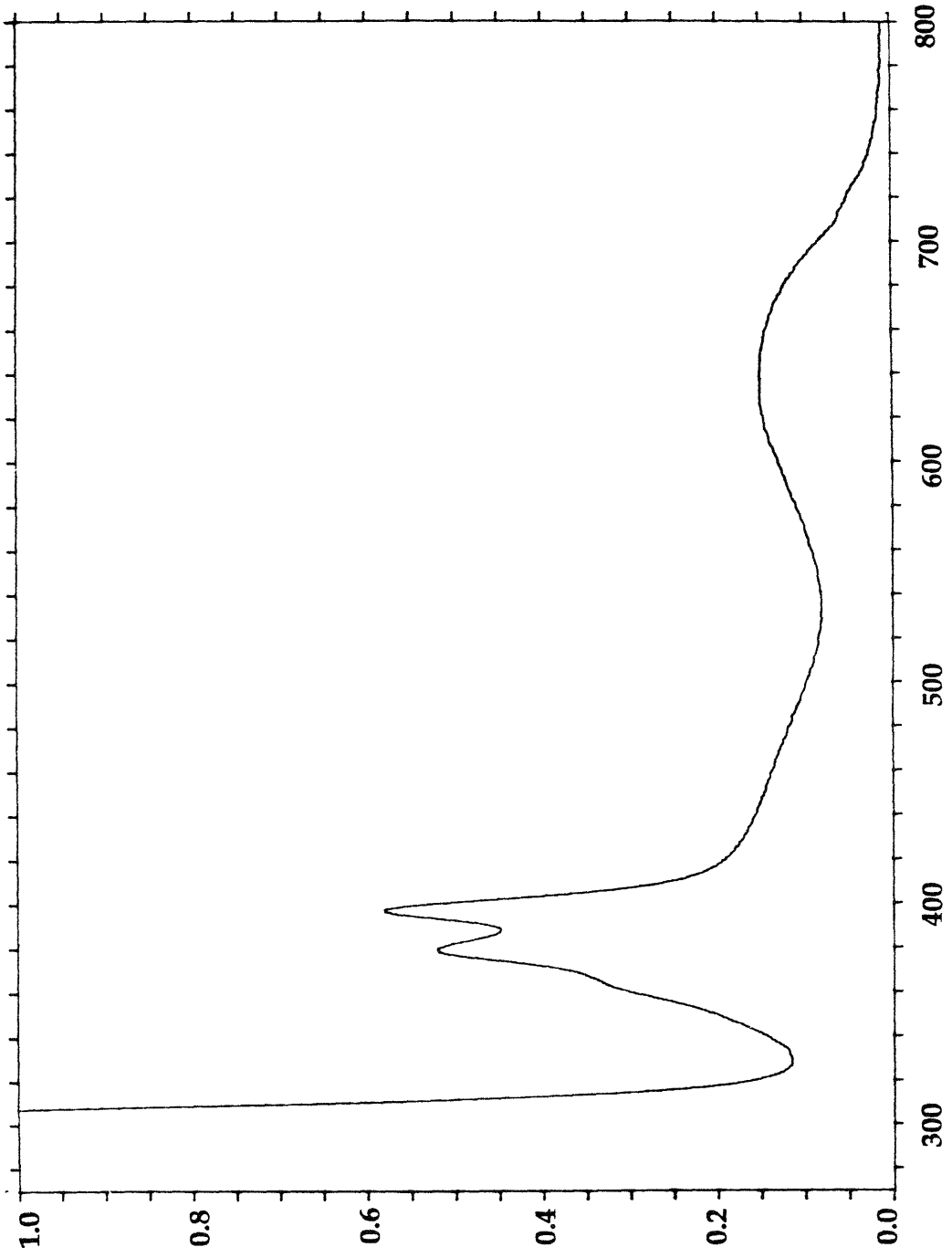

Figure 2. UV-visible absorption spectrum of BIDPhE (**3**) in CH_3CN (λ_{max}, nm (ε, M^{-1} cm^{-1})): 638 (430), 394 (1700), 378 (1500).

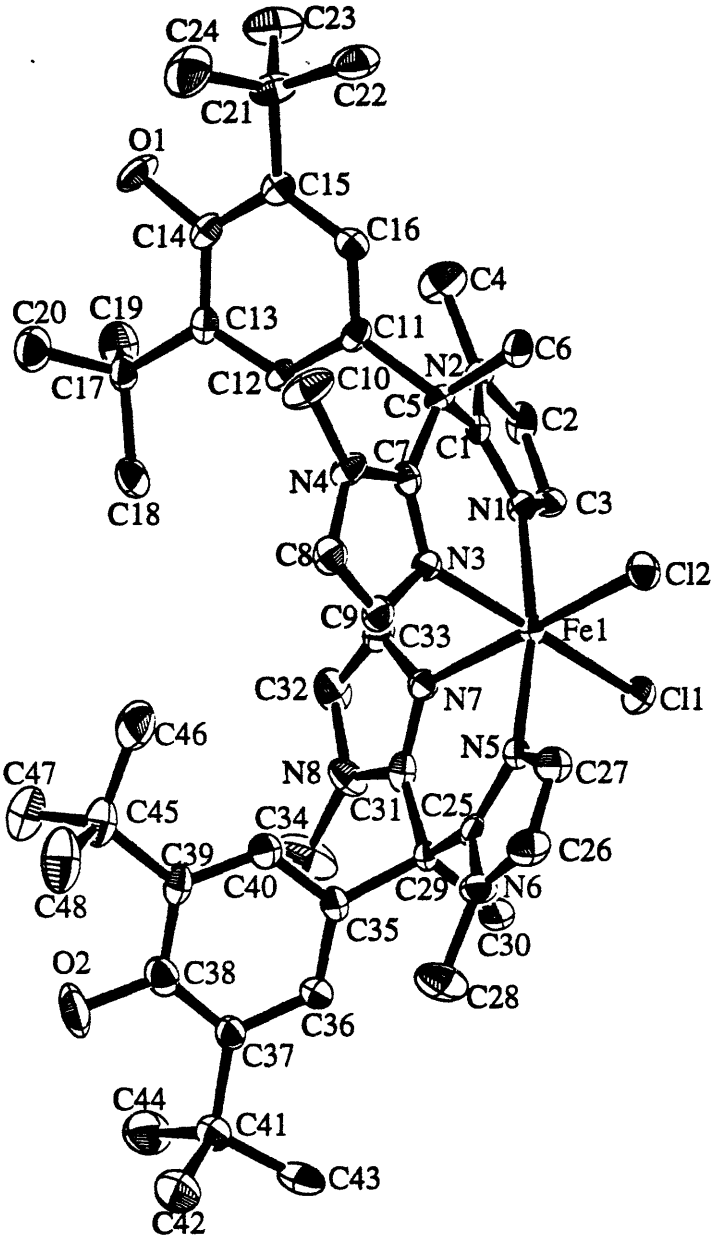

Figure 3. ORTEP diagram of the cation of $[Fe(BIDPhEH)_2Cl_2][FeCl_4] \cdot CH_3CN$ (**5b**). Thermal ellipsoids are drawn at the 50% probability level. Hydrogen atoms have been omitted for clarity.

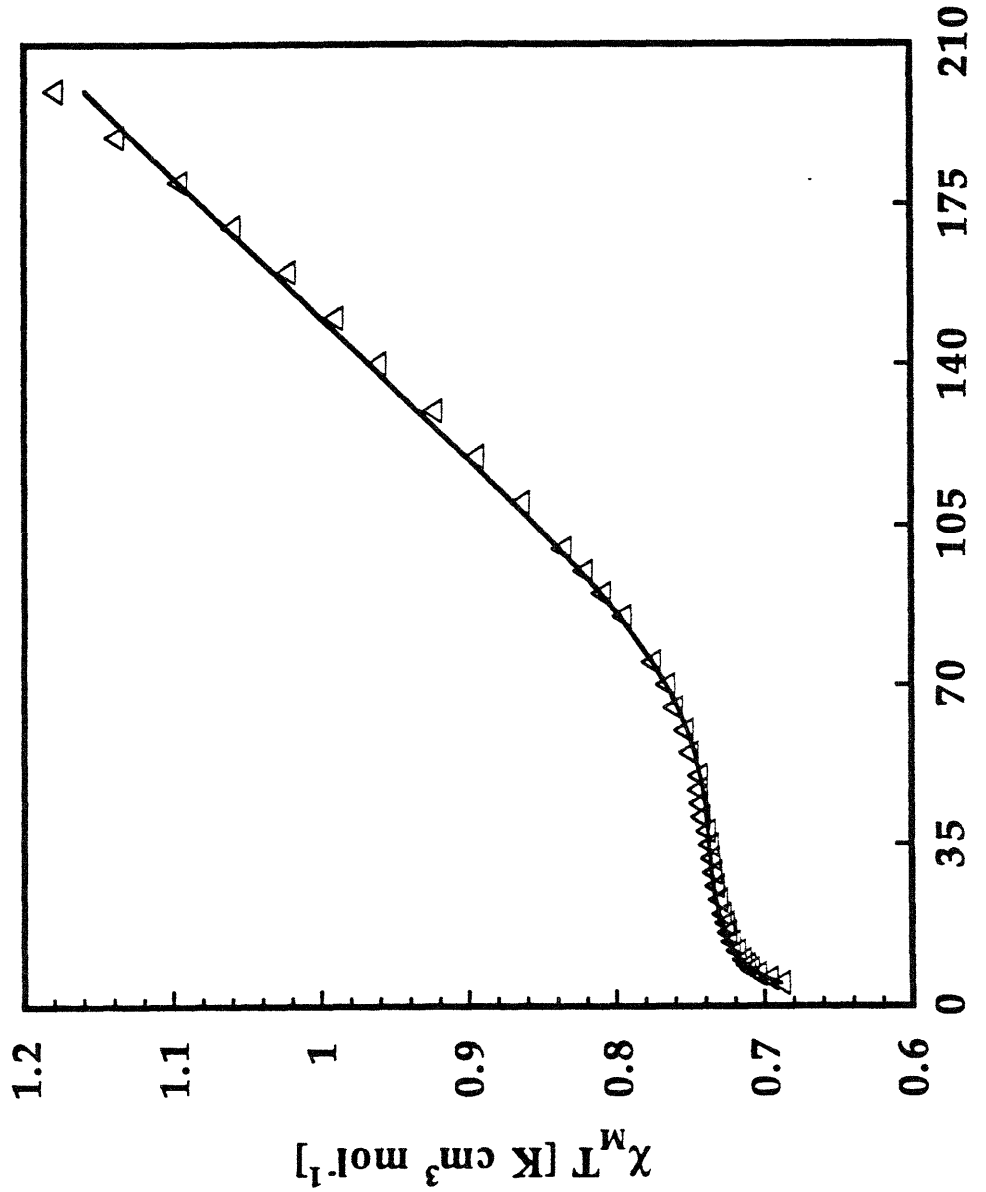

Figure 4. Plot of the molar susceptibility times temperature versus temperature for $[Fe_2O(XDK)(BIDPhE)_2(NO_3)_2]$ (**6**). The solid line represents the best fit by using the model given in eq. 1, with J = -117.5(4) cm^{-1} and θ = -0.47(2) K.

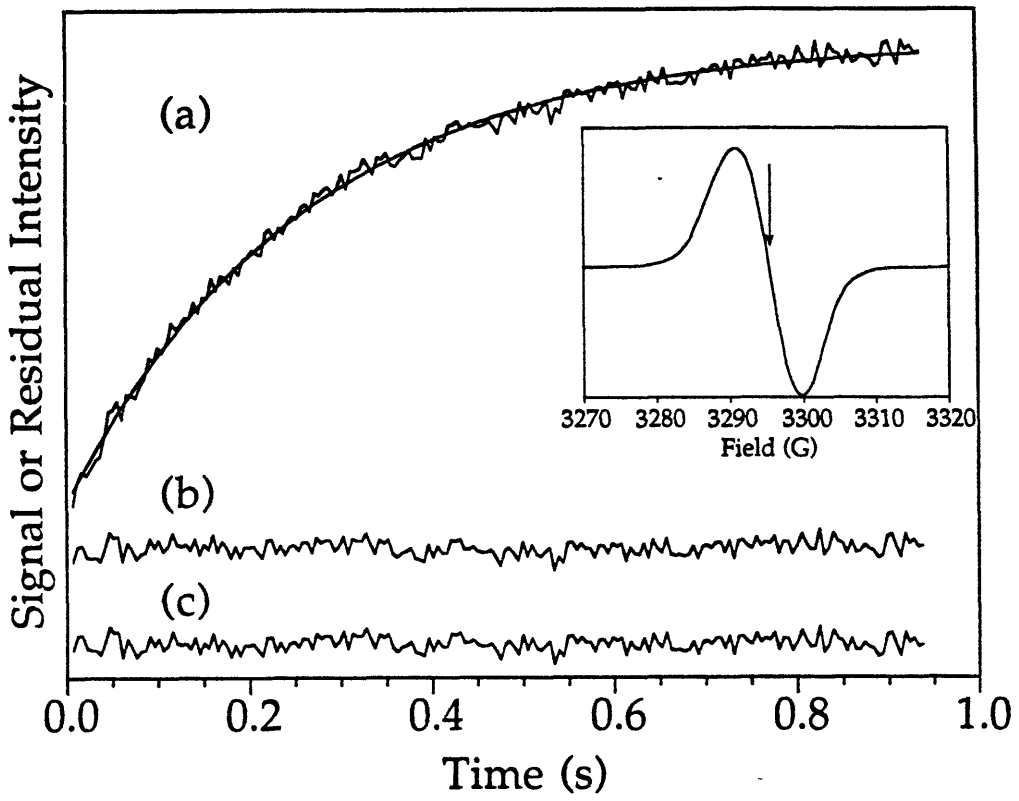

Figure 5. (a) Saturation-recovery EPR transient obtained for the BIDPhE radical in the [Zn(BIDPhE)Cl_2] compound (radical concentration 0.1 mM) at 9.0 K with a single-exponential fit superimposed. The observing microwave power was 0.18 μW, the saturating microwave power was 144 mW and the pulse was of 140 ms duration; (b) Residual difference between the experimental data and the fitted curve for the single-exponential fit; (c) Residual for the dipolar-model fit (eq 2-3).

Inset: Continuous-wave (cw), X-band first derivative EPR spectrum of the BIDPhE radical in the [Zn(BIDPhE)Cl_2] compound. The arrow points at the zero-crossing point, used as the field position setting in the saturation-recovery experiment. Experimental conditions for the cw spectrum were the following: temperature 10 K; microwave frequency, 9.07 GHz; field-modulation amplitude, 4.0 Gauss; microwave power, 0.45 μW; field-modulation frequency, 100 kHz.

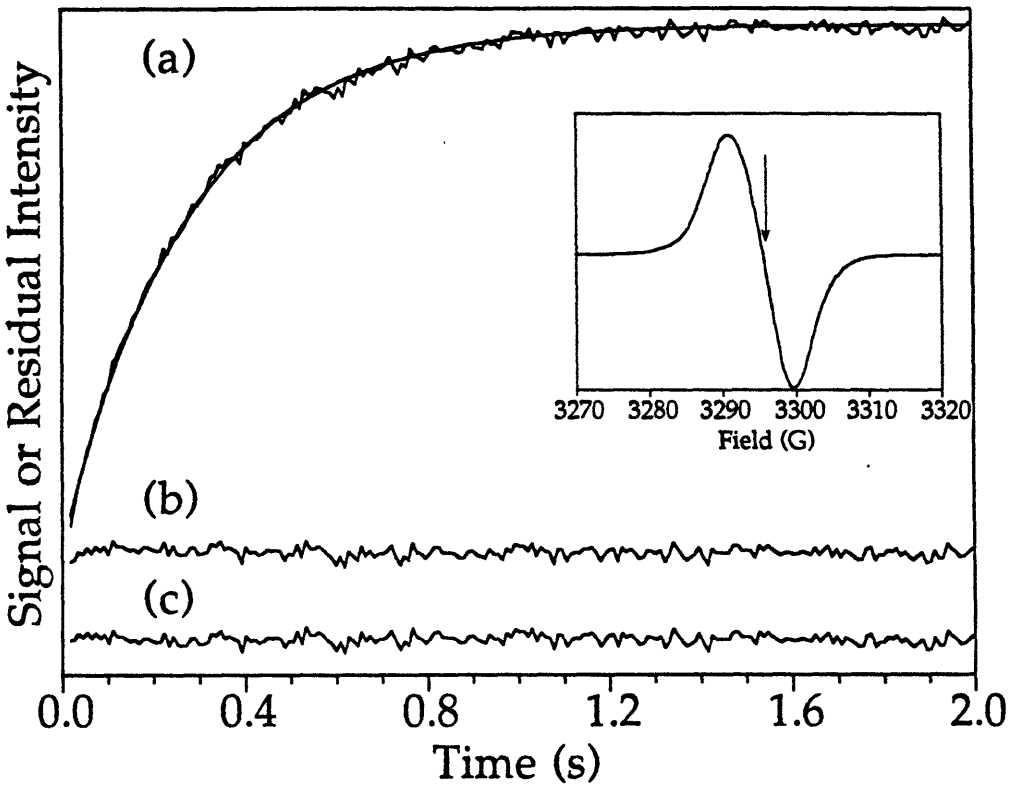

Figure 6. (a) Saturation-recovery EPR transient obtained for the BIDPhE radical in compound **6** (radical concentration 2 mM) at 6.7 K with a single-exponential fit superimposed. The observing microwave power was 0.29 μW, the saturating microwave power was 360 mW and the pulse was of 600 ms duration; (b) Residual for the single-exponential fit; (c) Residual for the dipolar-model fit (eqs. 2-3).

Inset: Continuous-wave (cw), X-band first derivative EPR spectrum of the BIDPhE radical in compound 6. The arrow points to the zero-crossing point, used as the field position setting in the saturation-recovery experiment. Experimental conditions for the cw spectrum were the following: temperature 11.2 K; microwave frequency, 9.07 GHz; field-modulation amplitude, 4.0 Gauss; microwave power, 0.72 μW; field-modulation frequency, 100 kHz.

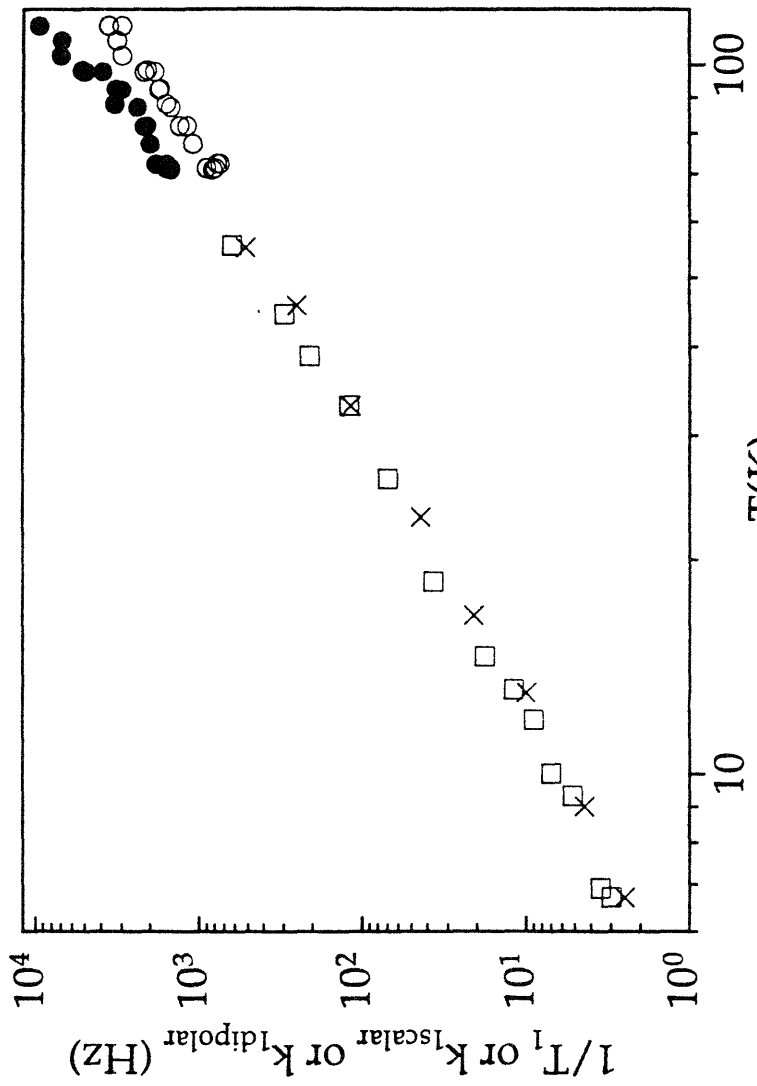

Figure 7. Temperature dependence of: (a) the intrinsic spin-lattice relaxation rate ($1/T_1$) of the BIDPhE radical in the $[Zn(BIDPhE)Cl_2]$ compound (X); (b) the intrinsic spin-lattice relaxation rate ($1/T_1$) of the BIDPhE radical in **6** (□); (c) the isotropic $k_{1scalar}$ rate constant of the BIDPhE radical in **6** (○); (d) the dipolar rate constant, $k_{1dipolar}$ ($\equiv k^B_{1_d}$), of the BIDPhE radical in **6** (●). The $1/T_1$ values were extracted from single-exponential fits to the experimental traces. The values of $k_{1scalar}$ and $k_{1dipolar}$ were obtained from the dipolar-model fits to the non-single exponential saturation-recovery traces (eqs 2, 3).

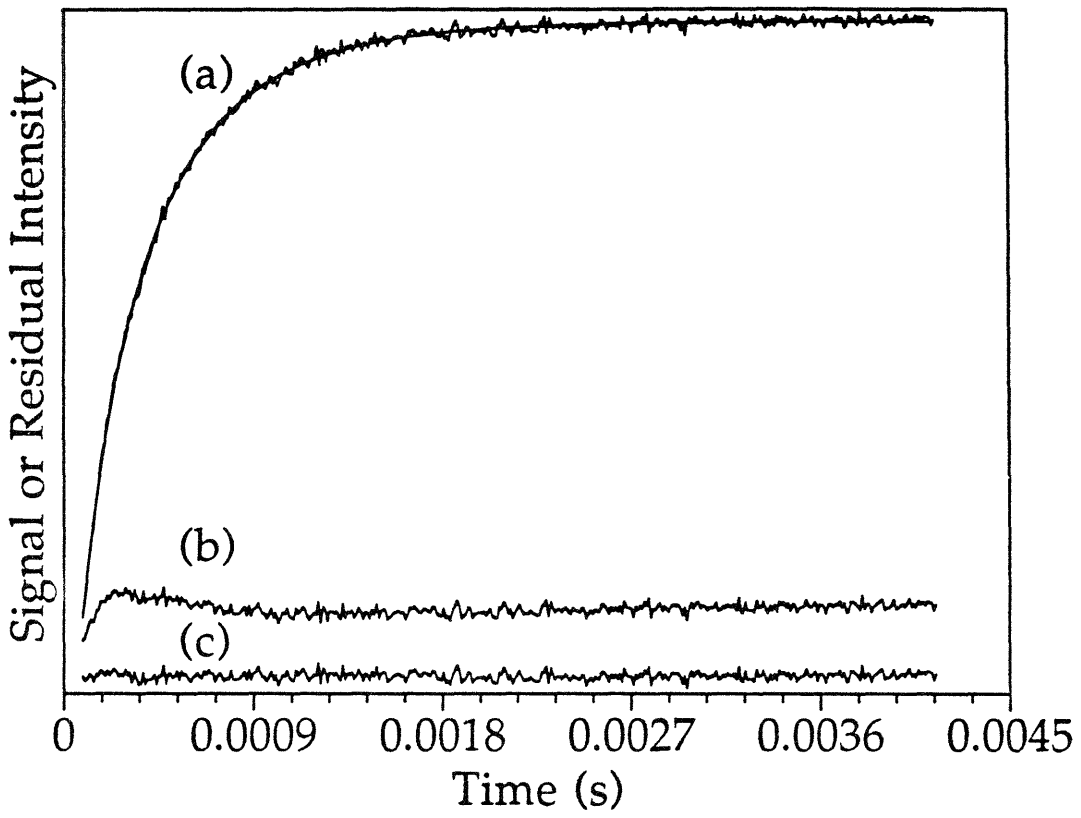

Figure 8. (a) Saturation-recovery EPR transient obtained for the BIDPhE radical in compound **6** (radical concentration 2 mM) at 87 K with a dipolar-model (eqs 2, 3) fit superimposed. The observing microwave power was 2.87 μW, the saturating microwave power was 720 mW and the pulse was of 1 ms duration; (b) Residual for the single-exponential fit; (c) Residual for the dipolar-model fit.

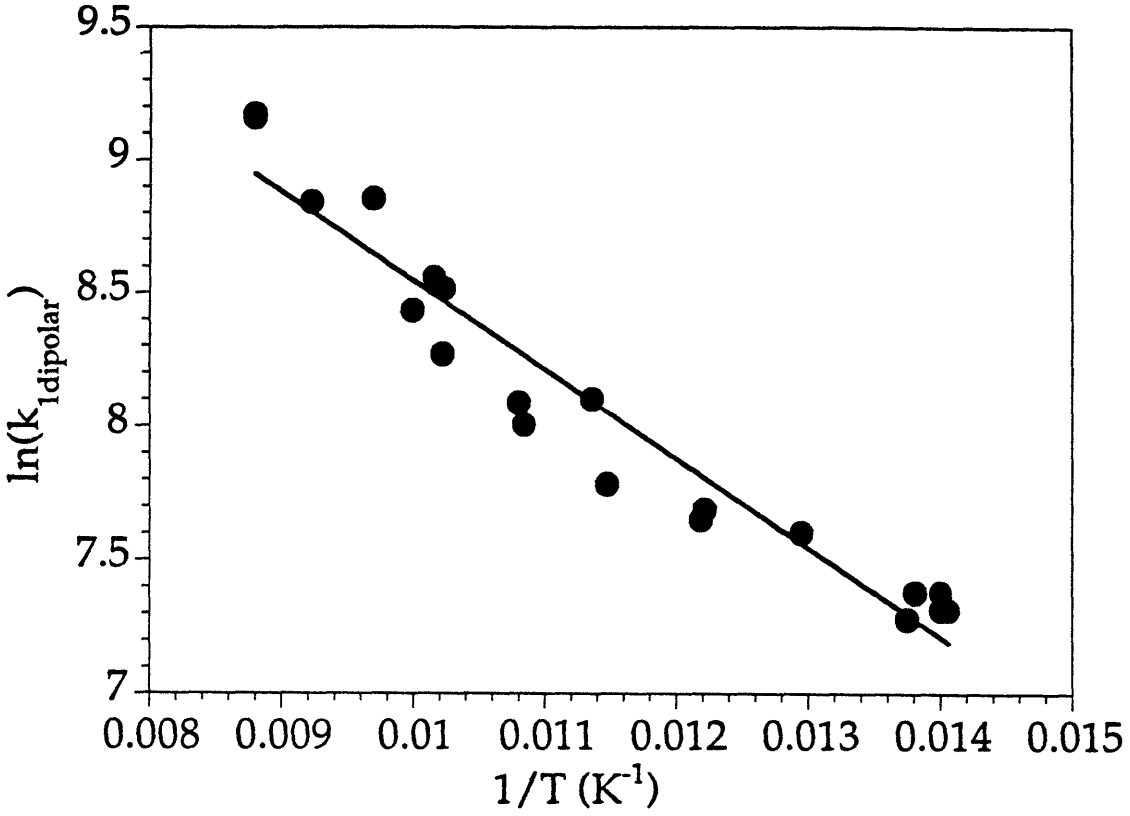

Figure 9. Natural logarithm of k_{1d}^{B} versus 1/T using the high temperature regime (72 K<T<115 K) data of Figure 7. The linear fit corresponds to the equation $\ln(k_{1d}^{B}) = (11.8 \pm 0.3) + (333 \pm 21)(1/T)$.

Chapter 3

Ferromagnetic versus Antiferromagnetic Exchange in Five Structurally Analogous Carboxylate-Bridged Trinuclear Ferrous Complexes

Introduction

The fully-reduced forms of the non-heme iron proteins methane monooxygenase hydroxylase (MMOH), ribonucleotide reductase R2 (R2), and hemerythrin (Hr) all contain a carboxylate-bridged diiron(II) active site in which the iron atoms are additionally coordinated to imidazole and carboxylate functionalities.[1-3] Understanding the structural and electronic properties of the diiron(II) centers in these proteins is an important part of deriving their functional mechanisms. Significant progress has been made in characterizing the magnetic behavior of all three proteins in their reduced forms. Weak ferromagnetic exchange coupling has been reported for $MMOH_{red}$ ($\mathcal{H} = JS_1 \cdot S_2$), J = -0.6 to - 1.0 cm^{-1},[4] for $R2_{red}$, J = -0.6 cm^{-1},[5] and for deoxyHrN_3, J = -2.4 cm^{-1}.[6] For both $MMOH_{red}$[7-9] and deoxyHrN_3,[6,10] a low field integer spin EPR signal ($g \approx 16$) has been observed, and recently ESEEM and ENDOR spectra have been obtained by utilizing this signal.[11] For $R2_{red}$, a similar low-field EPR signal was described,[12] although the origin of this signal is not fully understood.[5,13] The origin of the low-field EPR signal was in all cases attributed to a weakly ferromagnetically coupled diiron(II) system, a conclusion supported in the case of deoxyHrN_3 by magnetic susceptibility measurements.[6]

A small number of carboxylate-bridged diiron(II) complexes are available as models for the protein iron cores. The compounds $[Fe_2(\mu\text{-}OH)(\mu\text{-}OAc)_2(Me_3TACN)_2](ClO_4)$[14,15] and $[Fe_2(\mu\text{-}OH_2)(\mu\text{-}OAc)_2(OAc)_2(tmen)_2]$[16] contain bridging hydroxide and water ligands, respectively, as well as two bidentate bridging carboxylates. Antiferromagnetic coupling (J = 26 cm^{-1}) has been observed for the former compound. The alkoxo(carboxylato)-bridged complex $[Fe_2(OBz)(N\text{-Et-HPTB})](BF_4)_2$ also exhibits antiferromagnetic exchange (J = 22 cm^{-1}).[17] An analogous phenoxo-bridged complex, $[Fe_2(O_2CR)_2(BPMP)](BPh_4)$ (R = C_2H_5, Ph),[18] displays weak ferromagnetic coupling and a broad, low-field g ≈

16 EPR signal, and similar results have recently been obtained for the analogous compound $[Fe_2(O_2CPh)_2(BPCP)](BPh_4)$.[19] Other diiron(II) complexes having weak ($0 \geq J \geq -10$ cm^{-1}) ferromagnetic coupling and low-field EPR signals include the bis(phenoxo)-bridged complex $[Fe_2(H_2Hbab)_2(N\text{-}MeIm)_2]$,[20] and a series of di(μ-halo) complexes of the type $[Fe_2L_2X_2]$, where L = TLA, TMPza, TPA and X = Cl or F.[21] Another bis(phenoxo)-bridged complex, $[Fe_2(salmp)_2]^{2-}$,[22] was initially described as being weakly ferromagnetically coupled with J = -2.46 cm^{-1}. This compound has recently been reinvestigated and found to have a significantly larger J value of -13.7 cm^{-1}, obtained by fitting magnetization and Mössbauer data to a model incorporating zero-field splitting parameters.[23] The complex $[Fe_2(O_2CH)_4(BIPhMe)_2]$,[24] which contains a monodentate-bridging and two bidentate-bridging formate ligands, exhibits little or no magnetic exchange coupling. A fit of the magnetic susceptibility data gave J = 0.32 cm^{-1}, without inclusion of zero-field splitting parameters. This compound also displayed a low-field EPR signal.[25] The magnitude of J for these diiron(II) complexes is quite small compared to the values for related (μ-oxo)bis(μ-carboxylato)diiron(III) complexes, which are in the 160 - 260 cm^{-1} range.[2,26] Significant zero-field splitting (zfs) for high-spin ferrous ion makes it more difficult to fit the magnetic data for the Fe(II) complexes, especially when the zfs effects are of the same magnitude as the exchange coupling interaction.[10]

In the course of our continuing studies of synthetic models for the various forms of the carboxylate-bridged diiron centers in the reaction cycles of MMOH, Hr and R2, we have prepared a series of similar, but structurally and magnetochemically distinguishable, trinuclear ferrous complexes. Compounds of the general formula $[Fe_3(O_2CR)_6L_2]$, where L is one of the bidentate nitrogen donor ligands depicted in Figure 1, have been synthesized and characterized. Although the desired dinuclear structural type could not be obtained with simple

carboxylate bridging ligands, the resulting triiron(II) complexes are of considerable interest in their own right and relevant to the natural systems. The linear arrangement of metal atoms allows each "half" of the complex to be viewed as a dinuclear unit, and it is useful to compare the nature of the magnetic coupling between adjacent iron atoms in these trinuclear systems with that in the analogous dinuclear protein cores.

In the present article we report the synthesis, magnetic susceptibility, high-field magnetization and EPR properties, and electronic structures of these complexes. We also describe a procedure for fitting the magnetic susceptibility and high-field magnetization data to a theoretical model which incorporates zero-field splitting effects and single-ion g anisotropy. This model is more general than the conventional analytical method based on the Kambé coupling scheme and Van Vleck equations,[27,28] and should be of value in treating low-nuclearity polyiron(II) systems. One of these complexes, $[Fe_3(OAc)_6(BIPhMe)_2]$ (**1**), was previously reported to be ferromagnetically coupled.[29] The magnetic properties of this complex have been reinvestigated, and the initial qualitative description confirmed. We have now determined, however, that the magnetic moment obtained from the original measurement was artificially high, owing to partial mechanical torquing of the crystallites in the applied field.

Experimental Section

General Methods. Unless otherwise noted, materials were obtained from commercial sources and used as received. All manipulations and reactions were carried out under an inert atmosphere in a Vacuum Atmospheres drybox or by using standard Schlenk techniques. Solvents THF, diethyl ether, pentane and toluene were distilled from Na/benzophenone ketyl under nitrogen; CH_2Cl_2 and methanol were distilled from CaH_2 and magnesium methoxide, respectively, under nitrogen. The ligands (Fig. 1) bis-[2-((4*S*)-(1-methylethyl)-1,3-

oxazolinyl)]methane (^{i}PrOx),[30] 2,2'-bis(1-methylimidazolyl)phenylhydroxy-methane (BIPhOH),[24] 2,2'-bis(1-methylimidazolyl)phenylmethoxymethane (BIPhMe)[24] and 1,1-bis-(1-methylimidazolyl)-1-(3,5-di-*tert*-butyl-4-hydroxy-phenyl)ethane (BIDPhEH)[31] were prepared according to literature procedures. ^{1}H NMR spectra were recorded on a Bruker AC 250 spectrometer. Proton resonances reported in units of ppm downfield from tetramethylsilane (TMS), were reported to residual solvent protons. Electron-impact (EI) mass spectra were obtained on a Finnigan MAT 8200 mass spectrometer.

(3',5'-Di-*tert*-butyl-4'-hydroxyphenyl)-3-chloropropylketone (2a). A portion of 4-chlorobutyryl chloride (39.0 mL, 0.348 mol) was added to a previously cooled (-78 °C) solution of 2,6-di-*tert*-butyl phenol (71.53 g, 0.347 mol) in CH_2Cl_2 (400 mL). A 45.0 g (0.338 mol) quantity of $AlCl_3$ was added slowly to this solution. The mixture was stirred at -78 °C for 1 h and then warmed slowly to room temperature. The mixture was quenched by slow addition to an ice-cold solution of HCl (400 g ice and 10 mL of conc. HCl), and the product was extracted with ethyl acetate (5 x 200 mL). The organic layer was dried over $MgSO_4$, filtered, and the solvent was removed in vacuo. The crude product was purified by chromatography on a silica column (5% [v/v] ethyl acetate in CH_2Cl_2), affording 65.5 g (61 %) of a white solid. ^{1}H NMR (250 MHz, $CDCl_3$) δ 1.48 (s, 18 H, $C(CH_3)_3$), 2.23 (quintet, 2H, J=6.4 Hz, CH_2), 3.14 (t, 2H, J=6.4 Hz, $C(O)CH_2$), 3.69 (t, 2H, J=6.4 Hz, CH_2Cl), 5.75 (s, 1H, OH), 7.88 (s, 2H, C_6H_2); ^{13}C NMR (250 MHz, $CDCl_3$) δ 27.24, 30.02, 34.23, 34.58, 44.56, 125.60, 128.58, 135.84, 158.39, 198.12; mass spectrum (EI) *m/e* 310 (M^+).

2,6-Di-*tert*-butyl-4-(1',1'-dimethyl-4'-chlorobutyl)phenol (2b). A 3 mL aliquot of a 1 M solution of $TiCl_4$ in CH_2Cl_2 (3.0 mmol) was dissolved in CH_2Cl_2 (15 mL) and cooled to -40°C. To this solution was slowly added a 2 M solution of dimethyl zinc in toluene (1.5 mL, 3.0 mmol). The mixture was stirred at -40 °C

for 45 min. A solution of **2a** (0.4776 g, 1.54 mmol) in CH_2Cl_2 (10 mL) was added slowly to the reaction mixture, which turned from colorless to orange. The resulting solution was stirred at -40 °C for 2 h and warmed to room temperature over a period of 3 h. The reaction mixture was poured into an ice-cold solution of 1N HCl (20 mL) over approximately 100 mL of ice, and then extracted with CH_2Cl_2 (3 x 40 mL). The organic layer was dried over $MgSO_4$, filtered, and the solvent was removed in vacuo. The product was purified by chromatography on a silica column (1% [v/v] ethyl acetate in hexane), affording 0.372 g (74%) of a white solid. ^1H NMR (250 MHz, $CDCl_3$) δ 1.30 (s, 6H, $C(CH_3)_2$), 1.45 (s, 18H, $C(CH_3)_3$), 1.50-1.72 (m, 4H, $(CH_2)_2$), 3.43 (t, 2H, CH_2Cl), 5.05 (s, 1H, OH), 7.12 (s, 2H, C_6H_2); ^{13}C NMR (250 MHz, $CDCl_3$) δ 28.71, 29.23, 30.50, 34.58, 37.26, 41.88, 45.81, 122.22, 135.18, 139.14, 151.44; mass spectrum (EI) *m/e* 324 (M^+).

N,N,N'-Trimethyl, N'-[4,4-dimethyl-4-(3',5'-di-*tert*-butyl-4'-hydroxyphenyl)butyl]ethylenediamine (PheMe$_3$Eda) (2c). An amount of **2b** (8.75 g, 26.9 mmol) was added to N,N,N'-trimethylethylenediamine (12.70 g, 124 mmol) and refluxed for 4 h. The unreacted N,N,N'-trimethylethylene diamine was removed by vacuum distillation. The resulting mixture was partitioned between methylene chloride and water (100 mL/50 mL) and extracted with CH_2Cl_2 (3 x 50 mL). The organic layer was washed with brine (30 mL), dried over $MgSO_4$, and filtered, and the solvent was removed in vacuo. The product was purified by vacuum distillation, affording 8.08 g (77 %) of a colorless oil. ^1H NMR (250 MHz, $CDCl_3$) δ 1.28 (s, 6H, $(CH_3)_2$), 1.44 (s, 18H, $(CH_3)_3$), 1.5 (m, 4H, $(CH_2)_2$), 2.21 (s, 3H, N'-CH_3), 2.26 (s, 6H, N-$(CH_3)_2$), 2.3 (t, 2H, N'-CH_2), 2.46 (m, 4H, N-$(CH_2)_2$-N'), 5.05 (s, 1H, OH), 7.12 (s, 2H, C_6H_3); ^{13}C (250 MHz, $CDCl_3$) δ 22.20, 28.92, 30.35, 34.39, 37.26, 42.15, 45.45, 50.14, 54.94, 56.70, 58.68, 122.06, 134.91, 139.53, 151.17; mass spectrum (EI) *m/e* 390 (M^+).

$[Fe_3(OAc)_6(BIPhOH)_2]\cdot 2MeOH$ (3). To a suspension of $Fe(OAc)_2$ (0.22 g, 1.3 mmol) in MeOH (5 mL) was added BIPhOH (0.23 g, 0.857 mmol) to give a light green slurry. This slurry was stirred for 12 h and filtered. Vapor diffusion of THF into the filtrate gave 0.20 g (41%) of **3** as a colorless crystalline solid which was washed with THF and dried under vacuum for 15 min. Anal. Calcd. for $Fe_3C_{44}H_{58}O_{16}N_8$ (M_r 1122.53): C, 47.08; H, 5.21; N, 9.98. Found: C, 46.99; H, 5.16; N, 9.91.

$[Fe_3(OAc)_6(BIDPhEH)_2]$ (4). To a suspension of $Fe(OAc)_2$ (0.23 g, 1.34 mmol) in MeOH (6 mL) was added BIDPhEH (0.34 g, 0.86 mmol) in MeOH (4 mL) to give a light green slurry. This slurry was stirred for 12 h to assure dissolution of the $Fe(OAc)_2$, at which point the solvent was removed in vacuo. The resulting white solid was redissolved in CH_3CN (20 mL) with heating to boil, and the solution was filtered while hot. Vapor diffusion of diethyl ether into CH_3CN gave **4** as a colorless crystalline solid (0.45 g, 79% yield). The supernatant was decanted and the crystals were washed with diethyl ether and dried in vacuo for 12 h. Anal. Calcd. for $C_{60}H_{86}N_8O_{14}Fe_3$ (M_r 1310.93): C, 54.97; H, 6.61; N, 8.55. Found: C, 54.89; H, 6.59; N, 8.36.

$[Fe_3(O_2CPh)_6(^iPrOx)_2]$ (5). A mixture of $[Fe(H_2O)_6](BF_4)_2$ (1.216 g, 3.61 mmol), NaO_2CPh (1.701 g, 11.89 mmol), and ^{i}PrOx (0.911 g, 3.82 mmol) was dissolved in methanol (50 mL). The resulting light yellow solution was stirred for 15 min and the solvent was removed in vacuo. The product was dissolved in toluene (100 mL) and this solution was filtered through a Celite plug. The volume of this solution was reduced and vapor diffusion of pentane into the residual gave 0.509 g (31%) of **5** as light yellow crystals. Anal. Calcd. for $Fe_3C_{68}H_{74}N_4O_{16}$ (M_r 1370.90): C, 59.58; H, 5.44; N, 4.09. Found: C, 59.42; H, 5.53; N, 4.04.

$[Fe_3(OBz)_6(PheMe_3Eda)_2]$ (6). A solution of $[Fe(H_2O)_6](BF_4)_2$ (0.488 g, 1.45 mmol) in MeOH (5 mL) was added to a mixture of $PheMe_3Eda$ (0.571 g, 1.46 mmol) and NaO_2CPh (1.251 g, 8.68 mmol) in MeOH (20 mL). A light yellow solution and a white gel were obtained. The mixture was stirred at room temperature for 0.5 h and filtered over Celite, and the solvent was removed in vacuo. The product was extracted with benzene, filtered over Celite and the solvent was removed in vacuo. Vapor diffusion of pentane into a CH_2Cl_2 solution of the compound afforded 0.277 g (28%) of **6** as light yellow crystals. Anal. Calcd. for $Fe_3C_{92}H_{122}N_4O_{14}$ (M_r 1675.54): C, 65.95; H, 7.34; N, 3.34. Found: C, 65.27; H, 7.49; N, 3.33.

Crystallography. General Procedures. X-ray diffraction studies were performed with an Enraf-Nonius CAD-4F kappa geometry diffractometer and graphite-monochromatized Mo K$\bar{\alpha}$ radiation (λ = 0.71069 Å). The crystal temperature (see Table 1) was maintained by the use of an Enraf-Nonius FR558-S liquid nitrogen cryostat. The crystal specimen was transferred to a mounting stage on which it was bathed in a stream of cold nitrogen gas and mounted on the end of a quartz fiber with silicone grease. All calculations were performed with a VAXstation 4000-90 computer and the teXsan software package.[32] The Laue symmetry was determined by the unit cell parameters and confirmed by the examination of axial photographs. Two computer programs, TRANS and TRACER,[33] were employed to provide further confirmation of the choice of crystal system. The crystals were determined to be of sufficient quality for data collection as judged by the examination of rotational and axial photographs, the unit cell parameter errors, and the measurement of selected low angle peak widths at half-height $\Delta\bar{\omega}_{1/2}$ by open-counter ω scans.

Intensity data were collected with the ω-2θ scan technique, except for **6**, in which case ω scans were used. The intensities of three standard reflections were

measured after every 3600 seconds of exposure time. The data were corrected for Lorentz and polarization effects. The data for all complexes, with the exception of **4**, were corrected for absorption following the measurement of Ψ scans.[34] The direct methods program SHELXS-86[35] was used for the initial structure solutions, and final models were obtained by least-squares refinement in combination with difference Fourier syntheses. Hydrogen atoms were placed at calculated positions (C-H = 0.95 Å), and their *B* values were fixed at 1.2 times the B_{eq} of the atom to which they were bound, unless otherwise indicated. They were included, but not refined, in the final least-squares cycles. Scattering factors for the nonhydrogen[36] and hydrogen atoms[37] and anomalous dispersion terms[38,39] were taken from the usual sources.

A summary of crystallographic data for **3 - 6** can be found in Table 1. Atomic coordinates and B_{eq} for **3 - 6** excluding lattice solvent and hydrogen atoms are given in Tables 2 - 5. Selected bond distances and angles for compounds **3 - 6** are given in Tables 6 - 9. A complete listing of intramolecular bond distances and angles, atomic coordinates and B_{eq}, and anisotropic thermal parameters for **3 - 6** is provided in Tables 13 - 28. ORTEP diagrams of **3 - 6** can be found in Figures 3 - 6, respectively.

$[Fe_3(OAc)_6(BIPhOH)_2]\cdot 2MeOH$ (3). A colorless, irregular block-shaped crystal (0.30 x 0.20 x 0.10 mm), grown from MeOH/THF, was selected. The unit cell dimensions were obtained from a least-squares fit of 25 reflections in the range $10° < \theta < 15°$, and the Laue symmetry was determined to be $\bar{1}$. No decay correction was necessary during data collection since there was no significant fluctuation in the intensities of the three standard reflections. All nonhydrogen atoms were refined by using anisotropic thermal parameters. The largest positive peak in the final difference Fourier map had an electron density of 0.57 $e^-/Å^3$ and was located in the region near O7.

$[Fe_3(OAc)_6(BIDPhEH)_2]$ (4). A colorless block-shaped crystal (0.30 x 0.35 x 0.30 mm), grown from CH_3CN/Et_2O, was selected. The unit cell dimensions were obtained from a least-squares fit of 22 reflections in the range $9 < \theta < 17°$, and the Laue symmetry was determined to be 2/m. No absorption correction was applied because of the minimal anisotropy in transmission factors as estimated for an average transmission curve calculated from Ψ scans. No decay correction was necessary since there was no significant fluctuation in the intensities of the three standard reflections. All nonhydrogen atoms were refined by using anisotropic thermal parameters except for those of lattice solvent.

One acetonitrile molecule in the asymmetric unit was refined with isotropic thermal parameters with full occupancy. The other acetonitrile molecule was disordered over two positions with one shared carbon atom, C(33). This carbon atom was refined with isotropic thermal parameters at full occupancy, while the remaining electron density was modeled by C(34), C(35), N(6) and N(7), each with isotropic thermal parameters at half occupancy. The largest positive peak in the final difference Fourier map had an electron density of 0.83 $e^-/Å^3$ and was located in the region near N5.

$[Fe_3(O_2CPh)_6(^iPrOx)_2]$ (5). A light yellow crystal (0.33 x 0.48 x 0.45 mm) grown from pentane/CH_2Cl_2 was selected. The unit cell dimensions were obtained from a least-squares fit of 23 reflections in the range $10 < \theta < 14°$ and revealed the Laue symmetry was revealed to be mmm. No decay correction was necessary since there was no significant fluctuation in the intensities of the three standard reflections. The Fe, O and N atoms were refined with anisotropic thermal parameters and the C atoms refined with isotropic thermal parameters. The largest positive peak in the final difference Fourier map had an electron density of 0.54 $e^-/Å^3$, and was located in the region near C44.

$[Fe_3(OBz)_6(PheMe_3Eda)_2]$ (6). A light yellow crystal grown from pentane/CH_2Cl_2 was selected. The unit cell dimensions were obtained from a least-squares fit of 25 reflections in the range $7 < \theta < 19°$, the Laue symmetry was 2/m. A decay correction was applied to account for a 2.5 % loss in intensity over the 4 days of data collection. All nonhydrogen atoms were refined by using anisotropic thermal parameters. The largest positive peak in the final difference Fourier map had an electron density of 0.55 $e^-/Å^3$ and was located in the region near O1.

Magnetic Susceptibility Studies. Solid state magnetic susceptibility measurements on 30 - 60 mg samples of **1** and **3 - 6** were made by using a Quantum Design MPMS SQUID susceptometer equipped with a 5.5 T magnet and operating in the range 2.5 - 300 K. Samples were loaded in a drybox and sealed in nitrogen-filled vials for transport to the susceptometer. Care was taken to minimize exposure of the samples to air by transferring them to the sample transport chamber of the SQUID as quickly as possible once the vial seals were broken. On several occasions samples were immediately frozen in liquid nitrogen after removal from the susceptometer and returned to the drybox, whereupon examination of the powders revealed no observable color change, as would be expected if oxidation had taken place. The susceptibilities of the sample holder were measured at the same fields and temperatures for accurate corrections of its contribution to the total measured susceptibility. Diamagnetic corrections of -5.57×10^{-4}, -3.63×10^{-4}, -5.76×10^{-4}, -6.04×10^{-4} and -9.62×10^{-4} cm^3/mol for **1** and **3 - 6** respectively, were estimated from Pascal's constants[40,41] and subtracted from the experimental susceptibilities.

Magnetization Studies. Solid state magnetization measurements on 15 - 40 mg samples of **1** and **3 - 6** were made with a vibrating-sample (Foner) magnetometer at the Francis Bitter National Magnet Laboratory. Electronics

were modified for use in Bitter magnets. Samples were loaded in a drybox and sealed in nitrogen-filled vials for transport to the magnetometer. Sample holders were made from Teflon or Kel-F and fitted with plungers that allowed for compression of the powders by hand to prevent mechanical torquing in the applied field. Data were collected between 0 and 200 kOe for all samples.

EPR Studies. Spectra were recorded with a Bruker ESP-300 spectrometer equipped with an Oxford Instruments liquid-helium continuous-flow cryostat. In order to reduce to a minimum partial torquing of the crystallites in the applied magnetic field during the EPR experiment, powder samples of **1**, **3**, and **4** were pressed in parafilm in a drybox, and the parafilm pellet was then loaded into a 4 mm o.d. quartz EPR tube. Samples were immediately frozen in liquid nitrogen after removal from the drybox. Centering of the solid samples in the microwave cavity was carefully done manually to maximize signal-to-noise. Diphenylpicrylhydrazyl (DDPH) or an aqueous $CuSO_4$ solution was used as a standard for calibrating the magnetic field.

Magnetic Theory and Fitting. Magnetic susceptibility and magnetization data were fit by using a non-linear least-squares curve-fitting program, DSTEPIT.[42] This FORTRAN program was linked to subroutines that set up a 125 x 125 spin Hamiltonian matrix for the determination of the energy levels by matrix diagonalization with the EISPACK[42] subroutines and calculation of the powder susceptibility and magnetization data by using Van Vleck's equations.[28,41,43] Labelling of the spin sites $Fe_{1\text{-}3}$ and associated exchange coupling parameters is as indicated in Figure 2. The general spin Hamiltonian in eq. 1 was employed, incorporating the exchange coupling, zero-field splitting, and electronic Zeeman terms. As suggested by Griffith,[44] J, rather than $-J$, $-2J$, or

$$\mathcal{H} = \sum S_i \bullet J_{ij} \bullet S_j \; (i=1,3;\; j=2,3;\; j \neq i) + \sum S_i \bullet \boldsymbol{D}_i \bullet S_i \;\; (i=1,3) + \sum \boldsymbol{B} \bullet \boldsymbol{g}_i \bullet \; S_i \; (i=1,3) \qquad (1)$$

$2J$, was employed as the exchange coupling parameter. Several simplifications in each term were made so as to render the fitting procedure more tractable. First, an isotropic J was used; dipolar exchange interactions between spin sites were not taken into account.[45] Second, the electronic coordinate system for each of the three spin sites was assumed to have the same orientation (D_i, g_i, i=1,3 collinear), and only axial zero-field splitting was considered for each spin site (E_i = 0; i = 1-3). Third, in accord with the previous simplification, the **g** tensor was constrained to be axially symmetric ($g_{iy} = g_{ix}$; i = 1-3). These same approximations were made previously in a study of a linear Ni(II) trimer.[46] Finally, fourth order zero-field splitting terms were ignored, although these terms (e.g., F) can be present for $S \geq 2$.[47] Simulations were also performed without zero-field splitting ($D_i = 0$) and with only an isotropic single-ion g value, which we refer to as the "Kambé-type" model.[27]

Constraints were imposed on the fitting procedure that were based on the molecular symmetry. Individual magnetic parameters for the terminal ferrous sites were set to be equivalent: $D_1 = D_3$ and $g_{l1} = g_{l3}$; $l = x, y, z$. Exchange coupling between the terminal and middle ferrous sites were held to be equal: $J_{12} = J_{23}$. In general, the terminal-terminal exchange coupling was fixed at zero (J_{13} = 0), although this restriction is not symmetry imposed. The effect of $J_{13} \neq 0$ was explored in fits of the susceptibility data (see Results and Discussion). Calculations were performed on an IBM RS/6000 computer maintained by the Department of Chemistry, Northwestern University.

EPR Theory. A computer program employing full-matrix diagonalization, similar to the one employed in the magnetic data fitting, was used to generate EPR transition energies and probabilities. The latter were obtained by first determining magnetic dipole allowedness from the eigenvectors and then

applying the resonance condition with the microwave quantum (at X-band, ≈ 0.3 cm^{-1}). No attempt was made to generate powder patterns. Instead, three "single-crystal" calculations were made with $B_0 = B_x$, B_y, and B_z, successively. No iterative spectral simulations were performed. The function of the program was to confirm that the observed EPR signals could arise from the trinuclear system with the parameters determined from fitting of the magnetic data.

Results and Discussion

Syntheses. The ligand $PheMe_3Eda$ was originally prepared to provide a bidentate nitrogen donor ligand with a pendant phenol for use in generating a model for the active site of the ribonucleotide reductase R2 protein. Such a model, comprising an oxo-bridged diiron(III) unit and a non-coordinated phenoxyl radical moiety, was made by using BIDPhEH, as reported previously.[31] Both BIDPhEH and $PheMe_3Eda$ also afforded linear, carboxylate-bridged trinuclear Fe(II) complexes, analogous to $[Fe_3(OAc)_6(BIPhMe)_2]$.[29] These compounds allowed us to expand the class and to compare in detail the magnetic properties of a series of similar, but stucturally and magnetochemically distinguishable, trinuclear ferrous species.

Reaction of equimolar amounts of 2,6-di-*tert*-butylphenol, 4-chlorobutyryl chloride and $AlCl_3$ afforded the ketone (3',5'-di-*tert*-butyl-4'-hydroxyphenyl)-4-chlorobutanone (**2a**) in 62 % yield after purification by column chromatography. A previous report demonstrated that ketones can be dimethylated by using Me_2TiCl_2, prepared from Me_2Zn and $TiCl_4$, under very mild conditions.[48,49] This strategy was employed to obtain the methylated product **2b** from **2a** in 76% yield after purification by column chromatography. The final $PheMe_3Eda$ ligand was obtained by reaction of **2b** with N,N,N'-trimethylethylene diamine and isolated as an oil in 77% yield after vacuum distillation.

Two facile synthetic routes were devised for preparing the five trinuclear ferrous complexes reported here. The first, described elsewhere for **1**[29] and employed in the syntheses of **3** and **4**, combines $Fe(OAc)_2$ with the bidentate nitrogen donor ligand in a 3:2 ratio. The same general procedure was used to obtain the related Mn(II) complex, $[Mn_3(O_2CPh)_6(bpy)_2]$.[50] An analogous trinuclear V(II) complex, $[V_3(O_2CR)_6(TMEDA)_2]$ [R = Ph_2CH, $PhCH_2$; TMEDA = tetramethylethylenediamine], was prepared by treating $VCl_2(TMEDA)_2$ with neat carboxylic acid.[51] Crystallization of all three complexes in good yield was readily accomplished by vapor diffusion of the appropriate precipitating solvent. An alternative route, used for complexes **5** and **6**, combines $Fe(BF_4)_2{\cdot}6H_2O$, the appropriate bidentate nitrogen donor ligand, and a 2- to 5-fold excess of sodium benzoate. The resulting trinuclear complexes are neutral and easily extracted into aromatic solvents, allowing for purification from unreacted carboxylate salts. Complexes **5** and **6** were crystallized in good yield as described for **1**, **3**, and **4**.

Molecular Structures. A detailed description of the structure shared by the five trinuclear complexes has been presented previously for complex **1**[29] and this class of compounds in general,[52] and will not be reiterated here. Instead we highlight geometric parameters that are useful in understanding their magnetic properties. Compounds **3**, **4**, **5** and **6**, have a linear, trinuclear structure with a total of six bridging carboxylate ligands, four of which coordinate in a bidentate fashion through both oxygen atoms (Figs. 3 - 6). The remaining two carboxylate ligands use a single oxygen atom to bridge two metal centers, leaving the remaining oxygen atom of this ligand available to coordinate to the nearest terminal iron atom. The bidentate nitrogen donor ligands cap the two ends of the trinuclear structure through binding to a terminal metal atom. A generalized depiction of these structural features is provided in Figure 2, and a comparison of

selected bond distances and angles for compounds **1** and **3 - 6** is provided in Table 10.

The most striking difference among the structures of the five complexes is the Fe_t - O_d distance, which allows for their division into two classes. One class, comprised of compounds **1, 3,** and **4,** exhibits relatively weak bonding between O_d, the dangling oxygen atom, and Fe_t, the terminal metal atom, as revealed by the long $Fe_t \cdots O_d$ distances of 3.0 Å. The other consists of compounds **5** and **6,** which have much shorter distances, Fe_t-$O_d \approx 2.2$ Å, signifying coordination of the carboxylate oxygen atom. The movement of this atom toward the terminal iron atom in these two complexes pulls the bridging oxygen atom, O_b, away from Fe_m, and additionally lengthens the Fe_t-O_b bond by as much as 0.21 Å compared to the Fe_t-O_b distances in the first group of complexes (see Table 10).

The average Fe_t-N distance is significantly longer (0.1 Å) for both **5** and **6,** consistent with the higher coordination number of the terminal iron atoms in these complexes. The Fe_t atoms in both **5** and **6** exhibit geometries much nearer ideal octahedral symmetry than in **1, 3,** or **4,** as reflected by the N_p-Fe_t-O_b angles, illustrated in Figure 2 and listed in Table 10. The widening of this angle is another consequence of the short Fe_t-O_d distance. The difference in the Fe_t-O_d distances correlate well with a significant change in the magnetochemical properties of the two types of complexes, as discussed below.

Magnetic Susceptibility Studies. Temperature-dependent molar susceptibility data previously reported for **1** were erroneously high owing to torquing of the crystallites in the applied field. Such reorientation phenomena have been observed before, including in some Fe(II) systems.[53,54] The original measurement, made at 3 kG, correctly revealed ferromagnetic coupling for **1,** but at 4 K the effective magnetic moment derived from the low temperature data was 17.3 μ_B. The theoretical value of μ_{eff} for three fully ferromagnetically coupled

Fe(II) atoms having $S = 6$ is 12.96 μ_B for $g = 2.0$. We suggested that some intermolecular interaction might be the cause of the unexpectedly high moment. When the data were measured at a much lower field of 100 G to avoid possible reorientation of the crystallites, ferromagnetic coupling was maintained but μ_{eff} was 12.7 μ_B at 6 K, a value consistent with an $S = 6$ ground state.

To test our hypothesis that crystallites of **1** were mechanically reorienting in the field during the original measurement, we measured the effect of the applied field on the magnetic susceptibility. The molar susceptibility at several temperatures between 5 and 10 K was first measured in an applied field of 100 G, and then the field was increased to 3 kG and the points were remeasured at the same temperatures. The susceptibility increased by approximately 70 %. The applied field was then set to zero and the sample was warmed to 300 K and held at that temperature for several hours, after which time a field of 100 G was reapplied and the susceptibility measured once again at the same points between 5 - 20 K. The data continued to show an increase of 70 % from the values originally measured at low field. By holding the sample at room temperature and zero field for an extended period of time, we could rule out magnetic hysteresis as a mechanism for the increase in the susceptibility. The results are fully consistent with partial physical alignment of the crystallites with the field at 3 kG.

As final confirmation of the torquing phenomenon, we repeated the above magnetic history experiments, but removed the sample from the susceptometer after the measurement at 3 kG and vigorously shook the sample holder in order to randomize the orientation of the crystallites. Remeasurement of the susceptibility at 100 G and 8 K gave a value within 3% of the initial low field result, proving that the increase observed at 3 kG came from partial torquing of the crystallites.

Plots of the effective magnetic moment versus temperature for **1**, **3**, and **4** are shown in Figures 7, 8 and 9, respectively. Above 200 K, all three of these complexes exhibit effective magnetic moments close to the theoretical value of 8.48 μ_B expected for three independent $S = 2$ ferrous ions with $g = 2.0$. The steep rise in the effective moment is characteristic of ferromagnetic coupling below 80 K for all three complexes. As for **1**, the BIPhOH and BIDPhEH complexes have μ_{eff} values approaching the 12.96 μ_B theoretical value for an $S = 6$ system at low temperatures, with μ_{eff} = 11.7 μ_B at 7 K for **3** and μ_{eff} = 12.3 μ_B at 5 K for complex **4**.

The temperature dependence of μ_{eff} for complexes **5** and **6** is shown in Figures 10 and 11, respectively. Near 300 K, the effective moments are 9.52 μ_B and 9.50 μ_B for the ^{i}PrOx and PheMe$_3$Eda complexes, respectively. These values are similar to the spin-only value expected for three isolated $S = 2$ ions near 300 K, described above. As the temperature decreases, the effective moments also decrease, revealing antiferromagnetic coupling for both **5** and **6**. The ground state for full antiferromagnetic coupling and $S = 2$ has a theoretical spin-only value of 4.90 μ_B assuming $g = 2.0$. The ^{i}PrOx and PheMe$_3$Eda complexes have μ_{eff} values of 6.52 and 6.74 μ_B at 5 K, approaching this value.

Magnetization Studies. Plots of the reduced magnetization, M/Nμ_B, vs. field at 2 K for complexes **1**, **3**, and **4** are included as insets in Figs. 7, 8, and 9, respectively. In all of these ferromagnetically coupled complexes, a steep rise occurs in the reduced magnetization at low fields, followed by a slow, steady increase up to the maximum field of 200 kOe. Both **1** and **3** reach 11.5 μ_B in reduced magnetization at 200 kOe, and compound **4** obtains a value of 10.9 μ_B at this field. The theoretical value of M/Nμ_B is 12.0 μ_B for an $S = 6$ ground state, assuming $g = 2.0$, close to the experimental values of the reduced magnetization for **1**, **3**, and **4**. None of the curves exhibits a plateau region that would be

expected if the magnetization were saturated by the high fields. The slow approach of the reduced magnetization to the theoretical value reveals that a field of 200 kOe is not strong enough, even at these low temperatures, for the ferromagnetic ground state of these weakly-coupled complexes to be populated exclusively.

The antiferromagnetically coupled compounds **5** and **6** display a more gradual increase in $M/N\mu_B$ with increasing magnetic field, as indicated in the insets of figures 10 and 11. An $S = 2$ ground state should give rise to an $M/N\mu_B$ value 4.0 μ_B assuming $g = 2.0$. This increase in $M/N\mu_B$ above 4.4 μ_B occurs because the Zeeman term becomes more important as the field is increased (vide infra).

Theoretical Analysis of the Magnetization Data. We have performed least-squares fits of both the susceptibility and high-field magnetization data to eq. 1 for all five complexes with the programs described in the Experimental Section. Given a problem of this complexity, the final parameters for an individual fit can be quite sensitive to their initial values, so the following protocol was adopted for the susceptibility data. Initial values for the isotropic exchange coupling parameter ($J_{12} = J_{23}$; $J_{13} = 0$) were always fixed at zero and the g values were always initiated at 2.0. Fits were performed by using initial values for D_i of 0, -10, and +10 cm^{-1} ($i = 1 = 3, 2$). This range approximately corresponds to the values reported previously for mononuclear ferrous systems (vide infra).[55,56] As described below, considerable difficulty was encountered in obtaining the absolute signs of D_i, although the magnitudes could be estimated. In fitting the magnetization data, the same procedures were followed, but only an initial value of $D_i = 0$ was used. Attempts were also made to fit the magnetization curves by using the Kambé-type model, the results of which were compared to the fits obtained from the more general model of eq. 1.

In order to model completely a magnetic system having the complexity of the trinuclear ferrous systems described here, it would be necessary to measure the entire "magnetization surface," the three-dimensional space defined by temperature, external magnetic field, and the resulting magnetization. For a given compound, we have only two sections in this space, namely, variable temperature susceptibility at one fixed field and variable-field magnetization at one fixed temperature. As a consequence, the best-fit parameters for the former may not agree with those of the latter. We therefore give "consensus" magnetic parameters, summarized in Table 12, that best account for both the susceptibility and magnetization data for all five complexes.

*$[Fe_3(OAc)_6(BIPhMe)_2]$ (**1**).* The fit of μ_{eff} vs. T for this compound is shown in Figure 7. With an initial D_i of 0, the best-fit parameters were as follows (energies in cm^{-1}): J = -3.97, $D(Fe_{1,3})$ = -3.45, $D(Fe_2)$ = -0.46, $g_\perp(Fe_{1,3})$ = 2.08, $g_\parallel(Fe_{1,3})$ = 1.98, $g_\perp(Fe_2)$ = 1.99, $g_\parallel(Fe_2)$ = 2.02. The negative sign of J is consistent with ferromagnetic coupling. An initial D_i value of ± 10 cm^{-1} yielded similar magnetic parameters. Inclusion of J_{13} had little effect, giving $J_{12,23}$ = -4.62 cm^{-1} and J_{13} = +0.59 cm^{-1}. Clearly, $J = -4 \pm 1$ cm^{-1} is indicated.

The Kambé-type model failed to fit the high-field magnetization data, but inclusion of zero-field splitting succeeded quite well, as shown in the inset of Figure 7. The fit parameters were (energies in cm^{-1}): J fixed at -4.0, $D(Fe_{1,3})$ = 6.45, $D(Fe_2)$ = -10.1, all g values fixed at 2.00. Allowing all the fixed parameters to vary led to a slightly improved fit, but with J = -1.22 cm^{-1}, $D(Fe_{1,3})$ = +10.1 cm^{-1}, $D(Fe_2)$ = -1.11 cm^{-1}. Fixing the J values at -1.0 or -1.5 cm^{-1} led to a poor fit of the susceptibility data. Exact agreement of the magnetic parameters for the magnetization and susceptibility fits is simply not achievable, as indicated above. The consensus J value of -4 cm^{-1} fits the magnetization data adequately and the susceptibility data quite well.

[$Fe_3(OAc)_6(BIDPhEH)_2$] (4). Figure 9 shows a representative fit of the μ_{eff} vs. temperature curve for **4** employing the following parameters (energies in cm^{-1}): J = -4.80, $D(Fe_{1,3})$ = 5.85, $D(Fe_2)$ = 4.82, $g_\perp(Fe_{1,3})$ = 2.00, $g_\parallel(Fe_{1,3})$ = 2.38, $g_\perp(Fe_2)$ = 2.00, $g_\parallel(Fe_2)$ = 2.02. The fit used initial values for $D_i = 0$; initial values of ± 10 cm^{-1} yielded similar J and g values, and the final value for $D(Fe_2)$ remained near the initial one (e.g., $D(Fe_2)$ = 12.3 cm^{-1}, $D(Fe_{1,3})$ = 3.83 and J = -5.47 cm^{-1}). Only an estimate of $|D_i| = 10 \pm 10$ cm^{-1} can be made with confidence from the susceptibility data. Mononuclear Fe(II) complexes with distorted octahedral symmetry exhibit D values within this range, with $D \approx 10$ cm^{-1} being typical.[56] For example, magnetic studies of Fe^{2+} doped into $ZnSiF_6$ suggested D = +10.9 cm^{-1}, and EPR studies gave D = -20.2 cm^{-1}.[57] Magnetic studies in aqueous solution of Fe(II)EDTA, a complex having a ligand set resembling those described here, gave $|D|$ = 9.1 cm^{-1}; the EPR spectrum indicated a negative sign.[58] These examples serve to illustrate the difficulty of determining the sign of zfs parameters, even in mononuclear systems.

Values of 2.0 - 2.4 for g are as expected and arise from orbital angular momentum contributions. For d^6 ions in a cubic crystal field with significant spin-orbit coupling ($\lambda \approx 100$ cm^{-1}), an isotropic $g \leq 3.5$ is expected. Thus, for Fe(II) sites in MgO, g = 3.428 and, in NaF, g = 3.420.[47] In an axially distorted crystal field, as is the case with the present complexes, perturbation theory methods give $2.0 \leq g_\parallel, g_\perp \leq 2.4$.[57,59] For $Fe^{II}ZnSiF_6$, $g_\perp$ = 2.26 and $g_\parallel$ = 2.38 and for Fe(II)EDTA, using the EPR results but removing the rhombic contribution, $g_\perp$ = 2.02 and $g_\parallel$ = 2.20.

The J value can be reported with more confidence as -5 ± 1 cm^{-1}. Even allowing exchange coupling between the terminal ferrous sites had little effect: $J_{12} = J_{23}$ = -5.18 cm^{-1}; J_{13} = +0.34 cm^{-1}. The other parameters were similarly not substantially modified.

Use of a Kambé-type model failed completely to fit the variable field magnetization data for the BIDPhEH complex. Inclusion of zero-field splitting led to reasonably good fits, but with $J \approx 0$. Fixing J at -5.0 cm^{-1}, the value derived from the fits of the susceptibility data, allowed for the successful fit of the high-field magnetization data, as shown in the inset of Figure 9.

$[Fe_3(OAc)_6(BIPhOH)_2]$ (**3**). A successful fit of the susceptibility data for **3** is given in Figure 8. The fits gave g values near 2.0 and a J value of -2.8 cm^{-1}, indicative of ferromagnetic coupling. The value for $D(Fe_{1,3})$ of -19.2 cm^{-1} seems unreasonably high, however. Other fitting attempts with varying initial D values yielded $D(Fe_{1,3})$ of $\approx$ 6 cm^{-1}, but the resulting value for $g_{||}(Fe_2)$ was unreasonably low (< 0.8). Other interactions such as non-axial zfs terms, however, can manifest themselves in the apparent g value, leading to deviation of $g_{||}$ from 2.0, even with spin-orbit coupling quenched.[60]

A possible explanation for the difficulty in fitting the susceptibility data is that **3** exhibits antiferromagnetic coupling between the terminal ferrous sites (i.e., $J_{13} > 0$). Inclusion of J_{13} led to g values near 2.0 and $D(Fe_{1,3})$ of $\approx$ 6 cm^{-1}, although the fit was relatively poor in the high temperature region, where the molar susceptibility is quite low. Most of the fitting attempts for **3** consistently gave $D(Fe_2)$ values of very small magnitude, which may be related to the apparent relative importance of J_{13}. This result contrasts with those for **1** and **4**, for which the two zfs parameters $D(Fe_{1,3})$ and $D(Fe_2)$ were of comparable magnitude and inclusion of J_{13} had a negligible effect.

The magnetization data of **3**, are given in the inset of Figure 8 together with the best fit. Once again, attempts to fit the magnetization data with the Kambé-type model were ineffective. With the incorporation of zfs parameters, the fit was greatly improved. As was found with the susceptibility data fits, $D(Fe_2)$ consistently refined to nearly zero. Surprisingly, the magnetization fits

yielded $J \approx 0$ as well, with or without variation of g. Ferromagnetic coupling between terminal and center spin sites combined with terminal-terminal antiferromagnetic coupling could lead to approximate cancellation of these effects. Although no dramatic improvement in the magnetization fits resulted from inclusion of J_{13}, as can be seen for the fit with $J_{13} = +0.96$ cm^{-1} in Fig. 12, the fitting results as a whole suggest that this coupling may be significant for **3**. We conclude that net ferromagnetic coupling for the BIPhOH complex is significantly weaker than for **1** or **4**, as a consequence either of an inherently smaller terminal-to-center coupling or a competing antiferromagnetic interaction between terminal sites.

$[Fe_3(O_2CPh)_6(^iPrOx)_2]$ (5). The most reasonable fit to the susceptibility data for **5** in Figure 10 was obtained with the following refined parameters (energies in cm^{-1}): $J = +0.99$, $D(Fe_{1,3}) = 0$ (fixed), $D(Fe_2) = -11.5$, $g_\perp(Fe_{1,3}) = 2.14$, $g_\parallel(Fe_{1,3}) = 2.01$, $g_\perp(Fe_2) = 2.78$, $g_\parallel(Fe_2) = 2.13$. The positive J value between the terminal and middle iron atoms in this case reveals an antiferromagnetically coupled complex.

The inset of Fig. 10 shows the best fit of the magnetization data for **5**, obtained with $D_{1,3}$ fixed to zero. The J value refined to +0.72 cm^{-1}, in good agreement with that from the susceptibility fit. Fixing all g values to 2.00 and allowing $D(Fe_{1,3})$ to vary gave a worse fit, but similar values of $J = +1.45$ cm^{-1} and $D(Fe_{1,3}) = 0.09$ cm^{-1} resulted, as can be seen in Fig. 13. The above fits suggest that the $J = +1$ cm^{-1} and $D(Fe_{1,3}) = 0$ cm^{-1} values are well determined.

*$[Fe_3(O_2CPh)_6(PheMe_3EDA)_2]$ (**6**).* Modelling of the magnetic data for this compound gave results similar to **5**, the other antiferromagnetically coupled compound. Fixing $D(Fe_{1,3}) = 0$ yielded $D(Fe_2) = -11.3$ cm^{-1}, with $J = +1.0$ cm^{-1}, and the fit of the susceptibility data corresponding to these parameters is shown in Fig 11. Although some of the g values fluctuated far from $g = 2.00$, the J value

is positive as expected for antiferromagnetic coupling, and similar in magnitude to that of **5**.

As found for the ^{i}PrOx complex, a good fit of the magnetization data for **6** resulted in a J value near +1 cm^{-1} and a $D(Fe_{1,3})$ value close to zero, as shown in the inset of Fig. 11. When the g values were fixed to 2.00, the fit was of lower quality, as seen in Fig. 14, but the J and D values remained close to those obtained by the other susceptibility and magnetization fits.

General Comparisons. The large deviations from 2.00 for some of the refined g parameters for **5** and **6** are probably due to other interactions not taken into account by our model, as discussed above for the g values of the BIPhOH compound. The consistency of the J and D values for both **5** and **6** is noteworthy given the expected similarity in the magnetic behavior for these two antiferromagnetically coupled, structurally similar compounds. The Kambé-type model was more successful in fitting the magnetization data for **5** and **6** than for the ferromagnetic compounds. The success of the Kambé-type fit, which does not include any terms for zero-field splitting for these cases, may be correlated with the D values near zero determined for the terminal iron atoms. The negligible D value for $Fe_{1,3}$ obtained from the theoretical analysis is in satisfying agreement with the most important structural difference, the Fe_t-O_d distance, between complexes **5** and **6** as a class and the other three ferromagnetically coupled compounds. As discussed above, the shorter Fe_t-O_d distances in **5** and **6** give the terminal ferrous sites a geometry much closer to octahedral symmetry than the corresponding sites in **1**, **3**, and **4**. Accordingly, one might expect the zfs for these terminal iron atoms to be much smaller than in the less symmetric terminal sites of **1**, **3**, and **4**.

As described above, the reduced magnetization for the ferromagnetically-coupled complexes approaches the theoretical value for an $S = 6$ system at high

field, but the antiferromagnetically-coupled systems exhibit curves in which $M/N\mu_B$ largely exceeds the value expected for an $S = 2$ ground state. In order to explain this behavior, we describe the magnetics of the system in terms of the instructive approach employed by Kahn and coworkers in reporting high-field magnetization data for the structurally similar complex $[Mn_3(OAc)_6(bpy)_2]$.[61] The authors neglected zero-field splitting and, as appropriate for a d^5 high-spin system, used an isotropic $g = 2.0$ in their theoretical model. This treatment is equivalent to the Kambé model, and relies on the Heisenberg Hamiltonian shown in eq 2, from which the relative energies of the spin states can be calculated by using the expression for the eigenvalues (eq. 3), where $J = J_{12} = J_{23}$, $S_{13} = S_1 + S_3$, and $S_T = S_{13} + S_2$.

$$H = J(S_1 \bullet S_2 + S_2 \bullet S_3) + J_{13} S_1 \bullet S_3 \qquad (2)$$

$$E(S_T, S_{13}) = J/2\,[S_T(S_T+1)] - J/2[S_{13}(S_{13}+1)] + J_{13}/2[S_{13}(S_{13}+1)] \qquad (3)$$

Use of eq. 3 with the addition of a Zeeman term, $H_{zeeman} = g\beta B_z M_s$, leads to the simplified diagram for our antiferromagnetically coupled complexes depicted in Figure 15, in which the energies of selected spin state manifolds are plotted against magnetic field. This plot was constructed with $g = 2.0$, J_{13} set to zero and $J = +1$ cm^{-1}, values close to those obtained from the above fits (Table 12). As can be seen in Figure 15, the small J value brings the low-lying excited states $|S_T, S_{13}\rangle = |1, 3\rangle$ and $|3, 4\rangle$ within 5 cm^{-1} of the $|2, 4\rangle$ ground state in zero field, and the Zeeman interaction causes the $|S_T, S_{13}, M_s\rangle = |4, 4, -4\rangle$ state to cross the ground state $|2, 4, -2\rangle$ at a field close to 20 kOe. With such a small J value, antiferromagnetic exchange coupling cannot compete with the applied field and, just below 100 kOe, the fully *ferromagnetic* state $|S_T, S_{13}, M_s\rangle = |6, 4,$

-6> becomes the new ground state. These spin-state crossovers at high field result in the new ground states becoming selectively populated, and readily account for the increase in $M/N\mu_B$ above the value predicted for an antiferromagnetic, $S_T = 2$ ground state.

This picture is an extreme simplification of the true energy level diagram for our compounds, even when only considering $B = B_z$, since zfs effects have been neglected. Zero-field splitting removes the degeneracy of the single ion spin states so that the spin-coupled levels cannot be represented by the "pure" states shown in Fig. 15. In particular, inclusion of rhombic zfs ($E \neq 0$) terms would extensively mix the states. The qualitative picture represented by Fig. 15 remains valid for compounds **1** and **3 - 6**, in which the Zeeman effect can cause state crossover(s) at sufficiently high field. The state mixing caused by the significant zero-field splitting of each Fe(II) ion is probably the cause of the absence of sharp "steps" in the high field magnetization data for **5** and **6**, in contrast to the trimanganese system.[61]

EPR Studies. Given the recent interest in integer-spin EPR signals for the diiron(II) reduced forms of MMOH,[7-9,11] R2,[12] and deoxyHrN$_3$,[6,10,11] we wondered whether a similar feature might arise in our trinuclear ferrous systems, which also have integer-spin ground states. The X-band (9.43 GHz) EPR spectra for compounds **1**, **3**, and **4** ($S_{total} = 6$ ground state) at 4 K are displayed in Figure 16. These spectra were recorded on solid crystalline samples, diminishing the possibility of a signal arising from lower nucelarity ferrous species that may be present in solution if the trinuclear unit were to dissociate. All three complexes show a broad feature at very low field, and for compounds **1** and **4** the trough of the signal is centered at ≈ 50 mT, while for **3** the trough is closer to 70 mT. These spectra at least qualitatively bear a strong resemblance to those observed for the diiron(II) forms of the proteins and model complexes discussed above.

Extraction of specific magnetic parameters from these EPR spectra was not possible, but use of the analytical procedures described in the Experimental Section allowed for investigation into their origin. Parameters derived from the magnetic measurements were used to determine possible EPR transitions. For example, use of J = -5.0 cm^{-1}, $D(Fe_{1,3})$ = 6.0 cm^{-1}, and $D(Fe_2)$ = 5.0, and all g values = 2.00[62] resulted in EPR-allowed transitions (with $B_1 \perp B_0$; the transitions are with B_0 perpendicular to the zfs axis, B_x) from the ground (state 1) to the first excited (state 2) state. This transition is highly field-dependent; it occurs at g_{obs} = $\Delta E/\beta B$ = 90 for B = 40 mT, but at g_{obs} = 60 for B = 60 mT. These calculated EPR-allowed transitions, from states thermally populated at ≈ 4 K, have $\Delta E \approx 1$ cm^{-1}, which is far from resonance with the microwave quantum (0.314 cm^{-1} at 9.43 GHz).

Rhombic zfs terms ($E_i \neq 0$) were not included in the magnetic fits, where their contributions are relatively unimportant, but their effect on EPR transitions, particularly in integer-spin systems, is quite significant.[10,55,59] For example, inclusion of the very small term$E(Fe_{1,3})$ = 0.06 cm^{-1} (i.e., $|E/D| = 0.01$), leads to 1 $\rightarrow$ 2 transitions at g_{obs} = 82 and 56 and 2 $\rightarrow$ 3 transitions at g_{obs} = 21 and 14.5 at B = 40 mT and 60 mT, respectively. The actual situation is far more complex in that, as found for mono- and dinuclear integer-spin systems,[55,59] there is probably a distribution of E values. In an individual molecule, each of the three ferrous sites could have slightly differing E values. These subtle differences can significantly affect the EPR transitions. The above parameters, but with $E(Fe_3)$ = 0.03 cm^{-1}, yields the 2 $\rightarrow$ 3 transition in exact resonance with the microwave quantum $\Delta E \approx 0.3$ cm^{-1}, at g_{obs} = 15.9 and 11.2 at B = 40 and 60 mT, respectively. From these considerations, it is apparent that, as the magnetic field is swept, a variety of EPR transitions from different molecules come into partial resonance, giving rise to the observed broad envelope at low field.

Conclusions.

We have synthesized and crystallographically characterized four new linear, trinuclear ferrous complexes using either of two general and convenient synthetic routes. This series of carboxylate-bridged triiron(II) complexes has allowed us to correlate well-defined structural differences with a shift from ferromagnetic to antiferromagnetic coupling. Both susceptibility and high-field magnetization data were collected for all compounds and fit to a model allowing for zero-field splitting and **g** anisotropy, yielding reliable exchange-coupling constants (J), axial zfs parameters (D), and axial g values for all complexes. In the case of the high-field magnetization experiment, the Kambé model failed to give a good fit of the data, demonstrating the distinct advantages and necessity of the more sophisticated theory used here.

Integer-spin, low-field EPR spectra were observed for the ferromagnetically coupled complexes. These signals are quite similar to those observed for the diiron(II) forms of the proteins MMOH, deoxyHrN$_3$ and R2, and models of their diiron(II) cores, demonstrating that such signals taken alone cannot distinguish between a dinuclear and trinuclear ferrous core. Simple calculations showed that such EPR-allowed signals are expected for these trinuclear systems with $J \leq D \leq 10$ cm^{-1}.

Finally, weak exchange coupling, $|J| \leq 5$ cm^{-1}, occurs between adjacent ferrous ions with mono- and bidentate carboxylate bridges, the sign of J depending upon small perturbations in the geometry at each ferrous site. In particular, it appears that a geometry closer to idealized octahedral symmetry at the terminal ferrous sites favors antiferromagnetic exchange, as also observed for the orbitally symmetric triiron(III) or trimanganese(III) complexes. Significant axial distortion at these sites favors ferromagnetic exchange.

Acknowledgements. We are grateful to Dr. C. Bastos for the preparation of compounds **2a-c**, **5**, and **6** and help in collecting the SQUID data. We thank Professor J. Telser for fitting the SQUID and magnetization data, and EPR calculations. E. McNiff, Jr. of the Francis Bitter National Magnet Laboratory provided his services in collecting the high-field magnetization data, and K. E. Liu assisted in obtaining the EPR spectra. We thank Professor L. Que, Jr. for helpful discussions.

References

(1) Feig, A. L.; Lippard, S. J. *Chem. Rev.* **1994**, *94*, 759-805.

(2) Que, L., Jr.; True, A. E. In *Prog. in Inorg. Chem.*; S. J. Lippard, Ed.; John Wiley and Sons: New York, 1990; Vol. 38; pp 97-200.

(3) Vincent, J. B.; Olivier-Lilley, G. L.; Averill, B. A. *Chem. Rev.* **1990**, *90*, 1447-1467.

(4) Pulver, S.; Froland, W. A.; Fox, B. G.; Lipscomb, J. D.; Solomon, E. I. *J. Am. Chem. Soc.* **1993**, *115*, 12409-12422.

(5) Atta, M.; Scheer, C.; Fries, P. H.; Fontecave, M.; Latour, J.-M. *Angew. Chem. Int. Ed. Engl.* **1992**, *31*, 1513-1515.

(6) Hendrich, M. P.; Pearce, L. L.; Que, L., Jr.; Chasteen, D.; Day, E. P. *J. Am. Chem. Soc.* **1991**, *113*, 3039-3044.

(7) DeWitt, J. G.; Bentsen, J. G.; Rosenzweig, A. C.; Hedman, B.; Green, J.; Pilkington, S.; Papaefthymiou, G. C.; Dalton, H.; Hodgson, K. O.; Lippard, S. J. *J. Am. Chem. Soc.* **1991**, *113*, 9219-9235.

(8) Hendrich, M. P.; Münck, E.; Fox, B. G.; Lipscomb, J. D. *J. Am. Chem. Soc.* **1990**, *112*, 5861-5865.

(9) Fox, B. G.; Surerus, K. K.; Münck, E.; Lipscomb, J. D. *J. Biol. Chem.* **1988**, *263*, 10553-10556.

(10) Reem, R. C.; Solomon, E. I. *J. Am. Chem. Soc.* **1987**, *109*, 1216-1226.

(11) Hoffman, B. M.; Sturgeon, B. E.; Doan, P. E.; DeRose, V. J.; Liu, K. E.; Lippard, S. J. *J. Am. Chem. Soc.* **1994**, *116*, 6023-6024.

(12) Lynch, J. B.; Juarez-Garcia, C.; Münck, E.; Que, L., Jr. *J. Biol. Chem.* **1989**, *264*, 8091-8096.

(13) Elgren, T. E.; Hendrich, M. P.; Que, L., Jr. *J. Am. Chem. Soc.* **1993**, *115*, 9291-9292.

(14) Hartman, J. R.; Rardin, R. L.; Chaudhuri, P.; Pohl, K.; Wieghardt, K.; Nuber, B.; Weiss, J.; Papaefthymiou, G. C.; Frankel, R. B.; Lippard, S. J. *J. Am. Chem. Soc.* **1987**, *109*, 7387-7396.

(15) Abbreviations used: Me_3TACN, 1,4,7-trimethyl-1,4,7-triazacyclononane; tmen, N,N,N',N'-tetramethyl-1,2-diaminoethane; BPMP, the anion of 2,6-bis[[bis(2-pyridylmethyl)amino]methyl]-4-methylphenol; BPCP, the anion of 2,6-bis[[bis(2-pyridylmethyl)amino]methyl]-4-chlorophenol; HPTBP, N,N,N',N'-tetrakis(2-benzimidazolylmethyl)-2-hydroxy-1,3-diamino-propane; H_4Hbab, 1,2-bis(2-hydroxybenzamido)benzene; TLA, tris(6-methyl-2-pyridylmethyl)amine; TMPzA, tris(3,5-dimethyl-1-pyrazolylmethyl)amine; TPA, tris(2-pyridylmethyl)amine.

(16) Hagen, K. S.; Lachicotte, R. *J. Am. Chem. Soc.* **1992**, *114*, 8741-8742.

(17) Ménage, S.; Brennan, B. A.; Juarez-Garcia, C.; Münck, E.; Que, L., Jr. *J. Am. Chem. Soc.* **1990**, *112*, 6423-6425.

(18) Borovik, A. S.; Hendrich, M. P.; Holman, T. R.; Münck, E.; Papaefthymiou, V.; Que, L., Jr. *J. Am. Chem. Soc.* **1990**, *112*, 6031-6038.

(19) Jang, H. G.; Hendrich, M. P.; Que, L., Jr. *Inorg. Chem.* **1993**, *32*, 911-918.

(20) Stassinopoulos, A.; Schulte, G.; Papaefthymiou, G. C.; Caradonna, J. P. *J. Am. Chem. Soc.* **1991**, *113*, 8686-8697.

(21) Zang, Y.; Jang, H. G.; Chiou, Y.-M.; Hendrich, M. P.; Que, L., Jr. *Inorg. Chim. Acta* **1993**, *213*, 41-48.

(22) Snyder, B. S.; Patterson, G. S.; Abrahamson, A. J.; Holm, R. H. *J. Am. Chem. Soc.* **1989**, *111*, 5214-5223.

(23) Hendrich, M. P.; Day, E. P.; Wang, C.-P.; Snyder, B. S.; Holm, R. H.; Münck, E. *Inorg. Chem.* **1994**, *33*, 2848-2856.

(24) Tolman, W. B.; Liu, S.; Bentsen, J. G.; Lippard, S. J. *J. Am. Chem. Soc.* **1991**, *113*, 152-164.

(25) This low-field EPR signal is currently being further investigated. Hendrich, M. P.; Herold, S.; Goldberg, D. P; and Lippard, S. J., unpublished results.

(26) Kurtz, D. M., Jr. *Chem. Rev.* **1990**, *90*, 585-606.

(27) Kambé, K. *J. Phys. Soc. Japan* **1950**, *5*, 48-51.

(28) Sinn, E. *Coord. Chem. Rev.* **1970**, *5*, 313-347.

(29) Rardin, R. L.; Poganiuch, P.; Bino, A.; Goldberg, D. P.; Tolman, W. B.; Liu, S.; Lippard, S. J. *J. Am. Chem. Soc.* **1992**, *114*, 5240-5249.

(30) Lowenthal, R. E.; Abiko, A.; Masamune, S. *Tetrahedron Lett.* **1990**, *31*, 6005-6008.

(31) Goldberg, D. P.; Watton, S. P.; Masschelein, A.; Wimmer, L.; Lippard, S. J. *J. Am. Chem. Soc.* **1993**, *115*, 5346-5347.

(32) *Single Crystal Structure Analysis Software,* Version 1.6, Molecular Structure Corporation: The Woodlands, TX, 1993.

(33) Lawton, S. L. TRACER II, *A Fortran Transformation-Cell Reduction Program*; Mobil Oil Corporation: Paulsboro, NJ, 1967.

(34) North, A. C. T.; Phillips, D. C.; Mathews, F. S. *Acta Crystallogr.* **1968**, *A24*, 351-359.

(35) Sheldrick, G. M. *SHELXS86. Program for crystal structure determination*; University of of Göttingen: Göttingen, 1986.

(36) Cromer, D. T.; Waber, J. T. In *International Tables for X-ray Crystallography* Kynoch Press: Birmingham, 1974; Vol. 4; pp 71-98.

(37) Stewart, R. F.; Davidson, E. R.; Simpson, W. T. *J. Chem. Phys.* **1965**, *42*, 3175-3187.

(38) Ibers, J. A.; Hamilton, W. C. *Acta Cryst.* **1964**, *17*, 781-782.

(39) Creagh, D. C.; McAuley, W. J. In *International Tables for X-ray Crystallography* Kluwer Academic Publishers: Dordrecht, 1992; Vol. C.; pp 219-222.

(40) O'Connor, C. J. *Prog. Inorg. Chem.* **1982**, *29*, 203-283.

(41) Carlin, R. L. *Magnetochemistry;* Springer-Verlag: New York, 1986.

(42) Program #66, Quantum Chemistry Program Exchange, Indiana University, Bloomington, IN 47401.

(43) Drago, R. S. *Physical Methods for Chemists;* 2nd ed.; Saunders: Orlando, 1992, p 473-483.

(44) Griffith, J. S. *Struct. and Bond. (Berlin)* **1972**, *10*, 87-126.

(45) Weltner, W., Jr. *Magnetic Atoms and Molecules;* Dover: New York, 1989, p 304-312.

(46) Boyd, P. D. W.; Martin, R. L. *J. Chem. Soc., Dalton Trans.* **1979**, 92-95.

(47) Abragam, A.; Bleaney, B. *Electron Paramagnetic Resonance of Transition Ions;* Dover: New York, 1986, p 443-446.

(48) Reetz, M. T.; Westermann, J. *J. Org. Chem.* **1983**, *48*, 254-255.

(49) Reetz, M. T.; Westermann, J.; Steinbach, R. *J. Chem. Soc. Chem. Commun.* **1981**, 237-239.

(50) Christou, G. *Acc. Chem. Res.* **1989**, *22*, 328-335.

(51) Edema, J. J. H.; Gambarotta, S.; Hao, S.; Bensimon, C. *Inorg. Chem.* **1991**, *30*, 2584-2586.

(52) Rardin, R. L.; Tolman, W. B.; Lippard, S. J. *New. J. of Chem.* **1991**, *15*, 417-430.

(53) Charron, F. F., Jr.; Reiff, W. M. *Inorg. Chem.* **1986**, *25*, 2786-2790.

(54) Sessoli, R.; Tsai, H.-L.; Schake, A. R.; Wang, S.; Vincent, J. B.; Folting, K.; Gatteschi, D.; Christou, G.; Hendrickson, D. N. *J. Am. Chem. Soc.* **1993**, *115*, 1804-1816.

(55) Hendrich, M. P.; Debrunner, P. G. *Biophys. J.* **1989**, *56*, 489-506.

(56) Tinkham, M. *Proc. Roy. Soc. London* **1956**, *A236*, 535-548.

(57) Rubins, R. S. *Proc. Phys. Soc.* **1962**, *80*, 244-247.

(58) See ref. 55. These workers also determined $E = \pm 3$ and -1 cm^{-1}, based on EPR and magnetic susceptibility, respectively.

(59) Hendrich, M. P.; Debrunner, P. G. *J. Magn. Reson.* **1988**, *78*, 133-141.

(60) Tinkham, M. *Proc. Roy. Soc. London* **1958**, *A245*, 156-174.

(61) Ménage, S.; Vitols, S. E.; Bergerat, P.; Codjovi, E.; Kahn, O.; Girerd, J.-J.; Guillot, M.; Solans, X.; Calvet, T. *Inorg. Chem.* **1991**, *30*, 2666-2671.

(62) The actual g values deviate from 2.00, but this effect is minor relative to zfs contributions at these low magnetic fields, for example, a 10% increase of g to 2.2 changes g_{obs} by < 1%.

Table 1. Crystallographic Data for Complexes **3** - **6.**

Compound	**3**	**4**	**5**	**6**
chemical formula	$Fe_3C_{44}H_{58}N_8O_{16}$	$Fe_3C_{68}H_{98}N_{12}O_{14}$	$Fe_3C_{68}H_{74}N_4O_{16}$	$Fe_3C_{92}H_{122}N_4O_{14}$
formula weight	1122.53	1475.14	1370.89	1675.54
space group	$P\bar{1}$	$P2_1/n$	$P2_12_12_1$	$P2_1/n$
a (Å)	8.985(2)	12.809(5)	14.677(3)	10.111(1)
b (Å)	9.148(1)	22.214(5)	19.289(4)	31.389(2)
c (Å)	15.761(2)	13.793(5)	23.066(6)	14.243(2)
α (deg)	80.73(1)			
β (deg)	81.28(1)	91.19(2)		100.76(5)
γ (deg)	101.91(1)			
V (Å^3)	1228.0(4)	3924(2)	6530(4)	4441(1)
Z	1	2	4	2
ρ calcd g cm^{-3}	1.518	1.248	1.394	1.253
μ, cm^{-1}	9.51	6.10	7.25	5.46
range of 2θ	3-51	3-50	3-49.9	3-45
octants collected	$+h \pm k \pm l$	$+h +k \pm l$	$+h +k +l$	$+h +k \pm l$
Trans. coeff.	0.952 - 1.000	0.953 - 1.000	0.789 - 1.000	0.960 - 1.000

Table 1 contd. Crystallographic Data for Complexes **3 - 6.**

Compound	**3**	**4**	**5**	**6**
no. of unique data	4548	7318	6218	7093
Data with $F_o^2 > 3\sigma(F_o^2)$	3061	4871	3681	5312
R_{merge} (%)	4.1	2.0	4.7	3.8
no. of variables	323	393	480	511
$R\ (F_o)^a$	0.046	0.055	0.059	0.047
$R_w\ (F_o)^b$	0.056	0.076	0.065	0.063
goodness of fit	1.30	2.09	1.43	1.83
λ (Å)	0.71069	0.71069	0.71069	0.71069
t (C)	-78	-81	-80	-72

$^aR = \Sigma|\,|F_o| - |F_c|\,|/\Sigma|F_o|$; $^bR_w = [(\Sigma w(|F_o| - |F_c|/\Sigma w|F_o|^2]^{1/2}$; $w = 1/\sigma^2(F_o)$

Table 2. Selected Positional Parameters and B(eq) for $[Fe_3(OAc)_6(BIPhOH)_2] \cdot 2\,MeOH$ (**3**).[a]

atom	x	y	z	B(eq)[b]
Fe(1)	1.13464(8)	0.14942(7)	1.16609(4)	1.56(3)
Fe(2)	1.000	0	1.000	1.46(4)
O(1)	1.0304(4)	-0.0540(3)	1.1364(2)	1.9(2)
O(2)	0.9981(4)	-0.1709(4)	1.2737(2)	2.5(2)
O(3)	0.8710(4)	0.1561(4)	1.0334(2)	2.1(2)
O(4)	0.9494(4)	0.2460(4)	1.1486(2)	2.6(2)
O(5)	1.2198(4)	0.1674(4)	0.9636(2)	2.3(2)
O(6)	1.2800(4)	0.3020(4)	1.0652(2)	2.4(2)
O(7)	1.3493(4)	-0.0188(4)	1.4127(2)	2.0(2)
N(1)	1.1284(5)	0.1980(4)	1.2923(2)	1.7(2)
N(2)	1.1373(5)	0.1801(4)	1.4325(2)	1.9(2)
N(3)	1.3276(4)	0.0565(4)	1.1921(2)	1.7(2)
N(4)	1.5349(4)	0.0079(4)	1.2393(2)	1.8(2)
C(1)	1.0122(5)	-0.1757(5)	1.1950(3)	1.9(2)
C(2)	1.0112(7)	-0.3220(6)	1.1637(3)	3.0(3)
C(3)	0.8741(6)	0.2425(5)	1.0874(3)	2.0(2)
C(4)	0.7711(7)	0.3520(6)	1.0773(4)	2.9(3)
C(5)	1.3052(5)	0.2708(5)	0.9900(3)	1.8(2)
C(6)	1.4538(6)	0.3601(5)	0.9289(3)	2.2(2)
C(7)	1.3580(5)	0.1066(5)	1.3442(3)	1.4(2)
C(8)	1.4826(5)	0.2440(5)	1.3526(3)	1.6(2)
C(9)	1.5171(6)	0.3768(6)	1.2893(30)	2.0(2)
C(10)	1.6271(7)	0.5037(6)	1.2947(4)	2.8(3)

Table 2 contd. Selected Positional Parameters and B(eq) for $[Fe_3(OAc)_6(BIPhOH)_2] \cdot 2$ MeOH (**3**).[a]

atom	x	y	z	B(eq)[b]
C(11)	1.7029(6)	0.4994(6)	1.3658(4)	2.6(3)
C(12)	1.6684(6)	0.3685(6)	1.4293(3)	2.5(3)
C(13)	1.5586(6)	0.2408(6)	1.4227(3)	2.1(2)
C(14)	1.2048(5)	0.1570(5)	1.3543(3)	1.6(2)
C(15)	1.0082(5)	0.2506(6)	1.3334(3)	2.0(2)
C(16)	1.0135(6)	0.2395(6)	1.4187(3)	2.3(2)
C(17)	1.1852(6)	0.1601(6)	1.5174(3)	2.7(3)
C(18)	1.4026(5)	0.0593(5)	1.2574(3)	1.5(2)
C(19)	1.4118(6)	0.0004(5)	1.1297(3)	2.0(2)
C(20)	1.5389(6)	-0.0300(5)	1.1581(3)	2.2(2)
C(21)	1.6491(6)	-0.0144(6)	1.2939(4)	2.8(3)

[a]For atom-labelling scheme, see Figure 3. Estimated standard deviations in the least significant figure are given in parentheses.
[b]$B(\text{eq}) = 8/3\pi^2(U_{11}(aa^*)^2 + U_{22}(bb^*)^2 + U_{33}(cc^*)^2 + 2U_{12}aa^*bb^*\cos\gamma + 2U_{13}aa^*cc^*\cos\beta + 2U_{23}bb^*cc^*\cos\alpha)$

Table 3. Selected Positional Parameters and B(eq) for $[Fe_3(OAc)_6(BIDPhEH)_2]\cdot 4\ CH_3CN$.[a]

atom	x	y	z	B(eq)[b]
Fe(1)	0.03270(5)	0.96255(3)	0.22878(4)	2.51(3)
Fe(2)	0	1.0000	0	2.32(4)
O(1)	-0.2178(3)	0.7294(1)	0.6702(2)	3.1(1)
O(2)	0.0978(2)	0.9459(1)	0.0973(2)	2.4(1)
O(3)	0.2120(3)	0.8838(2)	0.1656(2)	3.5(2)
O(4)	-0.1394(3)	0.9832(2)	0.0860(2)	3.5(2)
O(5)	-0.1168(3)	0.9926(2)	0.2447(2)	3.7(2)
O(6)	0.0864(3)	1.0530(1)	0.2254(2)	3.7(2)
O(7)	0.0396(3)	1.0757(1)	0.0742(2)	3.2(1)
N(1)	0.0832(3)	0.9496(2)	0.3708(2)	2.3(1)
N(2)	0.1052(3)	0.9190(2)	0.5212(2)	2.5(2)
N(3)	-0.0188(3)	0.8716(2)	0.2355(3)	2.7(2)
N(4)	-0.0405(3)	0.7759(2)	0.2698(3)	2.7(2)
C(1)	0.0552(3)	0.8365(2)	0.4001(3)	2.2(2)
C(2)	0.1653(3)	0.8071(2)	0.3902(3)	2.9(2)
C(3)	-0.0131(3)	0.8067(2)	0.4759(3)	2.2(2)
C(4)	0.0197(3)	0.7600(2)	0.5341(3)	2.5(2)
C(5)	-0.0447(4)	0.7333(2)	0.6029(3)	2.6(2)
C(6)	-0.1483(3)	0.7539(2)	0.6063(3)	2.4(2)
C(7)	-0.1853(3)	0.8022(2)	0.5486(3)	2.2(2)
C(8)	-0.1152(3)	0.8278(2)	0.4850(3)	2.2(2)

Table 3 contd. Selected Positional Parameters and B(eq) for $[Fe_3(OAc)_6(BIDPhEH)_2] \cdot 4\,CH_3CN$.[a]

atom	x	y	z	B(eq)[b]
C(9)	0.0031(4)	0.6829(2)	0.6688(4)	3.3(2)
C(10)	0.1213(5)	0.6853(3)	0.6725(6)	7.5(4)
C(11)	-0.0296(5)	0.6221(2)	0.6287(4)	4.6(3)
C(12)	-0.0327(7)	0.6871(3)	0.7732(4)	7.9(4)
C(13)	-0.2972(4)	0.8259(2)	0.5531(3)	2.9(2)
C(14)	-0.3759(4)	0.7760(3)	0.5255(4)	4.2(3)
C(15)	-0.3199(4)	0.8494(2)	0.6556(4)	3.9(2)
C(16)	-0.3165(4)	0.8782(2)	0.4828(4)	3.4(2)
C(17)	0.0767(3)	0.9017(2)	0.4295(3)	2.1(2)
C(18)	0.1156(4)	0.9975(2)	0.4276(3)	2.6(2)
C(19)	0.1291(4)	0.9792(2)	0.5196(3)	2.8(2)
C(20)	0.1119(5)	0.8844(2)	0.6119(3)	3.8(2)
C(21)	-0.0014(3)	0.8298(2)	0.3029(3)	2.3(2)
C(22)	-0.0703(4)	0.8443(2)	0.1588(3)	3.2(2)
C(23)	-0.0838(4)	0.7858(2)	0.1795(3)	3.2(2)
C(24)	-0.0448(5)	0.7168(2)	0.3170(4)	4.0(3)
C(25)	0.1677(4)	0.9042(2)	0.0924(3)	2.6(2)
C(26)	0.1945(5)	0.8821(2)	-0.0071(4)	4.2(3)
C(27)	-0.1739(4)	0.9898(2)	0.1694(4)	3.0(2)
C(28)	-0.2892(5)	0.9957(3)	0.1831(5)	5.8(4)
C(29)	0.0698(4)	1.0891(2)	0.1576(3)	3.0(2)
C(30)	0.0835(6)	1.1553(2)	0.1770(4)	6.0(3)

[a]For atom-labelling scheme, see Figure 4. Estimated standard deviations in the least significant figure are given in parentheses.
[b]$B(\text{eq}) = 8/3\pi^2(U_{11}(aa^*)^2 + U_{22}(bb^*)^2 + U_{33}(cc^*)^2 + 2U_{12}aa^*bb^*\cos\gamma + 2U_{13}aa^*cc^*\cos\beta + 2U_{23}bb^*cc^*\cos\alpha)$

Table 4. Selected Positional Parameters and B(eq) for $[Fe_3(OBz)_6(^iPrOx)_2]$ (**5**).[a]

atom	x	y	z	B(eq)[b]
Fe(1)	0.8966(1)	0.16944(8)	0.44753(7)	1.71(8)
Fe(2)	0.8854(1)	-0.00369(9)	0.49971(8)	1.60(7)
Fe(3)	0.8998(1)	-0.18409(8)	0.54584(8)	1.85(8)
O(1)	0.9816(7)	0.3520(5)	0.3568(4)	3.3(5)
O(2)	0.6939(6)	0.3262(5)	0.4082(4)	3.0(5)
O(3)	0.7880(6)	-0.3844(4)	0.4895(4)	2.8(4)
O(4)	0.9833(6)	-0.3780(4)	0.6205(4)	2.4(4)
O(5)	0.8531(6)	0.1049(4)	0.5234(4)	2.1(4)
O(6)	0.8993(6)	0.2126(4)	0.5355(3)	2.1(4)
O(7)	1.0059(6)	0.0187(4)	0.4543(4)	2.2(4)
O(8)	1.0300(5)	0.1336(4)	0.4615(4)	2.3(4)
O(9)	0.7955(6)	0.0123(4)	0.4298(4)	2.1(4)
O(10)	0.8535(6)	0.1056(4)	0.3842(4)	2.0(4)
O(11)	0.9063(5)	-0.1122(4)	0.4728(3)	1.9(4)
O(12)	0.9984(6)	-0.2027(4)	0.4710(4)	2.5(4)
O(13)	0.9657(6)	-0.0127(5)	0.5731(4)	2.6(4)
O(14)	0.9940(6)	-0.1244(4)	0.5934(4)	2.3(4)
O(15)	0.7707(6)	-0.0383(4)	0.5462(4)	2.3(4)
O(16)	0.7803(6)	-0.1481(4)	0.5795(4)	2.4(4)
N(1)	0.9567(7)	0.2462(5)	0.3931(4)	1.8(5)
N(2)	0.7705(7)	0.2305(5)	0.4325(4)	1.6(5)
N(3)	0.8144(7)	-0.2702(5)	0.5038(5)	2.2(5)
N(4)	0.9488(8)	-0.2669(5)	0.5998(4)	2.2(5)

Table 4 contd. Selected Positional Parameters and *B*(eq) for $[Fe_3(OBz)_6(^iPrOx)_2]$ (**5**).[a]

atom	*x*	*y*	*z*	*B*(eq)[b]
C(1)	0.855(1)	0.3411(7)	0.4199(6)	3.1(3)
C(2)	0.935(1)	0.3090(7)	0.3898(6)	2.3(3)
C(3)	1.055(1)	0.3099(7)	0.3318(6)	3.0(3)
C(4)	1.039(1)	0.2378(7)	0.3550(6)	2.7(3)
C(5)	1.021(1)	0.1816(7)	0.3099(6)	3.0(3)
C(6)	0.944(1)	0.2010(8)	0.2694(6)	3.3(3)
C(7)	1.110(1)	0.1674(8)	0.2769(7)	4.6(4)
C(8)	0.773(1)	0.2944(7)	0.4222(6)	2.4(3)
C(9)	0.623(1)	0.2753(7)	0.4170(6)	3.1(3)
C(10)	0.675(1)	0.2064(7)	0.4207(5)	2.2(3)
C(11)	0.640(1)	0.1550(6)	0.4665(5)	2.3(3)
C(12)	0.544(1)	0.1315(8)	0.4503(7)	3.9(3)
C(13)	0.642(1)	0.1853(7)	0.5278(6)	3.1(3)
C(14)	0.9383(9)	-0.3551(6)	0.5222(5)	2.0(2)
C(15)	0.8449(9)	-0.3314(6)	0.5035(5)	1.8(2)
C(16)	0.698(1)	-0.3532(7)	0.4825(6)	2.9(3)
C(17)	0.717(1)	-0.2749(6)	0.4839(5)	2.4(3)
C(18)	0.703(1)	-0.2382(6)	0.4257(5)	2.1(2)
C(19)	0.770(1)	-0.2632(7)	0.3794(6)	3.2(3)
C(20)	0.697(1)	-0.1605(8)	0.4304(6)	3.7(3)
C(21)	0.9565(8)	-0.3286(6)	0.5822(5)	1.7(2)
C(22)	0.997(1)	-0.3410(7)	0.6763(6)	3.0(3)
C(23)	0.975(1)	-0.2659(7)	0.6617(6)	2.4(3)

Table 4 contd. Selected Positional Parameters and B(eq) for $[Fe_3(OBz)_6(^iPrOx)_2]$ (**5**).[a]

atom	x	y	z	B(eq)[b]
C(24)	0.902(1)	-0.2311(7)	0.6999(6)	3.2(3)
C(25)	0.810(1)	-0.2676(8)	0.6952(7)	4.6(4)
C(26)	0.932(1)	-0.2271(9)	0.7621(7)	4.9(4)
C(27)	0.8670(9)	0.1564(6)	0.5563(6)	2.1(2)
C(28)	0.8407(8)	0.1545(6)	0.6192(5)	1.7(2)
C(29)	0.854(1)	0.2122(7)	0.6549(6)	2.8(3)
C(30)	0.823(1)	0.2108(7)	0.7118(6)	3.3(3)
C(31)	0.779(1)	0.1526(7)	0.7316(6)	3.2(3)
C(32)	0.764(1)	0.0953(7)	0.6979(7)	3.5(3)
C(33)	0.796(1)	0.0947(7)	0.6412(6)	2.7(3)
C(34)	1.055(1)	0.0711(6)	0.4520(6)	2.1(2)
C(35)	1.1525(8)	0.0647(6)	0.4343(5)	1.4(2)
C(36)	1.215(1)	0.1174(7)	0.4394(6)	2.6(3)
C(37)	1.304(1)	0.1077(7)	0.4201(6)	3.1(3)
C(38)	1.330(1)	0.0454(8)	0.3975(7)	3.9(3)
C(39)	1.272(1)	-0.0072(8)	0.3929(7)	3.8(3)
C(40)	1.181(1)	0.0004(7)	0.4100(6)	2.7(3)
C(41)	0.8009(9)	0.0543(6)	0.3877(5)	1.6(2)
C(42)	0.733(1)	0.0450(6)	0.3384(6)	2.1(2)
C(43)	0.651(1)	0.0113(7)	0.3484(6)	3.0(3)
C(44)	0.588(1)	0.0093(7)	0.3023(6)	3.4(3)
C(45)	0.611(1)	0.0378(8)	0.2494(7)	4.3(3)
C(46)	0.693(1)	0.0686(8)	0.2394(7)	3.8(3)

Table 4 contd. Selected Positional Parameters and B(eq) for $[Fe_3(OBz)_6(^iPrOx)_2]$ (**5**).[a]

atom	x	y	z	B(eq)[b]
C(47)	0.752(1)	0.0733(7)	0.2855(6)	3.1(3)
C(48)	0.9671(9)	-0.1499(6)	0.4453(6)	2.2(2)
C(49)	0.994(1)	-0.1293(7)	0.3857(6)	2.6(3)
C(50)	0.942(1)	-0.0837(7)	0.3553(6)	3.0(3)
C(51)	0.969(1)	-0.0606(8)	0.3014(7)	3.7(3)
C(52)	1.047(1)	-0.0852(8)	0.2769(7)	4.0(3)
C(53)	1.100(1)	-0.1324(7)	0.3075(6)	3.5(3)
C(54)	1.074(1)	-0.1563(7)	0.3622(6)	2.5(3)
C(55)	1.0058(9)	-0.0588(6)	0.5989(5)	1.7(2)
C(56)	1.0772(8)	-0.0374(6)	0.6440(5)	1.5(2)
C(57)	1.103(1)	0.0304(7)	0.6475(7)	3.9(3)
C(58)	1.169(1)	0.0505(8)	0.6887(7)	4.5(4)
C(59)	1.206(1)	0.003(1)	0.7256(7)	4.4(4)
C(60)	1.181(1)	-0.0651(9)	0.7211(7)	4.3(4)
C(61)	1.118(1)	-0.0858(7)	0.6791(6)	3.3(3)
C(62)	0.741(1)	-0.0914(6)	0.5711(5)	2.2(3)
C(63)	0.640(1)	-0.0870(6)	0.5880(6)	2.2(2)
C(64)	0.594(1)	-0.0262(8)	0.5835(7)	4.4(4)
C(65)	0.501(1)	-0.0230(8)	0.6006(7)	4.4(4)
C(66)	0.459(1)	-0.0815(8)	0.6204(7)	4.0(3)
C(67)	0.506(1)	-0.1404(7)	0.6267(6)	3.1(3)
C(68)	0.596(1)	-0.1450(6)	0.6105(5)	2.4(2)

[a]For atom-labelling scheme, see Figure 5. Estimated standard deviations in the least significant figure are given in parentheses.
[b]$B(\text{eq}) = 8/3\pi^2(U_{11}(aa^*)^2 + U_{22}(bb^*)^2 + U_{33}(cc^*)^2 + 2U_{12}aa^*bb^*\cos\gamma + 2U_{13}aa^*cc^*\cos\beta + 2U_{23}bb^*cc^*\cos\alpha)$

Table 5. Selected Positional Parameters and B(eq) for $[Fe_3(OBz)_6(PheMe_3Eda)_2]$ (**6**).[a]

atom	x	y	z	B(eq)[b]
Fe(1)	0.19954(6)	0.09627(2)	1.00536(4)	1.62(3)
Fe(2)	0	0	1.0000	1.64(4)
O(1)	0.1835(3)	0.10434(9)	1.1592(2)	2.0(1)
O(2)	0.1521(3)	0.0416(1)	1.0906(2)	1.9(1)
O(3)	0.1165(3)	0.0021(1)	0.8937(2)	2.4(1)
O(4)	0.2099(4)	0.0665(1)	0.8809(2)	2.7(1)
O(5)	-0.0015(3)	0.1137(1)	0.9734(2)	2.2(1)
O(6)	-0.1160(3)	0.0528(1)	0.9398(2)	2.4(1)
O(7)	0.1711(3)	0.1803(1)	0.2502(2)	2.0(1)
N(1)	0.4273(4)	0.0902(1)	1.0527(3)	2.4(2)
N(2)	0.2590(4)	0.1625(1)	0.9713(3)	1.8(1)
C(1)	0.4826(5)	0.1280(2)	1.0121(4)	2.8(2)
C(2)	0.4002(5)	0.1672(2)	1.0219(4)	2.7(2)
C(3)	0.4757(6)	0.0904(2)	1.1564(4)	4.4(3)
C(4)	0.4810(6)	0.0513(2)	1.0133(5)	4.8(3)
C(5)	0.1757(5)	0.1956(2)	1.0070(3)	2.5(2)
C(6)	0.2557(5)	0.1695(1)	0.8675(3)	2.1(2)
C(7)	0.1181(5)	0.1674(1)	0.8022(3)	2.2(2)
C(8)	0.1422(5)	0.1722(2)	0.6989(3)	2.2(2)
C(9)	0.0186(5)	0.1742(1)	0.6183(3)	1.9(2)
C(10)	-0.0634(6)	0.1337(2)	0.6195(4)	3.6(3)
C(11)	-0.0701(6)	0.2128(2)	0.6341(3)	3.5(2)
C(12)	0.0616(5)	0.1785(1)	0.5202(3)	1.7(2)

Table 5 contd. Selected Positional Parameters and B(eq) for $[Fe_3(OBz)_6(PheMe_3Eda)_2]$ (**6**).[a]

atom	x	y	z	B(eq)[b]
C(13)	0.1960(5)	0.1806(1)	0.5104(3)	2.0(2)
C(14)	0.2362(4)	0.1822(1)	0.4224(3)	1.7(2)
C(15)	0.1344(5)	0.1814(1)	0.3402(3)	1.7(2)
C(16)	-0.0026(4)	0.1828(1)	0.3461(3)	1.7(2)
C(17)	-0.0346(5)	0.1809(1)	0.4364(3)	1.9(2)
C(18)	0.3872(5)	0.1823(2)	0.4163(3)	2.1(2)
C(19)	0.4763(5)	0.1879(2)	0.5143(4)	3.7(3)
C(20)	0.4242(5)	0.1398(2)	0.3770(4)	3.3(2)
C(21)	0.4192(5)	0.2188(2)	0.3536(4)	3.2(2)
C(22)	-0.1151(5)	0.1856(1)	0.2557(3)	2.0(2)
C(23)	-0.0915(5)	0.2252(2)	0.1974(4)	2.9(2)
C(24)	-0.2547(5)	0.1905(2)	0.2813(4)	3.1(2)
C(25)	-0.1181(5)	0.1460(2)	0.1937(4)	2.8(2)
C(26)	0.1593(4)	0.0644(1)	1.1647(3)	1.7(2)
C(27)	0.1470(5)	0.0447(1)	1.2576(3)	1.9(2)
C(28)	0.1364(6)	0.0698(2)	1.3358(3)	2.7(2)
C(29)	0.1275(6)	0.0502(2)	1.4229(4)	3.8(3)
C(30)	0.1321(6)	0.0065(2)	1.4304(4)	4.0(3)
C(31)	0.1442(6)	-0.0178(2)	1.3537(4)	3.9(3)
C(32)	0.1526(5)	0.0004(1)	1.2658(4)	2.6(2)
C(33)	0.1857(5)	0.0275(2)	0.8559(3)	2.2(2)
C(34)	0.2465(5)	0.0118(1)	0.7740(3)	2.2(2)
C(35)	0.2129(5)	-0.0280(2)	0.7351(3)	2.7(2)

Table 5 contd. Selected Positional Parameters and B(eq) for $[Fe_3(OBz)_6(PheMe_3Eda)_2]$ (**6**).[a]

atom	x	y	z	B(eq)[b]
C(36)	0.2742(6)	-0.0442(2)	0.6652(4)	3.4(2)
C(37)	0.3722(7)	-0.0219(2)	0.6324(4)	4.4(3)
C(38)	0.4070(9)	0.0176(3)	0.6702(5)	7.0(4)
C(39)	0.3428(8)	0.0347(2)	0.7400(5)	5.7(4)
C(40)	-0.1038(5)	0.0924(1)	0.9372(3)	1.8(2)
C(41)	-0.2198(5)	0.1181(1)	0.8833(3)	1.9(2)
C(42)	-0.3188(5)	0.0986(1)	0.8148(4)	2.4(2)
C(43)	-0.4155(5)	0.1229(2)	0.7585(4)	2.9(2)
C(44)	-0.4222(5)	0.1664(2)	0.7742(4)	3.2(2)
C(45)	-0.3296(5)	0.1855(2)	0.8448(4)	3.3(2)
C(46)	-0.2275(5)	0.1613(2)	0.8983(4)	2.4(2)

[a]For atom-labelling scheme, see Figure 6. Estimated standard deviations in the least significant figure are given in parentheses.
[b]$B(\text{eq}) = 8/3\pi^2(U_{11}(aa^*)^2 + U_{22}(bb^*)^2 + U_{33}(cc^*)^2 + 2U_{12}aa^*bb^*\cos\gamma + 2U_{13}aa^*cc^*\cos\beta + 2U_{23}bb^*cc^*\cos\alpha)$

Table 6. Selected Bond Lengths (Å) and Angles (deg) for $[Fe_3(OAc)_6(BIPhOH)_2] \cdot 2$ MeOH (**3**).[a]

(a) Distances

Fe(1)-Fe(2)	3.4081(6)	Fe(1)-N(3)	2.147(4)
Fe(1)-O(1)	2.063(3)	Fe(2)-O(1)	2.198(3)
Fe(1)-O(4)	2.072(3)	Fe(2)-O(3)	2.045(3)
Fe(1)-O(6)	2.021(3)	Fe(2)-O(5)	2.168(3)1
Fe(1)-N(1)	2.103(4)		

(b) Angles

Fe(1)-O(1)-Fe(2)	106.2(1)	O(4)-Fe(1)-N(3)	176.0(1)
O(6)-Fe(1)-O(1)	115.6(1)	N(1)-Fe(1)-N(3)	84.3(1)
O(6)-Fe(1)-O(4)	92.8(1)	O(3)-Fe(2)-O(5)	93.0(1)
O(6)-Fe(1)-N(1)	117.7(1)	O(3)-Fe(2)-O(5)'	87.0(1)
O(6)-Fe(1)-N(3)	88.3(1)	O(3)-Fe(2)-O(1)	89.2(1)
O(1)-Fe(1)-O(4)	93.4(1)	O(3)-Fe(2)-O(1)'	90.8(1)
O(1)-Fe(1)-N(1)	126.0(1)	O(5)-Fe(2)-O(1)	91.7(1)
O(1)-Fe(1)-N(3)	89.6(1)	O(5)-Fe(2)-O(1)'	88.3(1)
O(4)-Fe(1)-N(1)	91.8(1)		

[a]For atom-labelling scheme, see Figure 3. Estimated standard deviations in the least significant figure are given in parentheses.

Table 7. Selected Bond Lengths (Å) and Angles (deg) for $[Fe_3(OAc)_6(BIDPhEH)_2] \cdot 4\ CH_3CN$ (**4**).[a]

(a) Distances

Fe(1)-Fe(2)	3.282(1)	Fe(1)-N(3)	2.128(4)
Fe(1)-O(2)	2.045(3)	Fe(2)-O(2)	2.178(3)
Fe(1)-O(5)	2.043(4)	Fe(2)-O(4)	2.196(3)
Fe(1)-O(6)	2.126(3)	Fe(2)-O(7)	2.028(3)
Fe(1)-N(1)	2.070(4)		

(b) Angles

Fe(1)-O(1)-Fe(2)	101.9(1)	O(6)-Fe(1)-N(3)	178.5(1)
O(2)-Fe(1)-O(5)	123.7(1)	N(1)-Fe(1)-N(3)	85.3(1)
O(2)-Fe(1)-O(6)	90.8(1)	O(2)-Fe(2)-O(4)	92.1(1)
O(2)-Fe(1)-N(1)	133.5(1)	O(2)-Fe(2)-O(4)'	87.9(1)
O(2)-Fe(1)-N(3)	90.0(1)	O(2)-Fe(2)-O(7)	90.7(1)
O(5)-Fe(1)-O(6)	89.9(1)	O(2)-Fe(2)-O(7)'	89.3(1)
O(5)-Fe(1)-N(1)	102.6(1)	O(4)-Fe(2)-O(7)	93.8(1)
O(5)-Fe(1)-N(3)	90.8(1)	O(4)-Fe(2)-O(7)'	86.2(1)
O(6)-Fe(1)-N(1)	93.3(1)		

[a]For atom-labelling scheme, see Figure 4. Estimated standard deviations in the least significant figure are given in parentheses.

Table 8. Selected Bond Lengths (Å) and Angles (deg) for $[Fe_3(OBz)_6(^iPrOx)_2]$ (**5**).[a]

(a) Distances

Fe(1)-Fe(2)	3.554(2)	Fe(2)-O(9)	2.106(8)
Fe(2)-Fe(3)	3.645(3)	Fe(2)-O(11)	2.205(8)
Fe(1)-O(5)	2.242(8)	Fe(2)-O(13)	2.070(9)
Fe(1)-O(6)	2.194(8)	Fe(2)-O(15)	2.105(8)
Fe(1)-O(8)	2.100(8)	Fe(3)-O(11)	2.183(8)
Fe(1)-O(10)	2.013(8)	Fe(3)-O(12)	2.282(9)
Fe(1)-N(1)	2.13(1)	Fe(3)-O(14)	2.107(9)
Fe(1)-N(2)	2.22(1)	Fe(3)-O(16)	2.040(9)
Fe(2)-O(5)	2.216(8)	Fe(3)-N(3)	2.29(1)
Fe(2)-O(7)	2.099(9)	Fe(3)-N(4)	2.15(1)

(b) Angles

Fe(1)-O(5)-Fe(2)	105.7(3)	O(6)-Fe(1)-O(10)	155.4(3)
Fe(2)-O(11)-Fe(3)	112.3(3)	O(6)-Fe(1)-N(1)	105.9(3)
O(5)-Fe(1)-O(6)	59.6(3)	O(6)-Fe(1)-N(2)	87.6(3)
O(5)-Fe(1)-O(8)	87.9(3)	O(8)-Fe(1)-O(10)	101.7(3)
O(5)-Fe(1)-O(10)	97.9(3)	O(8)-Fe(1)-N(1)	86.2(4)
O(5)-Fe(1)-N(1)	164.5(3)	O(8)-Fe(1)-N(2)	167.2(3)
O(6)-Fe(1)-N(2)	100.3(3)	O(10)-Fe(1)-N(1)	97.3(4)
O(6)-Fe(1)-O(8)	88.1(3)	O(10)-Fe(1)-N(2)	87.0(3)

Table 8 contd. Selected Bond Lengths (Å) and Angles (deg) for $[Fe_3(OBz)_6(^iPrOx)_2]$ (**5**).

(b) Angles

N(1)-Fe(1)-N(2)	83.3(4)	O(11)-Fe(3)-O(12)	59.2(3)
O(5)-Fe(2)-O(7)	96.3(3)	O(11)-Fe(3)-O(14)	91.5(3)
O(5)-Fe(2)-O(9)	85.2(3)	O(11)-Fe(3)-O(16)	96.7(3)
O(5)-Fe(2)-O(11)	175.2(3)	O(11)-Fe(3)-N(3)	99.1(3)
O(5)-Fe(2)-O(13)	90.0(3)	O(11)-Fe(3)-N(4)	154.7(4)
O(5)-Fe(2)-O(15)	90.1(3)	O(12)-Fe(3)-O(14)	93.6(3)
O(7)-Fe(2)-O(9)	96.6(3)	O(12)-Fe(3)-O(16)	152.6(3)
O(7)-Fe(2)-O(11)	86.5(3)	O(12)-Fe(3)-N(3)	85.0(3)
O(7)-Fe(2)-O(13)	86.9(4)	O(12)-Fe(3)-N(4)	96.2(4)
O(9)-Fe(2)-O(15)	86.3(3)	O(14)-Fe(3)-O(16)	100.4(4)
O(11)-Fe(2)-O(13)	94.1(3)	O(14)-Fe(3)-N(3)	166.7(4)
O(11)-Fe(2)-O(15)	87.3(3)	O(14)-Fe(3)-N(4)	83.4(4)
O(13)-Fe(2)-O(15)	90.7(4)	O(16)-Fe(3)-N(3)	86.4(4)
O(7)-Fe(2)-O(15)	173.2(3)	O(16)-Fe(3)-N(4)	108.7(4)
O(9)-Fe(2)-O(11)	90.6(3)	N(3)-Fe(3)-N(4)	83.7(4)
O(9)-Fe(2)-O(13)	174.3(4)		

[a]For atom-labelling scheme, see Figure 5. Estimated standard deviations in the least significant figure are given in parentheses.

Table 9. Selected Bond Lengths (Å) and Angles (deg) for $[Fe_3(OBz)_6(PheMe_3Eda)_2]$ (**6**).[a]

(a) Distances

Fe(1)-Fe(2)	3.6263(6)	Fe(1)-N(1)	2.284(4)
Fe(1)-O(1)	2.241(3)	Fe(1)-N(2)	2.241(4)
Fe(1)-O(2)	2.206(3)	Fe(2)-O(2)	2.234(3)
Fe(1)-O(4)	2.023(3)	Fe(2)-O(3)	2.086(3)
Fe(1)-O(5)	2.072(3)	Fe(2)-O(6)	2.117(3)

(b) Angles

Fe(1)-O(2)-Fe(2)	109.5(1)	O(4)-Fe(1)-N(1)	90.4(1)
O(1)-Fe(1)-O(2)	59.2(1)	O(4)-Fe(1)-N(2)	100.3(1)
O(1)-Fe(1)-O(4)	159.0(1)	O(5)-Fe(2)-N(1)	168.7(1)
O(1)-Fe(1)-O(5)	86.5(1)	O(5)-Fe(2)-N(2)	90.0(1)
O(1)-Fe(1)-N(1)	88.5(1)	N(1)-Fe(2)-N(2)	81.0(1)
O(1)-Fe(1)-N(2)	100.2(1)	O(2)-Fe(2)-O(3)	88.8(1)
O(2)-Fe(1)-N(4)	100.1(1)	O(2)-Fe(2)-O(3)'	91.2(1)
O(2)-Fe(1)-O(5)	91.2(1)	O(2)-Fe(2)-O(6)	92.6(1)
O(2)-Fe(1)-N(1)	94.8(1)	O(2)-Fe(2)-O(6)'	87.4(1)
O(2)-Fe(1)-N(2)	159.2(1)	O(3)-Fe(2)-O(6)	91.5(1)
O(4)-Fe(1)-O(5)	97.9(1)	O(3)-Fe(2)-O(6)'	88.5(1)

[a]For atom-labelling scheme, see Figure 6. Estimated standard deviations in the least significant figure are given in parentheses.

Table 10. Selected Bond Distances (Å) and Angles (deg) for **1**, **3** - **6**.[a]

complex	Fe-Fe	Fe_t-O_d	Fe_t-O_b	Fe_m-O_b	Fe_t-N_{ave}[b]	N_p-Fe-O_b	Fe_t-O_b-Fe_m
1	3.3251(9)	3.005(4)	2.027(3)	2.151(3)	2.11(2)	124.6(1)	105.4(1)
3	3.4081(6)	3.043(3)	2.063(3)	2.198(3)	2.13(3)	126.0(1)	106.2(1)
4	3.282(1)	3.03(1)	2.045(3)	2.178(3)	2.10(4)	133.5(1)	101.9(1)
5	3.554(2)	2.194(8)	2.242(8)	2.216(8)	2.18(6)	164.5(3)	105.7(3)
	3.645(3)	2.282(9)	2.183(8)	2.205(8)	2.22(10)	166.7(4)	112.3(3)
6	3.6263(6)	2.241(3)	2.206(3)	2.234(3)	2.26(3)	159.2(1)	109.5(1)

[a]See Fig. 2 for definition of atom labels. [b]Values in parantheses are the standard deviations in the averaged metrical parameters.

Table 11. Summary of the Susceptibility Data for Complexes **1, 3 - 6.**

Complex	μ_{eff} (μ_B) at min. T (K)[a]	μ_{eff} (μ_B) at max. T (K)[b]
Calcd for **1, 3, 4**	12.96	8.49
1	12.7	9.03
3	11.7	9.08
4	12.3	9.21
Calcd for **5** and **6**	4.90	8.48
5	6.52	9.52
6	6.74	9.50

[a]The minimum temperatures are 3 - 7 K. [b]The maximum temperatures are 280 - 300 K.

Table 12. Consensus Magnetic Parameters from Magnetic Susceptibility and Magnetization Data Fits.[a]

Complex	J[b]	$\lvert D \rvert$ ($Fe_{1,3}$)	$\lvert D \rvert$ (Fe_2)	$g_\perp$ ($Fe_{1,3}$)	$g_\parallel$ ($Fe_{1,3}$)	$g_\perp$ (Fe_2)	$g_\parallel$ (Fe_2)
1	-4 ± 1	5 ± 5	5 ± 5	2.0 ± 0.1	2.0 ± 0.1	2.0 ± 0.1	2.0 ± 0.1
3[c]	$J_{12} = J_{23} = -2 \pm 2$; $J_{13} = 0.5 \pm 0.5$	6 ± 3	0 ± 5	≈ 2.0	≈ 2.0	≈ 2.0	≈ 2.0
4	-5 ± 1	5 ± 3	10 ± 10	2.0 ± 0.5	2.2 ± 0.2	2.0 ± 0.5	2.2 ± 0.2
5[c]	$+1.0 \pm 0.5$	0 ± 2	10 ± 5	≈ 2.0	≈ 2.0	≈ 2.0	≈ 2.0
6[c]	$+1.0 \pm 0.5$	0 ± 5	10 ± 5	≈ 2.0	≈ 2.0	≈ 2.0	≈ 2.0

[a]Energies are in cm^{-1}. See text for description of fitting procedure. [b]$\mathcal{H} = JS_iS_j$; $J = J_{12} = J_{23}$; $J_{13} = 0$, except as noted otherwise. [c]Significant variability in the g values was obtained for these compounds (see text for details).

Table 13. Intramolecular Bond Distances for $[Fe_3(OAc)_6(BIPhOH)_2]$ ·2 MeOH (**3**).[a]

atom	atom	distance	atom	atom	distance
Fe(2)	O(1)	2.198(3)	N(2)	C(17)	1.462(6)
Fe(2)	O(3)	2.045(3)	N(3)	C(19)	1.378(5)
Fe(2)	O(5)	2.168(3)	N(3)	C(18)	1.314(6)
Fe(1)	O(1)	2.063(3)	N(4)	C(18)	1.373(5)
Fe(1)	O(4)	2.072(3)	N(4)	C(20)	1.377(6)
Fe(1)	O(6)	2.021(3)	N(4)	C(21)	1.461(6)
Fe(1)	N(1)	2.103(4)	C(1)	C(2)	1.499(6)
Fe(1)	N(3)	2.147(4)	C(3)	C(4)	1.504(6)
O(1)	C(1)	1.290(5)	C(5)	C(6)	1.511(6)
O(2)	C(1)	1.237(5)	C(7)	C(8)	1.540(6)
O(3)	C(3)	1.254(5)	C(7)	C(14)	1.533(6)
O(4)	C(3)	1.261(6)	C(7)	C(18)	1.522(6)
O(5)	C(5)	1.257(5)	C(8)	C(9)	1.388(6)
O(6)	C(5)	1.262(5)	C(8)	C(13)	1.383(6)
O(7)	C(7)	1.423(5)	C(9)	C(10)	1.384(7)
O(8)	C(22)	1.437(6)	C(10)	C(11)	1.397(7)
O(8)	H(1)	1.014(3)	C(11)	C(12)	1.378(7)
N(1)	C(14)	1.326(6)	C(19)	C(20)	1.352(7)
N(1)	C(15)	1.385(5)	C(12)	C(13)	1.394(7)
N(2)	C(14)	1.358(5)	C(15)	C(16)	1.341(7)
N(2)	C(16)	1.366(6)			

[a]Distances are in angstroms. For atom-labelling scheme see Figure 3. Estimated standard deviations in the least significant figure are given in parentheses.

Table 14. Intramolecular Bond Angles for $[Fe_3(OAc)_6(BIPhOH)_2] \cdot 2$ MeOH (**3**).[a]

atom	atom	atom	angle	atom	atom	atom	angle
O(6)	Fe(1)	O(1)	115.6(1)	C(5)	O(5)	Fe(2)	142.8(3)
O(6)	Fe(1)	O(4)	92.8(1)	C(5)	O(6)	Fe(1)	120.9(3)
O(6)	Fe(1)	N(1)	117.7(1)	C(14)	N(1)	C(15)	105.7(4)
O(6)	Fe(1)	N(3)	88.3(1)	C(14)	N(1)	Fe(1)	130.7(3)
O(1)	Fe(1)	O(4)	93.4(1)	C(15)	N(1)	Fe(1)	121.8(3)
O(1)	Fe(1)	N(1)	126.0(1)	C(14)	N(2)	C(16)	107.3(4)
O(1)	Fe(1)	N(3)	89.6(1)	C(14)	N(2)	C(17)	130.0(4)
O(4)	Fe(1)	N(1)	91.8(1)	C(16)	N(2)	C(17)	122.6(4)
O(4)	Fe(1)	N(3)	176.0(1)	C(18)	N(3)	C(19)	106.7(4)
N(1)	Fe(1)	N(3)	84.3(1)	C(18)	N(3)	Fe(1)	131.0(3)
O(3)	Fe(2)	O(5)	93.0(1)	C(19)	N(3)	Fe(1)	121.6(3)
O(3)	Fe(2)	O(5)'	87.0(1)	C(18)	N(4)	C(20)	106.6(4)
O(3)	Fe(2)	O(1)	89.2(1)	C(18)	N(4)	C(21)	129.5(4)
O(3)	Fe(2)	O(1)'	90.8(1)	C(20)	N(4)	C(21)	123.8(4)
O(5)	Fe(2)	O(1)	91.7(1)	O(2)	C(1)	O(1)	121.1(4)
O(5)	Fe(2)	O(1)'	88.3(1)	O(2)	C(1)	C(2)	121.5(4)
C(1)	O(1)	Fe(1)	116.8(3)	O(1)	C(1)	C(2)	117.4(4)
O(6)	C(5)	C(6)	117.0(4)	O(3)	C(3)	O(4)	125.0(4)
O(7)	C(7)	C(18)	107.9(3)	O(3)	C(3)	C(4)	117.4(4)
O(7)	C(7)	C(14)	109.9(3)	O(4)	C(3)	C(4)	117.6(4)
O(7)	C(7)	C(8)	109.3(3)	O(5)	C(5)	O(6)	125.0(4)
C(18)	C(7)	C(14)	114.0(3)	O(5)	C(5)	C(6)	117.9(4)
C(18)	C(7)	C(8)	109.7(3)	C(11)	C(12)	C(13)	120.3(4)

[a]Angles are in degrees. Estimated standard deviations in the least significant figure are given in parentheses.

Table 14 Contd. Intramolecular Bond Angles for $[Fe_3(OAc)_6(BIPhOH)_2] \cdot 2\,MeOH$ (**3**).[a]

atom	atom	atom	angle	atom	atom	atom	angle
C(14)	C(7)	C(8)	106.0(3)	C(8)	C(13)	C(12)	120.5(4)
C(13)	C(8)	C(9)	118.8(4)	N(1)	C(14)	N(2)	110.4(4)
C(13)	C(8)	C(7)	122.0(4)	N(1)	C(14)	C(7)	128.3(4)
C(9)	C(8)	C(7)	119.1(4)	N(2)	C(14)	C(7)	121.0(4)
C(10)	C(9)	C(8)	121.2(4)	C(16)	C(15)	N(1)	109.5(4)
C(9)	C(10)	C(11)	119.5(5)	C(15)	C(16)	N(2)	107.0(4)
C(12)	C(11)	C(10)	119.7(5)	N(3)	C(18)	N(4)	110.5(4)
C(1)	O(1)	Fe(2)	136.7(3)	N(3)	C(18)	C(7)	128.5(4)
Fe(1)	O(1)	Fe(2)	106.2(1)	N(4)	C(18)	C(7)	121.0(4)
C(3)	O(3)	Fe(2)	139.3(3)	C(20)	C(19)	N(3)	109.4(4)
C(3)	O(4)	Fe(1)	128.1(3)	C(19)	C(20)	N(4)	106.8(4)

[a]Angles are in degrees. Estimated standard deviations in the least significant figure are given in parentheses.

Table 15. Positional Parameters and $B(eq)^a$ for $[Fe_3(OAc)_6(BIPhOH)_2] \cdot 2\,MeOH$ (**3**).

atom	x	y	z	$B(eq)$
Fe(2)	1.000	0	1.000	1.46(4)
Fe(1)	1.13464(8)	0.14942(7)	1.16609(4)	1.56(3)
O(1)	1.0304(4)	-0.0541(3)	1.1364(2)	1.9(2)
O(2)	0.9981(4)	-0.1709(4)	1.2737(2)	2.5(2)
O(3)	0.8710(4)	0.1561(4)	1.0334(2)	2.1(2)
O(4)	0.9494(4)	0.2460(4)	1.1486(2)	2.6(2)
O(5)	1.2198(4)	0.1674(4)	0.9636(2)	2.3(2)
O(6)	1.2800(4)	0.3020(4)	1.0652(2)	2.4(2)
O(7)	1.3493(4)	-0.0188(4)	1.4127(2)	2.0(2)
O(8)	1.1785(4)	-0.2731(4)	1.3783(2)	2.6(2)
N(1)	1.1284(5)	0.1980(4)	1.2923(2)	1.7(2)
N(2)	1.1373(5)	0.1801(4)	1.4325(2)	1.9(2)
N(3)	1.3276(4)	0.0565(4)	1.1921(2)	1.7(2)
N(4)	1.5349(4)	0.0079(4)	1.2393(2)	1.8(2)
C(1)	1.0122(5)	-0.1757(5)	1.1950(3)	1.9(2)
C(2)	1.0112(7)	-0.3220(6)	1.1637(3)	3.0(3)
C(3)	0.8741(6)	0.2425(5)	1.0874(3)	2.0(2)
C(4)	0.7711(7)	0.3520(6)	1.0773(4)	2.9(3)
C(5)	1.3052(5)	0.2708(5)	0.9900(3)	1.8(2)
C(6)	1.4538(6)	0.3601(5)	0.9289(3)	2.2(2)
C(7)	1.3580(5)	0.1066(5)	1.3442(3)	1.4(2)
C(8)	1.4826(5)	0.2440(5)	1.3526(3)	1.6(2)
C(9)	1.5171(6)	0.3768(6)	1.2893(3)	2.0(2)
C(10)	1.6271(7)	0.5037(6)	1.2947(4)	2.8(3)

$^aB(eq) = 8/3\pi^2(U_{11}(aa^*)^2 + U_{22}(bb^*)^2 + U_{33}(cc^*)^2 + 2U_{12}aa^*bb^*\cos\gamma + 2U_{13}aa^*cc^*\cos\beta + 2U_{23}bb^*cc^*\cos\alpha)$

Table 15 contd. Positional Parameters and $B(eq)^a$ for $[Fe_3(OAc)_6(BIPhOH)_2]\cdot 2$ MeOH (**3**).

atom	x	y	z	B(eq)
C(11)	1.7029(6)	0.4994(6)	1.3658(4)	2.6(3)
C(12)	1.6684(6)	0.3685(6)	1.4293(3)	2.5(3)
C(13)	1.5586(6)	0.2408(6)	1.4227(3)	2.1(2)
C(14)	1.2048(5)	0.1570(5)	1.3543(3)	1.6(2)
C(15)	1.0082(5)	0.2506(6)	1.3334(3)	2.0(2)
C(16)	1.0135(6)	0.2395(6)	1.4187(3)	2.3(2)
C(17)	1.1852(6)	0.1601(6)	1.5174(3)	2.7(3)
C(18)	1.4026(5)	0.0593(5)	1.2574(3)	1.5(2)
C(19)	1.4118(6)	0.0004(5)	1.1297(3)	2.0(2)
C(20)	1.5389(6)	-0.0300(5)	1.1581(3)	2.2(2)
C(21)	1.6491(6)	-0.0144(6)	1.2939(4)	2.8(3)
C(22)	1.2731(7)	-0.3571(6)	1.3338(4)	3.5(3)
H(1)	1.135	-0.223	1.329	8(2)
H(2)	0.915	-0.393	1.189	3.6
H(3)	1.024	-0.303	1.102	3.6
H(4)	1.094	-0.362	1.181	3.6
H(5)	0.777	0.411	1.122	3.4
H(6)	0.804	0.417	1.021	3.4
H(7)	0.667	0.296	1.083	3.4
H(8)	1.540	0.344	0.954	2.7
H(9)	1.460	0.328	0.875	2.7
H(10)	1.455	0.466	0.920	2.7
H(11)	1.464	0.381	1.241	2.5
H(12)	1.651	0.593	1.250	3.4

$^aB(eq) = 8/3\pi^2(U_{11}(aa^*)^2 + U_{22}(bb^*)^2 + U_{33}(cc^*)^2 + 2U_{12}aa^*bb^*\cos\gamma + 2U_{13}aa^*cc^*\cos\beta + 2U_{23}bb^*cc^*\cos\alpha)$

Table 15 contd. Positional Parameters and B (eq)[a] for[$Fe_3(OAc)_6(BIPhOH)_2$]· 2 MeOH (**3**).

atom	x	y	z	B(eq)
H(13)	1.778	0.586	1.370	3.2
H(14)	1.720	0.365	1.478	3.0
H(15)	1.536	0.151	1.467	2.5
H(16)	0.933	0.289	1.305	2.4
H(17)	0.944	0.268	1.461	2.7
H(18)	1.103	0.094	1.560	3.3
H(19)	1.273	0.117	1.513	3.3
H(20)	1.211	0.256	1.534	3.3
H(21)	1.385	-0.015	1.075	2.4
H(22)	1.616	-0.070	1.128	2.6
H(23)	1.648	-0.120	1.307	3.3
H(24)	1.749	0.042	1.263	3.3
H(25)	1.624	0.020	1.347	3.3
H(26)	1.321	-0.410	1.374	4.1
H(27)	1.210	-0.428	1.308	4.1
H(28)	1.351	-0.288	1.289	4.1

[a] $B(\text{eq}) = 8/3\pi^2(U_{11}(aa^*)^2 + U_{22}(bb^*)^2 + U_{33}(cc^*)^2 + 2U_{12}aa^*bb^*\cos\gamma + 2U_{13}aa^*cc^*\cos\beta + 2U_{23}bb^*cc^*\cos\alpha)$

Table. 16. U values for $[Fe_3(OAc)_6(BIPhOH)_2]\cdot$ 2MeOH (**3**).[a]

atom	U11	U22	U33	U12	U13	U23
Fe(1)	0.0221(4)	0.0224(3)	0.0170(3)	0.0061(3)	-0.0057(3)	-0.0073(3)
Fe(2)	0.0161(5)	0.0221(5)	0.0193(5)	0.0054(4)	-0.0038(4)	-0.0090(4)
O(1)	0.030(2)	0.022(2)	0.023(2)	0.005(1)	-0.010(1)	-0.006(1)
O(2)	0.036(2)	0.034(2)	0.023(2)	0.008(2)	-0.003(2)	-0.006(1)
O(3)	0.026(2)	0.033(2)	0.024(2)	0.012(2)	-0.007(1)	-0.012(1)
O(4)	0.035(2)	0.043(2)	0.034(2)	0.024(2)	-0.018(2)	-0.019(2)
O(5)	0.022(2)	0.027(2)	0.039(2)	0.001(1)	-0.004(2)	-0.014(2)
O(6)	0.043(2)	0.025(2)	0.020(2)	0.002(2)	-0.002(2)	-0.003(1)
O(7)	0.032(2)	0.025(2)	0.017(2)	0.008(2)	-0.006(1)	0.001(1)
O(8)	0.039(2)	0.034(2)	0.027(2)	0.010(2)	-0.005(2)	-0.007(2)
N(1)	0.022(2)	0.026(2)	0.019(2)	0.008(2)	-0.004(2)	-0.010(2)
N(2)	0.025(2)	0.033(2)	0.014(2)	0.007(2)	-0.002(2)	-0.009(2)
N(3)	0.021(2)	0.028(2)	0.018(2)	0.008(2)	-0.002(2)	-0.007(2)
N(4)	0.019(2)	0.025(2)	0.026(2)	0.007(2)	-0.003(2)	-0.007(2)
C(1)	0.019(3)	0.026(2)	0.026(3)	0.001(2)	-0.003(2)	-0.008(2)
C(2)	0.055(4)	0.022(3)	0.032(3)	0.004(3)	-0.008(3)	-0.001(2)
C(3)	0.023(3)	0.025(2)	0.025(2)	0.005(2)	-0.001(2)	-0.004(2)
C(4)	0.041(3)	0.041(3)	0.041(3)	0.024(3)	-0.016(3)	-0.020(3)
C(5)	0.019(3)	0.026(2)	0.025(2)	0.012(2)	-0.005(2)	-0.004(2)
C(6)	0.026(3)	0.030(3)	0.027(3)	0.001(2)	-0.006(2)	-0.008(2)
C(7)	0.018(2)	0.022(2)	0.013(2)	0.007(2)	-0.003(2)	-0.002(2)
C(8)	0.018(2)	0.023(2)	0.020(2)	0.006(2)	0.000(2)	-0.008(2)

Table. 16 contd. U values for $[Fe_3(OAc)_6(BIPhOH)_2]\cdot 2MeOH$ (**3**).[a]

atom	U11	U22	U33	U12	U13	U23
C(9)	0.026(3)	0.030(3)	0.022(2)	0.007(2)	-0.008(2)	-0.005(2)
C(10)	0.036(3)	0.029(3)	0.038(3)	0.001(2)	-0.007(2)	-0.007(2)
C(11)	0.022(3)	0.033(3)	0.045(3)	0.000(2)	-0.003(2)	-0.018(2)
C(12)	0.026(3)	0.044(3)	0.033(3)	0.008(2)	-0.014(2)	-0.018(2)
C(13)	0.023(3)	0.033(3)	0.023(2)	0.005(2)	-0.005(2)	-0.005(2)
C(14)	0.021(2)	0.023(2)	0.017(2)	0.002(2)	-0.000(2)	-0.008(2)
C(15)	0.019(3)	0.033(3)	0.031(3)	0.012(2)	-0.005(2)	-0.015(2)
C(16)	0.021(3)	0.036(3)	0.032(3)	0.010(2)	-0.000(2)	-0.014(2)
C(17)	0.033(3)	0.054(3)	0.018(2)	0.009(3)	-0.003(2)	-0.014(2)
C(18)	0.018(2)	0.020(2)	0.019(2)	0.004(2)	-0.001(2)	-0.006(2)
C(19)	0.026(3)	0.031(3)	0.019(2)	0.009(2)	-0.001(2)	-0.010(2)
C(20)	0.029(3)	0.023(2)	0.031(3)	0.007(2)	0.002(2)	-0.014(2)
C(21)	0.022(3)	0.043(3)	0.047(3)	0.015(2)	-0.013(2)	-0.017(3)
C(22)	0.053(4)	0.037(3)	0.041(3)	0.008(3)	-0.002(3)	-0.017(3)

[a]Estimated standard deviations in the least significant figure are given in parentheses. The anisotropic temperature factors are of the form $\exp[-2\pi^2(U_{11}h^2a^{*2}... + 2U_{12}hka^*b^* + ...)]$.

Table 17. Intramolecular Bond Distances for $[Fe_3(OAc)_6(BIDPhEH)_2]\cdot 4\,CH_3CN$ (**4**).[a]

atom	atom	distance	atom	atom	distance
Fe(1)	O(2)	2.045(3)	C(13)	C(16)	1.529(7)
Fe(1)	O(5)	2.043(4)	C(27)	C(28)	1.499(7)
Fe(1)	O(6)	2.126(3)	C(29)	C(30)	1.503(7)
Fe(1)	N(1)	2.070(4)	C(18)	C(19)	1.339(6)
Fe(1)	N(3)	2.128(4)	C(31)	C(32)	1.38(1)
Fe(2)	O(2)	2.178(3)	C(33)	C(34)	1.39(2)
Fe(2)	O(4)	2.196(4)	C(33)	C(35)	1.37(2)
Fe(2)	O(7)	2.028(3)	N(4)	C(21)	1.373(6)
O(1)	C(6)	1.377(5)	N(4)	C(23)	1.371(6)
O(1)	H(43)	1.045	N(4)	C(24)	1.466(6)
O(2)	C(25)	1.292(5)	N(5)	C(32)	1.28(1)
O(4)	C(27)	1.250(6)	N(6)	C(34)	1.14(2)
O(5)	C(27)	1.260(6)	N(7)	C(35)	1.15(2)
O(6)	C(29)	1.247(5)	C(1)	C(2)	1.562(6)
O(7)	C(29)	1.242(5)	C(1)	C(3)	1.529(6)
N(1)	C(17)	1.340(5)	C(1)	C(17)	1.529(6)
N(1)	C(18)	1.381(5)	C(1)	C(21)	1.518(6)
N(2)	C(17)	1.364(5)	O(3)	C(25)	1.234(5)
N(2)	C(19)	1.373(6)	C(3)	C(4)	1.373(6)
N(2)	C(20)	1.470(5)	C(3)	C(8)	1.398(6)
N(3)	C(21)	1.330(5)	C(4)	C(5)	1.400(6)
N(3)	C(22)	1.375(6)	C(5)	C(6)	1.406(6)
C(9)	C(10)	1.515(8)	C(5)	C(9)	1.559(6)
C(9)	C(11)	1.515(7)	C(6)	C(7)	1.413(6)
C(9)	C(12)	1.523(8)	C(7)	C(8)	1.390(6)
C(22)	C(23)	1.342(7)	C(7)	C(13)	1.530(6)
C(13)	C(14)	1.540(7)	C(25)	C(26)	1.503(6)
C(13)	C(15)	1.540(6)			

[a]Distances are in angstroms. For atom-labelling scheme see Figure 4. Estimated standard deviations in the least significant figure are given in parentheses.

Table 18. Intramolecular Bond Angles for $[Fe_3(OAc)_6(BIDPhEH)_2] \cdot 4\,CH_3CN$ (**4**).[a]

atom	atom	atom	angle	atom	atom	atom	angle
O(2)	Fe(1)	O(5)	123.7(1)	Fe(2)	O(7)	C(29)	137.4(3)
O(2)	Fe(1)	O(6)	90.8(1)	Fe(1)	N(1)	C(17)	131.3(3)
O(2)	Fe(1)	N(1)	133.5(1)	Fe(1)	N(1)	C(18)	121.0(3)
O(2)	Fe(1)	N(3)	90.0(1)	C(17)	N(1)	C(18)	106.8(4)
O(5)	Fe(1)	O(6)	89.9(1)	C(17)	N(2)	C(19)	108.3(3)
O(5)	Fe(1)	N(1)	102.6(1)	C(17)	N(2)	C(20)	130.6(4)
O(5)	Fe(1)	N(3)	90.8(1)	C(19)	N(2)	C(20)	121.0(4)
O(6)	Fe(1)	N(1)	93.3(1)	Fe(1)	N(3)	C(21)	130.3(3)
O(6)	Fe(1)	N(3)	178.5(1)	Fe(1)	N(3)	C(22)	121.9(3)
N(1)	Fe(1)	N(3)	85.3(1)	C(21)	N(3)	C(22)	107.5(4)
O(2)	Fe(2)	O(4)	92.1(1)	C(21)	N(4)	C(23)	107.4(4)
O(2)	Fe(2)	O(4)'	87.9(1)	C(21)	N(4)	C(24)	130.5(4)
O(2)	Fe(2)	O(7)	90.7(1)	C(23)	N(4)	C(24)	122.0(4)
O(2)	Fe(2)	O(7)'	89.3(1)	C(2)	C(1)	C(3)	114.2(3)
O(4)	Fe(2)	O(7)	93.8(1)	C(2)	C(1)	C(17)	105.2(3)
O(4)	Fe(2)	O(7)'	86.2(1)	C(2)	C(1)	C(21)	107.3(3)
Fe(1)	O(2)	Fe(2)	101.9(1)	C(3)	C(1)	C(17)	109.4(3)
Fe(1)	O(2)	C(25)	118.1(3)	C(3)	C(1)	C(21)	107.0(3)
Fe(2)	O(2)	C(25)	139.0(3)	C(1)	C(3)	C(4)	123.7(4)
Fe(2)	O(4)	C(27)	141.7(3)	C(1)	C(3)	C(8)	117.8(4)
C(6)	O(1)	H(43)	103.68	C(4)	C(3)	C(8)	118.5(4)
Fe(1)	O(5)	C(27)	115.2(3)	C(3)	C(4)	C(5)	122.6(4)
Fe(1)	O(6)	C(29)	125.0(3)	C(4)	C(5)	C(6)	117.1(4)

[a]Angles are in degrees. Estimated standard deviations in the least significant figure are given in parentheses.

Table 18 contd. Intramolecular Bond Angles for $[Fe_3(OAc)_6(BIDPhEH)_2] \cdot 4\ CH_3CN$ (**4**).[a]

atom	atom	atom	angle	atom	atom	atom	angle
C(4)	C(5)	C(9)	117.9(4)	C(5)	C(9)	C(12)	112.6(4)
C(6)	C(5)	C(9)	125.0(4)	C(15)	C(13)	C(16)	107.1(4)
O(1)	C(6)	C(5)	121.1(4)	C(17)	C(1)	C(21)	114.1(3)
O(1)	C(6)	C(7)	116.6(4)	C(10)	C(9)	C(11)	108.2(5)
C(5)	C(6)	C(7)	122.2(4)	C(10)	C(9)	C(12)	106.7(6)
C(6)	C(7)	C(8)	117.0(4)	C(11)	C(9)	C(12)	108.2(5)
N(1)	C(17)	N(2)	108.6(4)	C(7)	C(13)	C(14)	110.6(4)
N(1)	C(17)	C(1)	127.2(4)	C(7)	C(13)	C(15)	110.4(4)
N(2)	C(17)	C(1)	123.8(4)	C(7)	C(13)	C(16)	112.0(4)
N(1)	C(18)	C(19)	109.6(4)	C(14)	C(13)	C(15)	109.6(4)
N(2)	C(19)	C(18)	106.7(4)	C(14)	C(13)	C(16)	107.1(4)
O(4)	C(27)	O(5)	123.6(5)	N(3)	C(21)	N(4)	108.8(4)
O(4)	C(27)	C(28)	119.7(5)	N(3)	C(21)	C(1)	128.2(4)
O(5)	C(27)	C(28)	116.7(5)	N(4)	C(21)	C(1)	123.0(4)
O(6)	C(29)	O(7)	125.8(4)	N(3)	C(22)	C(23)	109.0(4)
O(6)	C(29)	C(30)	118.5(4)	N(4)	C(23)	C(22)	107.3(4)
O(7)	C(29)	C(30)	115.6(4)	O(2)	C(25)	O(3)	121.9(4)
C(6)	C(7)	C(13)	122.8(4)	O(2)	C(25)	C(26)	117.0(4)
C(8)	C(7)	C(13)	120.2(4)	O(3)	C(25)	C(26)	121.1(4)
C(3)	C(8)	C(7)	122.4(4)	N(5)	C(32)	C(31)	170(1)
C(5)	C(9)	C(10)	112.0(4)	N(6)	C(34)	C(33)	178(2)
C(5)	C(9)	C(11)	109.0(4)	N(7)	C(35)	C(33)	177(1)

[a]Angles are in degrees. Estimated standard deviations in the least significant figure are given in parentheses.

Table 19. Positional parameters and $B(eq)^a$ for $[Fe_3(OAc)_6(BIDPhEH)_2] \cdot 4\,CH_3CN$.

atom	x	y	z	$B(eq)$
Fe(1)	0.03270(5)	0.96255(3)	0.22878(4)	2.51(3)
Fe(2)	0	1.0000	0	2.32(4)
O(1)	-0.2178(3)	0.7294(1)	0.6702(2)	3.1(1)
O(2)	0.0978(2)	0.9459(1)	0.0973(2)	2.4(1)
O(3)	0.2120(3)	0.8838(2)	0.1656(2)	3.5(2)
O(4)	-0.1394(3)	0.9832(2)	0.0860(2)	3.5(2)
O(5)	-0.1168(3)	0.9926(2)	0.2447(2)	3.7(2)
O(6)	0.0864(3)	1.0530(1)	0.2254(2)	3.7(2)
O(7)	0.0396(3)	1.0757(1)	0.0742(2)	3.2(1)
N(1)	0.0832(3)	0.9496(2)	0.3708(2)	2.3(2)
N(2)	0.1052(3)	0.9190(2)	0.5212(2)	2.5(2)
N(3)	-0.0188(3)	0.8716(2)	0.2355(3)	2.7(2)
N(4)	-0.0405(3)	0.7759(2)	0.2698(3)	2.7(2)
N(5)	0.622(1)	0.1097(6)	0.445(1)	15.9(4)
N(6)	0.328(1)	0.1423(7)	0.071(1)	8.6(4)
N(7)	0.493(2)	0.076(1)	0.121(1)	13.6(6)
C(1)	0.0552(3)	0.8365(2)	0.4001(3)	2.2(2)
C(2)	0.1653(3)	0.8071(2)	0.3902(3)	2.9(2)
C(3)	-0.0131(3)	0.8067(2)	0.4759(3)	2.2(2)
C(4)	0.0197(3)	0.7600(2)	0.5341(3)	2.5(2)
C(5)	-0.0447(4)	0.7333(2)	0.6029(3)	2.6(2)
C(6)	-0.1483(3)	0.7539(2)	0.6063(3)	2.4(2)
C(7)	-0.1853(3)	0.8022(2)	0.5486(3)	2.2(2)
C(8)	-0.1152(3)	0.8278(2)	0.4850(3)	2.2(2)

$^aB(eq) = 8/3\pi^2(U_{11}(aa^*)^2 + U_{22}(bb^*)^2 + U_{33}(cc^*)^2 + 2U_{12}aa^*bb^*\cos\gamma + 2U_{13}aa^*cc^*\cos\beta + 2U_{23}bb^*cc^*\cos\alpha)$

Table 19 contd. Positional parameters and $B(eq)^a$ for $[Fe_3(OAc)_6(BIDPhEH)_2]$ · 4 CH_3CN (**4**).

atom	*x*	*y*	*z*	*B*(eq)
C(9)	0.0031(4)	0.6829(2)	0.6688(4)	3.3(2)
C(10)	0.1213(5)	0.6853(3)	0.6725(6)	7.5(4)
C(11)	-0.0296(5)	0.6221(2)	0.6287(4)	4.6(3)
C(12)	-0.0328(7)	0.6871(3)	0.7732(4)	7.9(4)
C(13)	-0.2972(4)	0.8259(2)	0.5531(3)	2.9(2)
C(14)	-0.3759(4)	0.7760(3)	0.5255(4)	4.2(3)
C(15)	-0.3199(4)	0.8494(2)	0.6556(4)	3.9(2)
C(16)	-0.3165(4)	0.8782(2)	0.4828(4)	3.4(2)
C(17)	0.0767(3)	0.9017(2)	0.4295(3)	2.1(2)
C(18)	0.1156(4)	0.9975(2)	0.4276(3)	2.6(2)
C(19)	0.1291(4)	0.9792(2)	0.5196(3)	2.8(2)
C(20)	0.1119(5)	0.8844(2)	0.6119(3)	3.8(2)
C(21)	-0.0014(3)	0.8298(2)	0.3029(3)	2.3(2)
C(22)	-0.0703(4)	0.8443(2)	0.1588(3)	3.2(2)
C(23)	-0.0838(4)	0.7858(2)	0.1795(3)	3.2(2)
C(24)	-0.0448(5)	0.7168(2)	0.3170(4)	4.0(3)
C(25)	0.1677(4)	0.9042(2)	0.0924(3)	2.6(2)
C(26)	0.1945(5)	0.8821(2)	-0.0071(4)	4.2(3)
C(27)	-0.1739(4)	0.9898(2)	0.1694(4)	3.0(2)
C(28)	-0.2892(5)	0.9957(3)	0.1831(5)	5.8(4)
C(29)	0.0698(4)	1.0891(2)	0.1576(3)	3.0(2)
C(30)	0.0835(6)	1.1553(2)	0.1770(4)	6.0(3)
C(31)	0.622(1)	0.0450(6)	0.607(1)	13.2(4)
C(32)	0.6167(9)	0.0751(5)	0.5190(9)	10.8(3)

$^aB(eq) = 8/3\pi^2(U_{11}(aa^*)^2 + U_{22}(bb^*)^2 + U_{33}(cc^*)^2 + 2U_{12}aa^*bb^*\cos\gamma + 2U_{13}aa^*cc^*\cos\beta + 2U_{23}bb^*cc^*\cos\alpha)$

Table 19 contd. Positional parameters and $B(eq)^a$ for $[Fe_3(OAc)_6(BIDPhEH)_2] \cdot 4\,CH_3CN$ (**4**).

atom	*x*	*y*	*z*	*B*(eq)
C(33)	0.3132(7)	0.0314(4)	0.1078(6)	7.6(2)
C(34)	0.322(1)	0.0924(7)	0.089(1)	5.7(3)
C(35)	0.411(1)	0.0550(7)	0.117(1)	6.2(3)
H(1)	0.1574	0.7661	0.3720	3.5
H(2)	0.2031	0.8279	0.3420	3.5
H(3)	0.2022	0.8095	0.4505	3.5
H(4)	0.0887	0.7451	0.5276	3.0
H(5)	-0.1376	0.8610	0.4462	2.6
H(6)	0.1475	0.6528	0.7105	9.0
H(7)	0.1472	0.6823	0.6086	9.0
H(8)	0.1435	0.7223	0.7006	9.0
H(9)	-0.1036	0.6199	0.6254	5.5
H(10)	-0.0024	0.6172	0.5656	5.5
H(11)	-0.0032	0.5912	0.6700	5.5
H(12)	-0.0090	0.7239	0.8010	9.5
H(13)	-0.1068	0.6857	0.7742	9.5
H(14)	-0.0048	0.6543	0.8094	9.5
H(15)	-0.4449	0.7910	0.5308	5.0
H(16)	-0.3648	0.7635	0.4606	5.0
H(17)	-0.3664	0.7427	0.5679	5.0
H(18)	-0.2745	0.8820	0.6707	4.6
H(19)	-0.3903	0.8626	0.6579	4.6
H(20)	-0.3089	0.8179	0.7014	4.6
H(21)	-0.2713	0.9106	0.4996	4.1

$^aB(eq) = 8/3\pi^2(U_{11}(aa^*)^2 + U_{22}(bb^*)^2 + U_{33}(cc^*)^2 + 2U_{12}aa^*bb^*\cos\gamma + 2U_{13}aa^*cc^*\cos\beta + 2U_{23}bb^*cc^*\cos\alpha)$

Table 19 contd. Positional parameters and $B(eq)^a$ for $[Fe_3(OAc)_6(BIDPhEH)_2] \cdot 4\,CH_3CN$ (**4**).

atom	*x*	*y*	*z*	*B*(eq)
H(22)	-0.3030	0.8653	0.4186	4.1
H(23)	-0.3870	0.8910	0.4867	4.1
H(24)	0.1267	1.0373	0.4050	3.1
H(25)	0.1510	1.0033	0.5732	3.3
H(26)	0.0662	0.9014	0.6579	4.6
H(27)	0.0922	0.8438	0.5995	4.6
H(28)	0.1815	0.8855	0.6369	4.6
H(29)	-0.0928	0.8638	0.1007	3.9
H(30)	-0.1172	0.7567	0.1390	3.8
H(31)	-0.1156	0.7055	0.3248	4.8
H(32)	-0.0108	0.6879	0.2780	4.8
H(33)	-0.0107	0.7189	0.3787	4.8
H(34)	0.1812	0.8402	-0.0114	5.1
H(35)	0.1531	0.9028	-0.0543	5.1
H(36)	0.2663	0.8896	-0.0183	5.1
H(37)	-0.3038	1.0334	0.2123	6.9
H(38)	-0.3244	0.9933	0.1219	6.9
H(39)	-0.3126	0.9642	0.2238	6.9
H(40)	0.1065	1.1611	0.2422	7.2
H(41)	0.1340	1.1712	0.1345	7.2
H(42)	0.0188	1.1754	0.1665	7.2
H(43)	-0.2211	0.6840	0.6505	4.0
H(44)	0.5947	0.0699	0.6561	15.8
H(45)	0.5822	0.0090	0.6022	15.8
H(46)	0.6927	0.0354	0.6222	15.8

$^aB(eq) = 8/3\pi^2(U_{11}(aa^*)^2 + U_{22}(bb^*)^2 + U_{33}(cc^*)^2 + 2U_{12}aa^*bb^*\cos\gamma + 2U_{13}aa^*cc^*\cos\beta + 2U_{23}bb^*cc^*\cos\alpha)$

Table 20. U values for $[Fe_3(OAc)_6(BIDPhEH)_2] \cdot 4\ CH_3CN$ (**4**).[a]

atom	U11	U22	U33	U12	U13	U23
Fe(1)	0.0466(4)	0.0256(4)	0.0234(3)	-0.0002(3)	0.0014(3)	0.0018(3)
Fe(2)	0.0441(5)	0.0213(5)	0.0227(4)	0.0009(4)	-0.0046(4)	-0.0004(3)
O(1)	0.052(2)	0.036(2)	0.032(2)	-0.013(2)	0.015(2)	0.001(1)
O(2)	0.037(2)	0.024(2)	0.029(2)	0.005(1)	0.001(1)	0.003(1)
O(3)	0.048(2)	0.047(2)	0.037(2)	0.022(2)	0.003(2)	0.003(2)
O(4)	0.055(2)	0.041(2)	0.039(2)	-0.003(2)	0.004(2)	0.002(2)
O(5)	0.053(2)	0.049(2)	0.038(2)	0.012(2)	-0.007(2)	-0.010(2)
O(6)	0.082(3)	0.029(2)	0.030(2)	-0.010(2)	-0.010(2)	0.004(1)
O(7)	0.065(2)	0.025(2)	0.030(2)	-0.003(2)	-0.012(2)	-0.004(1)
N(1)	0.034(2)	0.025(2)	0.027(2)	-0.002(2)	0.005(2)	-0.001(1)
N(2)	0.042(2)	0.031(2)	0.023(2)	0.002(2)	0.004(2)	0.004(2)
N(3)	0.039(2)	0.028(2)	0.034(2)	-0.003(2)	0.003(2)	0.001(2)
N(4)	0.045(2)	0.026(2)	0.034(2)	-0.002(2)	0.008(2)	-0.000(2)
C(1)	0.035(2)	0.023(2)	0.027(2)	0.005(2)	0.007(2)	0.004(2)
C(2)	0.033(3)	0.034(3)	0.043(3)	0.004(2)	0.011(2)	0.001(2)
C(3)	0.034(2)	0.024(2)	0.025(2)	-0.002(2)	0.004(2)	0.001(2)
C(4)	0.033(3)	0.027(2)	0.035(2)	0.000(2)	-0.000(2)	0.002(2)
C(5)	0.043(3)	0.025(2)	0.032(2)	-0.006(2)	-0.003(2)	0.005(2)
C(6)	0.040(3)	0.028(2)	0.023(2)	-0.010(2)	0.003(2)	-0.003(2)
C(7)	0.033(2)	0.029(2)	0.023(2)	-0.008(2)	0.002(2)	-0.003(2)
C(8)	0.033(2)	0.026(2)	0.024(2)	0.001(2)	-0.000(2)	0.005(2)
C(9)	0.046(3)	0.035(3)	0.046(3)	-0.007(2)	-0.006(2)	0.019(2)
C(10)	0.053(4)	0.101(6)	0.128(6)	-0.024(4)	-0.041(4)	0.083(5)
C(11)	0.063(4)	0.033(3)	0.079(4)	0.006(3)	-0.010(3)	0.006(3)

[a]Estimated standard deviations in the least significant figure are given in parentheses. The anisotropic temperature factors are of the form $\exp[-2\pi^2(U_{11}h^2a^{*2}... + 2U_{12}hka^*b^* + ...)]$.

Table 20 contd. U values for $[Fe_3(OAc)_6(BIDPhEH)_2] \cdot 4\ CH_3CN$ (**4**).[a]

atom	U11	U22	U33	U12	U13	U23
C(12)	0.184(8)	0.082(5)	0.035(3)	0.060(5)	-0.007(4)	0.021(3)
C(13)	0.036(3)	0.034(3)	0.038(3)	-0.006(2)	0.003(2)	-0.002(2)
C(14)	0.035(3)	0.051(3)	0.073(4)	-0.012(2)	-0.003(3)	0.002(3)
C(15)	0.053(3)	0.051(3)	0.043(3)	0.006(3)	0.016(2)	-0.004(2)
C(16)	0.031(3)	0.051(3)	0.048(3)	0.003(2)	0.000(2)	0.003(2)
C(17)	0.025(2)	0.030(2)	0.026(2)	0.001(2)	0.005(2)	0.003(2)
C(18)	0.041(3)	0.026(2)	0.032(2)	-0.003(2)	0.001(2)	-0.001(2)
C(19)	0.040(3)	0.032(3)	0.033(2)	-0.005(2)	-0.000(2)	-0.002(2)
C(20)	0.081(4)	0.042(3)	0.023(2)	-0.007(3)	-0.003(2)	0.008(2)
C(21)	0.034(2)	0.025(2)	0.030(2)	-0.001(2)	0.013(2)	-0.001(2)
C(22)	0.051(3)	0.038(3)	0.034(3)	-0.003(2)	-0.006(2)	-0.002(2)
C(23)	0.047(3)	0.035(3)	0.039(3)	-0.005(2)	0.001(2)	-0.010(2)
C(24)	0.080(4)	0.026(3)	0.047(3)	-0.010(3)	0.006(3)	0.001(2)
C(25)	0.043(3)	0.024(2)	0.030(2)	0.003(2)	0.004(2)	0.001(2)
C(26)	0.077(4)	0.044(3)	0.040(3)	0.027(3)	0.005(3)	-0.004(2)
C(27)	0.041(3)	0.031(3)	0.041(3)	-0.000(2)	0.001(2)	0.003(2)
C(28)	0.048(4)	0.100(6)	0.071(4)	-0.013(4)	0.008(3)	-0.003(4)
C(29)	0.049(3)	0.028(3)	0.035(3)	-0.005(2)	-0.005(2)	-0.001(2)
C(30)	0.149(7)	0.026(3)	0.050(3)	-0.015(4)	-0.030(4)	-0.003(2)

[a]Estimated standard deviations in the least significant figure are given in parentheses. The anisotropic temperature factors are of the form $\exp[-2\pi^2(U_{11}h^2a^{*2}... + 2U_{12}hka^*b^* + ...)]$.

Table 21. Intramolecular Distances for $[Fe_3(OBz)_6(^iPrOx)_2]$ (**5**).[a]

atom	atom	distance	atom	atom	distance
Fe(1)	O(5)	2.242(8)	O(5)	C(27)	1.27(1)
Fe(1)	O(6)	2.194(8)	O(6)	C(27)	1.28(1)
Fe(1)	O(8)	2.100(8)	O(7)	C(34)	1.24(1)
Fe(1)	O(10)	2.013(8)	O(8)	C(34)	1.28(1)
Fe(1)	N(1)	2.13(1)	O(9)	C(41)	1.27(1)
Fe(1)	N(2)	2.22(1)	O(10)	C(41)	1.26(1)
Fe(2)	O(5)	2.216(8)	O(11)	C(48)	1.31(1)
Fe(2)	O(7)	2.099(9)	O(12)	C(48)	1.26(1)
Fe(2)	O(9)	2.106(8)	O(13)	C(55)	1.22(1)
Fe(2)	O(11)	2.205(8)	O(14)	C(55)	1.28(1)
Fe(2)	O(13)	2.070(9)	O(15)	C(62)	1.25(1)
Fe(2)	O(15)	2.105(8)	O(16)	C(62)	1.25(1)
Fe(3)	O(11)	2.183(8)	N(1)	C(2)	1.26(2)
Fe(3)	O(12)	2.282(9)	N(1)	C(4)	1.50(2)
Fe(3)	O(14)	2.107(9)	N(2)	C(8)	1.26(2)
Fe(3)	O(16)	2.040(9)	N(2)	C(10)	1.51(2)
Fe(3)	N(3)	2.29(1)	N(3)	C(15)	1.26(2)
Fe(3)	N(4)	2.15(1)	N(3)	C(17)	1.50(2)
O(1)	C(2)	1.32(2)	N(4)	C(21)	1.26(1)
O(1)	C(3)	1.46(2)	N(4)	C(23)	1.48(2)
O(2)	C(8)	1.35(2)	C(1)	C(2)	1.50(2)
O(2)	C(9)	1.44(2)	C(1)	C(8)	1.50(2)
O(3)	C(15)	1.36(1)	C(3)	C(4)	1.51(2)

[a]Distances are in angstroms. For atom-labelling scheme see Figure 5. Estimated standard deviations in the least significant figure are given in parentheses.

Table 21 contd. Intramolecular Distances for $[Fe_3(OBz)_6(^iPrOx)_2]$ (**5**).[a]

atom	atom	distance	atom	atom	distance
O(3)	C(16)	1.46(2)	C(4)	C(5)	1.53(2)
O(4)	C(21)	1.36(1)	C(5)	C(6)	1.52(2)
O(4)	C(22)	1.48(2)	C(5)	C(7)	1.54(2)
C(9)	C(10)	1.53(2)	C(38)	C(39)	1.33(2)
C(10)	C(11)	1.53(2)	C(39)	C(40)	1.40(2)
C(11)	C(12)	1.53(2)	C(41)	C(42)	1.52(2)
C(11)	C(13)	1.53(2)	C(42)	C(43)	1.39(2)
C(14)	C(15)	1.51(2)	C(42)	C(47)	1.36(2)
C(14)	C(21)	1.50(2)	C(43)	C(44)	1.42(2)
C(16)	C(17)	1.54(2)	C(44)	C(45)	1.38(2)
C(17)	C(18)	1.53(2)	C(45)	C(46)	1.36(2)
C(18)	C(19)	1.53(2)	C(46)	C(47)	1.37(2)
C(18)	C(20)	1.51(2)	C(48)	C(49)	1.48(2)
C(22)	C(23)	1.52(2)	C(49)	C(50)	1.36(2)
C(23)	C(24)	1.54(2)	C(49)	C(54)	1.40(2)
C(24)	C(25)	1.52(2)	C(50)	C(51)	1.38(2)
C(24)	C(26)	1.50(2)	C(51)	C(52)	1.36(2)
C(27)	C(28)	1.50(2)	C(52)	C(53)	1.39(2)
C(28)	C(29)	1.40(2)	C(53)	C(54)	1.39(2)
C(28)	C(33)	1.42(2)	C(55)	C(56)	1.53(2)
C(29)	C(30)	1.39(2)	C(56)	C(57)	1.36(2)
C(30)	C(31)	1.37(2)	C(56)	C(61)	1.37(2)
C(31)	C(32)	1.37(2)	C(57)	C(58)	1.41(2)

[a]Distances are in angstroms. For atom-labelling scheme see Figure 5. Estimated standard deviations in the least significant figure are given in parentheses.

Table 21 contd. Intramolecular Distances for $[Fe_3(OBz)_6(^iPrOx)_2]$ (**5**).[a]

atom	atom	distance	atom	atom	distance
C(32)	C(33)	1.39(2)	C(58)	C(59)	1.36(2)
C(34)	C(35)	1.50(2)	C(59)	C(60)	1.37(2)
C(35)	C(36)	1.37(2)	C(60)	C(61)	1.40(2)
C(35)	C(40)	1.42(2)	C(62)	C(63)	1.53(2)
C(36)	C(37)	1.40(2)	C(63)	C(64)	1.36(2)
C(37)	C(38)	1.36(2)	C(63)	C(68)	1.39(2)
C(64)	C(65)	1.42(2)	C(66)	C(67)	1.34(2)
C(65)	C(66)	1.37(2)	C(67)	C(68)	1.38(2)

[a]Distances are in angstroms. For atom-labelling scheme see Figure 5. Estimated standard deviations in the least significant figure are given in parentheses.

Table 22. Intramolecular Bond Angles for $[Fe_3(OBz)_6(^iPrOx)_2]$ (**5**).[a]

atom	atom	atom	angle	atom	atom	atom	angle
O(5)	Fe(1)	O(6)	59.6(3)	O(9)	Fe(2)	O(15)	86.3(3)
O(5)	Fe(1)	O(8)	87.9(3)	O(11)	Fe(2)	O(13)	94.1(3)
O(5)	Fe(1)	O(10)	97.9(3)	O(11)	Fe(2)	O(15)	87.3(3)
O(5)	Fe(1)	N(1)	164.5(3)	O(13)	Fe(2)	O(15)	90.7(4)
O(5)	Fe(1)	N(2)	100.3(3)	O(11)	Fe(3)	O(12)	59.2(3)
O(6)	Fe(1)	O(8)	88.1(3)	O(11)	Fe(3)	O(14)	91.5(3)
O(6)	Fe(1)	O(10)	155.4(3)	O(11)	Fe(3)	O(16)	96.7(3)
O(6)	Fe(1)	N(1)	105.9(3)	O(11)	Fe(3)	N(3)	99.1(3)
O(6)	Fe(1)	N(2)	87.6(3)	O(11)	Fe(3)	N(4)	154.7(4)
O(8)	Fe(1)	O(10)	101.7(3)	O(12)	Fe(3)	O(14)	93.6(3)
O(8)	Fe(1)	N(1)	86.2(4)	O(12)	Fe(3)	O(16)	152.6(3)
O(8)	Fe(1)	N(2)	167.2(3)	O(12)	Fe(3)	N(3)	85.0(3)
O(10)	Fe(1)	N(1)	97.3(4)	O(12)	Fe(3)	N(4)	96.2(4)
O(10)	Fe(1)	N(2)	87.0(3)	O(14)	Fe(3)	O(16)	100.4(4)
N(1)	Fe(1)	N(2)	83.3(4)	O(14)	Fe(3)	N(3)	166.7(4)
O(5)	Fe(2)	O(7)	96.3(3)	O(14)	Fe(3)	N(4)	83.4(4)
O(5)	Fe(2)	O(9)	85.2(3)	O(16)	Fe(3)	N(3)	86.4(4)
O(5)	Fe(2)	O(11)	175.2(3)	O(16)	Fe(3)	N(4)	108.7(4)
O(5)	Fe(2)	O(13)	90.0(3)	N(3)	Fe(3)	N(4)	83.7(4)
O(5)	Fe(2)	O(15)	90.1(3)	C(2)	O(1)	C(3)	105(1)
O(7)	Fe(2)	O(9)	96.6(3)	C(8)	O(2)	C(9)	106(1)
O(7)	Fe(2)	O(11)	86.5(3)	C(15)	O(3)	C(16)	106(1)
O(7)	Fe(2)	O(13)	86.9(4)	C(21)	O(4)	C(22)	105.4(9)

[a]Angles are in degrees. Estimated standard deviations in the least significant figure are given in parentheses.

Table 22 contd. Intramolecular Bond Angles for $[Fe_3(OBz)_6(^iPrOx)_2]$ (**5**).[a]

atom	atom	atom	angle	atom	atom	atom	angle
O(7)	Fe(2)	O(15)	173.2(3)	Fe(1)	O(5)	Fe(2)	105.7(3)
O(9)	Fe(2)	O(11)	90.6(3)	Fe(1)	O(5)	C(27)	89.1(7)
O(9)	Fe(2)	O(13)	174.3(4)	Fe(2)	O(5)	C(27)	148.7(8)
Fe(1)	O(6)	C(27)	91.1(7)	O(1)	C(2)	N(1)	120(1)
Fe(2)	O(7)	C(34)	132.6(9)	O(1)	C(2)	C(1)	115(1)
Fe(1)	O(8)	C(34)	123.3(8)	N(1)	C(2)	C(1)	125(1)
Fe(2)	O(9)	C(41)	129.9(8)	O(1)	C(3)	C(4)	105(1)
Fe(1)	O(10)	C(41)	128.9(8)	N(1)	C(4)	C(3)	103(1)
Fe(2)	O(11)	Fe(3)	112.3(3)	N(1)	C(4)	C(5)	110(1)
Fe(2)	O(11)	C(48)	139.1(8)	C(3)	C(4)	C(5)	116(1)
Fe(3)	O(11)	C(48)	92.9(7)	C(4)	C(5)	C(6)	112(1)
Fe(3)	O(12)	C(48)	89.8(8)	C(4)	C(5)	C(7)	109(1)
Fe(2)	O(13)	C(55)	137.2(8)	C(6)	C(5)	C(7)	112(1)
Fe(3)	O(14)	C(55)	132.7(8)	O(2)	C(8)	N(2)	118(1)
Fe(2)	O(15)	C(62)	140.7(8)	O(2)	C(8)	C(1)	114(1)
Fe(3)	O(16)	C(62)	129.5(9)	N(2)	C(8)	C(1)	128(1)
Fe(1)	N(1)	C(2)	127(1)	O(2)	C(9)	C(10)	104(1)
Fe(1)	N(1)	C(4)	127.0(8)	N(2)	C(10)	C(9)	102(1)
C(2)	N(1)	C(4)	106(1)	N(2)	C(10)	C(11)	112(1)
Fe(1)	N(2)	C(8)	122(1)	C(9)	C(10)	C(11)	116(1)
Fe(1)	N(2)	C(10)	130.0(7)	C(10)	C(11)	C(12)	109(1)
C(8)	N(2)	C(10)	107(1)	C(10)	C(11)	C(13)	113(1)
Fe(3)	N(3)	C(15)	119.0(9)	C(12)	C(11)	C(13)	111(1)

[a]Angles are in degrees. Estimated standard deviations in the least significant figure are given in parentheses.

Table 22 contd. Intramolecular Bond Angles for $[Fe_3(OBz)_6(^iPrOx)_2]$ (5).[a]

atom	atom	atom	angle	atom	atom	atom	angle
Fe(3)	N(3)	C(17)	133.8(8)	C(15)	C(14)	C(21)	109(1)
C(15)	N(3)	C(17)	106(1)	O(3)	C(15)	N(3)	119(1)
Fe(3)	N(4)	C(21)	122.9(8)	O(3)	C(15)	C(14)	114(1)
Fe(3)	N(4)	C(23)	129.5(8)	N(3)	C(15)	C(14)	127(1)
C(21)	N(4)	C(23)	108(1)	O(3)	C(16)	C(17)	103(1)
C(2)	C(1)	C(8)	113(1)	N(3)	C(17)	C(16)	104(1)
N(3)	C(17)	C(18)	112(1)	O(7)	C(34)	O(8)	127(1)
C(16)	C(17)	C(18)	114(1)	O(7)	C(34)	C(35)	120(1)
C(17)	C(18)	C(19)	112(1)	O(8)	C(34)	C(35)	113(1)
C(17)	C(18)	C(20)	114(1)	C(34)	C(35)	C(36)	124(1)
C(19)	C(18)	C(20)	114(1)	C(34)	C(35)	C(40)	117(1)
O(4)	C(21)	N(4)	119(1)	C(36)	C(35)	C(40)	119(1)
O(4)	C(21)	C(14)	114(1)	C(35)	C(36)	C(37)	120(1)
N(4)	C(21)	C(14)	127(1)	C(36)	C(37)	C(38)	120(1)
O(4)	C(22)	C(23)	104(1)	C(37)	C(38)	C(39)	122(2)
N(4)	C(23)	C(22)	105(1)	C(38)	C(39)	C(40)	121(2)
N(4)	C(23)	C(24)	112(1)	C(35)	C(40)	C(39)	119(1)
C(22)	C(23)	C(24)	116(1)	O(9)	C(41)	O(10)	126(1)
C(23)	C(24)	C(25)	112(1)	O(9)	C(41)	C(42)	117(1)
C(23)	C(24)	C(26)	111(1)	O(10)	C(41)	C(42)	117(1)
C(25)	C(24)	C(26)	111(1)	C(41)	C(42)	C(43)	120(1)
O(5)	C(27)	O(6)	120(1)	C(41)	C(42)	C(47)	119(1)
O(5)	C(27)	C(28)	121(1)	C(43)	C(42)	C(47)	121(1)

[a]Angles are in degrees. Estimated standard deviations in the least significant figure are given in parentheses.

Table 22 contd. Intramolecular Bond Angles for $[Fe_3(OBz)_6(^iPrOx)_2]$ (**5**).[a]

atom	atom	atom	angle	atom	atom	atom	angle
O(6)	C(27)	C(28)	119(1)	C(42)	C(43)	C(44)	117(1)
C(27)	C(28)	C(29)	121(1)	C(43)	C(44)	C(45)	119(1)
C(27)	C(28)	C(33)	119(1)	C(44)	C(45)	C(46)	123(2)
C(29)	C(28)	C(33)	120(1)	C(45)	C(46)	C(47)	117(1)
C(28)	C(29)	C(30)	120(1)	C(42)	C(47)	C(46)	123(1)
C(29)	C(30)	C(31)	119(1)	O(11)	C(48)	O(12)	118(1)
C(30)	C(31)	C(32)	123(1)	O(11)	C(48)	C(49)	119(1)
C(31)	C(32)	C(33)	119(1)	O(12)	C(48)	C(49)	124(1)
C(28)	C(33)	C(32)	119(1)	C(48)	C(49)	C(50)	120(1)
C(48)	C(49)	C(54)	119(1)	C(65)	C(66)	C(67)	120(2)
C(50)	C(49)	C(54)	121(1)	C(66)	C(67)	C(68)	121(1)
C(49)	C(50)	C(51)	121(1)	C(63)	C(68)	C(67)	119(1)
C(50)	C(51)	C(52)	120(2)	C(58)	C(59)	C(60)	119(2)
C(51)	C(52)	C(53)	119(2)	C(59)	C(60)	C(61)	120(2)
C(52)	C(53)	C(54)	122(2)	C(56)	C(61)	C(60)	120(1)
C(49)	C(54)	C(53)	117(1)	O(15)	C(62)	O(16)	128(1)
O(13)	C(55)	O(14)	127(1)	O(15)	C(62)	C(63)	114(1)
O(13)	C(55)	C(56)	118(1)	O(16)	C(62)	C(63)	117(1)
O(14)	C(55)	C(56)	115(1)	C(62)	C(63)	C(64)	120(1)
C(55)	C(56)	C(57)	119(1)	C(62)	C(63)	C(68)	120(1)
C(55)	C(56)	C(61)	121(1)	C(64)	C(63)	C(68)	120(1)
C(57)	C(56)	C(61)	120(1)	C(63)	C(64)	C(65)	119(1)
C(56)	C(57)	C(58)	120(1)	C(64)	C(65)	C(66)	120(2)
C(57)	C(58)	C(59)	121(2)	C(65)	C(66)	C(67)	120(2)
C(66)	C(67)	C(68)	121(2)	C(63)	C(68)	C(67)	119(1)

[a]Angles are in degrees. Estimated standard deviations in the least significant figure are given in parentheses.

Table 23. Positional Parameters and $B(eq)^a$ for $[Fe_3(OBz)_6(^iPrOx)_2]$ (**5**).

atom	x	y	z	$B(eq)$
Fe(1)	0.8966(1)	0.16944(8)	0.44753(7)	1.71(8)
Fe(2)	0.8854(1)	-0.00369(9)	0.49971(8)	1.60(7)
Fe(3)	0.8998(1)	-0.18409(8)	0.54584(8)	1.85(8)
O(1)	0.9816(7)	0.3520(5)	0.3568(4)	3.3(5)
O(2)	0.6939(6)	0.3262(5)	0.4082(4)	3.0(5)
O(3)	0.7880(6)	-0.3844(4)	0.4895(4)	2.8(4)
O(4)	0.9833(6)	-0.3780(4)	0.6205(4)	2.4(4)
O(5)	0.8531(6)	0.1049(4)	0.5234(4)	2.1(4)
O(6)	0.8993(6)	0.2126(4)	0.5355(3)	2.1(4)
O(7)	1.0059(6)	0.0187(4)	0.4543(4)	2.2(4)
O(8)	1.0300(5)	0.1336(4)	0.4615(4)	2.3(4)
O(9)	0.7955(6)	0.0123(4)	0.4298(4)	2.1(4)
O(10)	0.8535(6)	0.1056(4)	0.3842(4)	2.0(4)
O(11)	0.9063(5)	-0.1122(4)	0.4728(3)	1.9(4)
O(12)	0.9984(6)	-0.2027(4)	0.4710(4)	2.5(4)
O(13)	0.9657(6)	-0.0127(5)	0.5731(4)	2.6(4)
O(14)	0.9940(6)	-0.1244(4)	0.5934(4)	2.3(4)
O(15)	0.7707(6)	-0.0383(4)	0.5462(4)	2.3(4)
O(16)	0.7803(6)	-0.1481(4)	0.5795(4)	2.4(4)
N(1)	0.9567(7)	0.2462(5)	0.3931(4)	1.8(5)
N(2)	0.7705(7)	0.2305(5)	0.4325(4)	1.6(5)
N(3)	0.8144(7)	-0.2702(5)	0.5038(5)	2.2(5)
N(4)	0.9488(8)	-0.2669(5)	0.5998(4)	2.2(5)

$^aB(eq) = 8/3\pi^2(U_{11}(aa^*)^2 + U_{22}(bb^*)^2 + U_{33}(cc^*)^2 + 2U_{12}aa^*bb^*\cos\gamma + 2U_{13}aa^*cc^*\cos\beta + 2U_{23}bb^*cc^*\cos\alpha)$

Table 23 contd. Positional Parameters and $B(eq)^a$ for $[Fe_3(OBz)_6(^iPrOx)_2]$ (**5**).

atom	x	y	z	$B(eq)$
C(1)	0.855(1)	0.3411(7)	0.4199(6)	3.1(3)
C(2)	0.935(1)	0.3090(7)	0.3898(6)	2.3(3)
C(3)	1.055(1)	0.3099(7)	0.3318(6)	3.0(3)
C(4)	1.039(1)	0.2378(7)	0.3550(6)	2.7(3)
C(5)	1.021(1)	0.1816(7)	0.3099(6)	3.0(3)
C(6)	0.944(1)	0.2010(8)	0.2694(6)	3.3(3)
C(7)	1.110(1)	0.1674(8)	0.2769(7)	4.6(4)
C(8)	0.773(1)	0.2944(7)	0.4222(6)	2.4(3)
C(9)	0.623(1)	0.2753(7)	0.4170(6)	3.1(3)
C(10)	0.675(1)	0.2064(7)	0.4207(5)	2.2(3)
C(11)	0.640(1)	0.1550(6)	0.4665(5)	2.3(3)
C(12)	0.544(1)	0.1315(8)	0.4503(7)	3.9(3)
C(13)	0.642(1)	0.1853(7)	0.5278(6)	3.1(3)
C(14)	0.9383(9)	-0.3551(6)	0.5222(5)	2.0(2)
C(15)	0.8449(9)	-0.3314(6)	0.5035(5)	1.8(2)
C(16)	0.698(1)	-0.3532(7)	0.4825(6)	2.9(3)
C(17)	0.717(1)	-0.2749(6)	0.4839(5)	2.4(3)
C(18)	0.703(1)	-0.2382(6)	0.4257(5)	2.1(2)
C(19)	0.770(1)	-0.2632(7)	0.3794(6)	3.2(3)
C(20)	0.697(1)	-0.1605(8)	0.4304(6)	3.7(3)
C(21)	0.9565(8)	-0.3286(6)	0.5822(5)	1.7(2)
C(22)	0.997(1)	-0.3410(7)	0.6763(6)	3.0(3)
C(23)	0.975(1)	-0.2659(7)	0.6617(6)	2.4(3)

$^aB(eq) = 8/3\pi^2(U_{11}(aa^*)^2 + U_{22}(bb^*)^2 + U_{33}(cc^*)^2 + 2U_{12}aa^*bb^*\cos\gamma + 2U_{13}aa^*cc^*\cos\beta + 2U_{23}bb^*cc^*\cos\alpha)$

Table 23 contd. Positional Parameters and $B(eq)^a$ for $[Fe_3(OBz)_6(^iPrOx)_2]$ (**5**).

atom	*x*	*y*	*z*	*B*(eq)
C(24)	0.902(1)	-0.2311(7)	0.6999(6)	3.2(3)
C(25)	0.810(1)	-0.2676(8)	0.6952(7)	4.6(4)
C(26)	0.932(1)	-0.2271(9)	0.7621(7)	4.9(4)
C(27)	0.8670(9)	0.1564(6)	0.5563(6)	2.1(2)
C(28)	0.8407(8)	0.1545(6)	0.6192(5)	1.7(2)
C(29)	0.854(1)	0.2122(7)	0.6549(6)	2.8(3)
C(30)	0.823(1)	0.2108(7)	0.7118(6)	3.3(3)
C(31)	0.779(1)	0.1526(7)	0.7316(6)	3.2(3)
C(32)	0.764(1)	0.0953(7)	0.6979(7)	3.5(3)
C(33)	0.796(1)	0.0947(7)	0.6412(6)	2.7(3)
C(34)	1.055(1)	0.0711(6)	0.4520(6)	2.1(2)
C(35)	1.1525(8)	0.0647(6)	0.4343(5)	1.4(2)
C(36)	1.215(1)	0.1174(7)	0.4394(6)	2.6(3)
C(37)	1.304(1)	0.1077(7)	0.4201(6)	3.1(3)
C(38)	1.330(1)	0.0454(8)	0.3975(7)	3.9(3)
C(39)	1.272(1)	-0.0072(8)	0.3929(7)	3.8(3)
C(40)	1.181(1)	0.0004(7)	0.4100(6)	2.7(3)
C(41)	0.8009(9)	0.0543(6)	0.3877(5)	1.6(2)
C(42)	0.733(1)	0.0450(6)	0.3384(6)	2.1(2)
C(43)	0.651(1)	0.0113(7)	0.3484(6)	3.0(3)
C(44)	0.588(1)	0.0093(7)	0.3023(6)	3.4(3)
C(45)	0.611(1)	0.0378(8)	0.2494(7)	4.3(3)
C(46)	0.693(1)	0.0686(8)	0.2394(7)	3.8(3)

$^aB(eq) = 8/3\pi^2(U_{11}(aa^*)^2 + U_{22}(bb^*)^2 + U_{33}(cc^*)^2 + 2U_{12}aa^*bb^*\cos\gamma + 2U_{13}aa^*cc^*\cos\beta + 2U_{23}bb^*cc^*\cos\alpha)$

Table 23 contd. Positional Parameters and $B(eq)^a$ for $[Fe_3(OBz)_6(^iPrOx)_2]$ (**5**).

atom	*x*	*y*	*z*	*B*(eq)
C(47)	0.752(1)	0.0733(7)	0.2855(6)	3.1(3)
C(48)	0.9671(9)	-0.1499(6)	0.4453(6)	2.2(2)
C(49)	0.994(1)	-0.1293(7)	0.3857(6)	2.6(3)
C(50)	0.942(1)	-0.0837(7)	0.3553(6)	3.0(3)
C(51)	0.969(1)	-0.0606(8)	0.3014(7)	3.7(3)
C(52)	1.047(1)	-0.0852(8)	0.2769(7)	4.0(3)
C(53)	1.100(1)	-0.1324(7)	0.3075(6)	3.5(3)
C(54)	1.074(1)	-0.1563(7)	0.3622(6)	2.5(3)
C(55)	1.0058(9)	-0.0588(6)	0.5989(5)	1.7(2)
C(56)	1.0772(8)	-0.0374(6)	0.6440(5)	1.5(2)
C(57)	1.103(1)	0.0304(7)	0.6475(7)	3.9(3)
C(58)	1.169(1)	0.0505(8)	0.6887(7)	4.5(4)
C(59)	1.206(1)	0.003(1)	0.7256(7)	4.4(4)
C(60)	1.181(1)	-0.0651(9)	0.7211(7)	4.3(4)
C(61)	1.118(1)	-0.0858(7)	0.6791(6)	3.3(3)
C(62)	0.741(1)	-0.0914(6)	0.5711(5)	2.2(3)
C(63)	0.640(1)	-0.0870(6)	0.5880(6)	2.2(2)
C(64)	0.594(1)	-0.0262(8)	0.5835(7)	4.4(4)
C(65)	0.501(1)	-0.0230(8)	0.6006(7)	4.4(4)
C(66)	0.459(1)	-0.0815(8)	0.6204(7)	4.0(3)
C(67)	0.506(1)	-0.1404(7)	0.6267(6)	3.1(3)
C(68)	0.596(1)	-0.1450(6)	0.6105(5)	2.4(2)
H(1)	0.8718	0.3523	0.4585	3.8

$^aB(eq) = 8/3\pi^2(U_{11}(aa^*)^2 + U_{22}(bb^*)^2 + U_{33}(cc^*)^2 + 2U_{12}aa^*bb^*\cos\gamma + 2U_{13}aa^*cc^*\cos\beta + 2U_{23}bb^*cc^*\cos\alpha)$

Table 23 contd. Positional Parameters and $B(eq)^a$ for $[Fe_3(OBz)_6(^iPrOx)_2]$ (**5**).

atom	*x*	*y*	*z*	*B*(eq)
H(2)	0.8383	0.3823	0.3998	3.8
H(3)	1.0512	0.3102	0.2907	3.5
H(4)	1.1125	0.3268	0.3437	3.5
H(5)	1.0895	0.2246	0.3782	3.3
H(6)	1.0045	0.1404	0.3297	3.6
H(7)	0.9587	0.2426	0.2495	3.9
H(8)	0.9346	0.1648	0.2421	3.9
H(9)	0.8897	0.2077	0.2913	3.9
H(10)	1.1560	0.1528	0.3035	5.6
H(11)	1.1006	0.1321	0.2489	5.6
H(12)	1.1299	0.2086	0.2581	5.6
H(13)	0.5910	0.2841	0.4520	3.8
H(14)	0.5817	0.2751	0.3854	3.8
H(15)	0.6730	0.1846	0.3838	2.7
H(16)	0.6792	0.1156	0.4659	2.7
H(17)	0.5049	0.1706	0.4489	4.6
H(18)	0.5454	0.1096	0.4134	4.6
H(19)	0.5225	0.0996	0.4785	4.6
H(20)	0.7017	0.1998	0.5371	3.8
H(21)	0.6016	0.2240	0.5296	3.8
H(22)	0.6224	0.1510	0.5547	3.8
H(23)	0.9407	-0.4043	0.5221	2.4
H(24)	0.9829	-0.3373	0.4962	2.4

$^aB(eq) = 8/3\pi^2(U_{11}(aa^*)^2 + U_{22}(bb^*)^2 + U_{33}(cc^*)^2 + 2U_{12}aa^*bb^*\cos\gamma + 2U_{13}aa^*cc^*\cos\beta + 2U_{23}bb^*cc^*\cos\alpha)$

Table 23 contd. Positional Parameters and $B(eq)^a$ for $[Fe_3(OBz)_6(^iPrOx)_2]$ (**5**).

atom	x	y	z	$B(eq)$
H(25)	0.6712	-0.3663	0.4466	3.5
H(26)	0.6585	-0.3662	0.5133	3.5
H(27)	0.6792	-0.2539	0.5121	2.9
H(28)	0.6448	-0.2527	0.4127	2.5
H(29)	0.7701	-0.3125	0.3784	3.8
H(30)	0.7520	-0.2458	0.3427	3.8
H(31)	0.8295	-0.2470	0.3884	3.8
H(32)	0.7557	-0.1423	0.4401	4.4
H(33)	0.6782	-0.1417	0.3943	4.4
H(34)	0.6549	-0.1483	0.4597	4.4
H(35)	0.9565	-0.3582	0.7052	3.6
H(36)	1.0579	-0.3455	0.6893	3.6
H(37)	1.0295	-0.2398	0.6652	2.9
H(38)	0.8940	-0.1850	0.6863	3.8
H(39)	0.7656	-0.2424	0.7164	5.5
H(40)	0.7924	-0.2701	0.6556	5.5
H(41)	0.8150	-0.3131	0.7106	5.5
H(42)	0.9379	-0.2725	0.7774	5.9
H(43)	0.9892	-0.2040	0.7641	5.9
H(44)	0.8883	-0.2020	0.7840	5.9
H(45)	0.8842	0.2521	0.6403	3.4
H(46)	0.8315	0.2495	0.7366	3.9
H(47)	0.7583	0.1520	0.7706	3.8

$^aB(eq) = 8/3\pi^2(U_{11}(aa^*)^2 + U_{22}(bb^*)^2 + U_{33}(cc^*)^2 + 2U_{12}aa^*bb^*\cos\gamma + 2U_{13}aa^*cc^*\cos\beta + 2U_{23}bb^*cc^*\cos\alpha)$

Table 23 contd. Positional Parameters and $B(eq)^a$ for $[Fe_3(OBz)_6(^iPrOx)_2]$ (**5**).

atom	x	y	z	$B(eq)$
H(48)	0.7316	0.0566	0.7131	4.2
H(49)	0.7874	0.0550	0.6175	3.2
H(50)	1.1974	0.1604	0.4561	3.1
H(51)	1.3471	0.1446	0.4226	3.7
H(52)	1.3911	0.0393	0.3848	4.7
H(53)	1.2923	-0.0503	0.3778	4.6
H(54)	1.1386	-0.0366	0.4054	3.2
H(55)	0.6384	-0.0096	0.3848	3.6
H(56)	0.5296	-0.0114	0.3077	4.1
H(57)	0.5680	0.0357	0.2187	5.1
H(58)	0.7083	0.0861	0.2022	4.6
H(59)	0.8076	0.0973	0.2803	3.8
H(60)	0.8868	-0.0673	0.3713	3.6
H(61)	0.9336	-0.0273	0.2814	4.5
H(62)	1.0650	-0.0704	0.2393	4.8
H(63)	1.1545	-0.1489	0.2906	4.2
H(64)	1.1103	-0.1892	0.3826	3.1
H(65)	1.0770	0.0639	0.6223	4.7
H(66)	1.1873	0.0976	0.6907	5.4
H(67)	1.2490	0.0174	0.7541	5.3
H(68)	1.2062	-0.0985	0.7467	5.1
H(69)	1.1026	-0.1334	0.6749	3.9
H(70)	0.6238	0.0140	0.5691	5.3
H(71)	0.4690	0.0195	0.5983	5.3
H(72)	0.3961	-0.0804	0.6298	4.8
H(73)	0.4770	-0.1800	0.6426	3.7
H(74)	0.6286	-0.1874	0.6148	2.9

$^aB(eq) = 8/3\pi^2(U_{11}(aa^*)^2 + U_{22}(bb^*)^2 + U_{33}(cc^*)^2 + 2U_{12}aa^*bb^*\cos\gamma + 2U_{13}aa^*cc^*\cos\beta + 2U_{23}bb^*cc^*\cos\alpha)$

Table 24. U Values for $[Fe_3(OBz)_6(^iPrOx)_2]$ (**5**).[a]

atom	U11	U22	U33	U12	U13	U23
Fe(1)	0.013(1)	0.026(1)	0.026(1)	-0.0006(8)	-0.0002(9)	0.0003(8)
Fe(2)	0.0116(9)	0.0232(8)	0.0260(8)	-0.0004(8)	0.0019(9)	0.0019(7)
Fe(3)	0.017(1)	0.027(1)	0.026(1)	0.0018(9)	-0.003(1)	0.0014(8)
O(1)	0.045(7)	0.036(6)	0.044(6)	-0.013(5)	0.007(5)	0.012(5)
O(2)	0.016(5)	0.041(6)	0.057(6)	0.012(4)	0.008(5)	0.012(5)
O(3)	0.024(5)	0.025(5)	0.058(7)	-0.005(4)	-0.011(5)	-0.003(5)
O(4)	0.038(6)	0.027(5)	0.026(5)	0.005(4)	-0.000(4)	0.002(4)
O(5)	0.018(5)	0.033(5)	0.028(5)	-0.001(4)	0.002(4)	-0.001(4)
O(6)	0.019(5)	0.034(5)	0.026(5)	-0.007(4)	-0.007(4)	-0.002(4)
O(7)	0.018(5)	0.031(5)	0.037(5)	-0.008(4)	0.005(4)	0.004(4)
O(8)	0.009(5)	0.044(5)	0.034(6)	-0.003(4)	-0.008(4)	0.001(4)
O(9)	0.020(5)	0.033(5)	0.028(5)	0.005(4)	0.002(4)	0.005(4)
O(10)	0.018(5)	0.030(5)	0.027(5)	-0.004(4)	0.004(4)	-0.003(4)
O(11)	0.009(4)	0.032(5)	0.030(5)	0.004(4)	-0.010(4)	0.002(4)
O(12)	0.021(5)	0.037(5)	0.036(5)	0.005(4)	0.001(4)	-0.004(4)
O(13)	0.029(6)	0.035(5)	0.033(5)	-0.001(4)	-0.009(4)	0.005(4)
O(14)	0.017(5)	0.030(5)	0.041(6)	-0.000(4)	-0.003(4)	0.003(4)
O(15)	0.023(5)	0.033(5)	0.031(5)	0.004(4)	0.017(4)	0.000(4)
O(16)	0.014(5)	0.030(5)	0.046(6)	0.007(4)	0.007(4)	0.006(4)
N(1)	0.017(6)	0.031(6)	0.022(6)	0.003(5)	-0.002(5)	-0.001(5)
N(2)	0.013(6)	0.026(6)	0.023(6)	0.001(5)	-0.002(5)	-0.004(4)
N(3)	0.008(6)	0.049(7)	0.028(6)	-0.005(5)	-0.003(5)	0.001(6)
N(4)	0.033(7)	0.028(6)	0.021(6)	0.002(5)	-0.005(5)	-0.005(5)

[a]Estimated standard deviations in the least significant figure are given in parentheses. The anisotropic temperature factors are of the form $\exp[-2\pi^2(U_{11}h^2a^{*2}... + 2U_{12}hka^*b^* + ...)]$.

Table 25. Intramolecular Bond Distances for $[Fe_3(OBz)_6(PheMe_3\text{-}Eda)_2]$ (**6**).[a]

atom	atom	distance	atom	atom	distance
Fe(1)	O(1)	2.241(3)	C(16)	C(17)	1.384(6)
Fe(1)	O(2)	2.206(3)	C(16)	C(22)	1.554(6)
Fe(1)	O(4)	2.023(3)	C(27)	C(28)	1.384(6)
Fe(1)	O(5)	2.072(3)	C(18)	C(19)	1.523(7)
Fe(1)	N(1)	2.284(4)	C(18)	C(20)	1.521(7)
Fe(1)	N(2)	2.241(4)	C(18)	C(21)	1.523(7)
Fe(2)	O(2)	2.234(3)	C(29)	C(30)	1.376(8)
Fe(2)	O(3)	2.086(3)	C(30)	C(31)	1.356(8)
Fe(2)	O(6)	2.117(3)	C(31)	C(32)	1.393(7)
O(1)	C(26)	1.282(5)	C(33)	C(34)	1.500(6)
O(2)	C(26)	1.267(5)	C(34)	C(35)	1.384(7)
O(3)	C(33)	1.247(5)	C(34)	C(39)	1.370(7)
O(4)	C(33)	1.286(6)	C(35)	C(36)	1.365(7)
O(5)	C(40)	1.258(5)	C(41)	C(46)	1.378(7)
O(6)	C(40)	1.251(5)	C(36)	C(37)	1.366(8)
O(7)	C(15)	1.400(5)	C(37)	C(38)	1.371(9)
N(1)	C(1)	1.475(6)	C(38)	C(39)	1.392(9)
N(1)	C(3)	1.466(6)	C(45)	C(46)	1.389(7)
N(1)	C(4)	1.488(7)	C(6)	C(7)	1.523(7)
N(2)	C(2)	1.481(6)	C(7)	C(8)	1.544(6)
N(2)	C(5)	1.487(6)	C(8)	C(9)	1.532(6)
N(2)	C(6)	1.490(6)	C(9)	C(10)	1.519(7)
C(1)	C(2)	1.505(7)	C(9)	C(11)	1.547(7)

[a]Distances are in angstroms. For atom-labelling scheme see Figure 6. Estimated standard deviations in the least significant figure are given in parentheses.

Table 25 contd. Intramolecular Bond Distances for $[Fe_3(OBz)_6(PheMe_3Eda)_2]$ (**6**).[a]

atom	atom	distance	atom	atom	distance
C(22)	C(23)	1.537(7)	C(9)	C(12)	1.546(6)
C(22)	C(24)	1.530(7)	C(26)	C(27)	1.487(6)
C(22)	C(25)	1.524(6)	C(27)	C(32)	1.396(6)
C(12)	C(13)	1.394(6)	C(28)	C(29)	1.405(7)
C(12)	C(17)	1.394(6)	C(40)	C(41)	1.510(6)
C(13)	C(14)	1.389(6)	C(41)	C(42)	1.402(6)
C(14)	C(15)	1.408(6)	C(42)	C(43)	1.375(7)
C(14)	C(18)	1.545(6)	C(43)	C(44)	1.388(7)
C(15)	C(16)	1.404(6)	C(44)	C(45)	1.377(7)

[a]Distances are in angstroms. For atom-labelling scheme see Figure 6. Estimated standard deviations in the least significant figure are given in parentheses.

Table 26 Intramolecular Bond Angles for $[Fe_3(OBz)_6(PheMe_3Eda)_2]$ (**6**).[a]

atom	atom	atom	angle	atom	atom	atom	angle
O(1)	Fe(1)	O(2)	59.2(1)	Fe(1)	O(1)	C(26)	89.9(3)
O(1)	Fe(1)	O(4)	159.0(1)	Fe(1)	O(2)	Fe(2)	109.5(1)
O(1)	Fe(1)	O(5)	86.5(1)	Fe(1)	O(2)	C(26)	91.9(3)
O(1)	Fe(1)	N(1)	88.5(1)	Fe(2)	O(2)	C(26)	137.5(3)
O(1)	Fe(1)	N(2)	100.2(1)	Fe(2)	O(3)	C(33)	140.5(3)
O(2)	Fe(1)	O(4)	100.1(1)	Fe(1)	O(4)	C(33)	130.0(3)
O(2)	Fe(1)	O(5)	91.2(1)	Fe(1)	O(5)	C(40)	130.3(3)
O(2)	Fe(1)	N(1)	94.8(1)	Fe(2)	O(6)	C(40)	137.8(3)
O(2)	Fe(1)	N(2)	159.2(1)	Fe(1)	N(1)	C(1)	104.6(3)
O(4)	Fe(1)	O(5)	97.9(1)	Fe(1)	N(1)	C(3)	115.2(3)
O(4)	Fe(1)	N(1)	90.4(1)	Fe(1)	N(1)	C(4)	112.1(3)
O(4)	Fe(1)	N(2)	100.3(1)	C(1)	N(1)	C(3)	108.2(4)
O(5)	Fe(1)	N(1)	168.7(1)	C(1)	N(1)	C(4)	108.7(4)
O(5)	Fe(1)	N(2)	90.0(1)	C(3)	N(1)	C(4)	107.9(4)
N(1)	Fe(1)	N(2)	81.0(1)	Fe(1)	N(2)	C(2)	105.1(3)
O(2)	Fe(2)	O(3)	88.8(1)	Fe(1)	N(2)	C(5)	112.5(3)
O(2)	Fe(2)	O(3)'	91.2(1)	Fe(1)	N(2)	C(6)	113.3(3)
O(2)	Fe(2)	O(6)	92.6(1)	C(2)	N(2)	C(5)	108.7(4)
O(2)	Fe(2)	O(6)'	87.4(1)	C(2)	N(2)	C(6)	108.0(4)
O(3)	Fe(2)	O(6)	91.5(1)	C(5)	N(2)	C(6)	109.0(3)
O(3)	Fe(2)	O(6)'	88.5(1)	N(1)	C(1)	C(2)	111.3(4)

[a]Angles are in degrees. Estimated standard deviations in the least significant figure are given in parentheses.

Table 26 contd. Intramolecular Bond Angles for $[Fe_3(OBz)_6(PheMe_3Eda)_2]$ (**6**).[a]

atom	atom	atom	angle	atom	atom	atom	angle
N(2)	C(2)	C(1)	111.9(4)	C(12)	C(17)	C(16)	123.4(4)
N(2)	C(6)	C(7)	116.6(4)	C(14)	C(18)	C(20)	109.4(4)
C(6)	C(7)	C(8)	106.8(4)	C(14)	C(18)	C(21)	110.8(4)
C(7)	C(8)	C(9)	117.8(4)	C(19)	C(18)	C(20)	107.1(4)
C(8)	C(9)	C(10)	109.2(4)	C(19)	C(18)	C(21)	107.3(4)
C(8)	C(9)	C(11)	109.7(4)	C(20)	C(18)	C(21)	110.5(4)
C(8)	C(9)	C(12)	110.7(4)	C(16)	C(22)	C(23)	109.3(4)
C(10)	C(9)	C(11)	108.7(4)	C(16)	C(22)	C(24)	111.9(4)
C(10)	C(9)	C(12)	109.2(4)	C(16)	C(22)	C(25)	111.4(4)
C(11)	C(9)	C(12)	109.4(4)	C(23)	C(22)	C(24)	107.0(4)
C(9)	C(12)	C(13)	122.6(4)	C(23)	C(22)	C(25)	109.7(4)
C(9)	C(12)	C(17)	120.6(4)	C(24)	C(22)	C(25)	107.4(4)
C(13)	C(12)	C(17)	116.7(4)	O(1)	C(26)	O(2)	119.0(4)
C(12)	C(13)	C(14)	123.2(4)	O(1)	C(26)	C(27)	120.7(4)
C(13)	C(14)	C(15)	117.3(4)	O(2)	C(26)	C(27)	120.3(4)
C(13)	C(14)	C(18)	120.6(4)	C(26)	C(27)	C(28)	120.7(4)
C(15)	C(14)	C(18)	122.0(4)	C(26)	C(27)	C(32)	118.7(4)
O(7)	C(15)	C(14)	118.9(4)	C(28)	C(27)	C(32)	120.5(4)
O(7)	C(15)	C(16)	119.3(4)	C(27)	C(28)	C(29)	119.2(5)
C(14)	C(15)	C(16)	121.7(4)	C(28)	C(29)	C(30)	119.9(5)
C(15)	C(16)	C(17)	117.3(4)	C(29)	C(30)	C(31)	120.3(5)
C(15)	C(16)	C(22)	122.0(4)	C(30)	C(31)	C(32)	121.6(5)
C(17)	C(16)	C(22)	120.7(4)	C(27)	C(32)	C(31)	118.4(5)

[a]Angles are in degrees. Estimated standard deviations in the least significant figure are given in parentheses.

Table26 contd. Intramolecular Bond Angles for $[Fe_3(OBz)_6(PheMe_3Eda)_2]$ (**6**).[a]

atom	atom	atom	angle	atom	atom	atom	angle
O(3)	C(33)	O(4)	125.6(4)	O(5)	C(40)	O(6)	126.4(4)
O(3)	C(33)	C(34)	118.0(4)	O(5)	C(40)	C(41)	115.2(4)
O(4)	C(33)	C(34)	116.3(4)	O(6)	C(40)	C(41)	118.3(4)
C(33)	C(34)	C(35)	120.2(4)	C(40)	C(41)	C(46)	120.5(4)
C(33)	C(34)	C(39)	121.6(5)	C(43)	C(44)	C(45)	120.0(5)
C(35)	C(34)	C(39)	118.0(5)	C(44)	C(45)	C(46)	119.8(5)
C(34)	C(35)	C(36)	121.2(5)	C(41)	C(46)	C(45)	120.7(5)
C(35)	C(36)	C(37)	121.0(5)	C(40)	C(41)	C(42)	120.4(4)
C(36)	C(37)	C(38)	118.6(6)	C(42)	C(41)	C(46)	119.0(4)
C(37)	C(38)	C(39)	120.6(6)	C(41)	C(42)	C(43)	120.1(4)
C(34)	C(39)	C(38)	120.5(6)	C(42)	C(43)	C(44)	120.2(5)

[a]Angles are in degrees. Estimated standard deviations in the least significant figure are given in parentheses.

Table 27. Positional Parameters and B(eq) for $[Fe_3(OBz)_6(PheMe_3Eda)_2]$ (**6**).

atom	x	y	z	B(eq)[a]
Fe(1)	0.19954(6)	0.09627(2)	1.00536(4)	1.62(3)
Fe(2)	0	0	1.0000	1.64(4)
O(1)	0.1835(3)	0.10434(9)	1.1592(2)	2.0(1)
O(2)	0.1521(3)	0.0416(1)	1.0906(2)	1.9(1)
O(3)	0.1165(3)	0.0021(1)	0.8937(2)	2.4(1)
O(4)	0.2099(4)	0.0665(1)	0.8809(2)	2.7(1)
O(5)	-0.0015(3)	0.1137(1)	0.9734(2)	2.2(1)
O(6)	-0.1160(3)	0.0528(1)	0.9398(2)	2.4(1)
O(7)	0.1711(3)	0.1803(1)	0.2502(2)	2.0(1)
N(1)	0.4273(4)	0.0902(1)	1.0527(3)	2.4(2)
N(2)	0.2590(4)	0.1625(1)	0.9713(3)	1.8(1)
C(1)	0.4826(5)	0.1280(2)	1.0121(4)	2.8(2)
C(2)	0.4002(5)	0.1672(2)	1.0219(4)	2.7(2)
C(3)	0.4757(6)	0.0904(2)	1.1564(4)	4.4(3)
C(4)	0.4810(6)	0.0513(2)	1.0133(5)	4.8(3)
C(5)	0.1757(5)	0.1956(2)	1.0070(3)	2.5(2)
C(6)	0.2557(5)	0.1695(1)	0.8675(3)	2.1(2)
C(7)	0.1181(5)	0.1674(1)	0.8022(3)	2.2(2)
C(8)	0.1422(5)	0.1722(2)	0.6989(3)	2.2(2)
C(9)	0.0186(5)	0.1742(1)	0.6183(3)	1.9(2)
C(10)	-0.0634(6)	0.1337(2)	0.6195(4)	3.6(3)
C(11)	-0.0701(6)	0.2128(2)	0.6341(3)	3.5(2)
C(12)	0.0616(5)	0.1785(1)	0.5202(3)	1.7(2)

[a] $B(\text{eq}) = 8/3\pi^2(U_{11}(aa^*)^2 + U_{22}(bb^*)^2 + U_{33}(cc^*)^2 + 2U_{12}aa^*bb^*\cos\gamma + 2U_{13}aa^*cc^*\cos\beta + 2U_{23}bb^*cc^*\cos\alpha)$

Table 27 contd. Positional Parameters and B(eq) for $[Fe_3(OBz)_6(PheMe_3Eda)_2]$ (**6**).

atom	x	y	z	B(eq)[a]
C(13)	0.1960(5)	0.1806(1)	0.5104(3)	2.0(2)
C(14)	0.2362(4)	0.1822(1)	0.4224(3)	1.7(2)
C(15)	0.1344(5)	0.1814(1)	0.3402(3)	1.7(2)
C(16)	-0.0026(4)	0.1828(1)	0.3461(3)	1.7(2)
C(17)	-0.0346(5)	0.1809(1)	0.4364(3)	1.9(2)
C(18)	0.3872(5)	0.1823(2)	0.4163(3)	2.1(2)
C(19)	0.4763(5)	0.1879(2)	0.5143(4)	3.7(3)
C(20)	0.4242(5)	0.1398(2)	0.3770(4)	3.3(2)
C(21)	0.4192(5)	0.2188(2)	0.3536(4)	3.2(2)
C(22)	-0.1151(5)	0.1856(1)	0.2557(3)	2.0(2)
C(23)	-0.0915(5)	0.2252(2)	0.1974(4)	2.9(2)
C(24)	-0.2547(5)	0.1905(2)	0.2813(4)	3.1(2)
C(25)	-0.1181(5)	0.1460(2)	0.1937(4)	2.8(2)
C(26)	0.1593(4)	0.0644(1)	1.1647(3)	1.7(2)
C(27)	0.1470(5)	0.0447(1)	1.2576(3)	1.9(2)
C(28)	0.1364(6)	0.0698(2)	1.3358(3)	2.7(2)
C(29)	0.1275(6)	0.0502(2)	1.4229(4)	3.8(3)
C(30)	0.1321(6)	0.0065(2)	1.4304(4)	4.0(3)
C(31)	0.1442(6)	-0.0178(2)	1.3537(4)	3.9(3)
C(32)	0.1526(5)	0.0004(1)	1.2658(4)	2.6(2)
C(33)	0.1857(5)	0.0275(2)	0.8559(3)	2.2(2)
C(34)	0.2465(5)	0.0118(1)	0.7740(3)	2.2(2)
C(35)	0.2129(5)	-0.0280(2)	0.7351(3)	2.7(2)

[a] $B(eq) = 8/3\pi^2(U_{11}(aa^*)^2 + U_{22}(bb^*)^2 + U_{33}(cc^*)^2 + 2U_{12}aa^*bb^*\cos\gamma + 2U_{13}aa^*cc^*\cos\beta + 2U_{23}bb^*cc^*\cos\alpha)$

Table 27 contd. Positional Parameters and $B(eq)^a$ for $[Fe_3(OBz)_6(PheMe_3Eda)_2]$ (**6**).

atom	*x*	*y*	*z*	*B*(eq)
C(36)	0.2742(6)	-0.0442(2)	0.6652(4)	3.4(2)
C(37)	0.3722(7)	-0.0219(2)	0.6324(4)	4.4(3)
C(38)	0.4070(9)	0.0176(3)	0.6702(5)	7.0(4)
C(39)	0.3428(8)	0.0347(2)	0.7400(5)	5.7(4)
C(40)	-0.1038(5)	0.0924(1)	0.9372(3)	1.8(2)
C(41)	-0.2198(5)	0.1181(1)	0.8833(3)	1.9(2)
C(42)	-0.3188(5)	0.0986(1)	0.8148(4)	2.4(2)
C(43)	-0.4155(5)	0.1229(2)	0.7585(4)	2.9(2)
C(44)	-0.4222(5)	0.1664(2)	0.7742(4)	3.2(2)
C(45)	-0.3296(5)	0.1855(2)	0.8448(4)	3.3(2)
C(46)	-0.2275(5)	0.1613(2)	0.8983(4)	2.4(2)
H(1)	0.5723	0.1326	1.0448	3.4
H(2)	0.4824	0.1231	0.9463	3.4
H(3)	0.4394	0.1909	0.9961	3.2
H(4)	0.4006	0.1720	1.0879	3.2
H(5)	0.4407	0.0663	1.1840	5.3
H(6)	0.5712	0.0894	1.1695	5.3
H(7)	0.4462	0.1157	1.1828	5.3
H(8)	0.4491	0.0267	1.0410	5.8
H(9)	0.4516	0.0506	0.9460	5.8
H(10)	0.5766	0.0518	1.0278	5.8
H(11)	0.2085	0.2230	0.9949	3.0
H(12)	0.0848	0.1929	0.9751	3.0

$^aB(eq) = 8/3\pi^2(U_{11}(aa^*)^2 + U_{22}(bb^*)^2 + U_{33}(cc^*)^2 + 2U_{12}aa^*bb^*\cos\gamma + 2U_{13}aa^*cc^*\cos\beta + 2U_{23}bb^*cc^*\cos\alpha)$

Table 27 contd. Positional Parameters and $B(eq)^a$ for $[Fe_3(OBz)_6(PheMe_3Eda)_2]$ (**6**).

atom	*x*	*y*	*z*	*B*(eq)
H(13)	0.1806	0.1920	1.0738	3.0
H(14)	0.2921	0.1970	0.8604	2.6
H(15)	0.3112	0.1485	0.8465	2.6
H(16)	0.0765	0.1408	0.8096	2.6
H(17)	0.0623	0.1898	0.8170	2.6
H(18)	0.1918	0.1978	0.6963	2.7
H(19)	0.1949	0.1486	0.6862	2.7
H(20)	-0.0910	0.1311	0.6794	4.3
H(21)	-0.1407	0.1349	0.5699	4.3
H(22)	-0.0101	0.1098	0.6097	4.3
H(23)	-0.0196	0.2383	0.6337	4.2
H(24)	-0.1469	0.2138	0.5843	4.2
H(25)	-0.0980	0.2100	0.6938	4.2
H(26)	0.2635	0.1811	0.5666	2.4
H(27)	-0.1271	0.1813	0.4414	2.3
H(28)	0.4601	0.1652	0.5550	4.4
H(29)	0.5682	0.1875	0.5079	4.4
H(30)	0.4563	0.2143	0.5410	4.4
H(31)	0.4086	0.1175	0.4188	4.0
H(32)	0.3706	0.1352	0.3156	4.0
H(33)	0.5166	0.1400	0.3721	4.0
H(34)	0.5114	0.2175	0.3485	3.9
H(35)	0.3647	0.2163	0.2918	3.9

$^aB(eq) = 8/3\pi^2(U_{11}(aa^*)^2 + U_{22}(bb^*)^2 + U_{33}(cc^*)^2 + 2U_{12}aa^*bb^*\cos\gamma + 2U_{13}aa^*cc^*\cos\beta + 2U_{23}bb^*cc^*\cos\alpha)$

Table 27 contd. Positional Parameters and $B(eq)^a$ for $[Fe_3(OBz)_6(PheMe_3Eda)_2]$ (**6**).

atom	*x*	*y*	*z*	*B*(eq)
H(36)	0.4014	0.2451	0.3814	3.9
H(37)	-0.0053	0.2234	0.1802	3.5
H(38)	-0.1589	0.2266	0.1412	3.5
H(39)	-0.0958	0.2501	0.2348	3.5
H(40)	-0.2562	0.2151	0.3198	3.7
H(41)	-0.3203	0.1932	0.2245	3.7
H(42)	-0.2743	0.1660	0.3157	3.7
H(43)	-0.1386	0.1218	0.2285	3.3
H(44)	-0.1849	0.1492	0.1376	3.3
H(45)	-0.0326	0.1421	0.1764	3.3
H(46)	0.1352	0.1000	1.3305	3.3
H(47)	0.1182	0.0670	1.4768	4.6
H(48)	0.1268	-0.0068	1.4895	4.9
H(49)	0.1472	-0.0479	1.3599	4.7
H(50)	0.1618	-0.0169	1.2127	3.2
H(51)	0.1461	-0.0444	0.7575	3.2
H(52)	0.2482	-0.0714	0.6389	4.1
H(53)	0.4153	-0.0335	0.5843	5.3
H(54)	0.4752	0.0335	0.6483	8.4
H(55)	0.3661	0.0624	0.7643	6.8
H(56)	-0.3189	0.0685	0.8073	2.9
H(57)	-0.4780	0.1098	0.7087	3.4
H(58)	-0.4907	0.1830	0.7363	3.8
H(59)	-0.3356	0.2152	0.8568	3.9
H(60)	-0.1622	0.1747	0.9457	2.9

$^aB(eq) = 8/3\pi^2(U_{11}(aa^*)^2 + U_{22}(bb^*)^2 + U_{33}(cc^*)^2 + 2U_{12}aa^*bb^*\cos\gamma + 2U_{13}aa^*cc^*\cos\beta + 2U_{23}bb^*cc^*\cos\alpha)$

Table 28. U values for $[Fe_3(OBz)_6(PheMe_3Eda)_2]$ (**6**).[a]

atom	U11	U22	U33	U12	U13	U23
Fe(1)	0.0234(4)	0.0185(3)	0.0192(3)	-0.0015(3)	0.0028(3)	0.0007(3)
Fe(2)	0.0274(5)	0.0151(5)	0.0204(5)	-0.0015(4)	0.0057(4)	0.0014(4)
O(1)	0.032(2)	0.020(2)	0.022(2)	-0.003(1)	0.005(1)	0.000(1)
O(2)	0.033(2)	0.021(2)	0.021(2)	-0.003(1)	0.007(1)	-0.000(1)
O(3)	0.035(2)	0.031(2)	0.029(2)	-0.009(2)	0.012(2)	0.001(2)
O(4)	0.051(2)	0.027(2)	0.026(2)	-0.009(2)	0.014(2)	-0.004(2)
O(5)	0.023(2)	0.027(2)	0.033(2)	0.002(2)	-0.001(2)	0.000(2)
O(6)	0.029(2)	0.021(2)	0.038(2)	0.000(1)	0.002(2)	0.005(1)
O(7)	0.028(2)	0.033(2)	0.016(2)	-0.003(1)	0.010(1)	0.000(1)
N(1)	0.026(2)	0.034(2)	0.028(2)	0.007(2)	0.000(2)	0.002(2)
N(2)	0.026(2)	0.023(2)	0.018(2)	-0.000(2)	0.005(2)	0.002(2)
C(1)	0.023(3)	0.052(3)	0.031(3)	-0.002(2)	0.004(2)	0.005(3)
C(2)	0.028(3)	0.034(3)	0.036(3)	-0.007(2)	-0.003(2)	0.003(2)
C(3)	0.034(3)	0.097(5)	0.033(3)	0.004(3)	-0.001(3)	0.022(3)
C(4)	0.045(4)	0.041(4)	0.096(5)	0.017(3)	0.011(4)	-0.008(3)
C(5)	0.043(3)	0.026(3)	0.027(3)	0.002(2)	0.007(2)	-0.002(2)
C(6)	0.033(3)	0.030(3)	0.021(2)	0.002(2)	0.013(2)	0.005(2)
C(7)	0.034(3)	0.027(3)	0.023(3)	0.005(2)	0.009(2)	0.003(2)
C(8)	0.030(3)	0.033(3)	0.023(3)	0.005(2)	0.007(2)	0.006(2)
C(9)	0.028(3)	0.029(3)	0.019(2)	-0.002(2)	0.012(2)	0.000(2)
C(10)	0.051(4)	0.060(4)	0.028(3)	-0.021(3)	0.013(3)	0.003(3)
C(11)	0.047(4)	0.064(4)	0.022(3)	0.027(3)	0.010(3)	0.005(3)
C(12)	0.023(2)	0.021(2)	0.022(2)	0.000(2)	0.010(2)	0.002(2)
C(13)	0.023(3)	0.032(3)	0.021(2)	0.001(2)	0.004(2)	-0.000(2)

[a]Estimated standard deviations in the least significant figure are given in parentheses. The anisotropic temperature factors are of the form $\exp[-2\pi^2(U_{11}h^2a^{*2}... + 2U_{12}hka^*b^* + ...)]$.

Table 28 contd. U values for $[Fe_3(OBz)_6(PheMe_3Eda)_2]$ (**6**).[a]

atom	U11	U22	U33	U12	U13	U23
C(14)	0.024(3)	0.018(2)	0.026(3)	0.000(2)	0.010(2)	-0.001(2)
C(15)	0.026(3)	0.020(2)	0.020(2)	0.000(2)	0.010(2)	-0.002(2)
C(16)	0.025(3)	0.017(2)	0.023(2)	-0.004(2)	0.007(2)	0.000(2)
C(17)	0.022(3)	0.028(3)	0.025(3)	-0.001(2)	0.009(2)	-0.003(2)
C(18)	0.018(2)	0.034(3)	0.028(3)	-0.003(2)	0.006(2)	-0.004(2)
C(19)	0.021(3)	0.079(4)	0.040(3)	-0.003(3)	0.005(2)	-0.014(3)
C(20)	0.033(3)	0.048(3)	0.047(3)	0.005(3)	0.012(3)	-0.003(3)
C(21)	0.028(3)	0.046(3)	0.051(4)	-0.008(3)	0.011(3)	0.005(3)
C(22)	0.023(3)	0.029(3)	0.024(3)	0.003(2)	0.006(2)	-0.001(2)
C(23)	0.034(3)	0.038(3)	0.039(3)	0.005(2)	0.005(3)	0.011(2)
C(24)	0.025(3)	0.054(4)	0.037(3)	0.002(3)	0.002(2)	0.002(3)
C(25)	0.033(3)	0.035(3)	0.034(3)	-0.005(2)	-0.002(2)	-0.008(2)
C(26)	0.016(2)	0.020(2)	0.027(3)	0.003(2)	0.001(2)	-0.002(2)
C(27)	0.028(3)	0.024(3)	0.021(2)	0.001(2)	0.006(2)	-0.001(2)
C(28)	0.051(3)	0.028(3)	0.025(3)	-0.004(3)	0.010(3)	0.001(2)
C(29)	0.064(4)	0.062(4)	0.021(3)	-0.005(3)	0.011(3)	0.001(3)
C(30)	0.066(4)	0.059(4)	0.029(3)	-0.001(3)	0.010(3)	0.020(3)
C(31)	0.068(4)	0.033(3)	0.046(4)	-0.002(3)	0.004(3)	0.015(3)
C(32)	0.043(3)	0.023(3)	0.033(3)	-0.001(2)	0.004(3)	0.005(2)
C(33)	0.029(3)	0.033(3)	0.019(2)	-0.003(2)	-0.001(2)	-0.001(2)
C(34)	0.035(3)	0.031(3)	0.021(2)	-0.002(2)	0.009(2)	0.002(2)
C(35)	0.039(3)	0.036(3)	0.028(3)	-0.000(2)	0.008(2)	-0.001(2)
C(36)	0.059(4)	0.036(3)	0.036(3)	0.007(3)	0.012(3)	-0.003(3)
C(37)	0.062(4)	0.072(5)	0.038(3)	-0.002(4)	0.020(3)	-0.015(3)

[a]Estimated standard deviations in the least significant figure are given in parentheses. The anisotropic temperature factors are of the form $\exp[-2\pi^2(U_{11}h^2a^{*2}... + 2U_{12}hka^*b^* + ...)]$.

Table 28 contd. U values for $[Fe_3(OBz)_6(PheMe_3Eda)_2]$ (**6**).[a]

atom	U11	U22	U33	U12	U13	U23
C(38)	0.129(7)	0.093(6)	0.068(5)	-0.054(5)	0.077(5)	-0.033(4)
C(39)	0.109(6)	0.064(4)	0.058(4)	-0.040(4)	0.056(4)	-0.032(4)
C(40)	0.028(3)	0.020(3)	0.020(2)	-0.001(2)	0.006(2)	0.001(2)
C(41)	0.024(3)	0.022(3)	0.028(3)	-0.004(2)	0.006(2)	0.004(2)
C(42)	0.028(3)	0.023(2)	0.038(3)	0.002(2)	-0.000(2)	0.005(2)
C(43)	0.030(3)	0.044(3)	0.032(3)	-0.001(2)	-0.001(2)	0.002(2)
C(44)	0.030(3)	0.049(4)	0.041(3)	0.009(3)	0.001(3)	0.014(3)
C(45)	0.040(3)	0.023(3)	0.062(4)	0.009(2)	0.011(3)	0.008(3)
C(46)	0.023(3)	0.029(3)	0.038(3)	-0.003(2)	0.002(2)	0.001(2)

[a]Estimated standard deviations in the least significant figure are given in parentheses. The anisotropic temperature factors are of the form $\exp[-2\pi^2(U_{11}h^2a^{*2}... + 2U_{12}hka^*b^* + ...)]$.

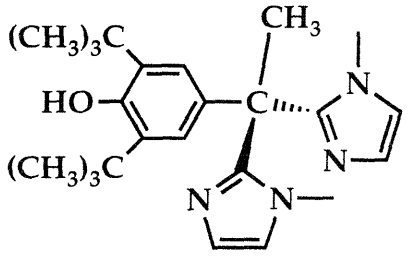

BIDPhEH

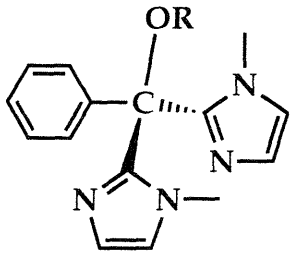

BIPhMe R = CH_3
BIPhOH R = H

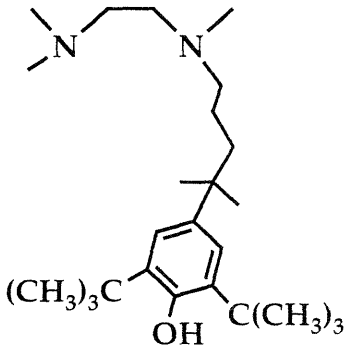

$PheMe_3Eda$

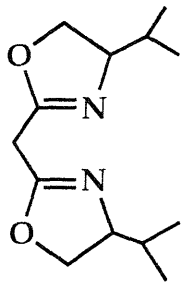

$^{i}PrOx$

Figure 1. Bidentate nitrogen donor ligands used in this study.

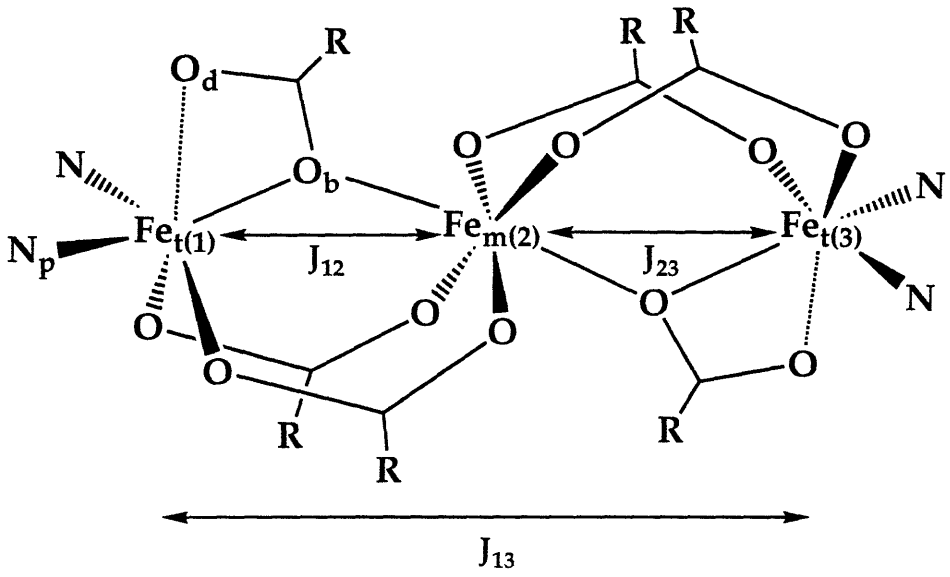

Figure 2. Generalized structure of the triiron(II) complexes.

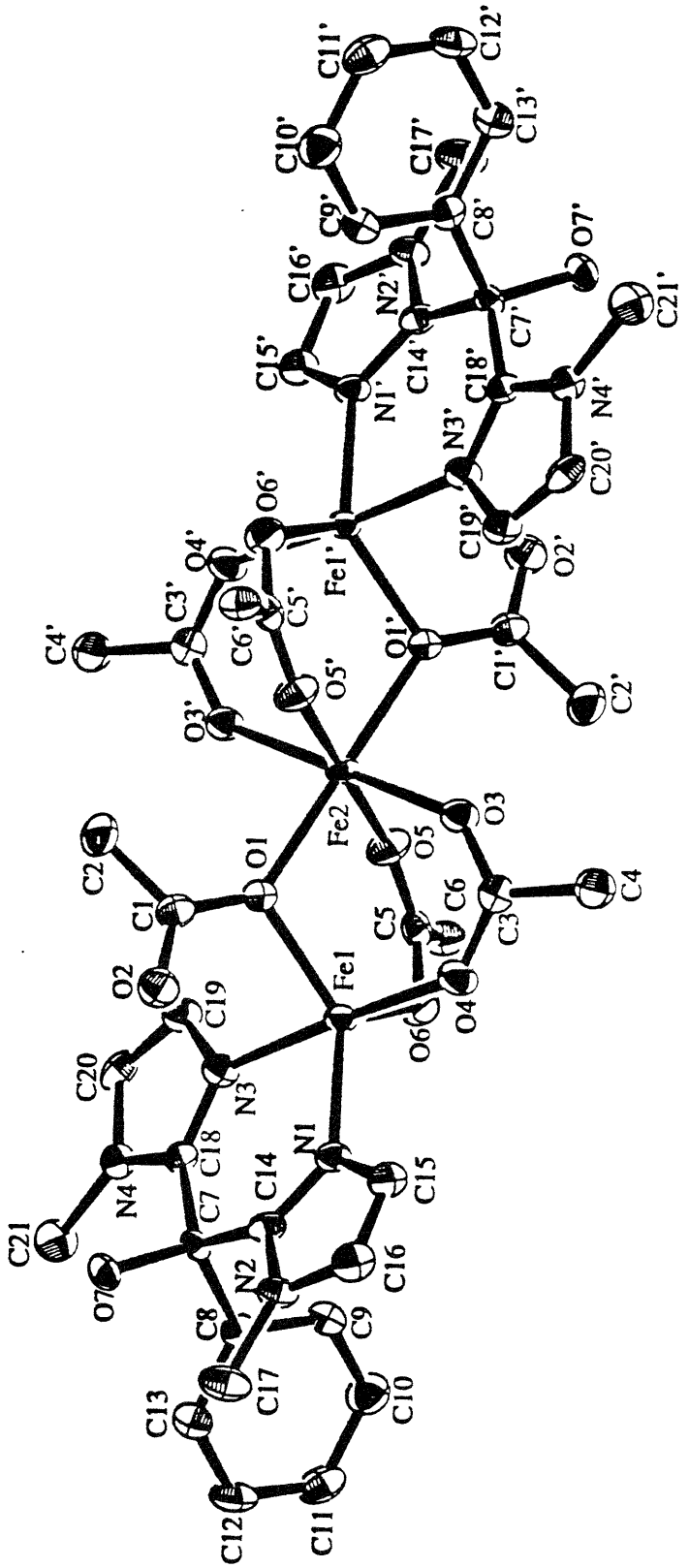

Figure 3. ORTEP diagram of $[Fe_3(OAc)_6(BIPhOH)_2]$ **(3)** showing the 50% probability thermal ellipsoids. Hydrogen atoms have been removed for clarity.

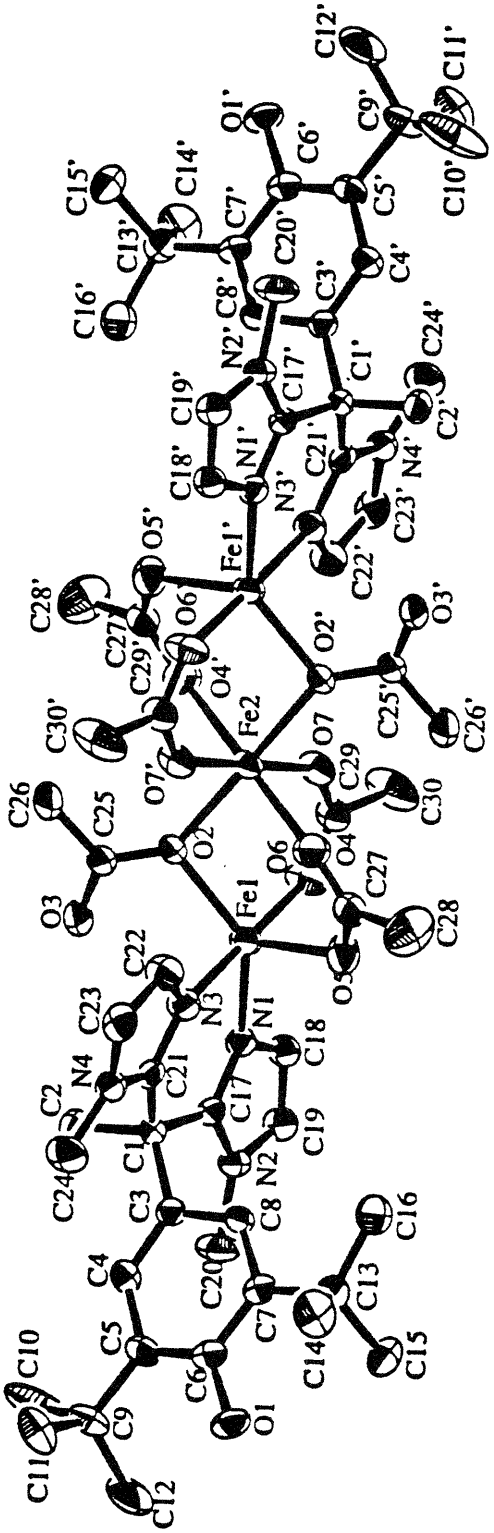

Figure 4. ORTEP diagram of $[Fe_3(OAc)_6(BIDPhEH)_2]$ (**4**) showing the 50% probability thermal ellipsoids. Hydrogen atoms have been removed for clarity.

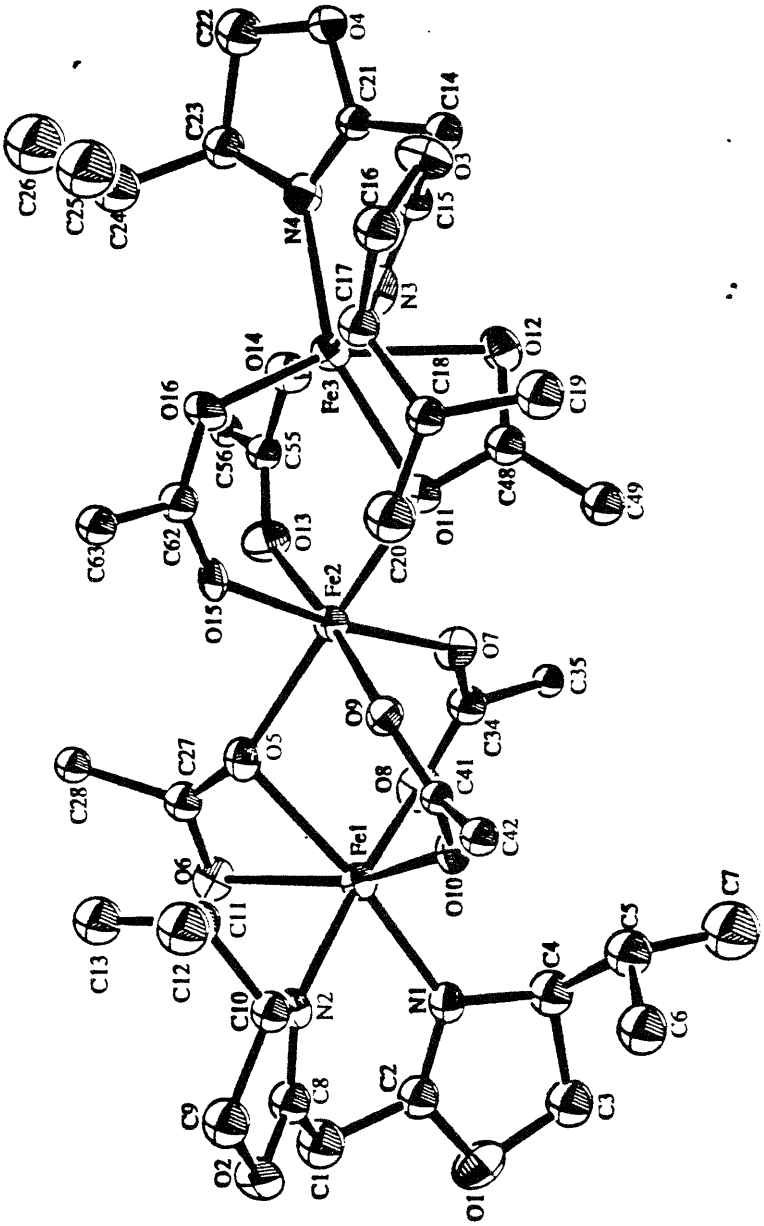

Figure 5. ORTEP diagram of $[Fe_3(OBz)_6(^iPrOx)_2]$ (5) showing the 50% probability thermal ellipsoids. All benzoate ring carbon atoms, except for the position of carboxylate attachment, and hydrogen atoms have been removed for clarity.

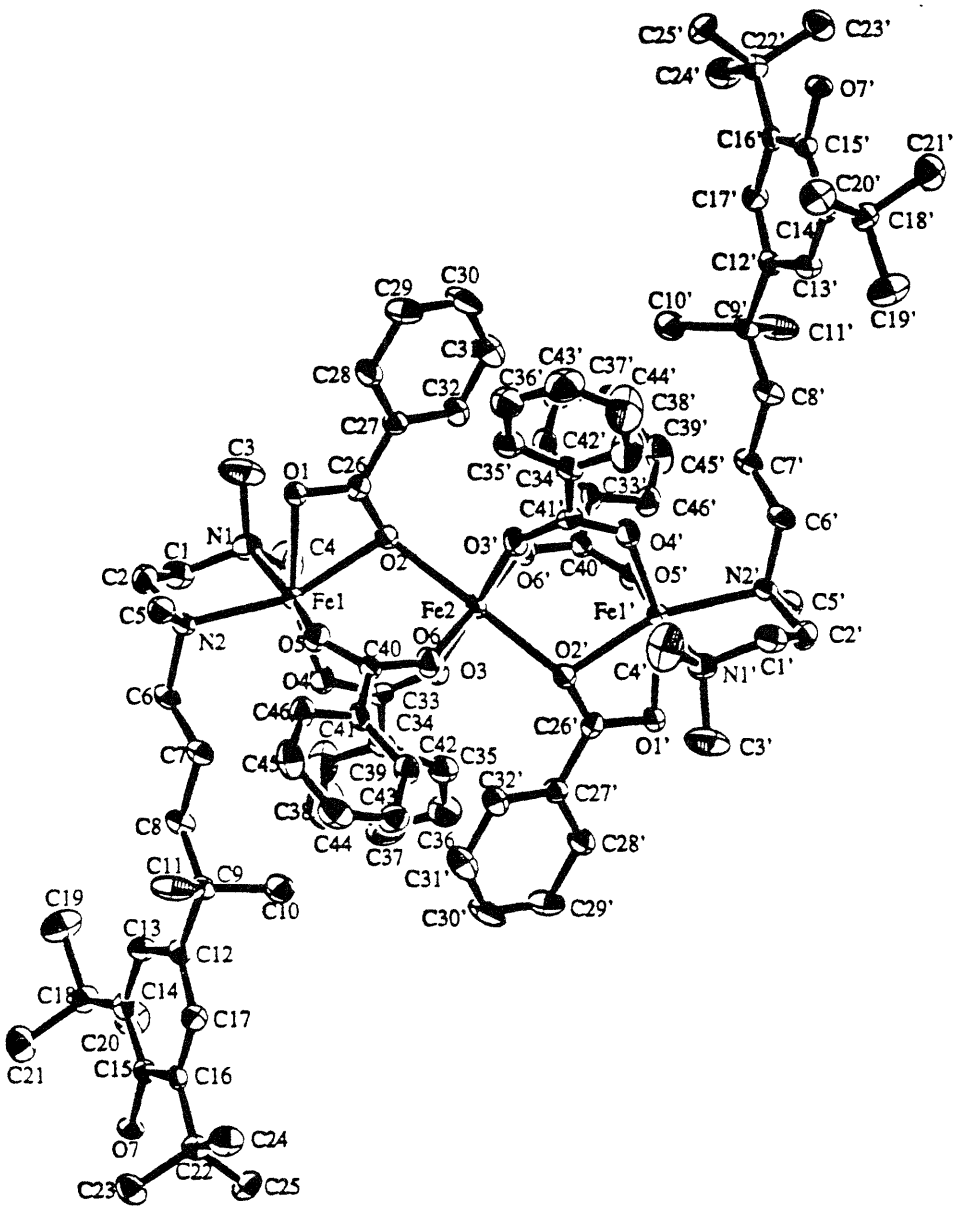

Figure 6. ORTEP diagram of $[Fe_3(OBz)_6(PheMe_3Eda)_2]$ (**6**) showing the 50% probability thermal ellipsoids. Hydrogen atoms have been removed for clarity.

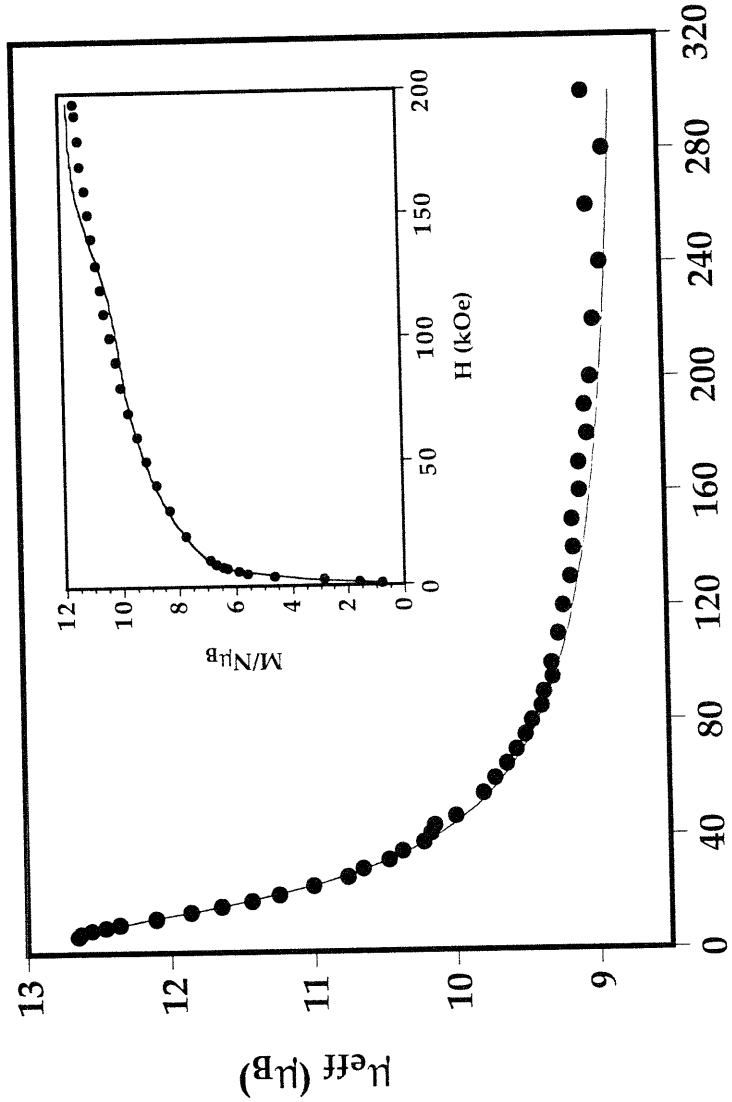

Figure 7. Plot of the effective magnetic moment vs. temperature for a polycrystalline sample of **1**, together with the best fit (solid line, energies in cm^{-1}): J = -3.97, $D_{1,3}$ = -3.45, D_2 = -0.46, $g_\perp(Fe_{1,3})$ = 2.08, $g_\parallel(Fe_{1,3})$ = 1.98, $g_\perp(Fe_2)$ = 1.99, $g_\parallel(Fe_2)$ = 2.02. Inset: Plot of the reduced magnetization vs. field for a polycrystalline sample of **1**, together with the best fit (solid line, energies in cm^{-1}): J = -4.00 (fixed), $D_{1,3}$ = 6.45, D_2 = -10.1, all g values fixed at 2.00.

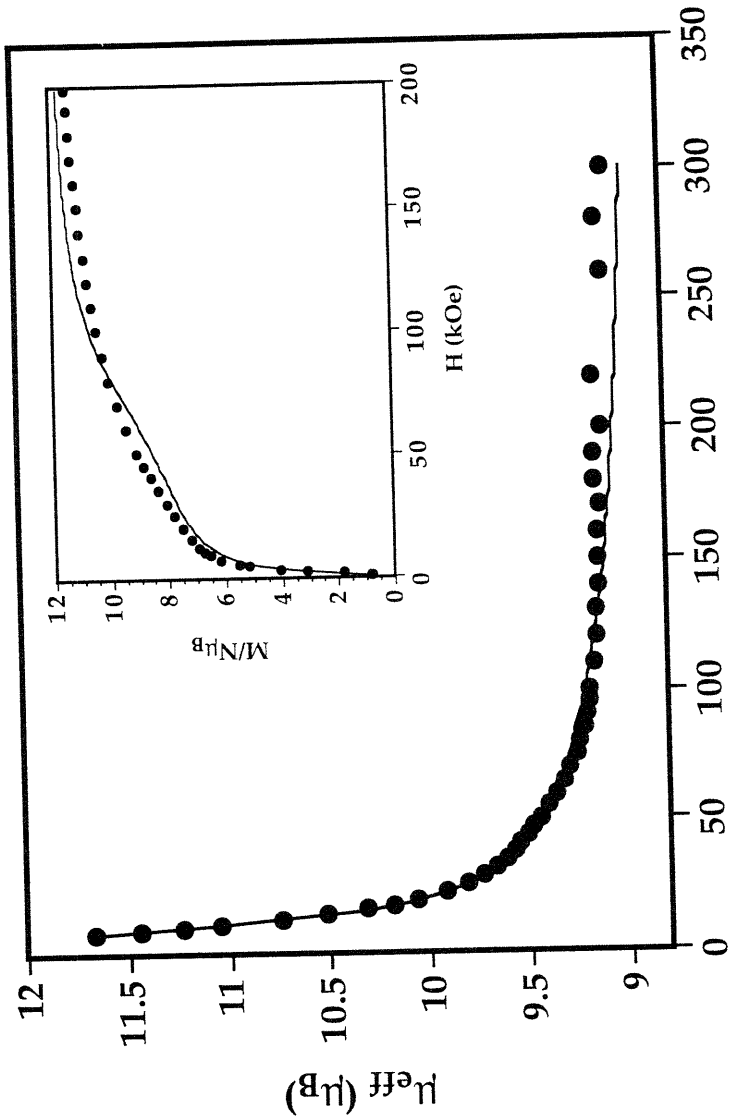

Figure 8. Plot of the effective magnetic moment vs. temperature for a polycrystalline sample of **3**, together with the best fit (solid line, energies in cm^{-1}): J = -2.81, $D_{1,3}$ -19.2, D_2 = +1.89, $g_{\perp}(Fe_{1,3})$ = 2.16, $g_{\parallel}(Fe_{1,3})$ = 2.00, $g_{\perp}(Fe_2)$ = 2.08, $g_{\parallel}(Fe_2)$ = 2.00. Inset: Plot of the reduced magnetization vs. field for a polycrystalline sample of **3**, together with the best fit (solid line, energies in cm^{-1}): J = -0.176, $D_{1,3}$ = -5.0, D_2 = 0.0, all g values fixed equal to 2.00.

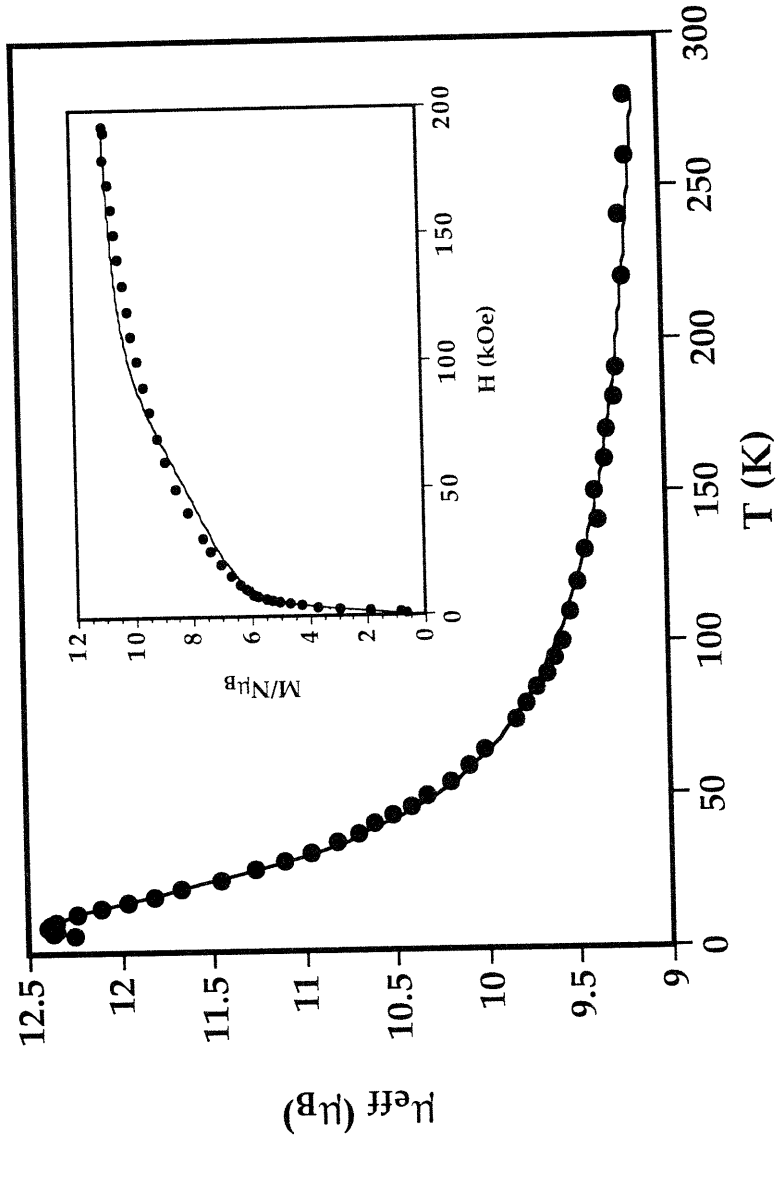

Figure 9. Plot of the effective magnetic moment vs. temperature for a polycrystalline sample of **4**, together with the best fit (solid line, energies in cm^{-1}): J = -4.80, $D_{1,3}$ = 5.85, D_2 = 4.82, $g_\perp(Fe_{1,3})$ = 2.00, $g_\parallel(Fe_{1,3})$ = 2.38, $g_\perp(Fe_2)$ = 2.00, $g_\parallel(Fe_2)$ = 2.02. Inset: Plot of the reduced magnetization vs. field for a polycrystalline sample of **4**, together with the best fit (solid line, energies in cm^{-1}): J = -5.0 (fixed), $D_{1,3}$ = -5.0, D_2 = 0.0, all g values fixed equal to 2.00.

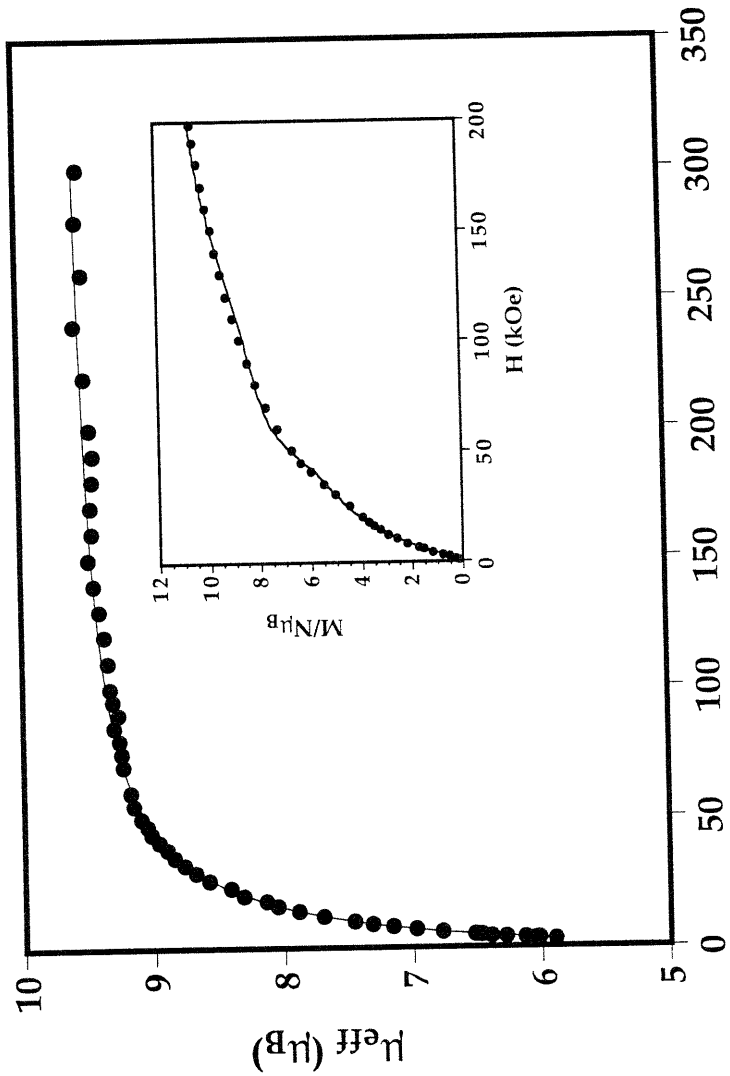

Figure 10. Plot of the effective magnetic moment vs. temperature for a polycrystalline sample of **5**, together with the best fit (solid line, energies in cm^{-1}): J = +0.99, $D_{1,3}$ = 0.0 (fixed), D_2 = -11.5, $g_\perp(Fe_{1,3})$ = 2.14, $g_\parallel(Fe_{1,3})$ = 2.01, $g_\perp(Fe_2)$ = 2.78, $g_\parallel(Fe_2)$ = 2.13. Inset: Plot of the reduced magnetization vs. field for a polycrystalline sample of **5**, together with the best fit (solid line, energies in cm^{-1}): J = +0.72, $D_{1,3}$ = 0.0 (fixed), D_2 = -12.2, $g_\perp(Fe_{1,3})$ = 1.76, $g_\parallel(Fe_{1,3})$ = 1.42, $g_\perp(Fe_2)$ = 3.03, $g_\parallel(Fe_2)$ = 1.27.

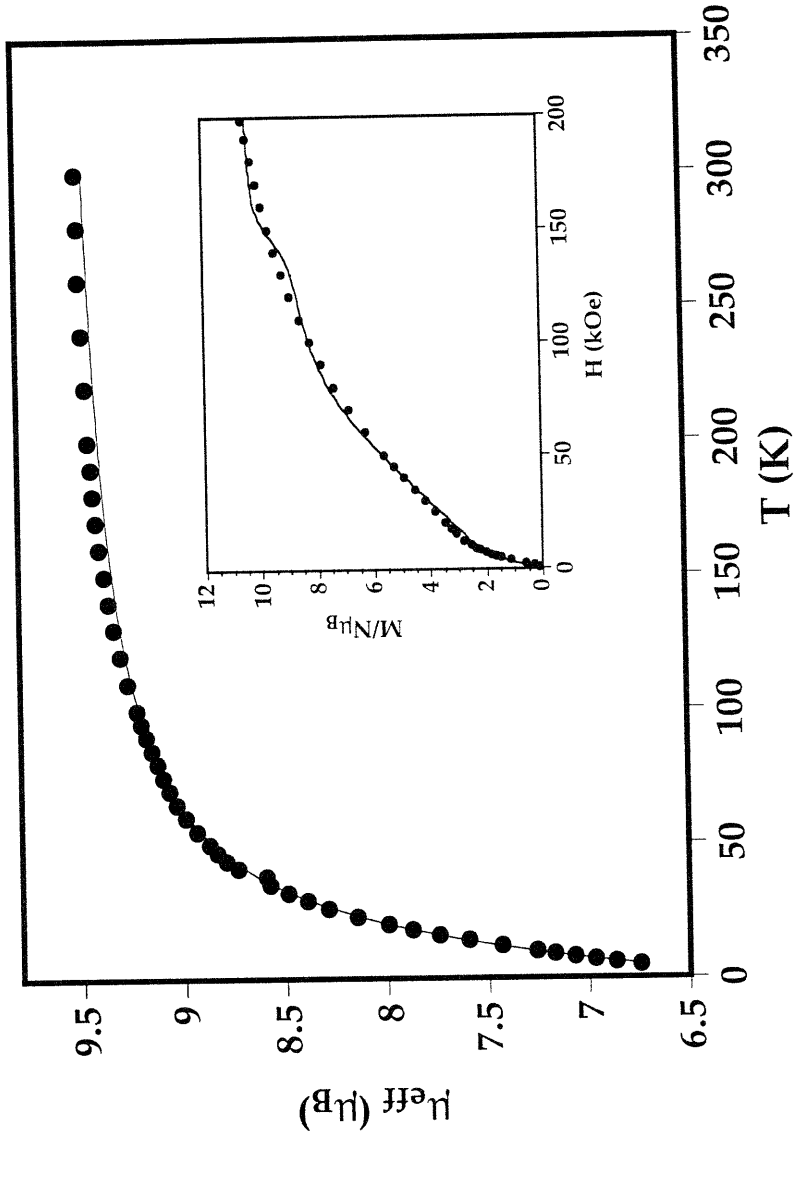

Figure 11. Plot of the effective magnetic moment vs. temperature for a polycrystalline sample of **6**, together with the best fit (solid line, energies in cm^{-1}): $J = +1.00$, $D_{1,3} = 0.0$ (fixed), $D_2 = -11.3$, $g_\perp(Fe_{1,3}) = 2.20$, $g_\parallel(Fe_{1,3}) = 1.93$, $g_\perp(Fe_2) = 2.94$, $g_\parallel(Fe_2) = 1.31$. Inset: Plot of the reduced magnetization vs. field for a polycrystalline sample of 6, together with the best fit (solid line, energies in cm-1): $J = +1.51$, $D_{1,3} = -3.2$, $D_2 = -10.7$, $g_\perp(Fe_{1,3}) = 2.88$, $g_\parallel(Fe_{1,3}) = 1.66$, $g_\perp(Fe_2) = 0.97$, $g_\parallel(Fe_2) = 0.90$.

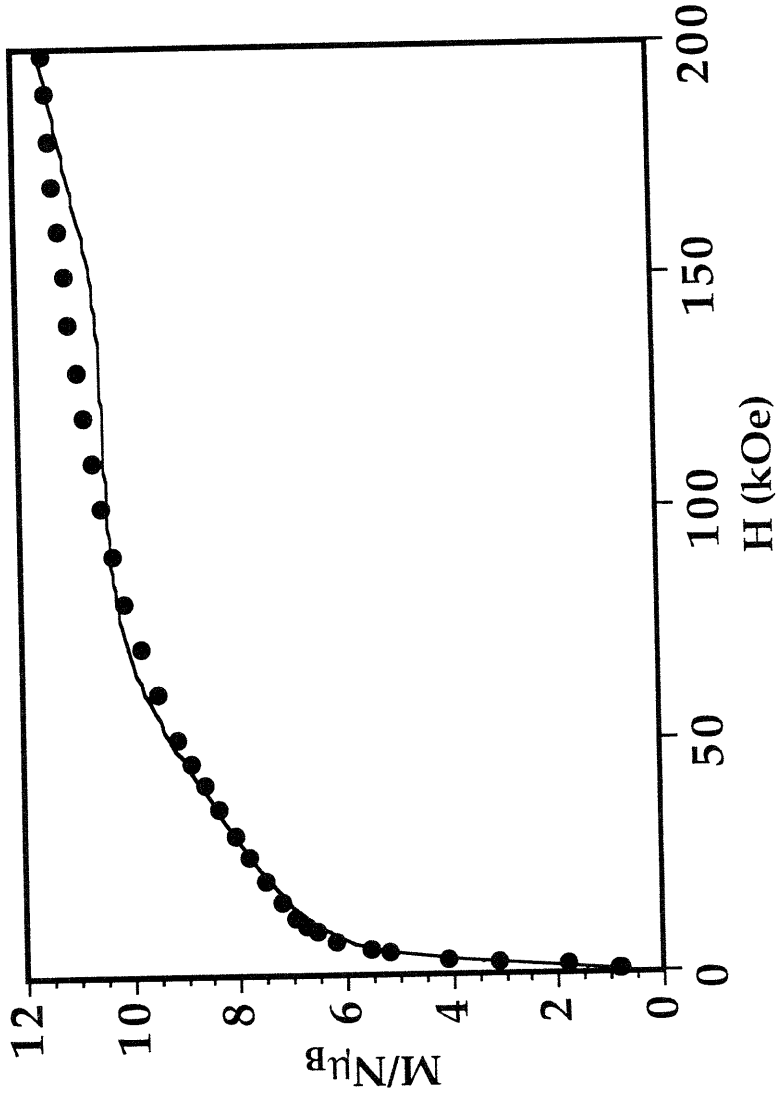

Figure 12. Plot of the reduced magnetization vs. field for **3** and a fit including terminal-terminal coupling, with all g values fixed at 2.00. Final parameters were (solid line, energies in cm^{-1}): $J_{12} = J_{23} = -1.75$, $J_{13} = +0.96$, $D_{1,3} = 6.1$, $D_2 = 0.77$.

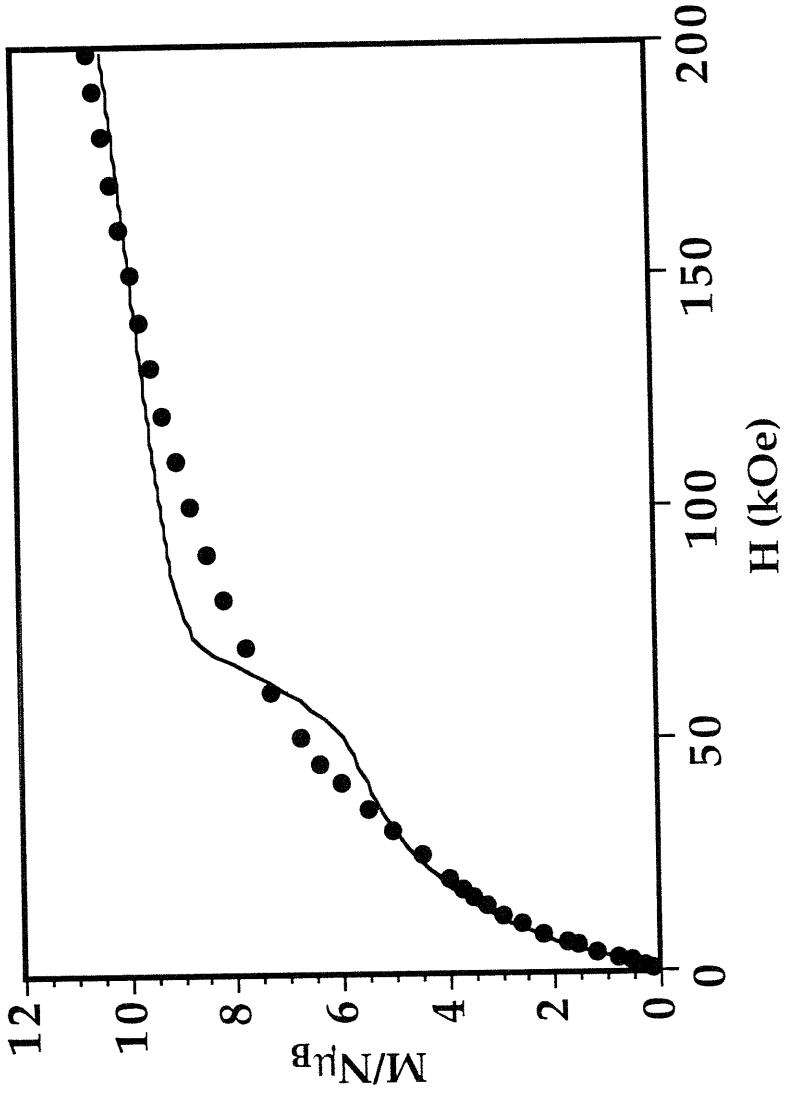

Figure 13. Plot of the reduced magnetization vs. field for **5** and a fit in which all *g* values were fixed at 2.00. The final parameters were (solid line, energies in cm^{-1}): J = +1.45, $D_{1,3}$ = 0.09, D_2 = -11.1.

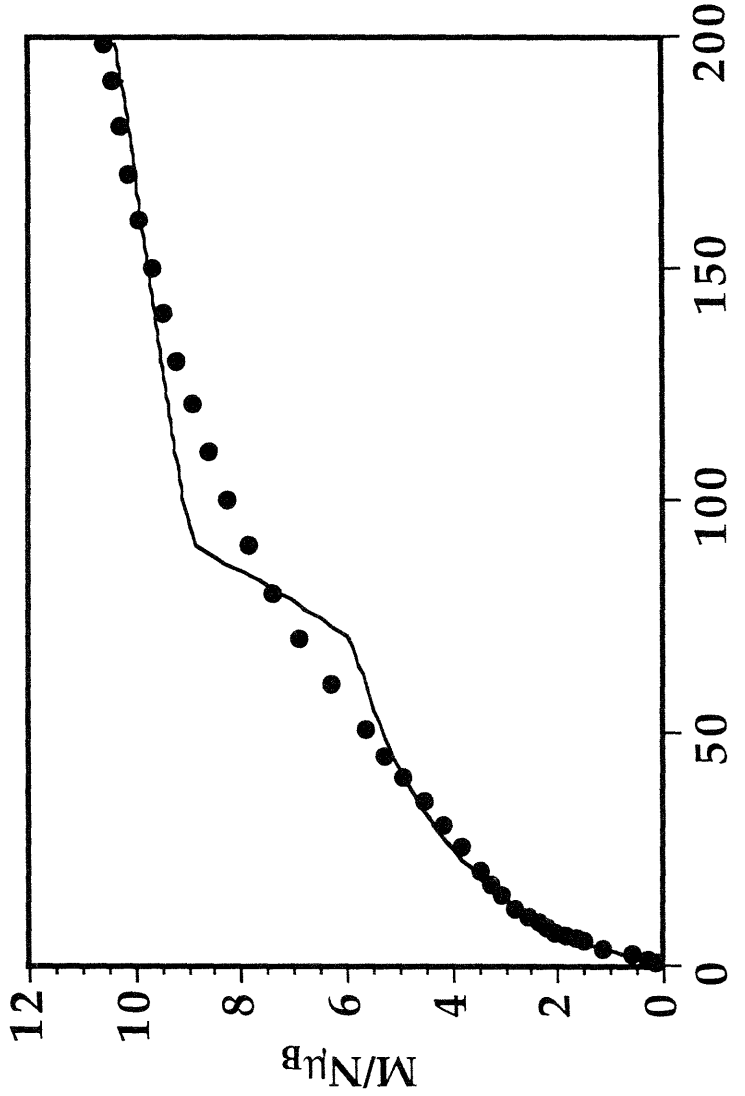

Figure 14. Plot of the reduced magnetization vs. field for **6** and a fit in which all g values were fixed at 2.00. The final parameters were (solid line, energies in cm^{-1}): J = +1.83, $D_{1,3}$ = -0.08, D_2 = -8.8.

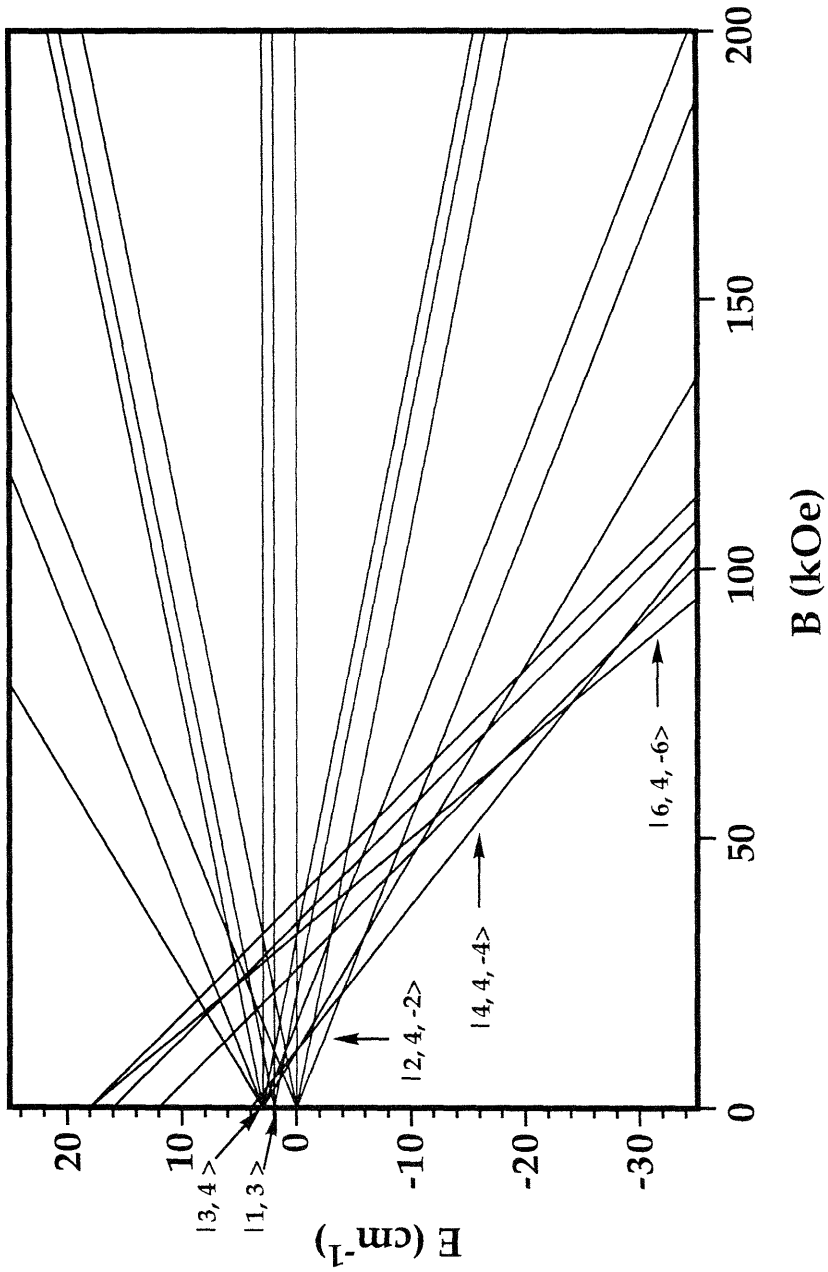

Figure 15. Schematic energy level diagram of complexes **5** and **6** showing the relative energies of the lower spin state manifolds vs. applied magnetic field.

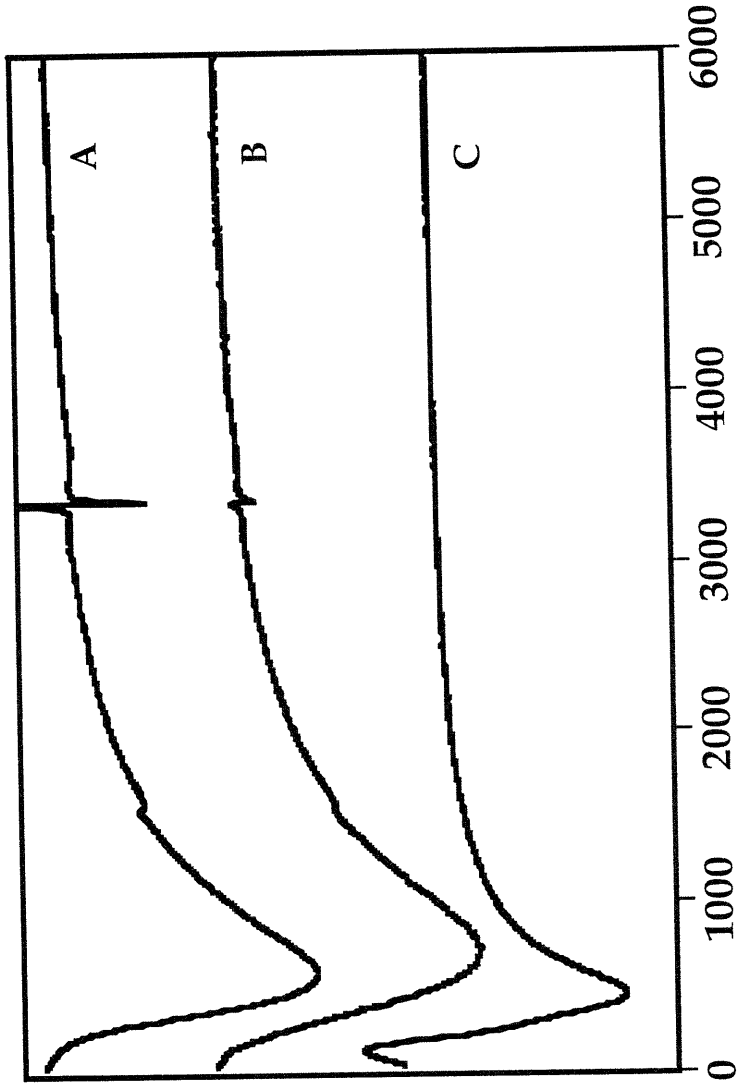

Figure 16. X-band EPR spectra at 4 K for polycrystalline samples of complexes (A) **1** (B) **3** and (C) **4**. The $g \approx 4.3$ signal probably arises from a small amount of mononuclear ferric impurity.

Chapter 4

A Decanuclear Manganese Cluster with Oxo and Halide Bridging Ligands : Magnetic Behavior of an S ≥ 12 System

Introduction

The synthesis and magnetic properties of high-nuclearity (≥ 4) manganese compounds have been the focus of intense research efforts in recent years. The large majority of these compounds are composed of manganese atoms in the +2, +3, or +4 oxidation states, with carboxylato and oxo ligands forming the bridges between metal centers. Impetus for studying the structural and physical properties of this class of molecules has come from a variety of sources. Understanding the structure and function of the polynuclear manganese core in Photosystem II is essential to unravelling the reductive coupling of water to form dioxygen, a key consequence of photosynthesis.[1] Important to this understanding is the development of a broad database of structurally-characterized polynuclear manganese complexes in which physical properties, such as magnetic exchange interactions, EPR spectra, and electrochemical behavior are well understood and can be rationalized with the structural information.

Polynuclear compounds of iron and manganese are interesting as possible molecular units for the construction of magnetic materials. Long-range magnetic ordering in these materials depends on the individual molecular units having large numbers of unpaired electrons, which can exhibit high spin multiplicities.[2] Another feature of high nuclearity spin clusters is their potential for providing examples of structurally characterized nanometer-scale materials in which each cluster can be considered as an independent single domain particle.[3,4]

With the above areas of interest in mind, we and others have synthesized a variety of polynuclear iron and manganese complexes and characterized them crystallographically, and by a number of other physical techniques. Several Mn_4 compounds have been prepared which exhibit

either a "butterfly"[5,6] or "distorted cubane"[7-10] structural motif, and form the basic unit of many of the higher nuclearity assemblies. Discrete complexes containing more than 4 atoms are considerably fewer in number. Examples include three Mn_6 compounds, one of which has six Mn(II) ions arranged in a ring and bridged by nitronyl nitroxide ligands,[11] the other two comprising smaller Mn_4O_2 butterfly-type units.[12-15] An Mn_7 compound has been described with six Mn(III) atoms and one Mn(II) atom, arranged as two butterfly-type units sharing one wing-tip metal atom,[16] and a similar Mn_7 compound with all Mn(III) atoms has been reported.[17] The preparation of three types of Mn_8 compounds has been accomplished by using Mn_4 butterfly-type compounds as starting materials, and these octanuclear complexes reveal structures consistent with a shared motif of this kind.[18-21] The two structural types of Mn_9 compounds reported thus far are each also composed of smaller, butterfly-type Mn_4O_2 units. One type is mixed-valent with eight Mn(III) atoms and one central Mn(II) atom linking two butterfly units through salicylate bridging ligands,[22] whereas the other type has nine Mn atoms in the +3 oxidation state with oxo, carboxylato bridges and either pyridine ligands[23] or an $[Na_2(O_2CPh)_2(MeCN)_2]$ unit occupying external coordination sites.[19]

The two known Mn_{10} complexes, plus the one described here, are distinguished by their novel architectures, which are not composed of Mn_4O_2 butterfly-type units, and are assembled in the absence of carboxylate ligands. One of these molecules, $[Mn_{10}O_{14}(tren)_6](CF_3SO_3)_8$ (tren = $N(CH_2CH_2NH_2)_3$), is an $Mn(III)_4Mn(IV)_6$ compound with a layered structure resembling the manganese oxide minerals chalcophanite and lithiophorite.[24] Another Mn_{10} compound, $(Et_4N)_2[Mn_{10}O_2Cl_8\{(OCH_2)_3CMe_3\}_6]$, is an $Mn(III)_8Mn(II)_2$ complex which is held together by multiply-bridging oxo groups and six tris-alkoxy donor ligands.[25]

A single undecanuclear complex has been prepared and crystallographically characterized, with the formula $[Mn_{11}O_{10}Cl_{12}(OAc)_{11}(bpy)_2(MeCN)_2(H_20)_2](ClO_4)_2 \cdot 8MeCN$. This species is mixed-valent, with two $[Mn(III)_3Mn(IV)O_3Cl]^{6+}$ distorted cubane subunits linked by a central linear $Mn(III)_3O_4$ unit. The cubane substructures are similar to species mentioned above, but the linear Mn_3 unit has not been observed in a discrete molecular species. This compound was prepared by addition of the carboxylate-abstracting agent Me_3SiCl to an Mn_4 butterfly-type starting material, a procedure employed with great success by Christou et al. for the preparation of higher-nuclearity products.[26]

A dodecanuclear manganese complex, containing 8 metal atoms in the +3 oxidation state and four in the +4 state, was first reported by Lis.[27] This cluster exhibited spectacular magnetic properties, including a high spin $S = 10$ ground state[28] and a highly anisotropic magnetization, as well as a remarkably long magnetization relaxation time which gives rise to a pronounced magnetic hysteretic effect.[29] Recently a reduced form of this complex has been prepared, containing four Mn(IV) and seven Mn(III) atoms, and one Mn(II) atom.[30] The Mn_6 nitronyl nitroxide compound[11] described above is the only other discrete molecule, beside the Mn_{10} cluster described here, which exhibits a spin multiplicity exceeding $S = 10$. A hexadeca manganese aggregate has also been crystallographically characterized, of formula $[Mn_{16}Ba_8Na_2ClO_4(OH)_4(CO_3)_4(H_2O)_{22}L_8]$ (L = 1,3-diamino-2-hydroxypropane-N,N,N',N'-tetraacetic acid). This compound has the highest nuclearity known for a discrete manganese complex, but the magnetic properties have as yet not been described.[31]

The synthesis, structure and magnetic properties of $[Me_4N]_4[(Mn_{10}O_4(biphen)_4Cl_{12}]$ (**1**)[32] were communicated previously, and we

present here the preparation and crystallographic characterization of two new bromide analogues of **1**, $[Me_4N]_4[(Mn_{10}O_4(biphen)_4Br_{12}]$ (**2**) and $[Et_3NH]_2[Mn(CH_3CN)_4(H_2O)_2](Mn_{10}O_4(biphen)_4Br_{12}]$ (**3**). A comprehensive description of the magnetic behavior and high-spin ground states of these clusters is provided through single-crystal magnetic susceptibility, magnetization and EPR measurements on **3**, as well as by powder susceptibility and high-field magnetization measurements on **2**. Values of $12 \leq S \leq 14$ for the ground states of compounds **1 - 3** are indicated by all of the magnetic data. The single crystal EPR data provide a direct experimental measure of the overall axial zero-field splitting parameter, D, for the $S = 12$ ground state of compound **3**. A satisfactory theoretical simulation of the magnetization data was made by using the two empirically determined values for S and D. A theoretical treatment of the magnetic properties of these molecules is presented through a series of three models of increasing complexity. These models successfully explain the high spin ground states of **1, 2,** and **3** in terms of the magnetic exchange coupling between the ten metal spin sites and are fully consistent with all of the magnetic data.

Experimental Section

General Methods. All materials were obtained from commercial sources and used as received. Where indicated, manipulations and reactions were carried out under an inert atmosphere in a Vacuum Atmospheres drybox. FTIR spectra were obtained by using a Bio-Rad SPC3200 FTIR instrument.

$[Me_4N]_4[(Mn_{10}O_4(biphen)_4X_{12}]$ (X = Cl, (1); X = Br, (2)). To a solution of $MnCl_2{\cdot}4H_2O$ (0.40 g, 2.0 mmol) and biphenH_2 (0.90 g, 4.8 mmol) in EtOH (10 mL) was added $Me_4NOH{\cdot}4H_2O$ (0.09 g, 0.50 mmol) to give a dark red-brown

solution. The reaction mixture was stirred for 15 min and filtered to remove a brown precipitate. Layering or slow vapor diffusion of CH_2Cl_2 into the filtrate gave **1** as a dark red-brown crystalline solid. This material was isolated by filtration and air-dried, affording 0.060 g (14 %) of product. The same procedure was followed to give 0.080 g (15 %) of **2** as a dark red-brown crystalline solid. Anal. Calcd. for **1**·CH_2Cl_2, $Mn_{10}C_{65}H_{82}Cl_{14}N_4O_{12}$ (M_r 2086.20): C, 36.19; H, 3.83; N, 2.60. Found: C, 35.95; H, 3.80; N, 2.54. Upon heating **1** at 111°C under vacuum for 24 h, the lattice solvent was removed. Anal. Calcd. for **1**, $Mn_{10}C_{64}H_{80}Cl_{12}N_4O_{12}$ (M_r 2072.17): C, 37.10; H, 3.89; N, 2.70. Found: C, 36.86; H, 3.85; N, 2.57. FTIR (KBr pellet): 1497, 1477, 1433, 1294, 1271, 1252, 1217, 1158, 1123, 1100, 1049, 1006, 948, 859, 837, 767, 729, 713, 669, 640, 611, 591, 540, 429 cm^{-1}. Anal. Calcd. for **2**, $Mn_{10}C_{64}H_{80}Br_{12}N_4O_{12}$ (M_r 2605.59): C, 29,50; H, 3.09; N, 2.15. Found: C, 29.21; H, 3.85; N, 2.70.

$[Et_3NH]_2[Mn(CH_3CN)_4(H_2O)_2](Mn_{10}O_4(biphen)_4Br_{12}] \cdot 6CH_3CN \cdot 2.5H_2O \cdot C_6H_6$ ($3 \cdot 6CH_3CN \cdot 2.5H_2O \cdot C_6H_6$). To a solution of $MnBr_2 \cdot 4H_2O$ (1.1 g, 3.83 mmol) and biphenH_2 (2.2 g, 11.8 mmol) in CH_3CN (90 mL) was added Et_3N (0.25 mL, 1.79 mmol) to give a dark red-brown solution. The reaction mixture was stirred for 15 min and filtered. Vapor diffusion of C_6H_6 into the CH_3CN reaction filtrate gave **3** as tetragonally-shaped dark red-brown crystals. Due to the slow air decomposition of crystals of **3** upon filtration and standing in air, the mother liquor containing crystals of **3** was degassed and brought into a glovebox. The crystals were isolated by decanting the mother liquor, and washed with pentane (5 x 10 mL) and dried under vacuum for 10 min, to give 0.435 g (36 %) of **3** as a crystalline solid. The presence of benzene was confirmed by the ^1H NMR spectrum of **3** in DMSO-d_6. Crystals of **3** were washed extensively with pentane and dried briefly in vacuum prior to the NMR measurement. The assignment of the benzene peak (δ 7.24) was

corroborated by the increase in intensity of this peak with the addition of benzene to the NMR tube. Anal. Calcd. for $Mn_{11}C_{86}H_{109}Br_{12}N_{12}O_{16.5}$ (M_r 3138.06): C, 32.92; H, 3.50; N, 5.36. Found: C, 33.45; H, 2.97; N, 5.02.

Crystallography. General Procedures. X-ray diffraction studies were performed with an Enraf-Nonius CAD-4F kappa geometry diffractometer and graphite-monochromatized Mo K$\bar{\alpha}$ radiation (λ = 0.71069 Å). The crystal temperature (see Table 1) was maintained by the use of an Enraf-Nonius FR558-S liquid nitrogen cryostat. The crystal specimen was mounted on the end of a quartz fiber with silicone grease. All calculations were performed with a VAXstation 4000-90 computer and the teXsan software package.[33] The Laue symmetry was determined by the unit cell parameters and confirmed by the examination of axial photographs. Two computer programs, TRANS and TRACER,[34] were employed to provide further confirmation of the Laue symmetry. The crystal was determined to be of sufficient quality for data collection as judged by the examination of axial photographs, the quality of the unit cell, and the measurement of selected peak widths at half-height ($\bar{\Delta}\omega^{1/2}$) by open-counter ω scans.

Intensity data were collected with the ω-2θ scan technique for **2** and with ω scans for **3**. The intensities of three standard reflections were measured after every 3600 seconds of exposure time. The data were corrected for Lorentz and polarization effects, and corrected for absorption following the measurement of Ψ scans.[35] The direct methods program SIR-92[36] was used for the initial structure solution, and a final model was obtained by least-squares refinement in combination with difference Fourier syntheses. Hydrogen atoms were placed at calculated positions (C-H = 0.95 Å), and their B values were fixed at 1.2 times the B_{eq} of the atom to which they were bound, unless otherwise indicated. They were included, but not refined, in

the final least-squares cycles. Scattering factors for the nonhydrogen[37] and hydrogen atoms[38] and anomalous dispersion terms[39,40] were taken from their usual sources.

A summary of crystallographic data for **2** and **3** can be found in Table 1. Selected bond distances and angles for **2** are listed in Table 2. A complete listing of intramolecular bond distances, angles, atomic coordinates and B_{eq}, and anisotropic thermal parameters are given in Tables 6 - 9 and and Tables 10 - 13 for **2** and **3**, respectively.

$[Me_4N]_4[(Mn_{10}O_4(biphen)_4Br_{12}] \cdot 4CH_3CN$ ($2 \cdot 4CH_3CN$). A dark red-brown crystal (0.25 x 0.26 x 0.40 mm) grown from CH_3CN/toluene was selected. The unit cell dimensions were obtained from a least-squares fit of 21 reflections with $2\theta \geq 24°$ and revealed the Laue symmetry to be $2/m$. No decay correction was necessary since there was no significant fluctuation in the intensities of the three standard reflections. The Mn, Br and O atoms were refined by using anisotropic thermal parameters, and the C and N atoms were refined with isotropic thermal parameters.

All of the cation and solvent molecules were well behaved except for one disordered Me_4N^+ cation. Several attempts at modelling its disorder, including the introduction of two cations at half occupancy and the use of rigid groups, failed to afford a satisfactory refinement. The model of the disordered cation used in the final analysis was composed of one Me_4N^+ molecule at full occupancy, represented by N(8), C(76), C(77), C(78), and C(79). A peak of significant electron density was consistently found near this cation but not within bonding distance. This peak was successfully modelled by a water molecule at a half occupancy, represented by O(13). The largest positive peak in the final difference Fourier map had an electron density of 1.44 $e^-/Å^3$ and was located in the region near C77.

$[Et_3NH]_2[Mn(CH_3CN)_4(H_2O)_2](Mn_{10}O_4(biphen)_4Br_{12}] \cdot 6CH_3CN \cdot 2.5H_2O$ ($3 \cdot 6CH_3CN \cdot 2.5H_2O$). A dark red-brown crystal (0.15 x 0.35 x 0.40 mm) grown from CH_3CN/C_6H_6 was selected. The unit cell dimensions were obtained from a least-squares fit of 23 reflections with $2\theta \geq 15°$ and revealed the Laue symmetry to be $4/m$. No decay correction was necessary since there was no significant fluctuation in the intensities of the three standard reflections. All of the atoms in the complex anion refined with anisotropic thermal parameters in a satisfactory manner, and no peaks of significant electron density were located in the final difference maps near the main cluster. The manganese atom, Mn(4), and coordinated acetonitrile atoms N(1), C(13), and C(14), of the isolated Mn(II) cation were successfully refined with anisotropic thermal parameters. The two oxygen atoms of the axial water molecules, O(4) and O(5), which lie on a 4-fold axis with the Mn(II) atom, refined well with anisotropic thermal parameters. The two Mn-O distances for these ligands are significantly different, with Mn(4)-O(4) = 2.15(4) Å, and Mn(4)-O(5) = 2.45(3) Å, but a peak with significant electron density (1.4 $e^-/Å^3$) was located quite close (0.57 Å) to O(5) in the final difference Fourier maps. This water ligand may be disordered in some way or hydrogen-bonded to other solvents in the lattice, which could account for the elongated Mn-O distance, but given the low quality of the structure (vide infra), we were unable to explain this elongated distance.

The Et_3NH^+ cation is severely disordered across a mirror plane (x, y, 0). Numerous attempts at modelling this disorder failed to result in a cation with reasonable bond distances or angles. In the final refinements, this electron density was modelled with a five carbon fragment, C(15) - C(19), which converged to a structure with the basic connectivity of part of the Et_3NH^+ cation, although bond distances and angles were far from ideal for

this fragment. If no atoms were included to model the disordered Et_3NH^+, difficulties were encountered with refining other parts of the structure.

One acetonitrile molecule was found with all three atoms at general positions, and was modelled by using the three carbon fragment C(20) - C(22), because the bond lengths did not clearly distinguish the nitrogen atom. One of these carbon atoms, C(23), is located close to the region of space occupied by the disordered Et_3NH^+ ion, and had to be fixed in position to keep it from moving toward the electron density of the cation in the final refinements. The other acetonitrile molecule in the asymmetric unit was disordered over two positions, in which all the atoms lie on the same mirror plane, and was modelled by C(23), C(24a), C(25a), C(24b), and C(25b). The atom C(23) is shared by both molecules, and was therefore refined with half occupancy. The other atoms were refined with an occupancy factor of 0.25. The atoms C(24a) and C(25a) were also fixed in position to keep from moving to unreasonable distances away from the carbons to which they were attached.

Finally, the oxygen atom of one of the water molecules, O(6), is located at (0, 0, 0), a site with $4/m$ symmetry, 2.12 Å away from O(7), the other water oxygen atom, which is located on a mirror plane. The atom O(7) is located 2.41 Å from C(18) of the Et_3NH^+, and 2.44 Å from C(20) of one of the acetonitrile molecules. The possibility that these solvent molecules may be less than fully-occupied, and the fact that the Et_3NH^+ is severely disordered, provide some rationale for these close contacts, besides the overall difficulty of modelling the lattice solvent and counterions. The largest positive peak in the final difference Fourier map had an electron density of 1.49 $e^-/Å^3$, located in a region of space isolated from the other contents of the asymmetric unit, but near 3 other peaks of electron density between 1.5 - 1.0 $e^-/Å^3$. No attempt was made to model these peaks.

Magnetic Susceptibility Studies. DC magnetic susceptibility measurements on polycrystalline samples of **1** and **2** were made by using a Quantum Design MPMS SQUID susceptometer equipped with a 5.5 T magnet and operating in the range 2.5 - 300 K. The susceptibilities of the sample holder were measured at the same fields and temperatures for accurate correction of its contribution to the total measured susceptibility. Diamagnetic corrections were estimated from Pascal's constants[41,42] and subtracted from the experimental susceptibilities. AC susceptibility measurements on polycrystalline samples of **1 - 3** were made with a home-built susceptometer operating at 98 Hz and capable of reaching temperatures as low as 1.4 K.

High Field Magnetization Studies. Solid state magnetization measurements on polycrystalline samples of **1** and **2** were made with a vibrating-sample (Foner) magnetometer at the Francis Bitter National Magnet Laboratory. Electronics were modified for use in Bitter magnets. Sample holders were made from Teflon or Kel-F and fitted with plungers that allowed for compression of the powders by hand to prevent mechanical torquing in the applied field. Data were collected between 0 and 200 kOe for all samples.

EPR Studies. A Varian E-9 spectrometer equipped with an Oxford Instruments ESR 9 liquid helium continuous flow cryostat was used to collect both polycrystalline and single crystal EPR spectra.

Results and Discussion

Synthesis. The preparation of the $[Mn_{10}O_4(biphen)_4Cl_{12}]^{4-}$ anion was accomplished by addition of Me_4NOH, a source of base, to a solution of $MnCl_2$ and $biphenH_2$ in EtOH. Layering of the filtered reaction mixture over CH_2Cl_2

gave X-ray quality crystals of **1**. Subsequent determination of the structure of **1** by X-ray crystallography revealed the geometry of the Mn_{10} anion, but was plagued by disorder of solvent molecules, most likely CH_2Cl_2, in the crystal lattice. A second structure of better quality was obtained on crystals of **1** grown by layering of benzene onto the filtered reaction mixture, and was reported elsewhere.[32] The utility of the $EtOH/C_6H_6$ solvent system was limited by the co-crystallization of a white product with the red-brown crystals of **1**, making the $EtOH/CH_2Cl_2$ system the one of choice for bulk preparation.

The mixed-valent cluster has four Mn(III) and six Mn(II) ions, the oxidizing agent necessary for the generation of the Mn(III) centers most likely being atmospheric dioxygen. The redox reaction is initiated by the addition of base, as evidenced by the immediate formation of the dark brown color. A formal balanced equation for the synthesis of **1** and **2** can be written as in equation 1. One-electron reduction of dioxygen by four Mn(II) ions

$$\begin{aligned} &10\,MnX_2{\cdot}4H_2O + 4\,biphenH_2 \\ &\quad + 4\,Me_4NOH + O_2 \end{aligned} \longrightarrow \begin{aligned} &[Me_4N]_4[Mn_{10}O_4(biphen)_4X_{12}] \\ &\quad + 12\,HX + 4\,H_2O \end{aligned} \qquad (1)$$

would result in the generation of the appropriate number of Mn(III) ions, and two of the four O^{2-} ligands. The deprotonation of two H_2O molecules would provide the other two O^{2-} ligands, giving four protons. A total of 12 protons would then be released during complex formation, eight of which come from the $biphenH_2$ ligands. This equation can only be viewed as an intriguing formalism, given the difficulty in determining the actual mechanism of assembly of such a large polynuclear cluster. We made no attempt to establish the source of the oxo ligands or the affect of O_2 stoichiometry on the preparation of **1** or **2**.

Given the critical role of the halide ion in holding together the structure of the Mn_{10} cluster, we wondered whether it would be possible to substitute Br^- for Cl^- and maintain the structural integrity of the complex. The structural framework of **1** would have to undergo a significant expansion upon substitution of the larger Br^- (ionic radius = 1.96 Å) for Cl^- (ionic radius = 1.81 Å) ion.[43] Moreover, very few well characterized, higher valent (≥ +3) Mn compounds are known with Br^- as ligand, possibly because of redox instability.[8,44,45] Despite these potential barriers, the preparation of the bromide derivative **2** was accomplished relatively easily, simply by substitution of $MnBr_2$ for $MnCl_2$ in the synthesis.

Preparation of the analogous bromide derivative in a manner identical to the preparation of **1** gave crystalline material of **2** that analyzed well for the corresponding Mn_{10} cluster.[32] X-ray quality crystals of **2** were grown by vapor diffusion of toluene into acetonitrile. The structure is described below. Since $MnBr_2$ is more soluble in CH_3CN than $MnCl_2$, compound **2** can be prepared by using CH_3CN as solvent in place of EtOH.

In order to explore the generality of the Mn_{10} complex synthesis, we attempted to prepare the cluster by addition of an exogeneous base other than Me_4NOH. Such a substitution would allow us to determine whether the redox reaction necessary to form the mixed-valent cluster could occur in the presence of of a base other than hydroxide ion, and to establish whether the $[Mn_{10}O_4(biphen)_4X_{12}]^{4-}$ anion could be assembled with a cation other than Me_4N^+.

The use of Et_3N as base led to the synthesis of compound **3**. Formation of the same dark red-brown color observed in the Me_4NOH reaction was observed immediately upon addition of Et_3N. Structural characterization of **3** by X-ray crystallography revealed it to contain the same Mn_{10} cluster as in **1**

and **2**, but with Et_3NH^+ and mononuclear Mn(II) cations in the lattice. Single crystals of **3** had tetragonal morphology, consistent with the Laue symmetry of the compound. When the scale of the reaction is reduced by a factor of four, including the solvent volume, dark red-brown crystals with a rectangular, block-shaped morphology co-crystallized with **3**. The unit cell of these block-shaped crystals was determined on the diffractometer to be orthorhombic,[46] but they were not of sufficient quality to afford a good structural determination. Upon increasing the concentration of reagents by a factor of four, only the orthorhombic crystals formed.

Crystals of **3** were readily separated under a microscope by hand from the orthorhombic material, since their morphologies are clearly distinguishable. Compound **3** was identified conclusively by a unit cell determination. The preparation given in the Experimental Section yields only the tetragonal-shaped crystals of **3**, but systematic investigation of the effects of varying the concentration of reagents in the synthesis of **3** was not carried out, so one must be aware that the orthorhombic material is a potential impurity. The high-symmetry space group of **3** was important for deconvoluting the magnetic behavior of the Mn_{10} unit, because it allowed for the collection and easy interpretation of both single-crystal susceptibility and EPR measurements.

When stored under an inert atmosphere at room temperature, compound **3** loses crystallinity owing to solvent loss. If crystals of **3** are allowed to stand in air for a few weeks, they decompose to give an amorphous material, as shown by the absence of a powder diffraction pattern. A variable temperature magnetic susceptibility study of this material showed a magnetic phase transition at $\approx$ 40 K. This transition is very similar to that observed for hausmannite (Mn_3O_4),[47,48] and it is possible that at least a part of

the material, most likely the Mn(II) cation, was being oxidized upon prolonged exposure to air to give this mineral. Successive washing of the material by acetone, CH_3CN, and EtOH led to the isolation of a pure inorganic compound which retained the magnetic phase transition near 40 K. This material was 70% by weight in manganese as determined by atomic absorption spectroscopy, close to the percentage of manganese in Mn_3O_4 (72.03%).

Molecular Structures. *$[Me_4N]_4[(Mn_{10}O_4(biphen)_4Br_{12}]$ (2).* An ORTEP diagram of the complex anion of **2** is shown in Figure 1. This complex has the same overall structure as the chloride derivative **1**. An adamantane-like inner core is formed by Mn(5), O(10), Mn(8), O(5), Mn(10), O(12), Mn(1), Mn(2), Mn(3) and O(4), with Mn(1) and Mn(8) being the two inner Mn(II) ions. The μ_4-oxo ligands, O(4), O(5), O(10), and O(12), are each bound to an outer Mn(II) ion, Mn(4), Mn(7), Mn(6), and Mn(9), respectively. The four Mn(III) ions are easily distinguished as the metal ions chelated by the four biphenoxide ligands. Each biphenoxide oxygen atom bridges a Mn(III) ion and an outer Mn(II) ion. The twelve bromide ligands in the cluster are bound in three different modes. Four bromide ions, Br(3), Br(6), Br(4), and Br(1), each bridge three metal ions. Four other bromide ions are bound in a doubly-bridging mode between two linear arrays of metal ions, Mn(9), Mn(1), Mn(4) along the front vertical edge, and Mn(6), Mn(8) and Mn(7) along the back horizontal edge of the cluster. The remaining bromide ions are coordinated in a terminal fashion to the outer Mn(II) ions.

The structure of compounds **1** and **2** bares a striking resemblance to a series of metal chalcogenide cluster complexes of formula $[E_4M_{10}(E'R)_{16}]^{4-}$ and $[E_4M_{10}(E'R)_{12}X_4]^{4-}$, with E, E' = S, Se, or Te and M = Zn or Cd and X = Cl, Br, or I.[49-51] These compounds are comprised of four fused adamantoid cages, and

their metal atoms form a framework very similar to that of **1** and **2**, although the metal sites exclusively exhibit tetrahedral geometries. An even closer structural relationship to **1** and **2** is found for the thiostannate cluster complex of composition $[Sn_{10}O_4S_{20}]^{8-}$,[52] which contains four μ_3-oxo ligands at the center of each adamantoid cage. The positions of these oxo bridges within the Sn_{10} framework are identical to the positions of the μ_4-oxo ligands in **1** and **2**, and indeed, the thiostannate polyanion would have an *identical* core structure to that of **1** and **2** if the oxo ligands were bonded to the fourth closest metal site.

Oxidation states for the manganese are readily assigned by examining the bond distances for the first coordination sphere of each metal. Many compounds containing Mn(III) ions exhibit the classic Jahn-Teller distorted geometry expected for a d^4 ion, making the identification of this oxidation state for manganese straightforward. As can be seen in Figure 1, the Mn(III) ions Mn(2), Mn(3), Mn(5) and Mn(10) have an octahedral environment with a Br_2O_4 donor set, and Tables 2 and 7 clearly reveal that the bromide ligands occupy axially-elongated sites, with an average Mn-Br distance of 2.84 Å. As one might expect, the Mn(III) ions are coordinated by the hardest set of ligand donor atoms, Br_2O_4, with the highest O/Br ratio compared to the other metal atoms

As shown in Table 3, the average distances of the oxygen ligands to the Mn(III) sites in **1** and **2** are significantly shorter than the Mn-O distances for the Mn(II) atoms. The manganese(II) atoms Mn(1) and Mn(8) have octahedral geometries while the remaining Mn(II) ions are bound in distorted trigonal bipyramidal sites.

To our knowledge, only two other compounds containing Mn(III)-Br bonds have been characterized by X-ray crystallography, one of which is

$[Mn_4O_3Br(OAc)_3(dbm)_3]$ (dbmH = dibenzoylmethane),[8] an $Mn(III)_3Mn(IV)$ complex with a distorted cubane structure. The bromide ligand in this molecule bridges three octahedral manganese(III) atoms and occupies an elongated axial position on each Jahn-Teller distorted Mn(III) site. The average Mn-Br distance in this compound is 2.803 Å, nearly identical to that in **2**. The other structurally characterized Mn(III)-Br compound is $Mn(C_6H_2Me_3)Br_2(PMe_3)_2$,[44] a high-spin organomanganese(III) complex with a distorted trigonal-bipyramidal geometry. The bromide ligands occupy equatorial positions, with a significantly shorter average Mn-Br distance of 2.50 Å, as expected in the absence of a Jahn-Teller distortion. Compound **2** is only the second example where a Br^- ion bridges Mn(III) centers, the first being the $Mn(III)_3Mn(IV)$ complex.

The lengthening of the Mn-halide bonds on going from Cl^- to Br^- is approximately 0.13 - 0.15 Å for all manganese centers in **1** and **2**, as can be seen in Table 3. This increase is in excellent agreement with the difference in the ionic radii of Br^- and Cl^-, 0.15 Å.[43]

*$[Mn(CH_3CN)_4(H_2O)_2][Et_3NH]_2[Mn_{10}O_4(biphen)_4Br_{12}]$ (**3**).* The crystal structure of **3** reveals an Mn_{10} complex that is isostructural with the anion in **2**. Although we encountered several difficulties in refining the lattice solvent and counterions, the metrical data for the Mn_{10} cluster of **3** is in excellent agreement with those of **2**, giving us confidence that the connectivity of the cluster is the same. The complex anion resides at a special position of $\bar{4}$ site symmetry, making only one-quarter of the atoms in the cluster unique. The remaining atoms in the anion are generated by the crystallographically-imposed S_4 axis, giving the complex strict D_{2d} symmetry. One of the manganese ions, Mn(3), resides on a crystallographically-imposed two-fold axis. The $[Mn_{10}O_4(biphen)_4Br_{12}]^{4-}$ units are stacked in an eclipsed fashion

along the S_4 axes, running parallel with the *c* axis. A packing diagram is shown in Figure 2 to highlight this stacking arrangement.

Powder Magnetic Studies. A plot of the product of the molar magnetic susceptibility versus temperature for powdered samples of **1** and **2** is shown in Fig. 3. The susceptibility data for **1**, published in a previous report,[32] is included for comparison. Substitution of Br^- for Cl^- ions clearly has no affect on the overall magnetic properties of the cluster. The χT curve for **2** steadily increases from 37.9 emu mol^{-1} K at 300 K, very close to 38.2 emu mol^{-1} K, the value expected if all of the manganese spins are uncorrelated, to 95.1 emu mol^{-1} K at 5 K. Measurements performed on **1** between 300 and 400 K reveal that χT decreases below the value expected for the uncorrelated spins, reaching a value of 35 emu mol^{-1} K near 400 K (data not shown). As found for **1**, the low temperature χT product lies between the theoretical values calculated for an $S = 13$ (χT_{calc} = 91 emu mol^{-1} K) and $S = 14$ (χT_{calc} = 105 emu mol^{-1} K) ground state, assuming an average *g* value of 2.0 for the cluster.

The insets of Figs. 3a and 3b show the saturation magnetization data for **1** and **2** at 4.2 K as a function of reduced magnetization versus magnetic field. At the high magnetic fields employed, the magnetization curves for **1** and **2** increase rapidly at low field and reach a plateau at the higher fields, with final saturation values of 27.1 μ_B and 28.3 μ_B for **1** and **2**, respectively. By using the simple relation $M_{sat}/N{\cdot}\mu_B = g{\cdot}S$, and assuming $g = 2.0$, a ground state near S = 14 is indicated for both **1** and **2**. The close similarity in the magnetic behavior of **1** and **2** suggests that the magnetic exchange interactions are little influenced by the bridging halide ions.

The magnetic susceptibility for a powdered sample of **3**, shown in Figure 4, exhibits similar behavior as compared to both **1** and **2**. The χT product steadily increases as the temperature is lowered, from a value at 300 K

of χT = 43 emu mol^{-1} K to a round maximum of χT = 82 emu mol^{-1} K near 10 K. This maximum value is in agreement with an S = 12 ground state given g = 2.0, and taking into account the contribution of the isolated S = 5/2 Mn(II) cation.

The magnetic susceptibility of **1** - **3** were measured in zero applied field down to temperatures as low as 1.4 K by the use of an AC susceptometer. In all cases paramagnetic behavior, with no imaginary component of the AC susceptibility, was observed.

Single-Crystal Magnetic Studies. The tetragonal symmetry of compound **3** and the macroscopic morphology of the crystals made it an excellent candidate for anisotropy measurements. Only two measurements, parallel and perpendicular to the unique axis, are necessary to determine the anisotropy tensor. The χT versus T curves for a single crystal of **3** with the applied magnetic field oriented parallel and perpendicular to the crystallographic *c* axis are shown in Figure 4. In the parallel orientation, $\chi_{||}T$ rapidly increases to a value of 128 emu mol^{-1} K at 2.2 K. When the external field is applied perpendicular to the *c* axis, $\chi_{\perp}T$ reaches a broad maximum of 80 emu mol^{-1} K near 15 K, followed by a decrease to 46 emu mol^{-1} K at 2.1 K. The calculated powder-average value of χT, using the relation $\chi T_{ave} = 1/3(2\chi_{\perp}T + \chi_{||}T)$ is 74 emu mol^{-1} K at 2.2 K, in good agreement with the observed value of 77 emu mol^{-1} K at this temperature. The system clearly exhibits an Ising-type anisotropy, with one axis of favorite magnetization and a hard plane, which cannot be attributed to **g** anisotropy owing to its large temperature dependence.

The saturation magnetization measured at 2 K for a single crystal of **3**, with the applied field parallel and perpendicular to the *c* axis is shown in Figure 5. As is evident from the plot, the reduced magnetization increases

much more rapidly with the applied field when it is applied parallel to the *c* axis. Above approximately 30 kOe the two curves become equal, and the reduced magnetization smoothly increases to a value near 29 μ_B at maximum field.

EPR Spectroscopy. The X-band EPR spectrum at room temperature of a powdered sample of **3** shows a broad, structureless line at $g = 2.0$ with $\Delta H_{pp} =$ 750 G. Upon lowering the temperature to 4.2 K, a complex spectrum arises with signals being observed up to 10 kG, which is difficult to interpret. The X-band spectrum of a single crystal of **3** at room temperature indicates that the linewidth of this broad $g = 2.0$ feature depends on the orientation of the crystallographic axes and the direction of the applied magnetic field, with $\Delta H_{pp} = 1020$ G when the *c* axis is held parallel to the applied field and $\Delta H_{pp} =$ 650 G when the field lies in the *ab* plane.

At temperatures below 70 K, a complex pattern in the EPR spectrum of a single crystal of **3** is resolved, irrespective of the magnetic field orientation. The EPR spectrum for a single crystal of **3** at liquid helium temperature with the field oriented parallel to the *c* axis is shown in Figure 6. A signal centered at $g = 2.0$ (3300 Gauss) complicates the analysis of this spectrum, but some critical features are apparent. In the high field region ($H \geq 5000$ G), nine equally spaced lines with intensity decreasing as the field increases are observed. The resonance of weakest intensity is observed near 11,800 G. The separation between these resonances is approximately 750 G.

Theoretical Analysis. A high spin ground state of multiplicity $12 \leq S \leq 14$ is supported by all of the powder susceptibility and high field magnetization data for compounds **1** and **2**. An exact theoretical fit of the susceptibility data is simply not possible because the dimensions of the spin Hamiltonian matrix for a system comprising six $S = 5/2$ and four $S = 2$ spins

are far too large to be handled by standard computing facilities, even with reductions in the size of the matrices brought about by the symmetry of the cluster.[53] The single crystal measurements made possible by the high symmetry of compound **3** provide invaluable information in further characterizing the magnetic properties of this decanuclear system. We attribute the magnetic anisotropy evident in the single crystal susceptibility data for **3** to arise from weak, axial zero-field splitting (D) of the high spin S = 12 ground state for this cluster. This zero-field splitting of the ground state probably arises from the single ion anisotropy of the d^4 Mn(III) ions, as suggested by theoretical calculations (vide infra). This Ising-type anisotropy, with a unique easy axis, c, and a hard plane indicates that the sign of the axial zfs parameter D should be negative with the $M_S = \pm 12$ doublet lowest in energy.

The single-crystal EPR data for **3** provide a spectacular demonstration of zero-field splitting of the high spin S = 12 ground state, and allow for a quantitative estimate of D, the axial zfs parameter. We assign the nine-line signal observed for **3** at 4 K, shown in Fig. 6, as arising from transitions within the S = 12 ground state multiplet. The fine structure of the spectrum, visible at fields above 5000 G, corresponds to the transitions -3 → -4, -4 → -5, up to -11 → -12. In the range 0 to 5300 G, the spectrum is complicated not only by the presence of a broad signal at g = 2.0, probably arising from the isolated Mn(II) cation, but also by additional transitions of the type -12 → -11, -11 → -10 down to -5 → -4. The separation between the lines is dependent on the magnitude of the zero-field splitting of the ground state. A spacing of 750 G is equal to $|2D|$, resulting in a value for $|D|$ of $|0.037|$ cm^{-1}. The sign of the zfs parameter is not provided by the EPR spectra but can be deduced by the single crystal magnetic measurements as mentioned above.

Using the estimate of the zfs parameter D from the EPR data, we were able to simulate the single-crystal magnetization curve for **3**. A simulated curve of reduced magnetization versus field for an $S = 12$ system with $D = -0.037$ cm^{-1}, and the field either parallel or perpendicular to the unique axis, is shown together with the data in Fig. 5. Given the complexity of such a high spin system and the relative crudeness of this model, the agreement between the calculated and experimental values is remarkable.

Very slow relaxation of the magnetization of a dodecanuclear manganese complex was recently published elsewhere,[29] opening new prospectives for magnetic memory at the molecular level. This complex has the formula $[Mn_{12}O_{12}(O_2CR)_{16}(H_2O)_4]$ (R = Ph, CH_3) and exhibits unprecedented relaxation phenomena through the combination of a high spin ground state, $S = 10$, and a large Ising-type anisotropy This behavior suggests that our Mn_{10} system would be a good candidate for displaying similar superparamagnetic-like behavior. Quantitative analysis of the magnetization curves shown in Fig. 5 allowed for an estimation of the macroscopic anisotropy constant, K_1, which, to a first approximation, is given by the difference in the work required to saturate the magnetization parallel and perpendicular to the easy axis.[54] This constant was estimated to be 3.4 erg/cm^3, approximately 10 times smaller than K_1 for the Mn_{12} complex.[55] The relative size of K_1 is in close agreement with the magnitude expected if we compare the molecular anisotropy of the two compounds, given approximately by DS^2, which is about 5.5 cm^{-1} for **3** and 50 cm^{-1} for the Mn_{12} complex.

The magnetization relaxation process follows an exponential law typical of a thermally activated process, having the form $\tau = \tau_0 \exp(\Delta/kBT)$, where τ_0 is the relaxation time at infinite temperature, and Δ is proportional

to K_1. These calculations show that compound **3** should have a much faster relaxation than the dodecanuclear complex, but superparamagnetic-like behavior should still be observable at temperatures not far below 1 K.

In order to provide a theoretical basis for the observed magnetic properties of compounds **1** - **3**, and especially to offer a rationale for the high spin ground state, we propose three related models for the exchange interactions in the Mn_{10} cluster, each one of increasing complexity. A schematic view of the spin topology of the cluster is given in Figure 7. The two $S = 5/2$ and four $S = 2$ spins, which correspond to the Mn(II) atoms Mn(1) and Mn(8) and the Mn(III) atoms Mn(5), Mn(2), Mn(3) and Mn(10) in compounds **1** and **2**, are arranged at the vertices of an "inner core" octahedron. Four $S = 5/2$ spins, corresponding to Mn(6), Mn(4), Mn(7) and Mn(9), cap the four faces of this octahedron, and we refer to these atoms as the "outer" Mn(II) atoms.

Only four distinct magnetic exchange pathways are assumed to be present. This assumption must be true for **3**, given the crystallographically-imposed D_{2d} symmetry, and is quite reasonable for the isostructural compounds **1** and **2**. The parameter J_{III} represents the coupling constant between Mn(III) atoms, the coupling between Mn(II) atoms is represented by J_{II}, the exchange between the Mn(III) and inner core Mn(II) atoms is labeled with J_c, and J_o represents the coupling between the Mn(III) and outer Mn(II) atoms. The μ_4-oxo bridges are assumed to be the dominant pathway of magnetic exchange coupling between Mn atoms. Although the μ_3-halide and μ_2-halide ligands could theoretically mediate the coupling, the fact that the magnetic data are extremely similar for **1** and **2** supports the assumption that the μ_4-oxo bridges dominate.

The three models of the exchange coupling put forth below assume Heisenberg exchange between all spins, and have made no allowance for the single ion anisotropy of the Mn(III) atoms. The first and most simple model takes into account only six spins, the 4 Mn(III) spins (S = 2) and the 2 Mn(II) spins (S = 5/2) of the inner octahedral core, and only two independent exchange parameters, J_{III} and J_c. The spin Hamiltonian for this model is given in eq. 2. An analytical expression for the eigenvalues of the

$$\mathcal{H} = J_c[\mathbf{S}_1\cdot\mathbf{S}_5 + \mathbf{S}_1\cdot\mathbf{S}_6 + \mathbf{S}_2\cdot\mathbf{S}_5 + \mathbf{S}_2\cdot\mathbf{S}_6 + \mathbf{S}_3\cdot\mathbf{S}_5 + \mathbf{S}_3\cdot\mathbf{S}_6 + \mathbf{S}_4\cdot\mathbf{S}_5 + \mathbf{S}_4\cdot\mathbf{S}_6] + J_{III}[\mathbf{S}_1\cdot\mathbf{S}_2 + \mathbf{S}_1\cdot\mathbf{S}_4 + \mathbf{S}_2\cdot\mathbf{S}_3 + \mathbf{S}_3\cdot\mathbf{S}_4] \quad (2)$$

Hamiltonian in eq. 2 was derived by using the Kambé operator replacement method,[56] and is given in equation 3.

$$E(|S_A,S_B,S_C,S_D,S_{tot}\rangle) = J_c[S_{tot}(S_{tot}+1) - S_D(S_D+1) - S_C(S_C+1) + J_{III}[S_D(S_D+1) - S_A(S_A+1) - S_B(S_B+1)] \quad (3)$$

where $\mathbf{S}_A = \mathbf{S}_1 + \mathbf{S}_3$, $\mathbf{S}_B = \mathbf{S}_2 + \mathbf{S}_4$, $\mathbf{S}_C = \mathbf{S}_5 + \mathbf{S}_6$, $\mathbf{S}_D = \mathbf{S}_A + \mathbf{S}_B$, and the total S value is $\mathbf{S}_{tot} = \mathbf{S}_C + \mathbf{S}_D$.

By using eq. 3, values for the relative energies of the possible spin states were calculated as a function of the ratio of the coupling constants. Two sets of antiferromagnetic exchange coupling parameters, referred to as *case a* and *case b* below, were found which give rise to a high spin ground state for the whole cluster.

Case a. If the ratio of $J_{III}/J_c \leq 0.5$, allowing for the possibility of ferromagnetic values for J_{III}, the model given by eqs. 2 and 3 yields the ground state $|S_A,S_B,S_C,S_D,S_{tot}\rangle = |4,4,5,8,3\rangle$. In this state the four S = 2 spins

are aligned parallel to each other as denoted by $S_D = 8$. The two $S = 5/2$ spins are also parallel to each other because $S_C = 5$, but must be antiparallel to the $S = 2$ spins to give $S_{tot} = 3 = |S_C - S_D|$. Now let us consider the outer Mn(II) atoms: if the ratio $J_{II} > J_o$ holds, then the four outer $S = 5/2$ spins would be aligned parallel to the $S = 2$ spins of the Mn(III) atoms, resulting in an $S_{tot} = (4 \times 5/2 + 3) = 13$ ground state for the entire cluster.

Case b. If the ratio $3 \leq J_{III}/J_c \leq 5$ holds, then by using eq. 3 the ground state is calculated to be $|4,4,5,1,4\rangle$. Given the definitions of S_A, S_B and S_D above, this ground state must have S_1 and S_3 parallel to each other as well as S_2 and S_4 parallel to each other, but S_1 and S_3 are not parallel to S_2 and S_4. These pairs of $S = 2$ spins must be oriented at some angle such that the resultant spin is $S_D = 1.0$. A total spin of $S_{tot} = 4 = |S_C - S_D|$ for the inner core is thus obtained. Again, we now consider the outer $S = 5/2$ spins. If $J_o > J_{II}$, then the four outer $S = 5/2$ spins will be aligned antiparallel to the vectorial sum S_D, but parallel to the two inner core Mn(II) spins. This configuration results in a total spin for the cluster given by $S_{tot} = [(4 \times 5/2) - 1 + (2 \times 5/2)] = 14$.

In order to substantiate either case *a* or case *b* as the configuration most likely to be responsible for the high spin ground state of the Mn_{10} complex, the spin Hamiltonian shown in eq. 4 was used, which is an expansion of eq. 2.

$$\mathcal{H} = (1) + J_o[\mathbf{S}_1 \cdot \mathbf{S}_7 + \mathbf{S}_2 \cdot \mathbf{S}_7] + J_{II}\mathbf{S}_6 \cdot \mathbf{S}_7 \qquad (4)$$

This second model includes seven manganese ions, six of the inner core plus one outer Mn(II) ion labeled S_7 in Fig. 7. The eigenvalues for the possible spin states were obtained in numerical form from a full-matrix diagonalization of the Hamiltonian in eq. 4.[57] The ratios between J_o and J_{II} necessary to obtain high spin ground states for case *a* and case *b* were investigated. For case *a*, in which the initial condition is $J_{III}/J_c \leq 0.5$, a high

spin ground state of $S = 11/2$, which corresponds to $S_{tot} = 13$ for the whole cluster, is found when the ratio $J_{II}/J_o > 2$ is satisfied. For case *b*, in which the initial condition is $3 \leq J_{III}/J_c \leq 5$, a ground state of $S = 13/2$, which corresponds to $S_{tot} = 14$ for the entire cluster, is not obtained for any ratio of coupling parameters. The highest spin ground state attainable for case *b* is $S = 11/2$, in which the two conditions $J_c > J_{II}$ and $J_c > J_o$ have to be met. The failure of case *b* to yield an $S_{tot} = 14$ ground state suggests that "arrows-up arrows-down" arguments for predicting the magnetic behavior of such a complex system is inappropriate, especially when conflicting antiferromagnetic interactions are present.

The third and most complex model incorporated four $S = 1$ and six $S = 3/2$ spins in place of the actual $S = 2$ and $S = 5/2$ spins of the real cluster. The spin hamiltonian for this model is shown in eq. 5, again an extension of eq. 2.

$$\mathcal{H} = (1) + J_o[\mathbf{S}_1\cdot\mathbf{S}_7 + \mathbf{S}_2\cdot\mathbf{S}_7 + \mathbf{S}_2\cdot\mathbf{S}_8 + \mathbf{S}_3\cdot\mathbf{S}_8 + \mathbf{S}_3\cdot\mathbf{S}_9 + \mathbf{S}_4\cdot\mathbf{S}_9\ \mathbf{S}_1\cdot\mathbf{S}_{10} + \mathbf{S}_4\cdot\mathbf{S}_{10}] + \quad (5)$$
$$J_{II}[\mathbf{S}_6\cdot\mathbf{S}_7 + \mathbf{S}_5\cdot\mathbf{S}_8 + \mathbf{S}_6\cdot\mathbf{S}_9 + \mathbf{S}_5\cdot\mathbf{S}_{10}]$$

As in the second model, numerical calculations of the eigenvalues of the possible spin states were performed through full-matrix diagonalization of eq. 4.[57,58] Again, cases *a* and *b* were investigated to find which ratios of the exchange parameters resulted in high spin ground states or reproduced other experimental observations.

Ground states obtained from a series of calculations for case *a* are shown in Table 4. In these calculations two of the coupling constants, J_c and J_{II}, were varied, while J_o and J_{III} were fixed at 10 cm^{-1} and -5 cm^{-1}, respectively. In this model, a spin ground state of $S = 7$ corresponds to both $S = 12$ and $S = 13$ for the actual cluster, since there is not a one-to-one

correspondence between the states of the reduced and the actual system given the many more possible *S* states for the latter. As shown in Table 4, in addition to the requirement of $J_{III}/J_c < 0.5$ for case *a*, J_c and J_{II} must be two times larger than J_o to produce a high spin ground state.

Fixing $J_c = 5$ cm^{-1} and $J_{III} = 20$ cm^{-1}, which satisfies the requirement for case *b*, and allowing J_{II} and J_o to vary led to the results shown in Table 5. In this case high spin ground states are observed for only a small region of the parameter space, and for most of them the energy levels are very closely spaced. Several calculations showed 100 states lie within 10 cm^{-1} of the ground state.

Although these models only yield qualitative results about the nature of the ground spin state, we can conclude that the large spin ground states for **1 - 3** can be found in two well-separated regions of parameter space defined by the following relations: case *a*) $J_{III} < J_o < J_c \approx J_{II}$ and case *b*) $J_{II} < J_c < J_o < J_{III}$. We suggest that case *a* is in fact the correct description for the spin topology of the ground states for compounds **1 - 3**. Several examples are available of complexes that exhibit very weak antiferromagnetic or even weak ferromagnetic coupling between Mn(III) centers mediated by μ-oxo bridging ligands. In these examples the Mn-O-Mn angles are close to 120°, as in **1 - 3**.[59] Antiferromagnetic coupling between Mn(II) and Mn(III) sites through oxo bridges appears to increase with an increase of the M-O-M angle from 100° to 115°, supporting the condition $J_c > J_o$, as is found for case *a*.[13]

Several pieces of experimental evidence favor case *a* as being the correct description. The high-field magnetization data for compounds **1** and **2** exhibit a smooth plateau, implying that the ground state is well-separated at high field. Compound **3** clearly exhibits a well-separated $S = 12$ ground state from the rounded maximum observed for the polycrystalline susceptibility

data. All of these data are incompatible with the results found for case *b*, in which several excited spin states lie close in energy to the high spin ground state. The results for case *a* predict that the spin of the ground state should not be very sensitive to the exact values of the exchange coupling constants, and this prediction is supported by the fact that all three complexes, **1**, **2** and **3**, exhibit large spin ground states. Case *a* predicts an $S = 13$ ground state, and the high-field magnetization data for **2** show a plateau value close to that expected for $S = 14$. The calculations for the reduced spin system of model 3 show that the $S = 14$ state should not lie close in energy to the $S = 13$ state, but the extension from the reduced model to the real system is not straightforward.

If a ground state of $S = 13$ arises from the coupling scheme of case *a*, the zero-field splitting of the fully coupled $S = 13$ state can be easily correlated in the strong exchange limit to the single-ion zero-field splitting of the individual Mn ions in the cluster.[60] Assuming the zero-field splitting to be dominated by the Jahn-Teller distorted Mn(III) atoms, the D value obtained from the EPR data, $|D_{(S=13)}| = 0.037$ cm^{-1}, corresponds to $|D_{Mn(III)}| = 2.03$ cm^{-1}. The $S = 12$ ground state observed for **3** must come from a configuration very close to that described by case *a*, and a similar relation of the zfs parameters holds. We favor case *a* as the most reasonable description of the exchange interactions and spin orientation for the Mn_{10} complex. Experimental proof of the spin orientation and correct set of exchange constants may only come from obtaining a spin density map from a single-crystal polarized neutron diffraction study.

Conclusions

We have synthesized and structurally characterized novel decanuclear mixed-valent manganese complexes. A detailed examination of the rich magnetic properties of these clusters has been successfully carried out, and has confirmed the remarkably high spin of the ground states of these molecules. Substitution of Br^- for Cl^- has little effect on the overall magnetic properties of this system. Single crystal magnetic measurements have allowed for characterization of the spin ground state, including a quantitative analysis of the Ising-type anisotropy manifest in the susceptibility and magnetization measurements. The zfs parameter, D, was estimated from single-crystal EPR data and successfully used to simulate the magnetization data. Several theoretical approaches were employed to explain the high spin ground state and describe the exchange interactions of this high-nuclearity cluster, and a plausible hypothesis consistent with all of the data was developed. The synthesis and magnetic characterization of such systems has far-reaching applications for understanding high spin polynuclear clusters found in biological systems, as well as in the development of new kinds of magnetic molecular materials.

Acknowledgements.

We thank Dr. A. Caneschi for assistance in the preparation of compounds **2** and **3** and for general help and discussions concerning the powder magnetic measurements. We are grateful to Dr. R. Sessoli for collection and interpretation of the single-crystal magnetic data, and for overall guidance in understanding the magnetochemistry of this complicated system. We thank Dr. C. Delfs for help with the theoretical calculations, and E. McNiff, Jr. for aide in obtaining the high-field magnetization data.

References.

(1) Debus, R. J. *Biochim. Biophys. Acta* **1992**, *1102*, 269-352.

(2) McCusker, J. K.; Schmitt, E. A.; Hendrickson, D. N. In *Magnetic Molecular Materials*; D. Gatteschi, O. Kahn, J. S. Miller and F. Palacio, Ed.; Kluwer Academic Publishers: 1991; pp 297-319.

(3) Caneschi, A.; Gatteschi, D.; Pardi, L.; Sessoli, R. *Science* **1994**, *265*, 1054.

(4) Papaefthymiou, G. *Phys. Rev. B.* **1992**, *46*, 10366-10375.

(5) Vincent, J. B.; Christmas, C.; Huffman, J. C.; Christou, G.; Chang, H.-R.; Hendrickson, D. N. *J. Chem. Soc. Chem. Comm.* **1987**, 236-238.

(6) Christou, G. *Acc. Chem. Res.* **1989**, *22*, 328-335.

(7) Wang, S.; Folting, K.; Streib, W. E.; Schmitt, E. A.; McCusker, J. K.; Hendrickson, D. N.; Christou, G. *Angew. Chem. Int. Ed. Eng.* **1991**, *30*, 305-306.

(8) Wang, S.; Tsai, H.-L.; Streib, W. E.; Christou, G.; Hendrickson, D. N. *J. Chem. Soc. Chem. Comm.* **1992**, 1427-1429.

(9) Hendrickson, D. N.; Christou, G.; Schmitt, E. A.; Libby, E.; Bashkin, J. S.; Wang, S.; Tsai, H.-L.; Vincent, J. B.; Boyd, P. D. W.; Huffman, J. C.; Folting, K.; Li, Q.; Streib, W. *J. Am. Chem. Soc.* **1992**, *114*, 2455-2471.

(10) Wemple, M. W.; Tsai, H.-L.; Folting, K.; Hendrickson, D. N.; Christou, G. *Inorg. Chem.* **1993**, *32*, 2025-2031.

(11) Caneschi, A.; Gatteschi, D.; Laugier, J.; Rey, P.; Sessoli, R.; Zanchini, C. *J. Am. Chem. Soc.* **1988**, *110*, 2795-2799.

(12) Baikie, A. R. E.; Howes, A. J.; Hursthouse, M. B.; Quick, A. B.; Thornton, P. *J. Chem. Soc. Chem. Comm.* **1986**, 1587.

(13) Schake, A. R.; Vincent, J. B.; Li, Q.; Boyd, P. D. W.; Folting, K.; Huffman, J. C.; Hendrickson, D. N.; Christou, G. *Inorg. Chem.* **1989**, *28*, 1915-1923.

(14) Bhula, R.; Collier, S.; Robinson, W. T.; Weatherburn, D. C. *Inorg. Chem.* **1990**, *29*, 4027-4032.

(15) Blackman, A. G.; Huffman, J. C.; Lobkovsky, E. B.; Christou, G. *Polyhedron* **1992**, *11*, 251-255.

(16) Bhula, R.; Weatherburn, D. C. *Angew. Chem. Int. Ed. Engl.* **1991**, *30*, 688-689.

(17) Wang, S.; Tsai, H.-L.; Streib, W. E.; Christou, G.; Hendrickson, D. N. *J. Chem. Soc. Chem. Comm.* **1992**, 677-679.

(18) Libby, E.; Folting, K.; Huffman, J. C.; Christou, G. *J. Am. Chem. Soc.* **1990**, *112*, 5354-5356.

(19) Wang, S.; Huffman, J. C.; Folting, K.; Streib, W. E.; Lobkovsky, E. B.; Christou, G. *Angew. Chem. Int. Ed. Engl.* **1991**, *30*, 1672-1674.

(20) Libby, E.; Folting, K.; Huffman, C. J.; Huffman, J. C.; Christou, G. *Inorg. Chem.* **1993**, *32*, 2549-2556.

(21) Wemple, M. W.; Tsai, H.-L.; Streib, W. E.; Hendrickson, D. N.; Christou, G. *J. Chem. Soc. Chem. Comm.* **1994**, 1031-1033.

(22) Christmas, C.; Vincent, J. B.; Chang, H.-R.; Huffman, J. C.; Christou, G.; Hendrickson, D. N. *J. Am. Chem. Soc.* **1988**, *110*, 823-830.

(23) Low, D. W.; Eichhorn, D. M.; Draganescu, A.; Armstrong, W. H. *Inorg. Chem.* **1991**, *30*, 878-880.

(24) Hagen, K. S.; Armstrong, W.; Olmstead, M. M. *J. Am. Chem. Soc.* **1989**, *111*, 774-775.

(25) Cavaluzzo, M.; Chen, Q.; Zubieta, J. *J. Chem. Soc. Chem. Comm.* **1993**, 131-133.

(26) Perlepes, S. P.; Huffman, J. C.; Christou, G. *J. Chem. Soc. Chem. Commun.* **1991**, 1657-1659.

(27) Lis, T. *Acta Cryst.* **1980**, *B36*, 2042-2046.

(28) Sessoli, R.; Tsai, H.-L.; Schake, A. R.; Wang, S.; Vincent, J. B.; Folting, K.; Gatteschi, D.; Christou, G.; Hendrickson, D. N. *J. Am. Chem. Soc.* **1993**, *115*, 1804-1816.

(29) Sessoli, R.; Gatteschi, D.; Caneschi, A.; Novak, M. A. *Nature* **1993**, *365*, 141-143.

(30) Tsai, H.-L.; Eppley, H. J.; deVries, N.; Folting, K.; Christou, G.; Hendrickson, D. N. *J. Chem. Soc. Chem. Commun.* **1994**, 1745.

(31) Gorun, S. M.; Stibrany, R. T. **1991**, U.S. Patent 5,041,575.

(32) Goldberg, D. P.; Caneschi, A.; Lippard, S. J. *J. Am. Chem. Soc.* **1993**, *115*, 9299-9300.

(33) *Single Crystal Structure Analysis Software,* Version 1.6, Molecular Structure Corporation: The Woodlands, TX, 1993.

(34) Lawton, S. L. TRACER II, *A Fortran Transformation-Cell Reduction Program*; Mobil Oil Corporation: Paulsboro, NJ, 1967.

(35) North, A. C. T.; Phillips, D. C.; Mathews, F. S. *Acta Crystallogr.* **1968**, *A24*, 351-359.

(36) Burla, M. C.; Camalli, M.; Cascarano, G.; Giacovazzo, C.; Polidori, G.; Spagna, R.; Viterbo, D. *J. Appl. Cryst.* **1989**, *22*, 389-393.

(37) Cromer, D. T.; Waber, J. T. In *International Tables for X-ray Crystallography* Kynoch Press: Birmingham, 1974; Vol. 4; pp 71-98.

(38) Stewart, R. F.; Davidson, E. R.; Simpson, W. T. *J. Chem. Phys.* **1965**, *42*, 3175-3187.

(39) Ibers, J. A.; Hamilton, W. C. *Acta Cryst.* **1964**, *17*, 781.

(40) Creagh, D. C.; McAuley, W. J. In *International Tables for X-ray Crystallography*Kluwer Academic Publishers: Dordrecht, 1992; Vol. C.; pp 219-222.

(41) Carlin, R. L. *Magnetochemistry*; Springer-Verlag: New York, 1986.

(42) O'Connor, C. J. *Prog. Inorg. Chem.* **1982**, *29*, 203-283.

(43) Shannon, R. D. *Acta Crystallogr. Sect. A* **1976**, *32*, 751-767.

(44) Morris, R. J.; Girolami, G. S. *Organomet.* **1987**, *6*, 1816-1819.

(45) Bryan, P. S.; Dabrowiak, J. C. *Inorg. Chem.* **1975**, *14*, 296-299.

(46) Unit cell parameters: a = 15.832(8), b = 18.923(8), c = 36.223(8).

(47) Srinivasan, G.; Seeline, M. S. *Phys. Rev. B* **1983**, *28*, 1.

(48) Dwight, K.; Menyuk, N. *Phys. Rev.* **1960**, *119*, 1470.

(49) Dance, I.; Fisher, K. In *Prog. in Inorg. Chem.*; K. D. Karlin, Ed.; John Wiley & Sons, Inc.: New York, 1994; Vol. 41; pp 637-803.

(50) Krebs, B.; Henkel, G. *Angew. Chem. Int. Ed. Engl.* **1991**, *30*, 769-788.

(51) Dance, I. G.; Choy, A.; Scudder, M. L. *J. Am. Chem. Soc.* **1984**, *106*, 6285-6295.

(52) Schiwy, W.; Krebs, B. *Angew. Chem. Int. Ed. Engl.* **1975**, *14*, 436.

(53) Matrices ranging in dimension from one (for S = 23) to 266360 (for S = 5) have to be diagonalized for a full-matrix calculation. The symmetry factorization reduces the dimension of the matrices by a factor of four.

(54) Morrish, A. H. *The Physical Principles of Magnetism*; John Wiley and Sons: New York, 1966.

(55) By expressing the volume magnetization in emu/cm^3 and the magnetic field in Oe the anisotropy constant has the dimensions of energy per volume unit, which is erg/cm^3 in cgs units.

(56) Kambé, K. *J. Phys. Soc. Japan* **1950**, *5*, 48-51.

(57) The locally-written program CLUMAG was used, which takes advantage of the irreducible tensor operators method.

(58) The D_{2d} point group symmetry of the Mn_{10} cluster was used to reduce the dimensions of the matrices before diagonalization.

(59) See Table VI in Ref. 13.

(60) Bencini, A.; Gatteschi, D. *EPR of Exchange Coupled Systems*; Springer Verlag: Berlin, 1990.

Table 1. Crystallographic Data for Compounds **2** and **3**.

Compound	**2**	**3**
chemical formula	$Mn_{10}C_{72}H_{94}N_8Br_{12}O_{13}$	$Mn_{11}C_{80}H_{103}N_{12}O_{16.5}Br_{12}$
formula weight	2787.81	3059.95
space group	$P2_1/n$	$I4/m$
a (Å)	22.073(4)	21.373(3)
b (Å)	17.903(3)	
c (Å)	26.269(6)	26.376(5)
α (deg)		
β (deg)	117.17(1)	
γ (deg)		
V (Å^3)	9680(3)	12048(3)
Z	4	4
d, calcd g cm^{-3}	1.91	1.69
μ, cm^{-1}	62.81	51.57
range of 2θ	3-49	3-50
octants collected	$+h\ +k\ \pm l$	$+h\ +k\ +l$
Trans. coeff.	0.913 - 1.000	0.544 - 1.000

Table 1 Contd. Crystallographic Data for Compounds **2** and **3**.

Compound	**2**	**3**
no. of unique data	16682	5668
Data with $F_o^2 > 3\sigma(F_o^2)$	5674	2621
R_{merge} (%)	8.9	9.4
no. of variables	632	265
R $(F_o)^a$	0.072	0.069
R_w $(F_o)^b$	0.064	0.091
goodness of fit	1.36	2.23
λ (Å)	0.71069	0.71069
t (C)	-60	-71

$^aR = \Sigma | |F_o| - |F_c| | / \Sigma |F_o|$;

$^bR_w = [(\Sigma w(|F_o| - |F_c| / \Sigma w |F_o|^2]^{1/2}$; $w = 1/\sigma^2(F_o)$

Table 2. Selected Bond Lengths (Å) and Angles (Deg) for $[Me_4N]_4$-$[Mn_{10}O_4(biphen)_4Br_{12}]\cdot 4CH_3CN \cdot 0.5H_2O$ (**2** $\cdot 4CH_3CN \cdot 0.5H_2O$).[a]

(a) Distances

Mn(1)-Br(3)	2.734(5)	Mn(5)-O(7)	1.94(1)
Mn(1)-Br(6)	2.730(5)	Mn(5)-O(9)	1.91(2)
Mn(1)-Br(10)	2.681(5)	Mn(5)-O(10)	1.88(1)
Mn(1)-Br(12)	2.649(5)	Mn(5)-O(12)	1.90(2)
Mn(1)-O(4)	2.14(2)	Mn(6)-Br(5)	2.626(5)
Mn(1)-O(12)	2.15(2)	Mn(6)-Br(8)	2.482(5)
Mn(2)-Br(1)	2.859(5)	Mn(6)-O(9)	2.14(2)
Mn(2)-Br(3)	2.839(5)	Mn(6)-O(10)	2.22(1)
Mn(2)-O(4)	1.88(2)	Mn(6)-O(11)	2.16(2)
Mn(2)-O(8)	1.95(1)	Mn(7)-Br(2)	2.596(5)
Mn(2)-O(10)	1.90(1)	Mn(7)-Br(11)	2.520(5)
Mn(2)-O(11)	1.92(2)	Mn(7)-O(1)	2.16(1)
Mn(3)-Br(1)	2.830(5)	Mn(7)-O(3)	2.17(1)
Mn(3)-Br(6)	2.823(4)	Mn(7)-O(5)	2.18(1)
Mn(3)-O(2)	1.94(2)	Mn(8)-Br(1)	2.752(5)
Mn(3)-O(3)	1.93(1)	Mn(8)-Br(2)	2.663(5)
Mn(3)-O(4)	1.91(1)	Mn(8)-Br(4)	2.755(5)
Mn(3)-O(5)	1.88(1)	Mn(8)-Br(5)	2.689(5)
Mn(4)-Br(7)	2.469(5)	Mn(8)-O(5)	2.15(1)
Mn(4)-Br(10)	2.609(5)	Mn(8)-O(10)	2.13(1)
Mn(4)-O(2)	2.13(1)	Mn(9)-Br(9)	2.493(5)
Mn(4)-O(4)	2.18(2)	Mn(9)-Br(12)	2.596(5)
Mn(4)-O(8)	2.13(1)	Mn(9)-O(6)	2.16(1)
Mn(5)-Br(3)	2.850(5)	Mn(9)-O(7)	2.14(1)
Mn(5)-Br(4)	2.812(4)	Mn(9)-O(12)	2.20(1)

Table 2 contd. Selected Bond Lengths (Å) and Angles (Deg) for $[Me_4N]_4[Mn_{10}O_4(biphen)_4Br_{12}]\cdot 4CH_3CN \cdot 0.5H_2O$ (**2** $\cdot 4CH_3CN \cdot 0.5H_2O$).[a]

(a) Distances

Mn(10)-Br(4)	2.850(5)	Mn(10)-O(5)	1.91(1)
Mn(10)-Br(6)	2.840(5)	Mn(10)-O(6)	1.90(1)
Mn(10)-O(1)	1.95(2)	Mn(10)-O(12)	1.88(1)

(b) Angles

Br(3)-Mn(1)-Br(6)	163.7(2)	Br(1)-Mn(2)-Br(3)	162.9(1)
Br(3)-Mn(1)-Br(10)	97.2(1)	Br(1)-Mn(2)-O(4)	82.6(5)
Br(3)-Mn(1)-Br(12)	96.6(1)	Br(1)-Mn(2)-O(8)	99.2(5)
Br(6)-Mn(1)-Br(10)	93.3(1)	Br(1)-Mn(2)-O(10)	86.0(4)
Br(6)-Mn(1)-Br(12)	94.3(1)	Br(1)-Mn(2)-O(11)	93.5(5)
Br(10)-Mn(1)-Br(12)	98.0(1)	Br(3)-Mn(2)-O(4)	86.2(5)
Br(3)-Mn(1)-O(12)	84.6(4)	Br(3)-Mn(2)-O(8)	92.6(5)
Br(6)-Mn(1)-O(4)	84.1(4)	Br(3)-Mn(2)-O(10)	82.4(4)
Br(6)-Mn(1)-O(12)	84.1(4)	Br(3)-Mn(2)-O(11)	98.3(5)
Br(6)-Mn(1)-O(12)	84.1(4)	O(4)-Mn(2)-O(8)	84.9(6)
Br(10)-Mn(1)-O(4)	85.7(4)	O(4)-Mn(2)-O(10)	96.3(6)
Br(10)-Mn(1)-O(12)	175.5(4)	O(4)Mn(2)-O(11)	174.9(7)
Br(12)-Mn(1)-O(4)	176.1(4)	O(8)-Mn(2)-O(10)	174.8(6)
Br(12)-Mn(1)-O(12)	85.9(4)	O(8)-Mn(2)-O(11)	92.6(6)
O(4)-Mn(1)-O(12)	90.4(6)	O(10)-Mn(2)-O(11)	86.6(6)

Table 2 contd. Selected Bond Lengths (Å) and Angles (Deg) for $[Me_4N]_4[Mn_{10}O_4(biphen)_4Br_{12}]\cdot 4CH_3CN \cdot 0.5H_2O$ (**2** · $4CH_3CN \cdot 0.5H_2O$).[a]

(b) Angles

Br(6)-Mn(3)-O(3)	97.3(5)	Br(10)-Mn(4)-O(4)	86.8(4)
Br(6)-Mn(3)-O(4)	85.8(5)	Br(10)-Mn(4)-O(8)	110.5(4)
Br(6)-Mn(3)-O(5)	83.1(4)	O(2)-Mn(4)-O(4)	73.5(6)
O(2)-Mn(3)-O(3)	93.7(6)	O(2)-Mn(4)-O(8)	125.9(6)
O(2)-Mn(3)-O(4)	84.1(7)	O(4)-Mn(4)-O(8)	73.7(5)
O(2)-Mn(3)-O(5)	175.8(7)	Br(4)-Mn(5)-O(10)	87.2(4)
O(3)-Mn(3)-O(4)	176.3(7)	Br(4)-Mn(5)-O(12)	83.2(5)
O(3)-Mn(3)-O(5)	84.8(6)	O(7)-Mn(5)-O(9)	93.8(6)
O(4)-Mn(3)-O(5)	97.6(6)	O(7)-Mn(5)-O(10)	176.0(6)
Br(1)-Mn(3)-Br(6)	164.0(2)	O(7)-Mn(5)-O(12)	84.9(6)
Br(1)-Mn(3)-O(2)	97.0(5)	O(9)-Mn(5)-O(10)	84.8(6)
Br(1)-Mn(3)-O(3)	94.3(5)	O(9)-Mn(5)-O(12)	176.1(7)
Br(1)-Mn(3)-O(4)	83.0(5)	O(10)-Mn(5)-O(12)	96.7(6)
Br(1)-Mn(3)-O(5)	87.1(4)	Br(3)-Mn(5)-Br(4)	164.0(2)
Br(6)-Mn(3)-O(2)	93.2(5)	Br(3)-Mn(5)-O(7)	94.0(4)
Br(7)-Mn(4)-Br(10)	109.5(2)	Br(3)-Mn(5)-O(9)	97.9(5)
Br(7)-Mn(4)-O(2)	98.9(4)	Br(3)-Mn(5)-O(10)	82.5(4)
Br(7)-Mn(4)-O(4)	163.6(5)	Br(3)-Mn(5)-O(12)	85.9(5)
Br(7)-Mn(4)-O(8)	100.7(4)	Br(4)-Mn(5)-O(7)	96.7(4)
Br(10)-Mn(4)-O(2)	109.3(4)	Br(4)-Mn(5)-O(9)	93.3(5)
Br(5)-Mn(6)-Br(8)	114.6(2)	Br(1)-Mn(8)-Br(2)	98.2(1)
Br(5)-Mn(6)-O(9)	108.8(5)	Br(1)-Mn(8)-Br(4)	164.0(2)
Br(5)-Mn(6)-O(10)	86.0(4)	Br(1)-Mn(8)-Br(5)	94.7(1)

Table 2 contd. Selected Bond Lengths (Å) and Angles (Deg) for $[Me_4N]_4[Mn_{10}O_4(biphen)_4Br_{12}]\cdot 4CH_3CN \cdot 0.5H_2O$ (**2** $\cdot 4CH_3CN \cdot 0.5H_2O$).[a]

(b) Angles

Br(5)-Mn(6)-O(11)	109.6(4)	Br(1)-Mn(8)-O(5)	84.3(4)
Br(8)-Mn(6)-O(9)	98.3(4)	Br(1)-Mn(8)-O(10)	84.8(4)
Br(8)-Mn(6)-O(10)	159.4(4)	Br(2)-Mn(8)-Br(4)	92.0(1)
Br(8)-Mn(6)-O(11)	99.6(5)	Br(2)-Mn(8)-Br(5)	97.9(1)
O(9)-Mn(6)-O(10)	72.0(6)	Br(2)-Mn(8)-O(5)	85.6(4)
O(9)-Mn(6)-O(11)	125.2(6)	Br(2)-Mn(8)-O(10)	174.7(4)
O(10)-Mn(6)-O(11)	73.4(5)	Br(4)-Mn(8)-Br(5)	96.1(1)
Br(2)-Mn(7)-Br(11)	108.6(2)	Br(4)-Mn(8)-O(5)	84.3(4)
Br(2)-Mn(7)-O(1)	108.9(4)	Br(4)-Mn(8)-O(10)	84.2(4)
Br(2)-Mn(7)-O(3)	113.4(4)	Br(5)-Mn(8)-O(5)	176.4(4)
Br(2)-Mn(7)-O(5)	86.8(4)	Br(5)-Mn(8)-O(10)	86.2(4)
Br(11)-Mn(7)-O(1)	103.1(4)	O(5)-Mn(8)-O(10)	90.3(5)
Br(11)-Mn(7)-O(3)	96.8(4)	O(7)-Mn(9)-O(12)	73.4(6)
Br(11)-Mn(7)-O(5)	164.1(4)	Br(9)-Mn(9)-Br(12)	109.2(2)
O(1)-Mn(7)-O(3)	123.7(6)	Br(9)-Mn(9)-O(6)	103.3(4)
O(1)-Mn(7)-O(5)	74.7(5)	Br(9)-Mn(9)-O(7)	98.1(4)
O(3)-Mn(7)-O(5)	72.6(5)	Br(9)-Mn(9)-O(12)	164.5(5)
Br(12)-Mn(9)-O(6)	108.0(5)	Br(6)-Mn(10)-O(1)	98.7(5)
Br(12)-Mn(9)-O(7)	113.2(4)	Br(6)-Mn(10)-O(5)	82.1(4)
Br(12)-Mn(9)-O(12)	86.3(4)	Br(6)-Mn(10)-O(6)	93.5(5)
O(6)-Mn(9)-O(7)	123.4(6)	Br(6)-Mn(10)-O(12)	85.9(5)
O(6)-Mn(9)O(12)	72.3(5)	O(1)-Mn(10)-O(5)	85.9(6)
Br(4)-Mn(10)-Br(6)	162.2(1)	O(1)-Mn(10)-O(6)	92.6(6)

Table 2 contd. Selected Bond Lengths (Å) and Angles (Deg) for $[Me_4N]_4[Mn_{10}O_4(biphen)_4Br_{12}]\cdot 4CH_3CN\cdot 0.5H_2O$ (**2** · $4CH_3CN\cdot 0.5H_2O$).[a]

(b) Angles			
Br(4)-Mn(10)-O(1)	93.6(5)	O(1)-Mn(10)-O(12)	175.1(7)
Br(4)-Mn(10)-O(5)	86.0(4)	O(5)-Mn(10)-O(6)	175.1(7)
Br(4)-Mn(10)-O(6)	98.8(5)	O(5)-Mn(10)O(12)	96.6(6)
Br(4)-Mn(10)-O(12)	82.4(5)	O(6)-Mn(10)-O(12)	85.3(6)

[a]For atom-labelling scheme, see Figure 1. Estimated standard deviations in the least significant figure are given in parentheses.

Table 3. Average Bond Distances for Compounds **1** and **2**.[b]

Mn oxid. state	geom.[a]	donor set X = Cl^-, Br^-	Compound **1** Mn-O_{ave} (Å)	Compound **2** Mn-O_{ave} (Å)	Compound **1** Mn-Cl_{ave} (Å)	Compound **2** Mn-Br_{ave} (Å)
Mn(II)	tbp	X_2O_3	2.18(2)	2.16(3)	2.40(7)	2.55(6)
Mn(II)	oct	X_4O_2	2.14(1)	2.14(1)	2.56(6)	2.71(4)
Mn(III)	oct	X_2O_4	1.91(2)	1.91(3)	2.71(3)	2.84(2)

[a]tbp = trigonal bipyramidal; oct = octahedral

[b]Values in parentheses are the standard deviations on the averaged parameters.

Table 4. Total spin, S_{tot}, of the ground state for *case a* as a function of the exchange coupling constants, with $J_{III} = -5\ cm^{-1}$ and $J_o = -10\ cm^{-1}$.[a]

	J_{II}							
J_c	1	2.5	5	10	20	30	40	50
10	5	5	5	3	1	1	1	1
20	5	5	5	4,5,3	5	7	7	7
30	5	5	5	6,7	7	7	7	7
40	5	5	5	5	7	7	7	7
50	5	5	5	5	7	7	7	7

[a]Values for J_{II} and J_c given in cm^{-1}.

Table 5. Total spin, S_{tot}, of the ground state for *case b* as a function of the exchange coupling constants, with $J_c = 5\ cm^{-1}$ and $J_{III} = 20\ cm^{-1}$.[a]

	J_o						
J_{II}	6	8	10	12	14	16	18
0	8	7	7	7	6	6	6
1	0,1,2,3	7	7	7	6	6	6
2	0,1,2,3	0,1,2,3	0,1,2,3	7,6,6,...	6	6	6
3	0,1,2,3	0,1,2,3	0,1,2,3	4,3	5,6,4,...	6	6
4	0,1,2,3	0,1,2,3	0,1,2,3	4,3	4,5,4,...	5,...1	4,...0
5	0,1,2,3	0,1,2,3	0,1,2,3	4	4	5,4	5,4

[a]Values for J_o and J_{II} given in cm^{-1}.

Table 6. Positional Parameters and B(eq) for $[Me_4N]_4[Mn_{10}O_4(biphen)_4Br_{12}] \cdot 4CH_3CN \cdot 0.5H_2O$ ($\mathbf{2} \cdot 4CH_3CN \cdot 0.5H_2O$).[a]

Atom	x	y	z	B(eq)[b]
Br(1)	1.0008(1)	0.0872(1)	0.8428(1)	2.2(1)
Br(2)	0.9127(1)	-0.1013(1)	0.8707(1)	2.2(1)
Br(3)	0.9733(1)	0.0748(1)	0.6212(1)	2.3(1)
Br(4)	0.8514(1)	-0.1317(1)	0.7132(1)	2.0(1)
Br(5)	0.8083(1)	0.0622(1)	0.7719(1)	2.4(1)
Br(6)	1.1210(1)	-0.1328(1)	0.7607(1)	2.2(1)
Br(7)	1.2226(2)	0.2025(2)	0.8199(2)	6.3(2)
Br(8)	0.7569(2)	0.2060(2)	0.6317(1)	3.9(1)
Br(9)	0.9015(2)	-0.2615(2)	0.5377(1)	4.3(2)
Br(10)	1.1680(1)	0.0453(2)	0.6955(1)	2.8(1)
Br(11)	1.0700(1)	-0.2420(2)	0.9436(1)	3.3(1)
Br(12)	1.0571(1)	-0.1161(2)	0.6003(1)	3.1(1)
Mn(1)	1.0585(2)	-0.0300(2)	0.6827(2)	2.0(2)
Mn(2)	0.9873(2)	0.1046(2)	0.7311(2)	1.7(1)
Mn(3)	1.0757(2)	-0.0234(2)	0.8158(1)	1.6(2)
Mn(4)	1.1392(2)	0.1084(2)	0.7733(2)	2.2(2)
Mn(5)	0.8965(2)	-0.0291(2)	0.6539(1)	1.6(2)
Mn(6)	0.8350(2)	0.1122(2)	0.6884(2)	1.9(2)
Mn(7)	1.0185(2)	-0.1557(2)	0.8638(1)	1.7(2)
Mn(8)	0.9145(2)	-0.0211(2)	0.7859(1)	1.8(2)

Table 6 contd. Positional Parameters and B(eq) for $[Me_4N]_4[Mn_{10}O_4(biphen)_4Br_{12}] \cdot 4CH_3CN \cdot 0.5H_2O$ (**2** $\cdot 4CH_3CN \cdot 0.5H_2O$).[a]

atom	x	y	z	B(eq)[b]
Mn(9)	0.9521(2)	-0.1672(2)	0.6106(2)	2.2(2)
Mn(10)	0.9864(2)	-0.1568(2)	0.7374(2)	1.6(1)
O(1)	0.9932(7)	-0.230(1)	0.7943(6)	1.6(7)
O(2)	1.1567(7)	0.032(1)	0.8389(6)	1.7(7)
O(3)	1.0973(7)	-0.076(1)	0.8843(6)	1.8(7)
O(4)	1.0553(8)	0.034(1)	0.7505(6)	2.0(7)
O(5)	1.0006(6)	-0.0833(8)	0.7934(5)	1.0(6)
O(6)	0.980(1)	-0.232(1)	0.6847(6)	2.1(7)
O(7)	0.8744(7)	-0.088(1)	0.5877(6)	1.7(7)
O(8)	1.0556(7)	0.1778(8)	0.7400(6)	1.6(7)
O(9)	0.8166(7)	0.026(1)	0.6288(6)	2.3(7)
O(10)	0.9186(7)	0.0339(7)	0.7153(5)	0.8(6)
O(11)	0.9219(8)	0.180(1)	0.7174(6)	2.4(8)
O(12)	0.9726(8)	-0.089(1)	0.6793(6)	2.0(7)
O(13)	1.159(2)	0.188(2)	0.916(2)	6(1)
N(1)	0.758(1)	0.198(2)	0.901(1)	5.2(7)
N(2)	0.267(1)	0.214(1)	0.627(1)	4.3(6)
N(3)	0.367(2)	0.244(2)	1.007(1)	7.6(8)
N(4)	0.467(2)	0.088(2)	0.981(2)	14(1)

Table 6 contd. Positional Parameters and B(eq) for $[Me_4N]_4[Mn_{10}O_4(biphen)_4Br_{12}] \cdot 4CH_3CN \cdot 0.5H_2O$ (**2** $\cdot 4CH_3CN \cdot 0.5H_2O$).[a]

atom	x	y	z	B(eq)[b]
N(5)	0.644(2)	0.061(2)	0.337(1)	10(1)
N(6)	0.341(2)	0.035(2)	0.125(1)	9.0(9)
N(7)	0.515(2)	0.031(2)	0.440(1)	8.7(9)
N(8)	1.084(2)	0.291(3)	0.986(2)	15(1)
C(1)	1.046(1)	0.240(1)	0.703(1)	1.7(5)
C(2)	1.078(1)	0.235(1)	0.668(1)	2.3(5)
C(3)	1.074(1)	0.294(2)	0.632(1)	3.8(6)
C(4)	1.038(1)	0.353(2)	0.637(1)	4.1(7)
C(5)	1.002(1)	0.359(1)	0.670(1)	3.2(6)
C(6)	1.007(1)	0.299(1)	0.706(1)	2.1(5)
C(7)	0.972(1)	0.299(1)	0.744(1)	1.9(5)
C(8)	0.975(1)	0.366(1)	0.773(1)	2.1(5)
C(9)	0.938(1)	0.374(2)	0.809(1)	3.5(6)
C(10)	0.898(1)	0.318(2)	0.810(1)	4.3(7)
C(11)	0.892(1)	0.252(1)	0.782(1)	2.1(5)
C(12)	0.929(1)	0.245(1)	0.749(1)	1.9(5)
C(13)	1.216(1)	0.001(1)	0.871(1)	1.7(5)
C(14)	1.260(1)	-0.006(1)	0.844(1)	2.2(5)
C(15)	1.322(1)	-0.033(1)	0.876(1)	2.4(5)
C(16)	1.339(1)	-0.051(1)	0.932(1)	2.7(6)

Table 6 contd. Positional Parameters and B(eq) for $[Me_4N]_4[Mn_{10}O_4(biphen)_4Br_{12}] \cdot 4CH_3CN \cdot 0.5H_2O$ (**2** $\cdot 4CH_3CN \cdot 0.5H_2O$).[a]

atom	x	y	z	B(eq)[b]
C(17)	1.294(1)	-0.042(1)	0.957(1)	2.7(6)
C(18)	1.230(1)	-0.017(1)	0.925(1)	1.8(5)
C(19)	1.184(1)	-0.007(1)	0.953(1)	2.3(5)
C(20)	1.202(1)	0.032(2)	1.004(1)	3.3(6)
C(21)	1.162(1)	0.037(2)	1.034(1)	3.3(6)
C(22)	1.100(1)	0.005(2)	1.015(1)	3.3(6)
C(23)	1.081(1)	-0.030(1)	0.964(1)	2.8(6)
C(24)	1.121(1)	-0.037(1)	0.935(1)	2.0(5)
C(25)	0.850(1)	-0.051(1)	0.539(1)	1.6(5)
C(26)	0.889(1)	-0.048(1)	0.506(1)	2.0(5)
C(27)	0.863(1)	-0.015(2)	0.455(1)	3.5(6)
C(28)	0.801(1)	0.017(2)	0.435(1)	4.0(7)
C(29)	0.763(1)	0.009(1)	0.465(1)	3.2(6)
C(30)	0.787(1)	-0.023(1)	0.518(1)	1.8(5)
C(31)	0.741(1)	-0.030(1)	0.547(1)	1.6(5)
C(32)	0.679(1)	-0.060(1)	0.521(1)	2.6(5)
C(33)	0.635(1)	-0.063(2)	0.548(1)	3.3(6)
C(34)	0.650(1)	-0.040(2)	0.600(1)	3.8(7)
C(35)	0.712(1)	-0.011(2)	0.627(1)	3.1(6)
C(36)	0.756(1)	-0.006(1)	0.602(1)	1.5(5)

Table 6 contd. Positional Parameters and B(eq) for $[Me_4N]_4[Mn_{10}O_4(biphen)_4Br_{12}] \cdot 4CH_3CN \cdot 0.5H_2O$ (**2** $\cdot 4CH_3CN \cdot 0.5H_2O$).[a]

atom	x	y	z	B(eq)[b]
C(37)	0.954(1)	-0.292(1)	0.783(1)	2.4(5)
C(38)	0.907(1)	-0.294(1)	0.807(1)	2.1(5)
C(39)	0.867(1)	-0.356(1)	0.800(1)	2.7(6)
C(40)	0.877(1)	-0.415(1)	0.770(1)	2.5(5)
C(41)	0.925(1)	-0.414(1)	0.745(1)	3.0(6)
C(42)	0.962(1)	-0.351(1)	0.752(1)	1.9(5)
C(43)	1.014(1)	-0.351(1)	0.728(1)	1.4(5)
C(44)	1.055(1)	-0.414(1)	0.738(1)	2.3(5)
C(45)	1.102(1)	-0.419(2)	0.716(1)	3.8(6)
C(46)	1.110(1)	-0.360(2)	0.684(1)	3.9(7)
C(47)	1.069(1)	-0.297(2)	0.675(1)	3.0(6)
C(48)	1.020(1)	-0.292(1)	0.695(1)	1.5(5)
C(49)	0.281(2)	0.287(2)	0.605(1)	6.5(9)
C(50)	0.329(2)	0.178(2)	0.653(2)	10(1)
C(51)	0.215(3)	0.180(3)	0.591(2)	15(1)
C(52)	0.247(2)	0.234(2)	0.675(2)	10(1)
C(53)	0.441(2)	0.260(3)	1.017(2)	11(1)
C(54)	0.343(3)	0.212(4)	0.954(3)	23(2)
C(55)	0.362(3)	0.202(4)	1.046(3)	20(2)
C(56)	0.337(2)	0.319(3)	1.006(2)	10(1)

Table 6 contd. Positional Parameters and B(eq) for $[Me_4N]_4[Mn_{10}O_4(biphen)_4Br_{12}] \cdot 4CH_3CN \cdot 0.5H_2O$ ($\mathbf{2} \cdot 4CH_3CN \cdot 0.5H_2O$).[a]

atom	x	y	z	B(eq)[b]
C(57)	0.696(2)	0.180(2)	0.857(2)	9(1)
C(58)	0.758(2)	0.277(2)	0.920(1)	6.6(9)
C(59)	0.760(2)	0.154(2)	0.949(2)	8(1)
C(60)	0.816(2)	0.181(2)	0.891(2)	11(1)
C(68)	0.284(2)	0.101(2)	0.183(1)	5.7(8)
C(69)	0.315(2)	0.063(2)	0.153(1)	4.8(7)
C(70)	0.691(2)	0.109(2)	0.273(1)	7(1)
C(71)	0.667(2)	0.087(3)	0.309(2)	9(1)
C(72)	0.546(2)	-0.059(2)	0.380(2)	9(1)
C(73)	0.523(2)	-0.013(2)	0.412(1)	5.8(8)
C(74)	0.535(2)	0.050(2)	0.918(1)	5.0(7)
C(75)	0.498(2)	0.069(2)	0.952(1)	6.6(9)
C(76)	1.139(2)	0.330(2)	0.973(2)	8(1)
C(77)	1.043(3)	0.275(4)	0.933(3)	22(2)
C(78)	1.108(2)	0.222(3)	1.007(2)	12(1)
C(79)	1.077(2)	0.343(3)	1.034(2)	13(1)
H(1)	0.931	-0.455	0.725	3.6
H(2)	1.104	0.192	0.669	2.7
H(3)	1.096	0.293	0.607	4.6
H(4)	1.037	0.395	0.614	4.9

Table 6 contd. Positional Parameters and B(eq) for $[Me_4N]_4[Mn_{10}O_4(biphen)_4Br_{12}] \cdot 4CH_3CN \cdot 0.5H_2O$ (**2** $\cdot 4CH_3CN \cdot 0.5H_2O$).[a]

atom	x	y	z	B(eq)[b]
H(5)	0.976	0.401	0.669	3.8
H(6)	1.002	0.405	0.770	2.5
H(7)	0.942	0.418	0.830	4.2
H(8)	0.871	0.325	0.831	5.1
H(9)	0.865	0.213	0.786	2.5
H(10)	1.075	-0.257	0.653	3.7
H(11)	1.143	-0.363	0.668	4.7
H(12)	1.130	-0.462	0.722	4.6
H(13)	1.050	-0.453	0.761	2.7
H(14)	0.902	-0.253	0.829	2.6
H(15)	0.834	-0.357	0.815	3.2
H(16)	0.850	-0.459	0.766	3.0
H(17)	0.931	-0.067	0.519	2.4
H(18)	0.889	-0.014	0.432	4.2
H(19)	0.786	0.043	0.402	4.8
H(20)	0.719	0.026	0.450	3.9
H(21)	1.038	-0.050	0.949	3.3
H(22)	1.072	0.006	1.035	4.0
H(23)	1.176	0.062	1.069	4.0
H(24)	1.243	0.055	1.018	4.0

Table 6 contd. Positional Parameters and B(eq) for $[Me_4N]_4[Mn_{10}O_4(biphen)_4Br_{12}] \cdot 4CH_3CN \cdot 0.5H_2O$ (**2** $\cdot 4CH_3CN \cdot 0.5H_2O$).[a]

atom	x	y	z	B(eq)[b]
H(25)	1.306	-0.053	0.994	3.3
H(26)	1.381	-0.068	0.952	3.3
H(27)	1.353	-0.041	0.859	2.8
H(28)	1.248	0.006	0.807	2.7
H(29)	0.667	-0.079	0.484	3.1
H(30)	0.724	0.004	0.664	3.7
H(31)	0.593	-0.083	0.529	3.9
H(32)	0.619	-0.044	0.617	4.5
H(33)	0.796	0.285	0.951	8.0
H(34)	0.758	0.310	0.892	8.0
H(35)	0.721	0.285	0.930	8.0
H(36)	0.661	0.194	0.869	1.1
H(37)	0.693	0.207	0.825	1.1
H(38)	0.694	0.128	0.850	1.1
H(39)	0.817	0.129	0.883	2.7
H(40)	0.816	0.209	0.860	2.7
H(41)	0.853	0.194	0.922	2.7
H(42)	0.722	0.165	0.957	9.5
H(43)	0.760	0.102	0.941	9.5
H(44)	0.798	0.166	0.979	9.5

Table 6 contd. Positional Parameters and B(eq) for $[Me_4N]_4[Mn_{10}O_4(biphen)_4Br_{12}] \cdot 4CH_3CN \cdot 0.5H_2O$ ($\mathbf{2} \cdot 4CH_3CN \cdot 0.5H_2O$).[a]

atom	x	y	z	B(eq)[b]
H(45)	0.318	0.310	0.631	7.8
H(46)	0.288	0.279	0.572	7.8
H(47)	0.245	0.320	0.598	7.8
H(48)	0.324	0.135	0.673	2.5
H(49)	0.346	0.162	0.626	2.5
H(50)	0.359	0.212	0.677	2.5
H(51)	0.283	0.258	0.702	1.5
H(52)	0.211	0.267	0.663	1.5
H(53)	0.236	0.190	0.689	1.5
H(54)	0.179	0.214	0.581	8.0
H(55)	0.224	0.167	0.559	8.0
H(56)	0.205	0.137	0.607	8.0
H(57)	0.359	0.343	1.040	2.5
H(58)	0.341	0.348	0.977	2.5
H(59)	0.292	0.313	1.001	2.5
H(60)	0.462	0.214	1.015	3.2
H(61)	0.443	0.293	0.990	3.2
H(62)	0.461	0.282	1.052	3.2
H(63)	0.298	0.201	0.944	7.3
H(64)	0.349	0.247	0.929	7.3

Table 6 contd. Positional Parameters and B(eq) for $[Me_4N]_4[Mn_{10}O_4(biphen)_4Br_{12}] \cdot 4CH_3CN \cdot 0.5H_2O$ ($\mathbf{2} \cdot 4CH_3CN \cdot 0.5H_2O$).[a]

atom	x	y	z	B(eq)[b]
H(65)	0.367	0.168	0.954	7.3
H(66)	0.317	0.191	1.039	4.6
H(67)	0.385	0.157	1.048	4.6
H(68)	0.379	0.228	1.080	4.6
H(69)	0.527	-0.001	0.907	6.0
H(70)	0.523	0.082	0.887	6.0
H(71)	0.580	0.056	0.939	6.0
H(72)	0.725	0.076	0.273	8.6
H(73)	0.658	0.109	0.237	8.6
H(74)	0.708	0.158	0.281	8.6
H(75)	0.310	0.141	0.203	6.9
H(76)	0.243	0.120	0.159	6.9
H(77)	0.276	0.067	0.208	6.9
H(78)	0.513	-0.093	0.360	1.1
H(79)	0.558	-0.030	0.355	1.1
H(80)	0.583	-0.086	0.403	1.1

[a]For atom-labelling scheme see Figure 1. Estimated standard deviations in the least significant figure are given in parentheses.
[b]$B(\text{eq}) = 8/3\pi^2(U_{11}(aa^*)^2 + U_{22}(bb^*)^2 + U_{33}(cc^*)^2 + 2U_{12}aa^*bb^*\cos\gamma + 2U_{13}aa^*cc^*\cos\beta + 2U_{23}bb^*cc^*\cos\alpha)$

Table 7. Intramolecular Bond Distances for $[Me_4N]_4[Mn_{10}O_4(biphen)_4Br_{12}] \cdot 4CH_3CN \cdot 0.5H_2O$ ($\mathbf{2} \cdot 4CH_3CN \cdot 0.5H_2O$).[a]

atom	atom	distance	atom	atom	distance
Br(1)	Mn(2)	2.859(5)	Mn(2)	O(4)	1.88(2)
Br(1)	Mn(3)	2.830(5)	Mn(2)	O(8)	1.95(1)
Br(1)	Mn(8)	2.752(5)	Mn(2)	O(10)	1.90(1)
Br(2)	Mn(7)	2.596(5)	Mn(2)	O(11)	1.92(2)
Br(2)	Mn(8)	2.663(5)	Mn(3)	O(2)	1.94(2)
Br(3)	Mn(1)	2.734(5)	Mn(3)	O(3)	1.93(1)
Br(3)	Mn(2)	2.839(5)	Mn(3)	O(4)	1.91(1)
Br(3)	Mn(5)	2.850(5)	Mn(3)	O(5)	1.88(1)
Br(4)	Mn(5)	2.812(4)	Mn(4)	O(2)	2.13(1)
Br(4)	Mn(8)	2.755(5)	Mn(4)	O(4)	2.18(2)
Br(4)	Mn(10)	2.850(5)	Mn(4)	O(8)	2.13(1)
Br(5)	Mn(6)	2.626(5)	Mn(5)	O(7)	1.94(1)
Br(5)	Mn(8)	2.689(5)	Mn(5)	O(9)	1.91(2)
Br(6)	Mn(1)	2.730(5)	Mn(5)	O(10)	1.88(1)
Br(6)	Mn(3)	2.823(4)	Mn(5)	O(12)	1.90(2)
Br(6)	Mn(10)	2.840(5)	Mn(6)	O(9)	2.14(2)
Br(7)	Mn(4)	2.469(5)	Mn(6)	O(10)	2.22(1)
Br(8)	Mn(6)	2.482(5)	Mn(6)	O(11)	2.16(2)
Br(9)	Mn(9)	2.493(5)	Mn(7)	O(1)	2.16(1)

Table 7 contd. Intramolecular Bond Distances for $[Me_4N]_4[Mn_{10}O_4(biphen)_4Br_{12}] \cdot 4CH_3CN \cdot 0.5H_2O$ (**2** $\cdot 4CH_3CN \cdot 0.5H_2O$).[a]

atom	atom	distance	atom	atom	distance
Br(10)	Mn(1)	2.681(5)	Mn(7)	O(3)	2.17(1)
Br(10)	Mn(4)	2.609(5)	Mn(7)	O(5)	2.18(1)
Br(11)	Mn(7)	2.520(5)	Mn(8)	O(5)	2.15(1)
Br(12)	Mn(1)	2.649(5)	Mn(8)	O(10)	2.13(1)
Br(12)	Mn(9)	2.596(5)	Mn(9)	O(6)	2.16(1)
Mn(1)	O(4)	2.14(2)	Mn(9)	O(7)	2.14(1)
Mn(1)	O(12)	2.15(2)	Mn(9)	O(12)	2.20(1)
Mn(10)	O(1)	1.95(2)	N(6)	C(69)	1.19(4)
Mn(10)	O(5)	1.91(1)	N(7)	C(73)	1.14(4)
Mn(10)	O(6)	1.90(1)	N(8)	C(76)	1.55(5)
Mn(10)	O(12)	1.88(1)	N(8)	C(77)	1.37(7)
O(1)	C(37)	1.36(3)	N(8)	C(78)	1.38(6)
O(2)	C(13)	1.38(3)	N(8)	C(79)	1.63(6)
O(3)	C(24)	1.43(2)	C(1)	C(2)	1.35(3)
O(6)	C(48)	1.34(3)	C(1)	C(6)	1.38(3)
O(7)	C(25)	1.36(2)	C(2)	C(3)	1.40(3)
O(8)	C(1)	1.44(3)	C(3)	C(4)	1.36(3)
O(9)	C(36)	1.38(2)	C(4)	C(5)	1.38(3)
O(11)	C(12)	1.40(3)	C(5)	C(6)	1.41(3)
N(1)	C(57)	1.47(4)	C(6)	C(7)	1.47(3)

Table 7 contd. Intramolecular Bond Distances for $[Me_4N]_4[Mn_{10}O_4(biphen)_4Br_{12}] \cdot 4CH_3CN \cdot 0.5H_2O$ ($\mathbf{2} \cdot 4CH_3CN \cdot 0.5H_2O$).[a]

atom	atom	distance	atom	atom	distance
N(1)	C(58)	1.50(4)	C(7)	C(8)	1.41(3)
N(1)	C(59)	1.46(4)	C(7)	C(12)	1.38(3)
N(1)	C(60)	1.42(4)	C(8)	C(9)	1.44(3)
N(2)	C(49)	1.51(4)	C(9)	C(10)	1.35(4)
N(2)	C(50)	1.46(4)	C(10)	C(11)	1.37(3)
N(2)	C(51)	1.33(5)	C(11)	C(12)	1.40(3)
N(2)	C(52)	1.52(4)	C(13)	C(14)	1.39(3)
N(3)	C(53)	1.59(5)	C(13)	C(18)	1.38(3)
N(3)	C(54)	1.41(7)	C(14)	C(15)	1.41(3)
N(3)	C(55)	1.31(7)	C(15)	C(16)	1.42(3)
N(3)	C(56)	1.49(5)	C(16)	C(17)	1.37(3)
N(4)	C(75)	1.24(4)	C(17)	C(18)	1.43(3)
N(5)	C(71)	1.13(5)	C(18)	C(19)	1.48(3)
C(19)	C(20)	1.44(3)	C(43)	C(44)	1.42(3)
C(19)	C(24)	1.39(3)	C(43)	C(48)	1.39(3)
C(20)	C(21)	1.39(3)	C(44)	C(45)	1.37(3)
C(21)	C(22)	1.39(3)	C(45)	C(46)	1.40(4)
C(22)	C(23)	1.38(3)	C(46)	C(47)	1.41(3)
C(23)	C(24)	1.37(3)	C(47)	C(48)	1.39(3)
C(25)	C(26)	1.43(3)	C(68)	C(69)	1.40(4)

Table 7 contd. Intramolecular Bond Distances for $[Me_4N]_4[Mn_{10}O_4(biphen)_4Br_{12}] \cdot 4CH_3CN \cdot 0.5H_2O$ (**2** $\cdot 4CH_3CN \cdot 0.5H_2O$).[a]

atom	atom	distance	atom	atom	distance
C(25)	C(30)	1.39(3)	C(35)	C(36)	1.38(3)
C(26)	C(27)	1.39(3)	C(37)	C(38)	1.42(3)
C(27)	C(28)	1.39(3)	C(37)	C(42)	1.40(3)
C(28)	C(29)	1.35(3)	C(38)	C(39)	1.38(3)
C(29)	C(30)	1.42(3)	C(39)	C(40)	1.38(3)
C(30)	C(31)	1.49(3)	C(40)	C(41)	1.45(3)
C(31)	C(32)	1.40(3)	C(41)	C(42)	1.35(3)
C(31)	C(36)	1.41(3)	C(42)	C(43)	1.49(3)
C(32)	C(33)	1.40(3)	C(70)	C(71)	1.32(5)
C(33)	C(34)	1.34(3)	C(72)	C(73)	1.40(5)
C(34)	C(35)	1.39(3)	C(74)	C(75)	1.44(4)

[a]Distances are in angstroms. For atom-labelling scheme, see Figure 1. Estimated standard deviations in the least significant figure are given in the parentheses.

Table 8. Intramolecular Bond Angles for $[Me_4N]_4[Mn_{10}O_4(biphen)_4Br_{12}] \cdot 4CH_3CN \cdot 0.5H_2O$ ($\mathbf{2} \cdot 4CH_3CN \cdot 0.5H_2O$).[a]

atom	atom	atom	angle	atom	atom	atom	angle
Mn(2)	Br(1)	Mn(3)	70.9(1)	Br(10)	Mn(1)	O(4)	85.7(4)
Mn(2)	Br(1)	Mn(8)	73.9(1)	Br(10)	Mn(1)	O(12)	175.5(4)
Mn(3)	Br(1)	Mn(8)	73.9(1)	Br(12)	Mn(1)	O(4)	176.1(4)
Mn(7)	Br(2)	Mn(8)	81.9(1)	Br(12)	Mn(1)	O(12)	85.9(4)
Mn(1)	Br(3)	Mn(2)	74.3(1)	O(4)	Mn(1)	O(12)	90.4(6)
Mn(1)	Br(3)	Mn(5)	74.4(1)	Br(1)	Mn(2)	Br(3)	162.9(1)
Mn(2)	Br(3)	Mn(5)	71.0(1)	Br(1)	Mn(2)	O(4)	82.6(5)
Mn(5)	Br(4)	Mn(8)	73.9(1)	Br(1)	Mn(2)	O(8)	99.2(5)
Mn(5)	Br(4)	Mn(10)	71.1(1)	Br(1)	Mn(2)	O(10)	86.0(4)
Mn(8)	Br(4)	Mn(10)	74.5(1)	Br(1)	Mn(2)	O(11)	93.5(5)
Mn(6)	Br(5)	Mn(8)	81.7(1)	Br(3)	Mn(2)	O(4)	86.2(5)
Mn(1)	Br(6)	Mn(3)	75.0(1)	Br(3)	Mn(2)	O(8)	92.6(5)
Mn(1)	Br(6)	Mn(10)	74.6(1)	Br(3)	Mn(2)	O(10)	82.4(4)
Mn(3)	Br(6)	Mn(10)	71.3(1)	Br(3)	Mn(2)	O(11)	98.3(5)
Mn(1)	Br(10)	Mn(4)	81.4(1)	O(4)	Mn(2)	O(8)	84.9(6)
Mn(1)	Br(12)	Mn(9)	82.4(1)	O(4)	Mn(2)	O(10)	96.3(6)
Br(3)	Mn(1)	Br(6)	163.7(2)	O(4)	Mn(2)	O(11)	174.9(7)
Br(3)	Mn(1)	Br(10)	97.2(1)	O(8)	Mn(2)	O(10)	174.8(6)
Br(3)	Mn(1)	Br(12)	96.6(1)	O(8)	Mn(2)	O(11)	92.6(6)
Br(3)	Mn(1)	O(4)	84.3(4)	O(10)	Mn(2)	O(11)	86.6(6)

Table 8 contd. Intramolecular Bond Angles for $[Me_4N]_4[Mn_{10}O_4(biphen)_4Br_{12}]\cdot 4CH_3CN\cdot 0.5H_2O$ (**2** $\cdot 4CH_3CN\cdot 0.5H_2O$).[a]

atom	atom	atom	angle	atom	atom	atom	angle
Br(3)	Mn(1)	O(12)	84.6(4)	Br(1)	Mn(3)	Br(6)	164.0(2)
Br(6)	Mn(1)	Br(10)	93.3(1)	Br(1)	Mn(3)	O(2)	97.0(5)
Br(6)	Mn(1)	Br(12)	94.3(1)	Br(1)	Mn(3)	O(3)	94.3(5)
Br(6)	Mn(1)	O(4)	84.1(4)	Br(1)	Mn(3)	O(4)	83.0(5)
Br(6)	Mn(1)	O(12)	84.1(4)	Br(1)	Mn(3)	O(5)	87.1(4)
Br(10)	Mn(1)	Br(12)	98.0(1)	Br(6)	Mn(3)	O(2)	93.2(5)
Br(6)	Mn(3)	O(3)	97.3(5)	Br(4)	Mn(5)	O(10)	87.2(4)
Br(6)	Mn(3)	O(4)	85.8(5)	Br(4)	Mn(5)	O(12)	83.2(5)
Br(6)	Mn(3)	O(5)	83.1(4)	O(7)	Mn(5)	O(9)	93.8(6)
O(2)	Mn(3)	O(3)	93.7(6)	O(7)	Mn(5)	O(10)	176.0(6)
O(2)	Mn(3)	O(4)	84.1(7)	O(7)	Mn(5)	O(12)	84.9(6)
O(2)	Mn(3)	O(5)	175.8(7)	O(9)	Mn(5)	O(10)	84.8(6)
O(3)	Mn(3)	O(4)	176.3(7)	O(9)	Mn(5)	O(12)	176.1(7)
O(3)	Mn(3)	O(5)	84.8(6)	O(10)	Mn(5)	O(12)	96.7(6)
O(4)	Mn(3)	O(5)	97.6(6)	Br(5)	Mn(6)	Br(8)	114.6(2)
Br(7)	Mn(4)	Br(10)	109.5(2)	Br(5)	Mn(6)	O(9)	108.8(5)
Br(7)	Mn(4)	O(2)	98.9(4)	Br(5)	Mn(6)	O(10)	86.0(4)
Br(7)	Mn(4)	O(4)	163.6(5)	Br(5)	Mn(6)	O(11)	109.6(4)
Br(7)	Mn(4)	O(8)	100.7(4)	Br(8)	Mn(6)	O(9)	98.3(4)
Br(10)	Mn(4)	O(2)	109.3(4)	Br(8)	Mn(6)	O(10)	159.4(4)

Table 8 contd. Intramolecular Bond Angles for $[Me_4N]_4[Mn_{10}O_4(biphen)_4Br_{12}]\cdot 4CH_3CN\cdot 0.5H_2O$ (**2** $\cdot 4CH_3CN\cdot 0.5H_2O$).[a]

atom	atom	atom	angle	atom	atom	atom	angle
Br(10)	Mn(4)	O(4)	86.8(4)	Br(8)	Mn(6)	O(11)	99.6(5)
Br(10)	Mn(4)	O(8)	110.5(4)	O(9)	Mn(6)	O(10)	72.0(6)
O(2)	Mn(4)	O(4)	73.5(6)	O(9)	Mn(6)	O(11)	125.2(6)
O(2)	Mn(4)	O(8)	125.9(6)	O(10)	Mn(6)	O(11)	73.4(5)
O(4)	Mn(4)	O(8)	73.7(5)	Br(2)	Mn(7)	Br(11)	108.6(2)
Br(3)	Mn(5)	Br(4)	164.0(2)	Br(2)	Mn(7)	O(1)	108.9(4)
Br(3)	Mn(5)	O(7)	94.0(4)	Br(2)	Mn(7)	O(3)	113.4(4)
Br(3)	Mn(5)	O(9)	97.9(5)	Br(2)	Mn(7)	O(5)	86.8(4)
Br(3)	Mn(5)	O(10)	82.5(4)	Br(11)	Mn(7)	O(1)	103.1(4)
Br(3)	Mn(5)	O(12)	85.9(5)	Br(11)	Mn(7)	O(3)	96.8(4)
Br(4)	Mn(5)	O(7)	96.7(4)	Br(11)	Mn(7)	O(5)	164.1(4)
Br(4)	Mn(5)	O(9)	93.3(5)	O(1)	Mn(7)	O(3)	123.7(6)
O(1)	Mn(7)	O(5)	74.7(5)	O(7)	Mn(9)	O(12)	73.4(6)
O(3)	Mn(7)	O(5)	72.6(5)	Br(4)	Mn(10)	Br(6)	162.2(1)
Br(1)	Mn(8)	Br(2)	98.2(1)	Br(4)	Mn(10)	O(1)	93.6(5)
Br(1)	Mn(8)	Br(4)	164.0(2)	Br(4)	Mn(10)	O(5)	86.0(4)
Br(1)	Mn(8)	Br(5)	94.7(1)	Br(4)	Mn(10)	O(6)	98.8(5)
Br(1)	Mn(8)	O(5)	84.3(4)	Br(4)	Mn(10)	O(12)	82.4(5)
Br(1)	Mn(8)	O(10)	84.8(4)	Br(6)	Mn(10)	O(1)	98.7(5)
Br(2)	Mn(8)	Br(4)	92.0(1)	Br(6)	Mn(10)	O(5)	82.1(4)

Table 8 contd. Intramolecular Bond Angles for $[Me_4N]_4[Mn_{10}O_4(biphen)_4Br_{12}]\cdot 4CH_3CN\cdot 0.5H_2O$ ($\mathbf{2}\cdot 4CH_3CN\cdot 0.5H_2O$).[a]

atom	atom	atom	angle	atom	atom	atom	angle
Br(2)	Mn(8)	Br(5)	97.9(1)	Br(6)	Mn(10)	O(6)	93.5(5)
Br(2)	Mn(8)	O(5)	85.6(4)	Br(6)	Mn(10)	O(12)	85.9(5)
Br(2)	Mn(8)	O(10)	174.7(4)	O(1)	Mn(10)	O(5)	85.9(6)
Br(4)	Mn(8)	Br(5)	96.1(1)	O(1)	Mn(10)	O(6)	92.6(6)
Br(4)	Mn(8)	O(5)	84.3(4)	O(1)	Mn(10)	O(12)	175.1(7)
Br(4)	Mn(8)	O(10)	84.2(4)	O(5)	Mn(10)	O(6)	175.1(7)
Br(5)	Mn(8)	O(5)	176.4(4)	O(5)	Mn(10)	O(12)	96.6(6)
Br(5)	Mn(8)	O(10)	86.2(4)	O(6)	Mn(10)	O(12)	85.3(6)
O(5)	Mn(8)	O(10)	90.3(5)	Mn(7)	O(1)	Mn(10)	99.1(6)
Br(9)	Mn(9)	Br(12)	109.2(2)	Mn(7)	O(1)	C(37)	129(1)
Br(9)	Mn(9)	O(6)	103.3(4)	Mn(10)	O(1)	C(37)	121(1)
Br(9)	Mn(9)	O(7)	98.1(4)	Mn(3)	O(2)	Mn(4)	101.4(6)
Br(9)	Mn(9)	O(12)	164.5(5)	Mn(3)	O(2)	C(13)	123(1)
Br(12)	Mn(9)	O(6)	108.0(5)	Mn(4)	O(2)	C(13)	127(1)
Br(12)	Mn(9)	O(7)	113.2(4)	Mn(3)	O(3)	Mn(7)	100.5(6)
Br(12)	Mn(9)	O(12)	86.3(4)	Mn(3)	O(3)	C(24)	122(1)
O(6)	Mn(9)	O(7)	123.4(6)	Mn(7)	O(3)	C(24)	123(1)
O(6)	Mn(9)	O(12)	72.3(5)	Mn(1)	O(4)	Mn(2)	113.3(7)
Mn(1)	O(4)	Mn(3)	112.8(7)	Mn(5)	O(10)	Mn(6)	100.2(6)
Mn(1)	O(4)	Mn(4)	106.0(7)	Mn(5)	O(10)	Mn(8)	112.9(6)

Table 8 contd. Intramolecular Bond Angles for $[Me_4N]_4[Mn_{10}O_4(biphen)_4Br_{12}]\cdot 4CH_3CN\cdot 0.5H_2O$ (**2** $\cdot 4CH_3CN\cdot 0.5H_2O$).[a]

atom	atom	atom	angle	atom	atom	atom	angle
Mn(2)	O(4)	Mn(3)	120.7(8)	Mn(6)	O(10)	Mn(8)	106.2(6)
Mn(2)	O(4)	Mn(4)	100.5(7)	Mn(2)	O(11)	Mn(6)	100.4(7)
Mn(3)	O(4)	Mn(4)	100.5(7)	Mn(2)	O(11)	C(12)	124(1)
Mn(3)	O(5)	Mn(7)	101.7(6)	Mn(6)	O(11)	C(12)	125(1)
Mn(3)	O(5)	Mn(8)	112.5(7)	Mn(1)	O(12)	Mn(5)	113.0(7)
Mn(3)	O(5)	Mn(10)	120.9(7)	Mn(1)	O(12)	Mn(9)	105.4(6)
Mn(7)	O(5)	Mn(8)	105.6(6)	Mn(1)	O(12)	Mn(10)	113.6(8)
Mn(7)	O(5)	Mn(10)	100.0(6)	Mn(5)	O(12)	Mn(9)	100.3(7)
Mn(8)	O(5)	Mn(10)	113.1(6)	Mn(5)	O(12)	Mn(10)	120.8(8)
Mn(9)	O(6)	Mn(10)	101.3(7)	Mn(9)	O(12)	Mn(10)	100.5(7)
Mn(9)	O(6)	C(48)	125(1)	C(57)	N(1)	C(58)	110(3)
Mn(10)	O(6)	C(48)	123(1)	C(57)	N(1)	C(59)	106(3)
Mn(5)	O(7)	Mn(9)	101.1(7)	C(57)	N(1)	C(60)	117(3)
Mn(5)	O(7)	C(25)	118(1)	C(58)	N(1)	C(59)	103(3)
Mn(9)	O(7)	C(25)	126(1)	C(58)	N(1)	C(60)	111(3)
Mn(2)	O(8)	Mn(4)	100.1(6)	C(59)	N(1)	C(60)	108(3)
Mn(2)	O(8)	C(1)	121(1)	C(49)	N(2)	C(50)	106(3)
Mn(4)	O(8)	C(1)	129(1)	C(49)	N(2)	C(51)	112(3)
Mn(5)	O(9)	Mn(6)	102.2(7)	C(49)	N(2)	C(52)	105(3)
Mn(5)	O(9)	C(36)	125(1)	C(50)	N(2)	C(51)	124(4)

Table 8 contd. Intramolecular Bond Angles for $[Me_4N]_4[Mn_{10}O_4(biphen)_4Br_{12}]\cdot 4CH_3CN\cdot 0.5H_2O$ ($\mathbf{2}\cdot 4CH_3CN\cdot 0.5H_2O$).[a]

atom	atom	atom	angle	atom	atom	atom	angle
Mn(6)	O(9)	C(36)	124(1)	C(50)	N(2)	C(52)	102(3)
Mn(2)	O(10)	Mn(5)	121.6(7)	C(51)	N(2)	C(52)	106(3)
Mn(2)	O(10)	Mn(6)	98.9(6)	C(53)	N(3)	C(54)	103(4)
Mn(2)	O(10)	Mn(8)	113.5(7)	C(53)	N(3)	C(55)	110(4)
C(53)	N(3)	C(56)	105(3)	C(10)	C(11)	C(12)	117(2)
C(54)	N(3)	C(55)	117(5)	O(11)	C(12)	C(7)	118(2)
C(54)	N(3)	C(56)	110(4)	O(11)	C(12)	C(11)	118(2)
C(55)	N(3)	C(56)	111(4)	C(7)	C(12)	C(11)	124(2)
C(76)	N(8)	C(77)	99(5)	O(2)	C(13)	C(14)	114(2)
C(76)	N(8)	C(78)	106(5)	O(2)	C(13)	C(18)	122(2)
C(76)	N(8)	C(79)	102(4)	C(14)	C(13)	C(18)	123(2)
C(77)	N(8)	C(78)	105(6)	C(13)	C(14)	C(15)	117(2)
C(77)	N(8)	C(79)	133(6)	C(14)	C(15)	C(16)	121(2)
C(78)	N(8)	C(79)	108(5)	C(15)	C(16)	C(17)	121(3)
O(8)	C(1)	C(2)	115(2)	C(16)	C(17)	C(18)	119(2)
O(8)	C(1)	C(6)	120(2)	C(13)	C(18)	C(17)	119(2)
C(2)	C(1)	C(6)	125(2)	C(13)	C(18)	C(19)	123(2)
C(1)	C(2)	C(3)	120(2)	C(17)	C(18)	C(19)	118(2)
C(2)	C(3)	C(4)	115(3)	C(18)	C(19)	C(20)	121(2)
C(3)	C(4)	C(5)	127(3)	C(18)	C(19)	C(24)	125(2)

Table 8 contd. Intramolecular Bond Angles for $[Me_4N]_4[Mn_{10}O_4(biphen)_4Br_{12}]\cdot 4CH_3CN\cdot 0.5H_2O$ (**2** $\cdot 4CH_3CN\cdot 0.5H_2O$).[a]

atom	atom	atom	angle	atom	atom	atom	angle
C(4)	C(5)	C(6)	117(3)	C(20)	C(19)	C(24)	114(2)
C(1)	C(6)	C(5)	116(2)	C(19)	C(20)	C(21)	123(3)
C(1)	C(6)	C(7)	122(2)	C(20)	C(21)	C(22)	120(3)
C(5)	C(6)	C(7)	121(2)	C(21)	C(22)	C(23)	118(3)
C(6)	C(7)	C(8)	116(2)	C(22)	C(23)	C(24)	122(3)
C(6)	C(7)	C(12)	127(2)	O(3)	C(24)	C(19)	119(2)
C(8)	C(7)	C(12)	117(2)	O(3)	C(24)	C(23)	118(2)
C(7)	C(8)	C(9)	121(2)	C(19)	C(24)	C(23)	123(2)
C(8)	C(9)	C(10)	118(3)	O(7)	C(25)	C(26)	119(2)
C(9)	C(10)	C(11)	124(3)	O(7)	C(25)	C(30)	124(2)
C(26)	C(25)	C(30)	117(2)	C(37)	C(42)	C(43)	121(2)
C(25)	C(26)	C(27)	120(2)	C(41)	C(42)	C(43)	118(2)
C(26)	C(27)	C(28)	121(3)	C(42)	C(43)	C(44)	116(2)
C(27)	C(28)	C(29)	120(3)	C(42)	C(43)	C(48)	121(2)
C(28)	C(29)	C(30)	120(3)	C(44)	C(43)	C(48)	123(2)
C(25)	C(30)	C(29)	121(2)	C(43)	C(44)	C(45)	120(2)
C(25)	C(30)	C(31)	122(2)	C(44)	C(45)	C(46)	119(3)
C(29)	C(30)	C(31)	117(2)	C(45)	C(46)	C(47)	120(3)
C(30)	C(31)	C(32)	120(2)	C(46)	C(47)	C(48)	123(3)
C(30)	C(31)	C(36)	123(2)	O(6)	C(48)	C(43)	122(2)
C(32)	C(31)	C(36)	117(2)	O(6)	C(48)	C(47)	121(2)

Table 8 contd. Intramolecular Bond Angles for $[Me_4N]_4[Mn_{10}O_4(biphen)_4Br_{12}]\cdot 4CH_3CN\cdot 0.5H_2O$ (**2** $\cdot 4CH_3CN\cdot 0.5H_2O$).[a]

atom	atom	atom	angle	atom	atom	atom	angle
C(31)	C(32)	C(33)	120(2)	C(43)	C(48)	C(47)	116(2)
C(32)	C(33)	C(34)	123(3)	N(6)	C(69)	C(68)	177(4)
C(33)	C(34)	C(35)	119(3)	N(5)	C(71)	C(70)	172(6)
C(34)	C(35)	C(36)	120(3)	N(7)	C(73)	C(72)	168(4)
O(9)	C(36)	C(31)	119(2)	N(4)	C(75)	C(74)	177(4)
O(9)	C(36)	C(35)	120(2)	C(37)	C(38)	C(39)	120(2)
C(31)	C(36)	C(35)	121(2)	C(38)	C(39)	C(40)	119(2)
O(1)	C(37)	C(38)	116(2)	C(39)	C(40)	C(41)	122(2)
O(1)	C(37)	C(42)	123(2)	C(40)	C(41)	C(42)	118(2)
C(38)	C(37)	C(42)	121(2)	C(37)	C(42)	C(41)	120(2)

[a]Angles are in degrees. For atom-labelling scheme, see Figure 1. Estimated standard deviations in the least significant figure are given in parentheses.

Table 9. U Values for $[Me_4N]_4[Mn_{10}O_4(biphen)_4Br_{12}] \cdot 4CH_3CN \cdot 0.5H_2O$ ($\mathbf{2} \cdot 4CH_3CN \cdot 0.5H_2O$).[a]

atom	U11	U22	U33	U12	U13	U23
Br(1)	0.029(2)	0.026(2)	0.028(2)	0.001(1)	0.008(1)	-0.007(1)
Br(2)	0.029(2)	0.034(2)	0.024(2)	-0.001(1)	0.015(1)	-0.001(1)
Br(3)	0.033(2)	0.028(2)	0.024(2)	-0.002(1)	0.009(1)	0.005(1)
Br(4)	0.024(2)	0.026(2)	0.025(2)	-0.005(1)	0.009(1)	-0.005(1)
Br(5)	0.024(2)	0.033(2)	0.037(2)	0.005(1)	0.016(1)	-0.001(1)
Br(6)	0.027(2)	0.025(2)	0.035(2)	0.009(1)	0.014(1)	0.002(1)
Br(7)	0.039(2)	0.042(2)	0.124(4)	-0.016(2)	-0.015(2)	0.008(2)
Br(8)	0.040(2)	0.036(2)	0.060(2)	0.011(2)	0.003(2)	0.008(2)
Br(9)	0.079(3)	0.035(2)	0.040(2)	-0.002(2)	0.010(2)	-0.015(2)
Br(10)	0.029(2)	0.042(2)	0.042(2)	0.001(1)	0.021(2)	0.007(1)
Br(11)	0.051(2)	0.039(2)	0.029(2)	0.003(2)	0.007(2)	0.010(1)
Br(12)	0.054(2)	0.039(2)	0.041(2)	-0.005(2)	0.035(2)	-0.008(1)
Mn(1)	0.027(3)	0.022(2)	0.032(3)	-0.001(2)	0.018(2)	-0.001(2)
Mn(2)	0.014(2)	0.020(2)	0.029(2)	0.002(2)	0.006(2)	0.001(2)
Mn(3)	0.021(2)	0.019(2)	0.021(2)	-0.002(2)	0.007(2)	-0.003(2)
Mn(4)	0.016(2)	0.025(2)	0.041(3)	0.001(2)	0.008(2)	0.005(2)
Mn(5)	0.023(2)	0.019(2)	0.017(2)	-0.001(2)	0.006(2)	-0.006(2)
Mn(6)	0.023(2)	0.022(2)	0.028(2)	0.002(2)	0.009(2)	-0.003(2)
Mn(7)	0.024(2)	0.021(2)	0.020(2)	-0.001(2)	0.009(2)	-0.001(2)
Mn(8)	0.021(2)	0.025(2)	0.023(2)	0.001(2)	0.009(2)	-0.000(2)
Mn(9)	0.038(3)	0.026(2)	0.024(2)	0.002(2)	0.015(2)	0.000(2)
Mn(10)	0.024(2)	0.020(2)	0.018(2)	0.003(2)	0.008(2)	-0.002(2)

Table 9 contd. U Values for $[Me_4N]_4[Mn_{10}O_4(biphen)_4Br_{12}] \cdot 4CH_3CN \cdot 0.5H_2O$ ($\mathbf{2} \cdot 4CH_3CN \cdot 0.5H_2O$).[a]

atom	U11	U22	U33	U12	U13	U23
O(1)	0.02(1)	0.01(1)	0.03(1)	0.001(8)	0.01(1)	-0.010(8)
O(2)	0.02(1)	0.03(1)	0.01(1)	-0.01(1)	-0.002(8)	-0.003(8)
O(3)	0.03(1)	0.03(1)	0.01(1)	-0.01(1)	0.00(1)	-0.01(1)
O(4)	0.04(1)	0.02(1)	0.02(1)	0.00(1)	0.01(1)	0.01(1)
O(5)	0.01(1)	0.03(1)	0.00(1)	0.001(8)	-0.001(7)	-0.003(7)
O(6)	0.06(1)	0.01(1)	0.02(1)	0.01(1)	0.02(1)	0.002(8)
O(7)	0.02(1)	0.02(1)	0.02(1)	0.006(8)	0.01(1)	0.014(8)
O(8)	0.01(1)	0.01(1)	0.04(1)	0.001(7)	0.01(1)	-0.002(8)
O(9)	0.02(1)	0.04(1)	0.03(1)	0.01(1)	0.00(1)	-0.01(1)
O(10)	0.01(1)	0.01(1)	0.02(1)	-0.001(7)	0.012(8)	-0.001(7)
O(11)	0.04(1)	0.02(1)	0.03(1)	-0.00(1)	0.01(1)	-0.01(1)
O(12)	0.04(1)	0.02(1)	0.03(1)	0.02(1)	0.02(1)	0.00(1)

[a]For atom-labelling scheme, see Figure 1. Estimated standard deviations in the least significant figure are given in parentheses. The anisotropic temperature factors are of the form $\exp[-2\pi^2(U_{11}h^2a^{*2}... + 2U_{12}hka^*b^* + ...)]$.

Table 10. Positional Parameters and B(eq) for $[Mn(CH_3CN)_4(H_2O)_2][Et_3NH]_2[Mn_{10}O_4(biphen)_4Br_{12}] \cdot 6CH_3CN \cdot 2.5H_2O$ (**3** $\cdot$ $6CH_3CN \cdot 2.5H_2O$).[a]

atom	x	y	z	B(eq)[b]
Br(1)	0.5884(1)	0.0266(1)	0.0889(1)	3.0(1)
Br(2)	0.7610(1)	0.0699(1)	0.1466(1)	4.1(1)
Br(3)	0.4668(1)	0.12240(9)	0.1728(1)	2.5(1)
Mn(1)	0.5545(1)	0.0943(1)	0.2506(1)	1.9(1)
Mn(2)	0.6522(1)	0.0421(1)	0.1723(1)	2.2(1)
Mn(3)	1/2	0	0.1572(2)	2.2(2)
Mn(4)	1.000	0	0.2876(4)	4.2(3)
O(1)	0.5667(5)	0.0182(5)	0.2160(5)	1.9(6)
O(2)	0.6226(5)	0.1260(5)	0.2127(5)	2.4(6)
O(3)	0.6694(5)	-0.0466(5)	0.2102(5)	2.1(6)
O(4)	1.000	0	0.369(2)	10(2)
O(5)	1.000	0	0.195(1)	2.9(8)
O(6)	1.000	0	1.000	8(1)
O(7)	1.089(2)	-0.045(2)	0	12(1)
N(1)	0.8968(9)	0.0206(9)	0.287(1)	7(1)
C(1)	0.696(1)	-0.099(1)	0.190(1)	3(1)
C(2)	0.695(1)	-0.108(1)	0.140(1)	4(1)
C(3)	0.723(1)	-0.162(1)	0.116(1)	6(2)
C(4)	0.756(1)	-0.204(1)	0.148(1)	5(1)

Table 10 contd. Positional Parameters and B(eq) for $[Mn(CH_3CN)_4(H_2O)_2][Et_3NH]_2[Mn_{10}O_4(biphen)_4Br_{12}] \cdot 6CH_3CN \cdot 2.5H_2O$ (**3** · $6CH_3CN \cdot 2.5H_2O$).[a]

atom	x	y	z	B(eq)[b]
C(5)	0.757(1)	-0.193(1)	0.197(1)	4(1)
C(6)	0.730(1)	-0.143(1)	0.219(1)	3(1)
C(7)	0.6223(9)	0.188(1)	0.193(1)	3(1)
C(8)	0.615(1)	0.198(1)	0.142(1)	4(1)
C(9)	0.615(1)	0.260(1)	0.123(1)	5(2)
C(10)	0.624(1)	0.308(1)	0.157(1)	5(1)
C(11)	0.631(1)	0.298(1)	0.206(1)	4(1)
C(12)	0.6309(8)	0.2381(9)	0.226(1)	2(1)
C(13)	0.846(1)	0.030(1)	0.286(1)	6(2)
C(14)	0.781(1)	0.038(1)	0.287(1)	7(2)
C(15)	1.266(3)	0.025(3)	0	12(2)
C(16)	1.235(5)	-0.011(5)	0	23(3)
C(17)	1.245(3)	-0.082(3)	0	14(2)
C(18)	1.175(2)	-0.114(2)	-0.016(2)	7(2)
C(19)	1.289(3)	-0.148(3)	0	15(2)
C(20)	1.116(2)	0.041(2)	0.057(2)	18(2)
C(21)	1.118(2)	0.057(2)	0.110(2)	12(1)
C(22)	1.134(1)	0.072(1)	0.158(1)	6.1(7)

Table 10 contd. Positional Parameters and B(eq) for $[Mn(CH_3CN)_4(H_2O)_2][Et_3NH]_2[Mn_{10}O_4(biphen)_4Br_{12}] \cdot 6CH_3CN \cdot 2.5H_2O$ (**3** · $6CH_3CN \cdot 2.5H_2O$).[a]

atom	x	y	z	B(eq)[b]
C(23)	0.530(2)	-0.101(2)	1.000	7(1)
C(24b)	0.488(3)	-0.160(4)	1.000	5(2)
C(24a)	0.590	-0.110	1.000	12(3)
C(25b)	0.457(3)	-0.197(3)	1.000	5(2)
C(25a)	0.658	-0.130	1.000	10(2)
H(1)	0.675	-0.078	0.119	4.9
H(2)	0.720	-0.169	0.080	7.2
H(3)	0.776	-0.239	0.134	5.5
H(4)	0.779	-0.222	0.218	4.6
H(5)	0.610	0.164	0.119	4.7
H(6)	0.610	0.268	0.088	6.0
H(7)	0.625	0.350	0.145	5.4
H(8)	0.637	0.333	0.228	4.5
H(9)	0.771	0.081	0.286	8.5
H(10)	0.763	0.017	0.258	8.5
H(11)	0.764	0.020	0.317	8.5

[a] Estimated standard deviations in the least significant figure are given in parentheses. [b] $B(eq) = 8/3\pi^2(U_{11}(aa^*)^2 + U_{22}(bb^*)^2 + U_{33}(cc^*)^2 + 2U_{12}aa^*bb^*\cos\gamma + 2U_{13}aa^*cc^*\cos\beta + 2U_{23}bb^*cc^*\cos\alpha)$

Table 11. Intramolecular Bond Distances for $[Mn(CH_3CN)_4(H_2O)_2]$-$[Et_3NH]_2[Mn_{10}O_4(biphen)_4Br_{12}] \cdot 6CH_3CN \cdot 2.5H_2O$ (**3** $\cdot 6CH_3CN \cdot$-$2.5H_2O$).[a]

atom	atom	distance	atom	atom	distance
Br(1)	Mn(2)	2.608(4)	N(1)	C(13)	1.10(2)
Br(1)	Mn(3)	2.671(4)	C(3)	C(4)	1.41(4)
Br(2)	Mn(2)	2.495(3)	C(4)	C(5)	1.32(3)
Br(3)	Mn(1)	2.843(4)	C(5)	C(6)	1.35(3)
Br(3)	Mn(1)'	2.810(4)	C(6)	C(12)	1.47(3)
Br(3)	Mn(3)	2.742(2)	C(7)	C(8)	1.37(3)
Mn(1)	O(1)	1.88(1)	C(7)	C(12)	1.40(3)
Mn(1)	O(2)	1.89(1)	C(8)	C(9)	1.41(3)
Mn(1)	O(3)	1.92(1)	C(9)	C(10)	1.37(4)
Mn(2)	O(1)	2.22(1)	C(10)	C(11)	1.31(3)
Mn(2)	O(2)	2.18(1)	C(11)	C(12)	1.40(3)
Mn(2)	O(3)	2.17(1)	C(13)	C(14)	1.41(3)
Mn(3)	O(1)	2.14(1)	C(15)	C(16)	1.0(1)
Mn(4)	O(4)	2.15(4)	C(16)	C(17)	1.5(1)
Mn(5)	O(5)	2.45(3)	C(17)	C(18)	1.68(7)
Mn(4)	N(1)	2.25(2)	C(17)	C(19)	1.70(8)
O(2)	C(7)	1.43(2)	C(20)	C(21)	1.42(6)
O(3)	C(1)	1.35(2)	C(21)	C(22)	1.38(5)

Table 11 contd. Intramolecular Bond Distances for $[Mn(CH_3CN)_4(H_2O)_2][Et_3NH]_2[Mn_{10}O_4(biphen)_4Br_{12}] \cdot 6CH_3CN \cdot 2.5H_2O$ (**3** $\cdot 6CH_3CN \cdot 2.5H_2O$).[a]

atom	atom	distance	atom	atom	distance
C(1)	C(2)	1.35(3)	C(23)	C(24a)	1.29(4)
C(1)	C(6)	1.41(3)	C(24b)	C(25b)	1.03(9)
C(2)	C(3)	1.44(3)	C(24a)	C(25a)	1.4995(2)
C(23)	C(24b)	1.55(8)			

[a]Distances are in angstroms. Estimated standard deviations in the least significant figure are given in the parentheses.

Table 12. Intramolecular Bond Angles for $[Mn(CH_3CN)_4(H_2O)_2][Et_3NH]_2$-$[Mn_{10}O_4(biphen)_4Br_{12}] \cdot 6CH_3CN \cdot 2.5H_2O$ (**3**$\cdot 6CH_3CN \cdot 2.5H_2O$).[a]

atom	atom	atom	angle	atom	atom	atom	angle
Mn(2)	Br(1)	Mn(3)	80.1(1)	Br(1)	Mn(3)	Br(1)'	95.2(2)
Mn(1)	Br(3)	Mn(1)'	71.2(1)	Br(1)	Mn(3)	Br(3)	94.67(8)
Mn(1)'	Br(3)'	Mn(3)'	74.7(1)	Br(1)'	Mn(3)	Br(3)	96.95(9)
Mn(1)	Br(3)'	Mn(3)'	74.6(1)	Br(1)	Mn(3)	O(1)	88.8(3)
Br(3)	Mn(1)	Br(3)'	163.3(1)	Br(1)	Mn(3)	O(1)'	175.9(4)
Br(3)	Mn(1)	O(1)'	85.6(4)	Br(3)	Mn(3)	Br(3)'	162.7(2)
Br(3)	Mn(1)	O(1)	82.0(4)	Br(3)	Mn(3)	O(1)	83.7(3)
Br(3)	Mn(1)	O(2)	92.9(4)	Br(3)	Mn(3)	O(1)'	83.8(3)
Br(3)	Mn(1)	O(3)'	98.9(4)	O(1)	Mn(3)	O(1)'	87.2(7)
Br(3)'	Mn(1)	O(1)	82.9(4)	O(4)	Mn(4)	N(1)	90.4(8)
Br(3)'	Mn(1)	O(1)'	86.8(4)	N(1)	Mn(4)	O(5)	89.6(8)
Br(3)'	Mn(1)	O(2)	98.5(4)	O(3)	C(1)	C(2)	120(2)
Br(3)'	Mn(1)	O(3)'	92.7(4)	O(3)	C(1)	C(6)	124(2)
O(1)	Mn(1)	O(1)'	94.1(7)	C(2)	C(1)	C(6)	116(2)
O(1)	Mn(1)	O(2)	86.9(5)	C(1)	C(2)	C(3)	124(3)
O(1)	Mn(1)	O(3)'	175.5(6)	C(2)	C(3)	C(4)	116(3)
O(1)'	Mn(1)	O(2)	174.7(6)	C(3)	C(4)	C(5)	120(2)
O(1)'	Mn(1)	O(3)'	86.4(5)	C(4)	C(5)	C(6)	123(2)
O(2)	Mn(1)	O(3)'	93.0(5)	C(1)	C(6)	C(5)	122(2)

Table 12 contd. Intramolecular Bond Angles for $[Mn(CH_3CN)_4(H_2O)_2][Et_3NH]_2[Mn_{10}O_4(biphen)_4Br_{12}] \cdot 6CH_3CN \cdot 2.5H_2O$ (**3**$\cdot 6CH_3CN \cdot 2.5H_2O$).[a]

atom	atom	atom	angle	atom	atom	atom	angle
Br(1)	Mn(2)	Br(2)	106.8(1)	C(1)	C(6)	C(12)	118(2)
Br(1)	Mn(2)	O(1)	88.7(4)	C(5)	C(6)	C(12)	120(2)
Br(1)	Mn(2)	O(2)	111.4(4)	O(2)	C(7)	C(8)	120(2)
Br(1)	Mn(2)	O(3)	111.4(4)	O(2)	C(7)	C(12)	119(2)
Br(2)	Mn(2)	O(1)	164.5(4)	C(8)	C(7)	C(12)	121(2)
Br(2)	Mn(2)	O(2)	102.0(3)	C(7)	C(8)	C(9)	119(2)
Br(2)	Mn(2)	O(3)	100.1(3)	C(8)	C(9)	C(10)	118(3)
O(1)	Mn(2)	O(2)	72.3(4)	C(9)	C(10)	C(11)	123(2)
O(1)	Mn(2)	O(3)	72.6(4)	C(10)	C(11)	C(12)	121(2)
O(2)	Mn(2)	O(3)	122.8(5)	C(6)	C(12)'	C(7)'	123(2)
Mn(1)	O(1)	Mn(1)'	121.9(7)	C(6)	C(12)'	C(11)'	119(2)
Mn(1)	O(1)	Mn(2)	99.6(5)	C(7)	C(12)	C(11)	117(2)
Mn(1)	O(1)	Mn(3)	114.6(5)	N(1)	C(13)	C(14)	176(3)
Mn(1)'	O(1)	Mn(2)	100.1(5)	C(15)	C(16)	C(17)	131(13)
Mn(1)'	O(1)	Mn(3)	113.5(5)	C(16)	C(17)	C(18)	106(6)
Mn(2)	O(1)	Mn(3)	102.4(6)	C(16)	C(17)	C(19)	154(7)
Mn(1)	O(2)	Mn(2)	100.8(5)	C(18)	C(17)	C(19)	99(5)

Table 12 contd. Intramolecular Bond Angles for $[Mn(CH_3CN)_4(H_2O)_2][Et_3NH]_2[Mn_{10}O_4(biphen)_4Br_{12}] \cdot 6CH_3CN \cdot 2.5H_2O$ (**3**$\cdot 6CH_3CN \cdot 2.5H_2O$).[a]

atom	atom	atom	angle	atom	atom	atom	angle
Mn(1)	O(2)	C(7)	122(1)	C(20)	C(21)	C(22)	166(5)
Mn(2)	O(2)	C(7)	126(1)	C(24b)	C(23)	C(24a)	117(4)
Mn(1)'	O(3)	Mn(2)	100.5(5)	C(23)	C(24b)	C(25b)	176(8)
Mn(1)'	O(3)	C(1)	119(1)	C(23)	C(24a)	C(25a)	172(2)
Mn(2)	O(3)	C(1)	128(1)				
Mn(4)	N(1)	C(13)	179(3)				

[a]Angles are in degrees. Estimated standard deviations in the least significant figure are given in parentheses.

Table 13. U values for $[Mn(CH_3CN)_4(H_2O)_2][Et_3NH]_2[Mn_{10}O_4(biphen)_4Br_{12}] \cdot 6CH_3CN \cdot 2.5H_2O$ (**3** $\cdot 6CH_3CN \cdot 2.5H_2O$).[a]

atom	U11	U22	U33	U12	U13	U23
Br(1)	0.036(1)	0.038(1)	0.040(2)	-0.003(1)	0.005(1)	0.001(1)
Br(2)	0.028(1)	0.043(1)	0.084(2)	-0.008(1)	0.018(1)	0.002(1)
Br(3)	0.029(1)	0.021(1)	0.047(1)	0.000(1)	-0.003(1)	0.007(1)
Mn(1)	0.018(2)	0.017(2)	0.039(2)	-0.001(1)	0.001(2)	-0.002(2)
Mn(2)	0.021(2)	0.021(2)	0.043(2)	-0.001(1)	0.007(2)	-0.000(2)
Mn(3)	0.022(2)	0.022(2)	0.038(3)	-0.002(2)	0	0
Mn(4)	0.028(2)	0.028	0.105(8)	0	0	0
O(1)	0.020(7)	0.015(7)	0.038(9)	-0.000(5)	0.002(7)	0.003(7)
O(2)	0.023(7)	0.016(7)	0.05(1)	-0.007(6)	0.013(7)	0.008(7)
O(3)	0.021(7)	0.013(7)	0.05(1)	0.005(6)	0.006(7)	-0.003(7)
O(4)	0.15(3)	0.15	0.07(4)	0	0	0
O(5)	0.04(1)	0.04	0.03(2)	0	0	0
N(1)	0.04(1)	0.03(1)	0.20(3)	0.00(1)	-0.04(2)	0.00(2)
C(1)	0.03(1)	0.03(1)	0.05(2)	-0.00(1)	0.02(1)	0.00(1)
C(2)	0.03(1)	0.05(2)	0.08(2)	0.02(1)	0.00(1)	-0.00(2)
C(3)	0.06(2)	0.07(2)	0.10(3)	0.01(2)	0.04(2)	-0.04(2)
C(4)	0.05(2)	0.03(1)	0.10(2)	0.03(1)	0.03(2)	0.01(2)
C(5)	0.05(2)	0.05(2)	0.05(2)	0.01(1)	0.03(1)	-0.00(1)
C(6)	0.04(1)	0.03(1)	0.04(2)	0.01(1)	0.01(1)	0.01(1)

Table 13 contd. U values for $[Mn(CH_3CN)_4(H_2O)_2][Et_3NH]_2[Mn_{10}O_4(biph-en)_4Br_{12}] \cdot 6CH_3CN \cdot 2.5H_2O$ ($\mathbf{3} \cdot 6CH_3CN \cdot 2.5H_2O$).[a]

atom	U11	U22	U33	U12	U13	U23
C(7)	0.01(1)	0.03(1)	0.06(2)	0.00(1)	0.01(1)	-0.00(1)
C(8)	0.04(1)	0.06(2)	0.05(2)	-0.02(1)	-0.01(1)	-0.00(1)
C(9)	0.05(2)	0.06(2)	0.08(2)	0.01(1)	0.02(2)	0.04(2)
C(10)	0.05(2)	0.02(1)	0.10(3)	-0.00(1)	0.00(2)	-0.00(2)
C(11)	0.05(2)	0.03(1)	0.06(2)	-0.00(1)	0.02(2)	0.00(1)
C(12)	0.01(1)	0.02(1)	0.06(2)	-0.011(9)	0.01(1)	-0.01(1)
C(13)	0.02(1)	0.03(1)	0.19(4)	-0.00(1)	-0.02(2)	-0.01(2)
C(14)	0.04(2)	0.08(2)	0.16(3)	0.01(1)	-0.00(2)	0.01(2)

[a]Estimated standard deviations in the least significant figure are given in parentheses. The anisotropic temperature factors are of the form $\exp[-2\pi^2-(U_{11}h^2a^{*2}... + 2U_{12}hka^*b^* + ...)]$.

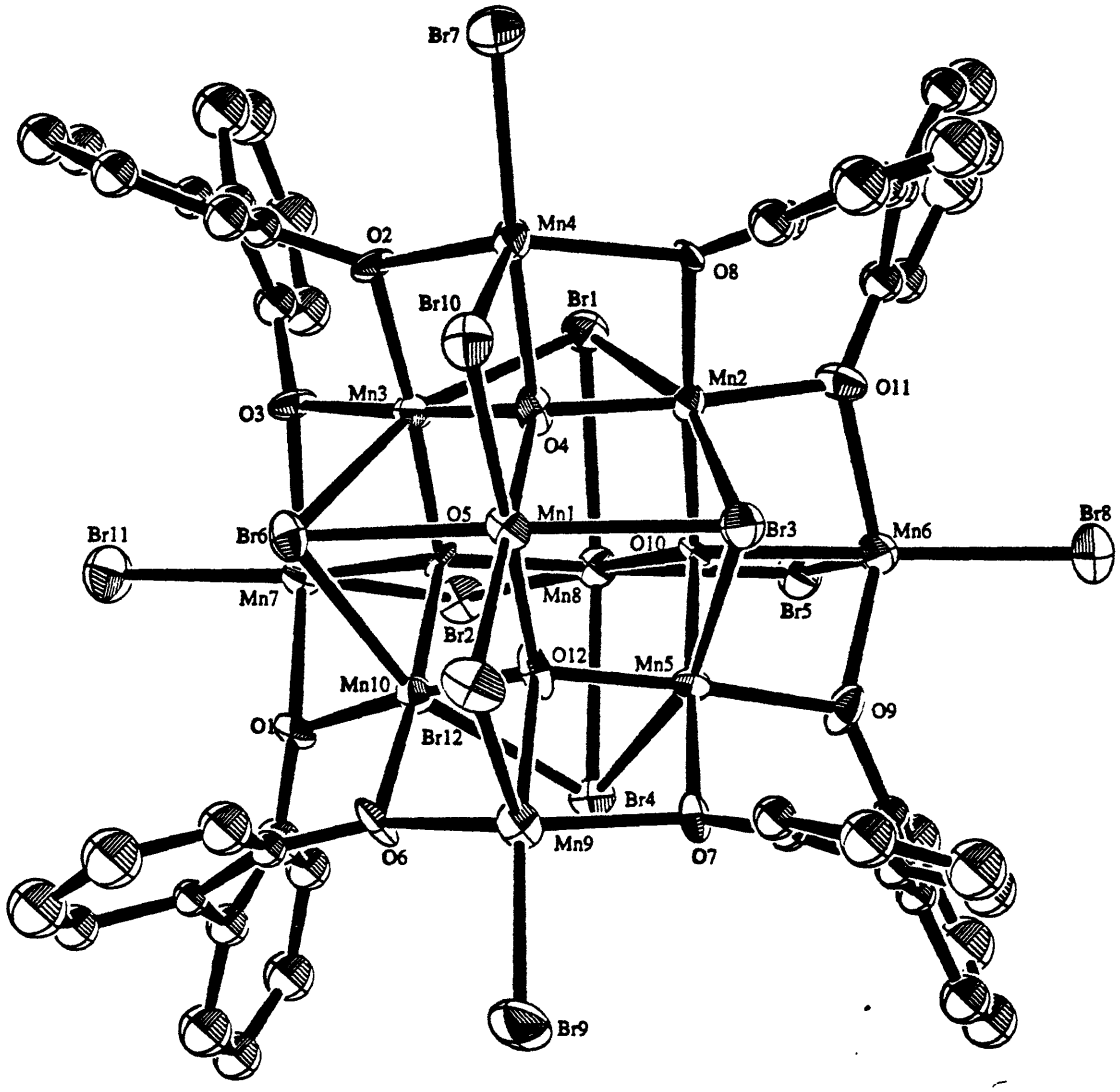

Figure 1. ORTEP diagram showing the anion of $[Me_4N]_4[Mn_{10}O_4(biphen)_4Br_{12}]$ (**2**) with 50% probability thermal ellipsoids. Hydrogen atoms have been omitted for clarity.

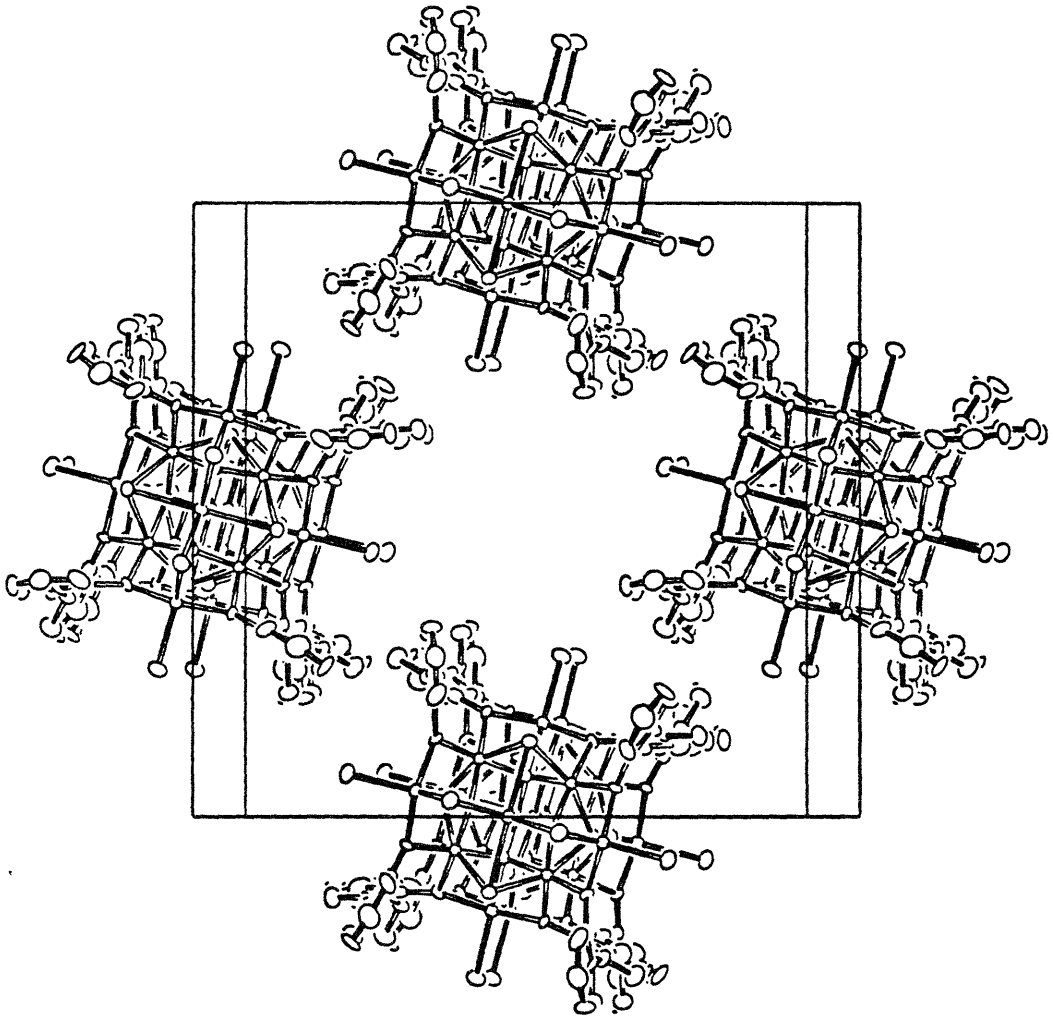

Figure 2. Packing diagram showing non-hydrogen atoms of the anion of $[Et_3NH]_2[Mn(CH_3CN)_4\text{-}(H_2O)_2][Mn_{10}O_4(biphen)_4Br_{12}]$ (**3**).

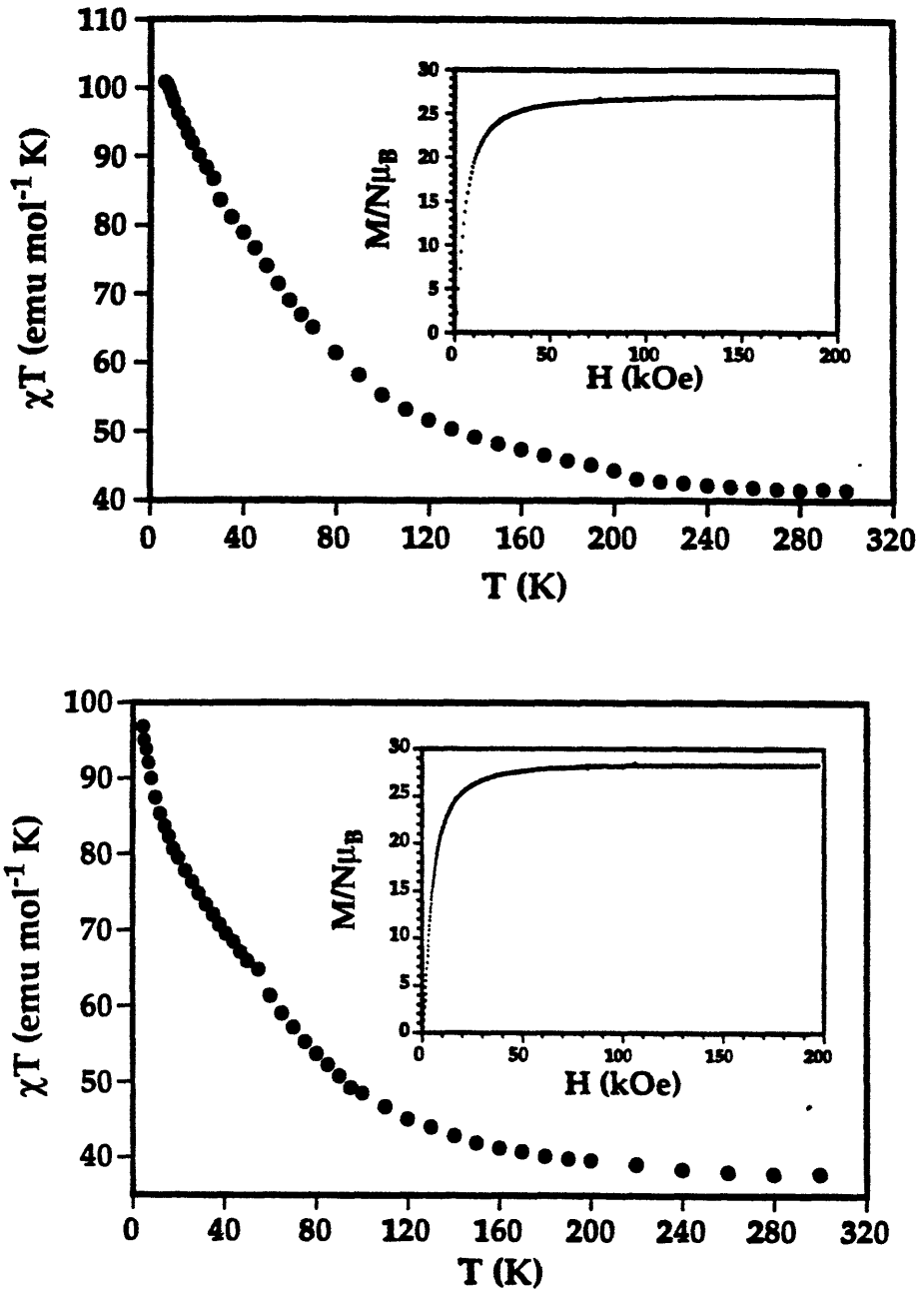

Figure 3. (a) Plot of the product of the temperature times molar susceptibility versus temperature for **1**. Inset: Plot of the reduced magnetization versus field, where *N* is Avogadro's number and μ_B is the Bohr magneton, at 4.2 K for **1**. (b) Plot of the product of the temperature times molar susceptibility versus temperature for **2**. Inset: Plot of the reduced magnetization versus field, where *N* is Avogadro's number and μ_B is the Bohr magneton, at 4.2 K for **2**.

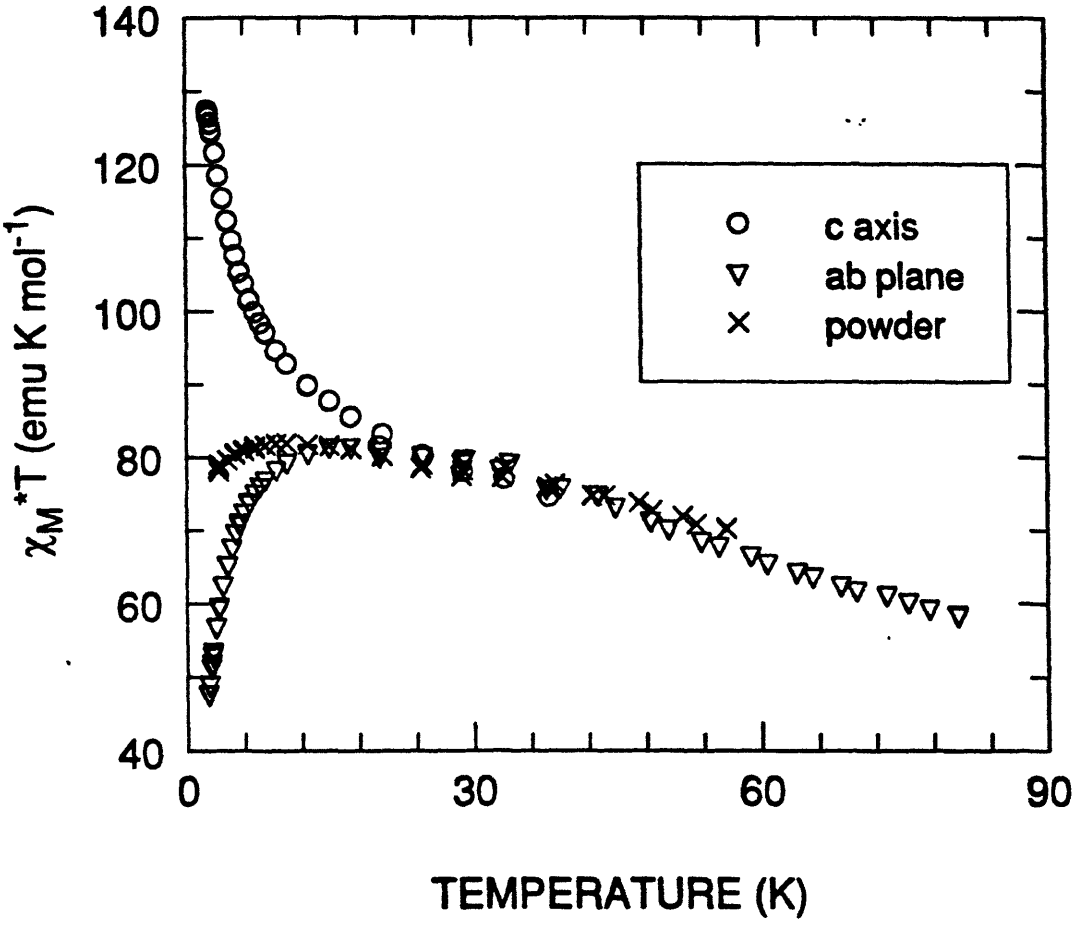

Figure 4. Plot of the product of the temperature times molar susceptibility versus temperature for (3) on a powder sample (x), a single crystal with the applied field parallel (o) and perpendicular (∇) to the tetragonal *c* axis. H = 1000 Oe.

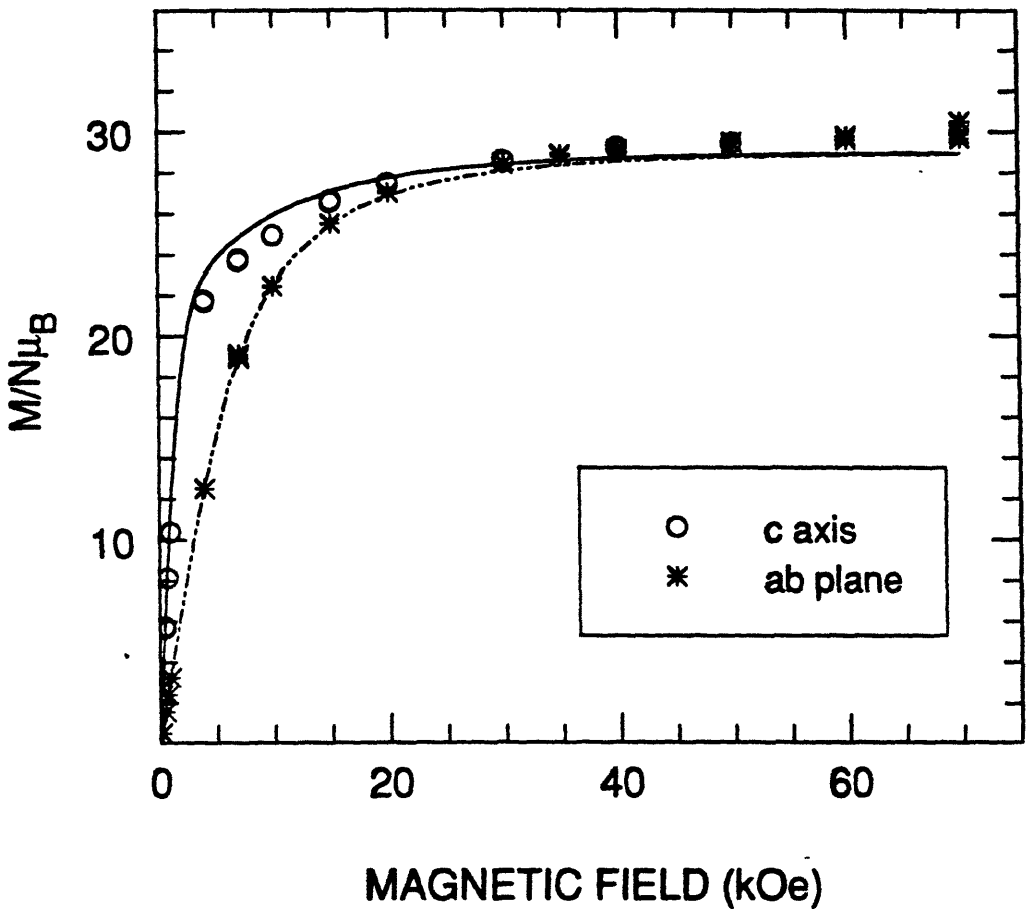

Figure 5. Plot of the reduced magnetization versus field for a single crystal of **3** at 2 K with the applied field parallel (o) and perpendicular (∇) to the tetragonal *c* axis. The solid and dashed lines correspond to the simulated curve for an $S = 12$ system with $g = 2.0$ and $D = -0.37$ cm^{-1}, including a simple Brillioun function taking into account the paramagnetic contribution from the isolated $S = 5/2$ Mn(II) cation.

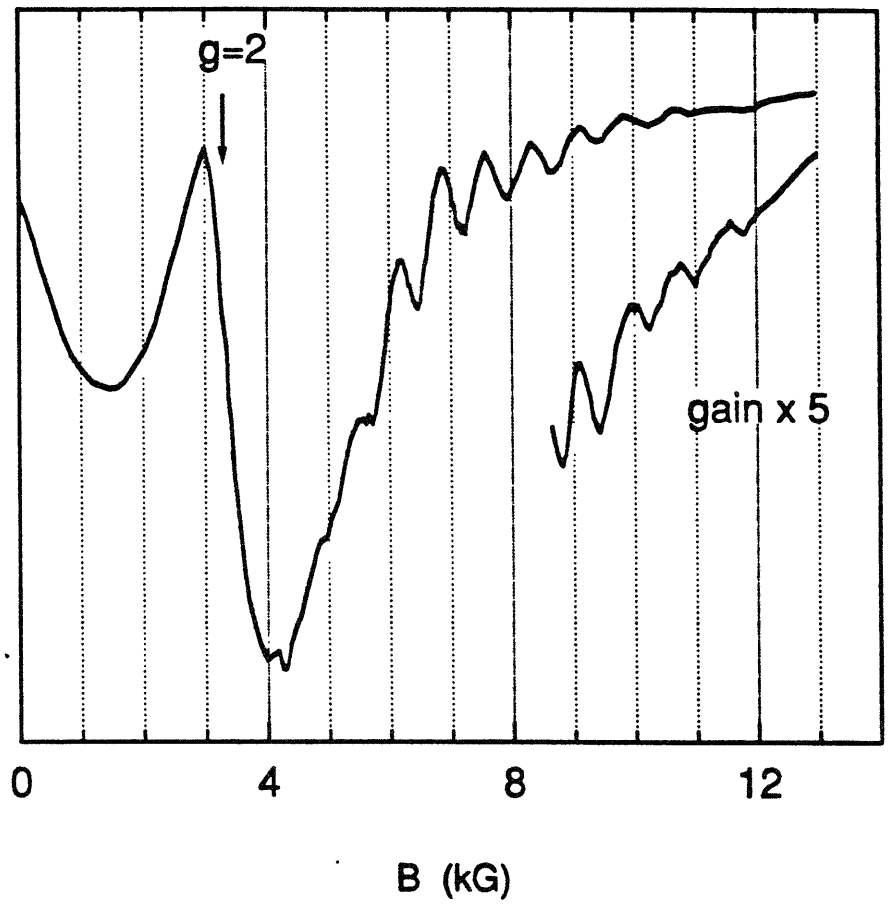

Figure 6. X-Band EPR spectrum of a single crystal of **3** at 4.2 K with the static magnetic field oriented parallel to the tetragonal *c* axis.

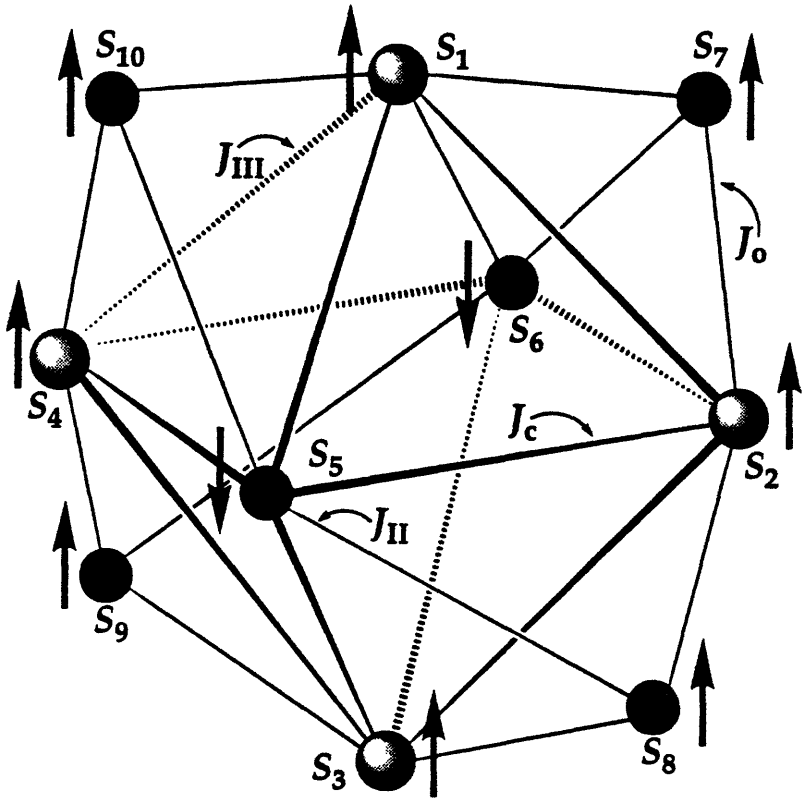

$S_1 \longrightarrow Mn_2$	$S_6 \longrightarrow Mn_8$
$S_2 \longrightarrow Mn_5$	$S_7 \longrightarrow Mn_6$
$S_3 \longrightarrow Mn_{10}$	$S_8 \longrightarrow Mn_9$
$S_4 \longrightarrow Mn_3$	$S_9 \longrightarrow Mn_7$
$S_5 \longrightarrow Mn_1$	$S_{10} \longrightarrow Mn_4$

Figure 7. Diagram of the spin topology and magnetic exchange coupling pathways for the $[Mn_{10}O_4(biphen)_4X_{12}]^{4-}$ anion (X = Cl^-, Br^-). Black spheres are Mn(II) sites and grey spheres are Mn(III) sites. The large arrows represent the direction for the spin vectors at each manganese site as described by case *a* (see Theoretical Analysis). The spin labels are correlated with the manganese atoms shown in Figure 1.